UNIVERSITY OF ADELAIDE LIBRARY
22·2·01

Transient Phase Conjugation using Stimulated Brillouin Scattering

by

Shahraam Afshaarvahid

Thesis submitted for the degree of
Doctor of Philosophy
in
The University of Adelaide
Department of Physics and Mathematical Physics
January, 2001

This work contains no material which has been accepted for the award of any other degree or diploma in any University or other tertiary institution and, to the best of my knowledge and belief, contains no material previously published or written by another person, except where due reference has been made in the text.

I give consent to this copy of my thesis, when deposited in the University Library, being available for loan and photocopying.

SIGNED:
DATE:

Supervisor: Prof. J. Munch

Acknowledgments

I would like to use this opportunity to thank all the people who have supported and influenced this Ph.D.

Firstly, I like to thank Zari and Shayan (my wife and my son). Words just can't express my feelings, gratitude and appreciation to them. Their continual love, support, encouragement, bearing, tolerance and patience made this work at all possible. They were there for me whenever I was confused, lost and disappointed. I would like to express my heartfelt appreciation to Zari, especially. What she has sacrificed and given me during these years is priceless.

My appreciations also goes to the rest of my family in Iran. I really appreciate my mom, dad, brothers and sister for their endless support, encouragement and concern.

I specially thank my supervisor, Prof. Jesper Munch. His critical and thoughtful approach towards problems were always constructive. I owe him for lots of delicate points that he taught me. His care about me was beyond his role as a supervisor and I never forget this.

Special thanks to my friend Vladimir Devrelis who always was there to help me. I enjoyed working and discussing with him and I appreciate him for this. Special thanks also to my friend Martin O'Connor. He always was keen to help me either with experiment or theory. My appreciation also goes to him for his contribution in the reading of this thesis.

Many thanks to my friends Ali Kazempour, Armin Ardekani and Setayesh Behin-Ain for their valuable help. My gratitude also goes towards Kerry Corbett and Martin Ostermeyer for their helpful discussion and contribution in the reading of this thesis.

Thanks to Murray Hamilton, Peter Veitch, Patrick Klovekorn, Damien Mudge, Igor Anikeev, Peter Foster, Blair Middlemiss, Avudai, Tim Hill, Shu Lee, Alex Hemming and the rest of optics group who made the optics group very pleasant and interesting place to work.

My study and lifestyle during the course of Ph.D. was supported by a scholarship from the Ministry of Culture and Higher Education of Iran (MCHEI). Their support is appreciated. I also appreciate Anthony W. Thomas and the Center for Subatomic Structure of Matter (CSSM) for making the computer facilities available for this research.

I like to thank the members of the Physics Department and the faculty of science for their support, specially Rod Crewther, Alastair Blake, Mike Shorthose, Ramona Adorjan, Arlene Shaw, Carmel Palumbo, Mary Genovese and Heather Duff.

Abstract

It is known that transient effects limit the efficiency of phase conjugation using Stimulated Brillouin Scattering (SBS). Most of the present knowledge of transients in SBS is due to experimental observations, supported by greatly simplified theoretical models which makes the present knowledge of transient SBS incomplete. In this thesis, a one and three dimensional transient model of SBS are developed to investigate the transient regime of SBS and recognize different transient phenomena that affect the performance of SBS. A one dimensional model of transient SBS is initially developed. This model includes the initiation of SBS from noise in a finite cell geometry. Using this model, two transient phenomena are examined carefully; 1) the deterministic threshold oscillations at the beginning of the Stokes pulse and 2) the stochastic intensity fluctuations in the output Stokes pulse. It is shown that the threshold oscillations depend on the phonon lifetime of the SBS material and the immersion length of the laser beam into the SBS cell. It also becomes clear that the pulse compression phenomenon can be understood in terms of the threshold oscillations. The intensity fluctuations in the Stokes pulse, contrary to the threshold oscillations, have stochastic nature. Their occurrence, position in the pulse and their energy content are all random. The effects of the phonon lifetime, immersion length, input energy and pulse duration on these fluctuations are examined. The best parameter space for excellent SBS performance is determined.

Next, the one dimensional model is developed into a three dimensional cylindrically symmetric model. We use a decomposition method to expand the Stokes, pump and sound fields in terms of transverse spatial modes. By introducing block-vectors and matrices, App. B, and using a noniterative method employed by Chu *et al.* [1], we have developed a numerical algorithm that enables us to treat compactly any arbitrary finite number of spatial modes of the Stokes and pump fields. This efficient numerical algorithm could also be useful for the simulation of broad-band SBS, where many temporal modes exist in the input pulse. The model provides an opportunity to study the effects of transient phenomena on the efficiency of phase conjugation (fidelity) by SBS and the mode structure of the Stokes and pump pulse inside the SBS cell. The effect of parameters such as phonon lifetime, input pulse shape and input energy on the transient fidelity of SBS is investigated. A new transient phenomenon which causes SBS fidelity degradation at high focal intensity (short Rayleigh range) is examined.

List of Symbols and abbreviations

Throughout this thesis, several symbols will be used repeatedly to represent specific quantities or parameters, the following is a list of these symbols and short descriptions for the readers convenience. This list is not exhaustive but every effort has been made to maintain conformity of symbols used here. Whereever possible standard symbols and notation have been used which appear in most laser texts.

SBS	...	Stimulated Brillouin Scattering
SRS	...	Stimulated Raman Scattering
PC	...	Phase Conjugation
FWM	...	Four-Wave Mixing
$DFWM$	...	Degenerate Four-Wave Mixing
SS	...	Stimulated Scattering
G_0	...	Steady state gain of SBS process (for non-focusing geometries)

UNIVERSITY OF ADELAIDE LIBRARY

List of Figures

2.1 Time reversal concept. In (a) an incident beam is diffracted by a transparent media. The time reversal phenomena of (a) is shown in (b): multi-directional diffracted beams are incident on the transparent media and produce a highly directional beam. 21

2.2 A hypothetical phase conjugating mirror is used to phase conjugate the incident beams. Phase conjugated beams reconstruct the initial incident beam in passing through the transparent media. 21

2.3 Schematic of degenerate four-wave mixing. E_1 and E_2 are two colinear counter-propagating pump beams. E_3 is a weaker probe laser beam incident at a small angle to the pump beams. E_4 is the output and is phase conjugated of E_3. 31

3.1 SBS experimental setup. Input pump pulse with frequency ω_l is diffracted initially from thermal noise. The diffracted and the incoming beam induce an acoustic wave Ω which propagates in the same direction as the input pulse. 36

3.2 Introducing focusing geometry to SBS process. 43

3.3 Threshold power is examined as a function of cell length/Rayleigh range. For cell lengths over 2.5×Rayleigh range the threshold power remains constant. 46

3.4 Reflectivity as a function of G/G_{th} where $G = \frac{gP_l(L)}{\lambda}\tan^{-1}(\frac{L-z_0}{z_R})$ and $G_{th} = 25$. Threshold reflectivity $R \sim 0.1$ occurs at $G = G_{th}$. 47

3.5 Numerical results of the input, Stokes and transmitted pulse. The SBS reflectivity as a function of energy is shown in the right graph. E_{th} is the threshold energy. The numerical results are calculated according to our 1D model developed in Chap. 4. 48

3.6 Typical experimental results [2] for the pump and Stokes pulses. The reflectivity as a function of energy is shown as well. Experimental results were obtained for Freon-113. E_{th} is the threshold energy. . . . 49

3.7 The experimental setup to demonstrate the phase conjugation property of SBS. The plate distorts the phase front of the passing beam. The cameras $C_1$and C_2 record the input, and backscattered beam profiles, respectively. The SBS cell is filled with methane. Figure is based on figures in [3] 50

3.8 Diagram of the Near and Far field diagnostic technique for the measurement of the time resolved and time averaged fidelity [2]. 51

3.9 (a) Typical numerical (see Chap. 5 for details) and (b) experimental [2] results for the fidelity of SBS. Experimental results are obtained for Freon-113. 52

3.10 Response function as a function of frequency for different values of γ. There is no maximum for large and small values of γ. L is a dimentionless length paprameter and is $L = 40$ for the above plot. 58

3.11 Maximum value of the response function κ as function of γ. For small γ i.e., $G_0 \gg \Gamma T_t$, the maximum of the response function is very small resulting a smaller ratio of noise/(total stokes intensity). 59

4.1 Typical occurrence of fluctuation in the output of Stokes pulse in SBS experiment using Freon 113. After V. Devrelis [2] 62

4.2 Experimental results showing the occurrence of phase jumps in the phase of the output Stokes pulse. After V. Devrelis [2] 63

4.3 Geometry used for modeling of the SBS process. 71

4.4 (a) Typical threshold oscillation in the Stokes beam obtained for the following parameters: cell length100 cm, focal length 100 cm, immersion length 70 cm, phonon lifetime 0.85 ns, medium gain 0.006 cm/MW, FWHM pulse length 20 ns, and input energy 114 mJ. (b) shows no corresponding variation in the phase of the Stokes. 81

4.5 Experimental results showing: (a) Near field temporal profile of laser input pulse, (b) Near field temporal profiles of Stokes returns for different focusing depths. After M. O'Connor [4] 82

4.6 Threshold oscillations are reduced for longer phonon lifetime. (a) Phonon lifetime is 0.5 ns and (b) phonon lifetime is 1.25 ns. Other parameters are as those of Fig. 4.4. 83

4.7 A shorter relaxation oscillation is achieved for long phonon lifetime. The graph shows how $T_\circ$ (a time interval over which the oscillations are visible, see Fig. 4.6) is reduced for long phonon lifetime. 84

4.8 Response of the acoustic field to a zig-zag driving force. The driving force is shown as solid lines in graphs (a)-(d). The responses of the acoustic field are shown for different values of Γ as dashed-lines. The width of the driving force is $2\pi/b$, where $b = 1$. See the text for explanation. 86

4.9 Smaller focal spot (higher intensity) results in a suppression of threshold oscillations. Oscillations are reduced in graph (b) (focal length 60 cm) in comparison with graph(a) (focal length 90 cm). Other parameters as in Fig. 4.4. 87

4.10 Modulations present in (a) (focal length=100 cm, immersion length=40 cm) are almost suppressed in (b) (focal length=100 cm, immersion length=10 cm). Shorter immersion length provides a better suppression. Other parameters as in Fig. 4.4. 88

4.11 Pump and Stokes as function of time at the entrance to the cell. By reducing the pump energy, we remove extra oscillations from the threshold oscillations, resulting in a pulse compressed beam. Cell length=80 cm, focal length=80 cm and immersion length =70 cm with all other parameters as in Fig. 4.4. In 9(d) the delay in peak Stokes and peak pump is due to the round trip time of the cell and building to threshold. 89

4.12 3D graph of pulse compression [(d) in Fig. 4.11]. Stokes power in time and space shows how the center of maximum reflectivity moves towards the entrance of the SBS cell (z = 80 cm) resulting in pulse compression. Parameters as in Fig. 4.11. 90

4.13 Threshold oscillations disappear for short focal length and immersion length. Immersion length =20 cm and focal length =60 cm, other parameters as standard set shown in Fig. 4.4. 91

4.14 Corresponding and simultaneous to each fluctuation in the Stokes output (a) there is a jump in the Stokes phase [dashed curve in (b)]. Parameters are set as: cell length 60 cm, focal length 60 cm, immersion length 30 cm, Phonon lifetime 0.85 ns, gain of the medium 0.0063 cm/MW, refractive index 1.36 and input energy 119 mJ. 92

4.15 The temporal position of phase jump and the beginning of the amplitude fluctuation (in Fig. 4.14) as they initiate at about $z = 0.46L$ (a) inside the cell (where L is the cell length) and propagate through points $z = 0.56L$ (b) and $z = 0.71L$ (c) to the entrance of the cell (d). 93

4.16 The average of the fluctuation energies (normalised to output energy) reduces for longer phonon lifetimes. Other parameters are as in Fig. 4.14. 94

4.17 The effect of the energy fluctuations, measured by $\langle E_{fluc}/E_{output}\rangle$ % is reduced for shorter immersion lengths (constant focal length and large cell to lens separation). 95

4.18 Experimental results of the effect of the immersion length on intensity fluctuations. Average of the fluctuation amplitudes as a percentage of the Stokes peak versus the immersion length. After V. Devrelis [2]. 96

4.19 Histogram of output energies (normalised to the mean) for two different input energies 387 mJ and 205 mJ. Operating at high input energy reduces the effect of fluctuations. 97

4.20 A reduction in averaged fluctuation energy ($\langle E_{fluc}/E_{output}\rangle$ %) occurs at high energies. 98

4.21 Experimental results of the effects of the input energy and interaction length on intensity fluctuations. Average of fluctuation amplitudes as a percentage of the Stokes peak versus the input energy for two focusing geometries. For focal length =100 mm, the interaction length is 100 mm and for focal length = 300 mm, the interaction length is 300 mm. After V. Devrelis [2]. 98

4.22 For a constant energy, reducing the duration of the input pulse dramatically suppress the fluctuation in the output Stokes. The effect of pulse duration on the suppression of fluctuations is shown for two energies: 115 mJ and 205 mJ. 99

5.1 The geometry used for the SBS process. Input beam parameters are shown at input plane 1. 115

5.2 Typical results for the Stokes, pump and transmitted pulses obtained when a perfect Gaussian beam (fundamental mode of the Laguerre-Gaussian functions) is focused into a SBS cell with the standard set of parameters: cell length 60 cm, focal length 50 cm, immersion length 40 cm, input energy 140 mJ, phonon lifetime 0.85 ns and refractive index, n=1.0. 118

5.3 Time-resolved reflectivity and fidelity. Other parameters as in Fig. 5.2.119

5.4 Time-resolved fidelity [solid line in graph (b)] shows a rapid reduction, simultaneous to the fluctuation in the Stokes pulse. 120

5.5 The relative distribution of the Stokes energy, into different modes, $E_i/E_{Tot}(\%)$. Other parameters are as in Fig. 5.2 121

5.6 Different modes of the Stokes pulse are initiated at the focal plane ($z = 20\ cm$) and propagated towards the entrance of the cell. The distribution of the fields inside the cell is shown at time $t = 40\ ns$. The entrance of the cell is at z=60 cm. See Fig 5.1 for the focusing geometry and propagation directions. Other parameters as in Fig. 5.2121

5.7 The fundamental mode of the pump beam is depleted as it propagates towards the end of the cell (z=0 cm). The other modes of the pump are initiating at the entrance (z=60 cm) and propagating to the end of the cell. Fields are shown inside the cell at the time $t = 40\ ns$. See Fig 5.1 for the focusing geometry and propagation directions. Other parameters as in Fig. 5.2. 122

5.8 The transmitted power for different modes is shown as a function of time. Not only the fundamental mode but also all the other modes contribute in the transmitted power. 123

5.9 The spot sizes of the Stokes and pump beams are compared with the spot size of the fundamental mode as functions of z. The entrance of the cell is at z=60 cm. See Fig 5.1 for the focusing geometry and propagation directions. 124

5.10 Reflectivity and Fidelity saturate at high energy. Energy is varied from below to 30 times above threshold energy ($E_{th} \approx 16\ mJ$) while the other parameters are as in Fig. 5.2. 126

5.11 Reflectivity and fidelity are shown for sharp rise [(a) phonon lifetime $\tau = 2.0\ ns$ and (c) phonon lifetime = $16.0\ ns$] and smooth input [(b) phonon lifetime $\tau = 2.0\ ns$ and (d) phonon lifetime $\tau = 16.0\ ns$]. Input pulses are shown in the bottom of each graph. 126

5.12 The relative distribution of the Stokes energy among the different modes E_i/E_{Tot} (%) varies as the input energy increases. Near threshold (reflectivity about 11% and fidelity about 58%) the Stokes energy is distributed as 58% in mode 0, 25% in mode I, 10% in mode II etc. At high input energy $E_i/E_{Tot} = 30$, the reflected Stokes energy is concentrated mainly in the fundamental mode resulting in a higher fidelity. The energy range and other parameters are as in Fig. 5.10. . 127

5.13 The relative distribution of the transmitted energy among the different modes E_i/E_{Tot} (%) as a function of input energy. 127

5.14 The behaviour of the Stokes and pump spot size at low (a), 23mJ, and high energy (b), 392mJ, are shown. The entrance of the cell is at z=60 cm. See Fig 5.1 for the focusing geometry and propagation directions. 129

5.15 The near field Stokes spot size approaches that of the pump at high energy. 129

5.16 The spot size of the pump and Stokes beams at the focal plane $z \simeq 20$ cm and at low (a) 23mJ, and high energy (b), 392mJ. 130

5.17 Using different individual modes of Laugerre-Gaussian functions as an input pump pulse (with parameters given as in Fig. 5.2), the behaviour of the reflectivity (a) and fidelity (b) is shown as a function of energy. The threshold is increasing while the fidelity saturation level is decreasing for higher order modes. 130

5.18 Fidelity and reflectivity as a function of the fundamental beam parameter ω_i. Here the input intensity has been kept constant by increasing the power. Although the reflectivity saturates at large values of ω_i, the fidelity of the non-fundamental modes decreases. Points "A" and "B" correspond to the highest (92%) and lowest (31%) fidelity of mode II and are discussed in the text. The Rayleigh range values corresponding to different ω_i are shown. All the other parameters are as in Fig. 5.2. 132

5.19 Time-resolved reflectivity and fidelity for the two points "A" and "B", marked in Fig. 5.18. For the point "B" the fidelity curve fails to follow the reflectivity right at the threshold. 133

5.20 Reflectivity and fidelity as a function of time. The value of the mode II to mode I phase matched coupling constant, ε_{2211}, has been changed manually from (a) $\varepsilon_{2211} = 0.0$ to (b) $\varepsilon_{2211} = 0.08$, (c) $\varepsilon_{2211} = 0.0995$, and (d) $\varepsilon_{2211} = 0.11$. The threshold fidelity (indicated by circles) decreases from (a) to (d). The total reflectivity (time averaged) for all of the (a)-(d) curves is 90%, while the the total fidelities (time averaged) are 90%, 82%, 69% and 35% for (a), (b), (c) and (d) curves, respectively. The value of $\varepsilon_{2211} = 0.0995$ for curve (c), is the actual value of ε_{2211} calculated according to Eq. 5.22. 134

5.21 Input (solid lines) and output (dashed lines) intensity distributions for an aberrated input beam at two different geometries. In (a) the fundamental beam parameter ω_1 is 0.5 cm (Rayleigh-range 0.34 cm) and the input energy is 823 mJ, while in (b) ω_1 is 0.35 cm (Rayleigh-range 0.70 cm) and the input energy is 403 mJ. A fidelity of 88% is achieved for (b) while only 47% fidelity is obtained for (a). 137

5.22 As for single-mode input beams (see Fig. 5.18), there is a focusing geometry that results in a maximum fidelity for aberrated input beams. The Rayleigh range values corresponding to different ω_1 are shown. . 137

5.23 Experimental and Numerical results of the SBS reflectivity vs. energy for Freon 113. The triangles are the experimental results obtained by A. Heuer and R. Menzel. The solid line is the numerical model results. 139

5.24 The temporal profiles of the input and output (Stokes) pulses in the SBS experiment in Freon 113. The solid lines are the experimental results obtained by A. Heuer and R. Menzel. The dashed lines are the results of the numerical model. In all cases the input pulses for the experiment and numerical model are the same. All the powers are in MW but have been normalised to peak pump power of 1MW to make the comparison easier. 140

5.25 SBS reflectivity vs. energy for pure SF_6 at 20 bar pressure. The triangles are the experimental results obtained by A. Heuer and R. Menzel. The solid line is the numerical results. The error bars are showing the range of numerical values for the reflectivity for different initial noise term. 141

5.26 Temporal profiles of the input and output pulses in a SBS experiment using pure SF_6 at 20 bar pressure. The blue lines are the experimental results obtained by A. Heuer and R. Menzel. The red lines are the numerical model results. All the powers are in MW but have been normalised to peak pump power of 1MW to make the comparison easier. 142

D.1 Focusing geometry used for SBS process. 159

List of Tables

2.1 The χ^3 form and K factors for different third order nonlinear processes. 28

3.1 Frequency shift, linewidth and gain coefficient of SBS for some materials. Except Fluorinert and Freon 113, values have been quoted from "*Nonlinear Optics*" by Boyd [5]. 41

5.1 Numerical values of ε_{knij}. 117

Contents

1 Introduction 15

2 Phase Conjugation 19

2.1 Principle of Phase Conjugation 19
2.2 Different methods of phase conjugation 23
2.2.1 Nonlinear interaction of light and material 24
2.2.2 Degenerate Four-Wave Mixing (DFWM) 30
2.3 Summary 32

3 Theory of Phase conjugation using SBS 33

3.1 Introduction 33
3.2 Stimulated Light Scattering 33
3.3 Stimulated Brillouin Scattering 35
3.3.1 Steady state regime of SBS 40
3.4 Phase conjugation property of SBS 48
3.4.1 Transient regime of SBS 52
3.5 Summary 58

4 1-dimensional model of SBS 61

4.1 Abstract 61
4.2 Introduction 61
4.3 Theory 65
4.3.1 Langevin noise 65
4.3.2 Numerical Solution of the SBS Equations 68
4.4 Results of the 1-dimensional model 79

4.4.1 Model parameters and geometry . . . 80
4.4.2 A: Deterministic Threshold Oscillation . . . 80
4.4.3 B: Stochastic fluctuations of phase and amplitude . . . 90
4.4.4 Conclusion . . . 99

5 3-Dimensional model of SBS 103
5.1 Abstract . . . 103
5.2 Introduction . . . 103
5.3 Theory . . . 105
5.4 Results and Discussion . . . 114
5.4.1 Single-mode input beams . . . 115
5.4.2 Aberrated input beams . . . 136
5.5 Comparison between numerical and experimental results . . . 138
5.5.1 SBS experiment using Freon 113 . . . 138
5.5.2 SBS experiment using SF_6 . . . 139
5.6 Conclusions . . . 141

6 Conclusion and Future works 145
6.1 Future work . . . 147

A Generating a Gaussian Distribution 149

B Block-matrices 153

C Recurrence Relation 157

D SBS focusing system 159

E Publications 163
E.1 **Papers** . . . 163
E.2 **Conferences** . . . 163
E.3 Paper I . . . 165
E.4 Paper II . . . 167

Chapter 1

Introduction

Phase conjugating mirrors using stimulated Brillouin scattering (SBS) have been used extensively since 1971 [6] to compensate for optical aberrations in high power laser systems, resulting in lasers with greatly improved beam quality. SBS in certain materials is thus capable of producing efficient and high fidelity phase conjugation of high power input radiation, but only for a restricted range of laser parameters. Much research has gone into extending this range of parameters, with most of the research concentrating on characterizing SBS materials and the type of spatial aberrations which can be compensated. The emphasis has thus been on the improvement of average beam quality during a laser pulse, with comparatively little emphasis on time dependent phenomena. This approach is reasonable as long as the time dependent phenomena represent a small fraction of the total energy in a pulse, as is often the case for single frequency, Q-switched solid state lasers. There are however laser systems where transient effects are not negligible, including many high power, short pulse lasers, and systems where short coherence lengths are required, such as range finders and phase conjugated oscillators. For these applications some investigations of transient phenomena have been made, but mostly for restricted parameter regimes and geometries [7, 8, 9, 10, 11, 12, 13, 1, 14, 15, 16, 17, 18, 19, 20], leaving the overall understanding of transient phenomena incomplete. As a consequence the use of SBS in these applications has been very limited.

It is known that transient effects limit the efficiency and fidelity of phase conjugated systems. Experimental [15, 16, 19, 2] and theoretical [9, 10, 11, 13, 20] investigations suggest that a complete understanding of SBS must include transient effects. Most of the present knowledge of transients in SBS is due to experimental observations, supported by greatly simplified theoretical models. Transient effects are responsible for threshold oscillations [1, 17, 20], temporal and spatial fidelity degradation due to amplitude and phase jump fluctuations [9, 11, 13, 2, 20], and the reduction in fidelity for input pulses with sharp rise times [15, 2]. Furthermore, the transient regime is essential for SBS of pulses with amplitude variations on time scales comparable to the response time of the material, represented by the phonon lifetime of the material, as is often the case for broad band lasers.

Analytical solutions of one-dimensional differential equations describing transient SBS (e.g. refs. [8, 13] and references given therein) as well as numerical simulations of two and three dimensional, steady state SBS (e.g. ref. [21, 22]) exist for the undepleted pump approximation, valid only near the threshold of SBS. Numerical models of depleted steady state SBS, for one [23, 24] and three [25, 26, 27, 28, 29] dimensions have also been reported. There are also published reports on the depleted and transient regime of SBS for one [7, 11, 1, 20] and three dimensions [17] (zero-order solution). One-dimensional numerical models are not able to simulate the measured fidelity of SBS, which is the main characteristic of the SBS process and represents the degree of phase conjugation of the Stokes return. Two or three-dimensional models of SBS have been considered both in fibers [25, 26, 21, 30, 17], where electric fields are expanded according to propagation modes of the waveguide, and in the cell geometry [22, 27, 28, 29], where electric fields are expanded in terms of Hermite-Gaussian [27, 28, 29] or Laguerre-Gaussian [22] functions. However, these models are for either undepleted [21, 22] or steady state [25, 26, 30, 27, 28, 29] regimes of SBS.

The objective of this thesis is to develop generalized, practical models of phase conjugating SBS mirrors, in conjunction with experimental investigations which are already being undertaken, in order to: 1) understand the physics of the limitations on phase conjugation using SBS, especially in the transient and short coherence length regimes, 2) help the experimental studies to find an extended parameter regime for excellent SBS and 3) eventually develop models capable of handling the SBS process of short coherence length lasers.

The experimental studies, initiated at the University of Adelaide, concentrated on two main experiments 1): SBS experiment in a cell geometry for long and short coherence length lasers [2, 19], 2): SBS oscillators with one and two SBS mirrors [31, 4, 32]. Using two 1.86 GHz (3db frequency) transient digitizers (Tektronix SCD1000), the temporal profile of the input, output, reflectivity and fidelity of the SBS process in Freon 113 was examined experimentally. In addition to the poor performance of SBS for short coherence length lasers, the experimental observations showed new limitations on SBS possibly caused by stochastic fluctuations in the intensity and phase of the Stokes beam [2].

The theoretical studies were initially concentrated on developing a transient, real-fields, one-dimensional model of SBS initiated from constant noise, based on previous works by Chu *et al.* [1] and Menzel *et al.* [24]. This model then was improved to include a focusing geometry using the idea of Menzel *et al.* [24]. At the next stage, the constant noise term in the SBS equations was replaced by a Gaussian random noise, enabling the model to simulate the initial thermal fluctuations in the material, which are the source of the SBS process. At the final stage of the development, complex fields were introduced into the model to simulate the possible existence of phase and intensity fluctuations. This model was very successful in 1) explaining the nature of phase and intensity modulations in the Stokes output, 2) providing the best focusing geometry and material parameters for avoiding these fluctuations, 3) understanding the threshold oscillations, 4) determining the parameters that affect the threshold oscillations. The results of this model were published in Phys. Rev. A [20] (App. E), IQEC'96 [19], CLEO/Pacific Rim'97 [33] and AOS XI [34]. The one-dimensional model, although very successful, did not enable the study of fidelity due to its one-dimensional nature. The next generation of the model was a three-dimensional one with cylindrical symmetry. In addition to having all the features of one-dimensional model, this new model enabled, for the first time, the study of transient SBS fidelity. In this model, we developed a new efficient algorithm, which made the computer code run more quickly and efficiently. We believe that our new algorithm can be used in the modeling of the SBS process of short coherence length lasers. The model was very successful. It did not only produce results consistent with experiments on SBS phase conjugation in the transient regime but also predict a new transient phenomenon that has not yet been observed experimentally. The results of this model were published at CLEO'99 [35] and accepted for publication in Journal of Nonlinear Optical Physics and Materials (App. E).

This thesis reports the details of the theoretical models and their results. Chap. 2 of this thesis reviews the phase conjugation phenomenon and the nonlinear interaction of light and matter. These are the two fundamental concepts behind nonlinear optical phase conjugation. We concentrate on the two main methods of phase conjugation, Stimulated Scattering (SS) and Degenerate Four-Wave Mixing (DFWM). A brief review of phase conjugation using DFWM is given at the end of Chap. 2. A review of phase conjugation using SS is provided in Chap. 3. It is shown that all of the SS process can be discussed uniquely in the framework of parametric interaction. The main SS process that is used for phase conjugation is SBS. In Chap. 3, we review the SBS process and develop the basic theoretical formulas that describe SBS. A summary of transient SBS and its effect on different aspects of SBS is given at the end of Chap. 3. Chap. 4 is devoted to the details of our one dimensional model and its results. The extension of our one dimensional model to a three dimensional one with cylindrical symmetry is described in Chap. 5. The results of the model and discussion are given at the end of this chapter. The summary and conclusion of the whole study including possible ways of further investigations are presented at Chap. 6. Attached in App. E are the papers which have been published on the subject of this thesis. The content of Chaps. 4 and 5 is very similar to that of the papers I and II in the App. E.

Chapter 2

Phase Conjugation

In this chapter, we first describe the principle of phase conjugation (PC) and different methods of achieving PC. Next, a general theoretical description of the interaction of light and matter is developed by introducing polarization field. This together with the Maxwell's equations are then employed to derive the basic wave equations governing the nonlinear optical processes which result in PC. Degenerate Four-Wave Mixing (DFWM) is then studied as an explicit example of a nonlinear optical process that leads to PC.

2.1 Principle of Phase Conjugation

Optical phase conjugation (OPC) is a technique to reverse both the propagation direction and the overall phase of an arbitrary light wave relative to its propagation direction [36, 37, 38, 39]. The concept of phase conjugation can be understood in terms of *time-reversal* [37, 38, 39]. By *time-reversal*, we mean transforming $t \longrightarrow -t$ in the wave equation of motion. Consider a light beam,

$$E(\mathbf{r}, t) = \varepsilon(\mathbf{r}) \cos[\omega t - kz + \phi(\mathbf{r})],$$

propagating along the z direction. The *time-reversed* wave, obtained by transforming $t \longrightarrow -t$ in $E(\mathbf{r},t)$, is a wave propagating along $-z$ direction with phase $-\phi(\mathbf{r})$:

$$E_{rev}(\mathbf{r},t) = C\varepsilon(\mathbf{r})\cos[\omega t + kz - \phi(\mathbf{r})].$$

Here, C is a constant and $E_{rev}(\mathbf{r},t) = CE(\mathbf{r},-t)$. Considering $E(\mathbf{r},t)$ and $E_{rev}(\mathbf{r},t)$ as the real parts of

$$\begin{aligned} E(\mathbf{r},t) &= \mathrm{Re}[\varepsilon(\mathbf{r})e^{-\imath\omega t}e^{\imath[kz-\phi(\mathbf{r})]}] = \mathrm{Re}[\varepsilon(\mathbf{r})e^{-\imath\omega t}e^{\imath\Phi(\mathbf{r})}], \quad \varepsilon^*(\mathbf{r}) = \varepsilon(\mathbf{r}), \\ E_{rev}(\mathbf{r},t) &= C\,\mathrm{Re}[\varepsilon(\mathbf{r})e^{-\imath\omega t}e^{-\imath[kz-\phi(\mathbf{r})]}] = C\,\mathrm{Re}[\varepsilon(\mathbf{r})e^{-\imath\omega t}e^{-\imath\Phi(\mathbf{r})}], \end{aligned}$$

it is seen that the *time-reversed* beam $E_{rev}(\mathbf{r},t)$ can be obtained from $E(\mathbf{r},t)$ by replacing $e^{\imath\Phi(\mathbf{r})}$ by its complex conjugate $e^{-\imath\Phi(\mathbf{r})}$. Therefore, the process of *time-reversal* is mathematically equivalent to a *phase conjugation* process. The concepts of *time-reversal* and phase conjugation can be understood by a hypothetical example. Consider an optical process in which a laser beam is diffracted by a nonabsorbent transparent media into small beams of different directions as shown in Fig. 2.1(a). Then, one can think of the time-reversed process: small multi-directional light beams incident on a transparent media produce a highly directional beam as shown in Fig. 2.1 (b). In order for this to happen, the light beams incident on the media in Fig. 2.1(b) have to be the *time-reversed* or phase conjugate of the diffracted beams in Fig. 2.1(a). This is very exciting because if one can find a mirror that reflects beams into their phase conjugated ones and use it in the experiment shown in Fig. 2.1, then it will be possible to reconstruct the original beam before diffraction (see Fig. 2.2). This hypothetical mirror is a phase conjugating mirror. In reality, there are some nonlinear optical processes that can be used in the PC mirrors. Although, there is always some energy loss in these nonlinear optical processes, in some processes one can achieve reflectivity and phase conjugation efficiency (defined as fidelity and will be discussed in the next chapter) of more than 90 %.

The wavefront reconstruction concept and its promising applications have motivated many experimental and theoretical investigations. The early work on the wavefront reconstruction was the invention of holography by Gabor [40, 41]. Ga-

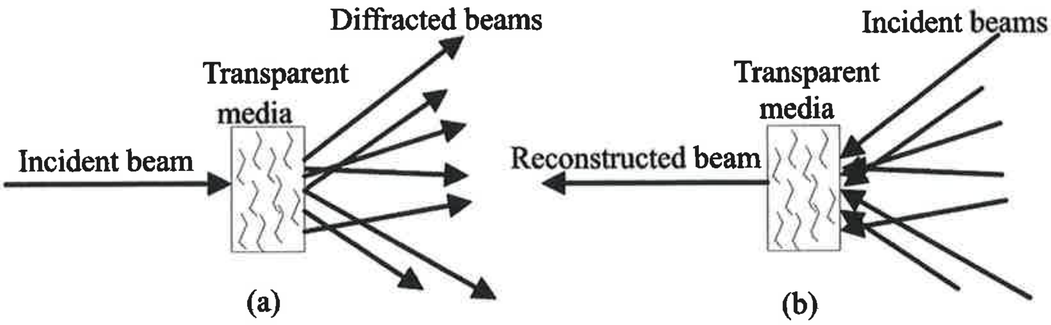
Diffracted beams
Transparent media
Incident beam
(a)
Incident beams
Transparent media
Reconstructed beam
(b)

Figure 2.1: Time reversal concept. In (a) an incident beam is diffracted by a transparent media. The time reversal phenomena of (a) is shown in (b): multi-directional diffracted beams are incident on the transparent media and produce a highly directional beam.

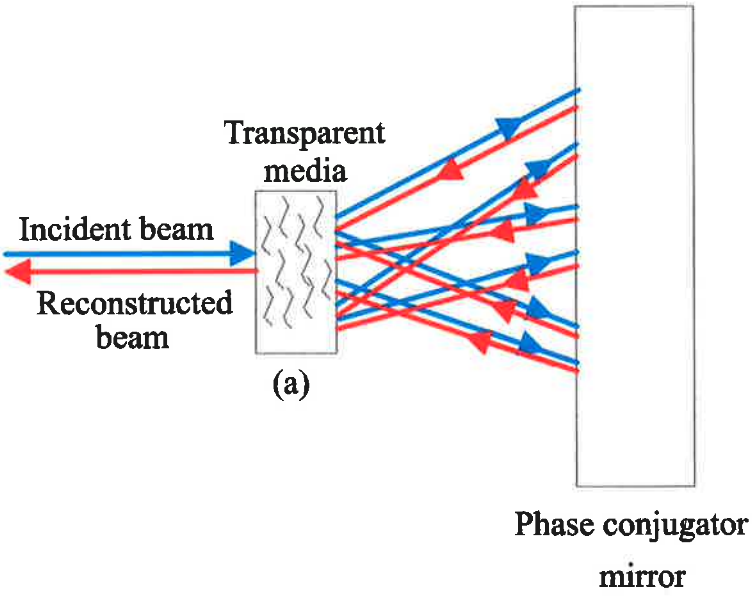
Transparent media
Incident beam
Reconstructed beam
(a)
Phase conjugator mirror

Figure 2.2: A hypothetical phase conjugating mirror is used to phase conjugate the incident beams. Phase conjugated beams reconstruct the initial incident beam in passing through the transparent media.

bor had the idea of using holography to improve the resolving power of an electron microscope by reading a hologram and compensate for spherical aberrations. This idea didn't turn out to be of much practical use due to spatial coherence and intensity requirements of beams, necessary for writing and reading of the hologram. The development of the laser with a high degree of temporal and spatial coherence and high intensities in 1960's, opened the doors for practical development of holography. A group of researchers at the University of Michigan were the first to report a successful demonstration of holography [42, 43]. Soon after that, holograms were used to correct the static phase distortion introduced into an optical wavefront by stationary objects [44, 45, 46]. The possibility of extending static holography to real-time (dynamic) holography was introduced by Gerritsen [47] who observed that holograms can be stored temporarily in media whose index of refraction depends on the intensity of light. Later on, the first demonstration of using dynamic holography to compensate for wave front distortion was reported by Stepanov [48]. In the early 1970's a team of Russian scientists led by Dr. B. Ya. Zel'dovich [6] noticed that the back scattered pulses generated by stimulated Brillouin scattering exhibited excellent spatial quality even though they had passed through a distorter in front of the SBS medium. In 1972, Nosach et al. [49] demonstrated wavefront correction using Brillouin scattering. The phase reversed or phase conjugated back scattered beam can compensate the distortion effects of the distorter by passing back through it. Much later, Yariv [50] showed that real-time holography (dynamic holography) was equivalent to a certain type of phase conjugation achieved by a process called Degenerate Four-Wave Mixing (DFWM).

Over the past few decades, remarkable progress has been achieved in the field of nonlinear optical phase conjugation and this phenomenon has been the topic of intense research efforts. In addition to being considered as a technique for all optical, real time adaptive optical compensation, the field of nonlinear optical phase conjugation has grown to encompass a large variety of potential applications for both high-power and low-power systems, including propagation compensation, novel optical cavities and oscillators, energy scaling, optical data computing and processing, remote sensing and diagnostics (including spectroscopic investigations), low-noise free-space and guided-wave communication systems, compensated image transmission, metrology, nondestructive testing, and data storage and cache memories, to mention a few [51].

2.2 Different methods of phase conjugation

Phase conjugation has been observed in a variety of nonlinear phenomena including degenerate four-wave mixing, stimulated (Brillouin, Raman and Rayleigh) scattering and photorefractive effect.

Under certain conditions phase conjugation is possible via backward stimulated scattering. One of the required conditions for phase conjugation is that the phase mismatch $(k_p - k_s)L$ must be small, where $(k_p - k_s) = 2\pi n\Delta\nu/c$ is the wavenumber difference between the incident pump and the scattered Stokes pulses and L is the interaction length. In Raman scattering, (since $(k_p - k_s)$ is usually large, of order k_p), phase conjugation is seen in specific circumstances of short interaction lengths, high intensity and high gain [51]. Phase conjugation by Raman scattering was demonstrated by Zel'dovich et al. [52]. They were successful in restoring an aberrated laser beam using stimulated Raman scattering from the 656-cm^{-1} excitation of liquid CS_2. Kurdriavtseva et al. [53] observed phase conjugation in stimulated Raman scattering with short pulses of 25 ns duration. They also achieved image reconstruction at Stokes frequency shift of less than 5 cm^{-1}. Raman scattering is not very useful in efficient laser systems however, because the Stokes beam is frequency shifted outside the gain. Since the Brillouin phonon lifetime is usually longer than the Raman phonon lifetime, stimulated Raman scattering dominates stimulated Brillouin scattering for very short pulses.

Stimulated Brillouin scattering (SBS), FWM and the photorefractive effect are the main nonlinear mechanisms for phase conjugation. SBS-based phase conjugators are typically used in applications requiring high power or energy such as laser oscillators whilst the photorefractive mechanism is used in low power applications such as optical data processing [51]. SBS does not require pump waves of high quality for good phase conjugation whereas sufficient quality pump beams, which are difficult to obtain when using high power lasers, and delicate alignments are required in FWM. Overall, SBS is the easiest and most popular method of phase conjugation when using intense pulsed laser sources.

The theory of stimulated scattering (SS) and phase conjugation using SS will be discussed in the next chapter with emphasis on SBS. It can be shown that all of the stimulated scattering phenomena and FWM can be treated in the framework of a nonlinear parametric interaction. In parametric interactions a few intense laser beams interact with a nonlinear medium and induce a nonlinear polarisation. Next, this nonlinear polarisation itself is a source of a new laser beam with a new frequency. In general the frequency of the new emitted laser beam is equal to either the sum, the difference, or the combination of sum and difference of the initial frequencies. This classifies the nonlinear interaction as either sum-frequency generation, difference-frequency generation, and combination of sum and difference-frequency generation. The parametric interaction is a difference-frequency generation, for which the frequency of the new laser beam is the difference of the incident frequencies.

In the next section, we discuss the theory of nonlinear interaction to: 1) understand parametric interactions and 2) develop the theory of DFWM and stimulated scatterings (which will be discussed in the next chapter).

2.2.1 Nonlinear interaction of light and material

The key element of nonlinear optics is the induced polarization $\mathbf{P}(t)$ and its relation with the driving electric field $\mathbf{E}(t)$. Upon the incidence of a beam or beams of light on a nonlinear material, the total electric field interacts with the material at the atomic or molecular level and induces different processes such as exciting the system to a higher energy level, changing the charge or density distribution and so on. The effects of these induced processes regardless of their nature can be summarised in an induced polarization field $\mathbf{P}(t)$. This polarization field can be described in terms of a power series as

$$\mathbf{P}(t) = \mathbf{P}^{(0)}(t) + \mathbf{P}^{(1)}(t) + \mathbf{P}^{(2)}(t) + \cdots + \mathbf{P}^{(n)}(t) + \cdots , \qquad (2.1)$$

where $\mathbf{P}^{(1)}(t)$ is linear in the total electric field, $\mathbf{P}^{(2)}(t)$ is quadratic, and so on. $\mathbf{P}^{(0)}(t)$ is the static polarization that exists in some crystals and is independent of electric field. For a general case, where we assume that the response of the medium to the electric field is not instantaneous, one can relate different orders of the polarization field to the electric field as

$$\begin{aligned}
\mathbf{P}^{(1)}(t) &= \varepsilon_0 \int_{-\infty}^{+\infty} d\tau \mathbf{R}^{(1)}(\tau)|\mathbf{E}(t-\tau), \\
\mathbf{P}^{(2)}(t) &= \varepsilon_0 \int_{-\infty}^{+\infty} d\tau_1 \int_{-\infty}^{+\infty} d\tau_2 \mathbf{R}^{(2)}(\tau_1,\tau_2)|\mathbf{E}(t-\tau_1)\mathbf{E}(t-\tau_2), \\
&\vdots \\
\mathbf{P}^{(n)}(t) &= \varepsilon_0 \int_{-\infty}^{+\infty} d\tau_1 \cdots \int_{-\infty}^{+\infty} d\tau_n \mathbf{R}^{(n)}(\tau_1,\cdots,\tau_n)|\mathbf{E}(t-\tau_1)\cdots\mathbf{E}(t-\tau_n).
\end{aligned}$$

Here, $\mathbf{R}^{(n)}(\tau_1,\cdots\tau_n)$ is a real $(n+1)$-rank tensor indicating the polarization response function of the medium and the vertical bar ($|$) represents the tensorial product. $\mathbf{R}^{(n)}(\tau_1,\cdots\tau_n)$ is zero if any of the τ_i is negative and its components $R^{(n)}_{\mu\alpha_1\ldots\alpha_n}(\tau_1,\cdots\tau_n)$ are invariant under any $n!$ permutation of pairs $(\alpha_1,\tau_1),\cdots,(\alpha_n,\tau_n)$. Eqs. (2.1) describe the polarization response of the material in the time domain. Using the Fourier transform of $\mathbf{P}^{(n)}(t)$ and $\mathbf{E}(t)$ i.e.,

$$\begin{aligned}
\mathbf{P}^{(n)}(t) &= \int_{-\infty}^{+\infty} d\omega \mathbf{P}^{(n)}(\omega)\exp(-\imath\omega t), \\
\mathbf{E}(t) &= \int_{-\infty}^{+\infty} d\omega \mathbf{E}(\omega)\exp(-\imath\omega t),
\end{aligned} \tag{2.2}$$

one can derive the equivalent frequency domain equations:

$$\begin{aligned}
\mathbf{P}^{(1)}(\omega) &= \varepsilon_0 \int_{-\infty}^{+\infty} d\omega_1 \boldsymbol{\chi}^{(1)}(-\omega_\sigma;\omega_1)|\mathbf{E}(\omega_1)\delta(\omega-\omega_\sigma), \\
\mathbf{P}^{(2)}(\omega) &= \varepsilon_0 \int_{-\infty}^{+\infty} d\omega_1 \int_{-\infty}^{+\infty} d\omega_2 \boldsymbol{\chi}^{(2)}(-\omega_\sigma;\omega_1,\omega_2)|\mathbf{E}(\omega_1)\mathbf{E}(\omega_2)\delta(\omega-\omega_\sigma), \\
&\vdots \\
\mathbf{P}^{(n)}(\omega) &= \varepsilon_0 \int_{-\infty}^{+\infty} d\omega_1 \cdots \int_{-\infty}^{+\infty} d\omega_n \boldsymbol{\chi}^{(n)}(-\omega_\sigma;\omega_1,\cdots,\omega_n)|\mathbf{E}(\omega_1)\cdots\mathbf{E}(\omega_n)\delta(\omega-\omega_\sigma),
\end{aligned} \tag{2.3}$$

where $\boldsymbol{\chi}^{(n)}(\omega_\sigma;\omega_1,\cdots,\omega_n)$ is a $(n+1)$-rank tensor called susceptibility tensor and $\omega_\sigma = \omega_1+\omega_2+\cdots+\omega_n$ is the sum of optical driving frequencies. One can think of different sets of $(\omega_1, \cdots, \omega_n)$ with a sum $\omega_\sigma = \omega_1 + \omega_2 + \cdots + \omega_n$. The convenience of using $(-\omega_\sigma; \omega_1, \cdots, \omega_n)$ as the argument of the susceptibility tensor will become clearer later when we find the induced polarization due to monochromatic electric fields at frequencies $\omega_1, \cdots, \omega_n$. It will be shown that (Eq. 2.9) the induced polarization field at the frequency ω_σ depends on the susceptibility tensors with different sets of $(\omega_1, \cdots, \omega_n)$ but same $\omega_\sigma = \omega_1 + \omega_2 + \cdots + \omega_n$. The susceptibility tensor can be explicitly evaluated according to the detailed interaction of the system with the electric fields. Like the time domain representation, $\mathbf{P}(\omega)$ can be written as a power series:

$$\mathbf{P}(\omega) = \sum_{r=0}^{\infty} \mathbf{P}^{(r)}(\omega). \tag{2.4}$$

The above equations apply generally for any incident electric fields. As an application, we consider monochromatic incident waves, which can be represented in the time domain as

$$\mathbf{E}(t) = \frac{1}{2} \sum_{\omega' \geq 0} [\mathbf{E}_{\omega'} \exp(-\imath\omega' t) + \mathbf{E}_{-\omega'} \exp(\imath\omega' t)] \quad \text{where } \mathbf{E}^*_{\omega'} = \mathbf{E}_{-\omega'}, \tag{2.5}$$

or equivalently in the frequency domain as (2.6)

$$\mathbf{E}(\omega) = \frac{1}{2} \sum_{\omega' \geq 0} [\mathbf{E}_{\omega'} \delta(\omega - \omega') + \mathbf{E}_{-\omega'} \delta(\omega + \omega')]. \tag{2.7}$$

For such an electric field one can write $\mathbf{P}^{(n)}(t)$ in the same form as $\mathbf{E}(t)$ in Eq. 2.5 i.e.,

$$\mathbf{P}^{(n)}(t) = \frac{1}{2} \sum_{\omega \geq 0} [\mathbf{P}^{(n)}_{\omega} \exp(-\imath\omega t) + \mathbf{P}^{(n)}_{-\omega} \exp(\imath\omega t)] \quad \text{where } (\mathbf{P}^{(n)}_{\omega})^* = \mathbf{P}^{(n)}_{-\omega}. \tag{2.8}$$

By substituting (2.7) into (2.3), a compact but general relation, which can be used to describe all different nonlinear processes, is obtained as

$$\mathbf{P}^{(n)}_{\omega_\sigma} = \varepsilon_0 \sum_{\omega} K(-\omega_\sigma; \omega_1, \ldots, \omega_n) \boldsymbol{\chi}^{(n)}(-\omega_\sigma; \omega_1, \ldots, \omega_n) | \mathbf{E}_{\omega_1} \ldots \mathbf{E}_{\omega_n}, \tag{2.9}$$

in vectorial form or,

$$(P^{(n)}_{\omega_\sigma})_\mu = \varepsilon_0 \sum_{\alpha_1\ldots\alpha_n} \sum_{\omega} K(-\omega_\sigma;\omega_1,\ldots,\omega_n)\chi^{(n)}_{\mu\alpha_1\ldots\alpha_n}(-\omega_\sigma;\omega_1,\ldots,\omega_n)(E_{\omega_1})_{\alpha_1}\ldots(E_{\omega_n})_{\alpha_n}. \tag{2.10}$$

in component form. In the former, the first sum is over the components of the tensor χ and the vectors $\mathbf{E}_\omega$ and the second sum is over all possible distinct combinations of $(\omega_1,\ldots,\omega_n)$ which satisfy $\omega_1+\ldots+\omega_n=\omega_\sigma$. $K(-\omega_\sigma;\omega_1,\ldots,\omega_n)$ is a numerical factor that depends on the number of distinct permutations of $(\omega_1,\ldots,\omega_n)$ and the order of the nonlinearity. As an example for $n=3$, the third order nonlinear processes are given [54] in Table 2.1. All of these processes are contributing in the total third order nonlinear polarization $(P^{(n)}_{\omega_\sigma})_\mu$ through Eq. 2.10. However, due to resonance enhancement, phase matching or spectral selectivity there is only one nonlinear process that gives rise to the dominant polarization in Eq. 2.10 and thus should be considered [54].

Wave Equations

Starting from Maxwell's equations, one can easily derive the wave equation for the electric field inside a nonlinear material as [54]

$$\nabla\times\nabla\times\mathbf{E}(t) = -\frac{1}{c^2}\frac{\partial^2}{\partial t^2}\mathbf{E}(t) - \mu_0\frac{\partial^2}{\partial t^2}\mathbf{P}(t), \tag{2.11}$$

in the time domain or

$$\nabla\times\nabla\times\mathbf{E}(\omega) = \frac{\omega^2}{c^2}\mathbf{E}(\omega) + \omega^2\mu_0\mathbf{P}(\omega), \tag{2.12}$$

in the frequency domain. Ignoring the static polarization in 2.4 and substituting $\mathbf{P}(\omega)$ in (2.12) using (2.3) and (2.4), we find

$$\begin{aligned}\nabla\times\nabla\times\mathbf{E}(\omega) &= \frac{\omega^2}{c^2}\mathbf{E}(\omega) + \omega^2\mu_0\varepsilon_0\boldsymbol{\chi}^{(1)}(-\omega;\omega)|\mathbf{E}(\omega) + \omega^2\mu_0\mathbf{P}^{NL}(\omega), \\ &= \frac{\omega^2}{c^2}\boldsymbol{\varepsilon}(\omega)|\mathbf{E}(\omega) + \omega^2\mu_0\mathbf{P}^{NL}(\omega),\end{aligned} \tag{2.13}$$

Table 2.1: The χ^3 form and K factors for different third order nonlinear processes.

Process	$\chi^3(-\omega_\sigma;\omega_1,\omega_2,\omega_3)$	K
d.c. Kerr effect (quadratic electro-optic effect)	$\chi^3(-\omega;0,0,\omega)$	3
d.c.-induced second harmonic generation	$\chi^3(-2\omega;0,\omega,\omega)$	$\frac{3}{2}$
Third harmonic generation	$\chi^3(-3\omega;\omega,\omega,\omega)$	$\frac{1}{4}$
General four wave mixing	$\chi^3(-\omega_4;\omega_1,\omega_2,\omega_3)$	$\frac{3}{2}$
Third-order sum and difference frequency mixing	$\chi^3(-\omega_3;\pm\omega_1,\omega_2,\omega_2)$	$\frac{3}{4}$
Coherent anti-Stokes Raman scattering	$\chi^3(-\omega_{AS};\omega_P,\omega_p,\omega_S)$	$\frac{3}{4}$
Stimulated Raman scattering stimulated Brillouin scattering	$\chi^3(-\omega_S;\omega_P,-\omega_P,\omega_S)$	$\frac{3}{2}$
self focusing degenerate four-wave mixing	$\chi^3(-\omega;\omega,-\omega,\omega)$	$\frac{3}{4}$
Two-photon absorption/ionisation/ emission	$\chi^3(-\omega_1;-\omega_2,-\omega_2,\omega_1)$ or $\chi^3(-\omega;\omega,-\omega,\omega)$	3

where $\varepsilon(\omega) = 1 + \chi^{(1)}(-\omega;\omega)$ and $\mathbf{P}^{NL}(\omega) = \sum_{r=2}^{\infty} \mathbf{P}^{(n)}(\omega)$. We assume that $\mathbf{E}(\omega)$ consists of infinite, colinear, and monochromatic plane waves propagating in an arbitrary direction e.g., z as,

$$\mathbf{E}(\omega) = \frac{1}{2}\sum_{\omega_j \geq 0} [\mathbf{E}_{\omega_j} \exp(\imath k_j z)\delta(\omega - \omega_j) + \mathbf{E}^*_{\omega_j} \exp(-\imath k_j z)\delta(\omega + \omega_j)].$$

We also assume that the direction of the field vector $\mathbf{E}(\omega)$ is perpendicular to the propagation direction. Such an assumption requires that the medium is isotropic, which is not generally true, but works for the stimulated scattering processes that we study here. Finally, we consider the slowly varying envelope approximation, in which we assume that the spatial variation of $\mathbf{E}(\omega)$ (both in amplitude and phase) is small such that

$$\left|\frac{\partial^2}{\partial z^2}\mathbf{E}(z,\omega)\right| \ll \left|k\frac{\partial}{\partial z}\mathbf{E}(z,\omega)\right|.$$

The real significance of the slowly varying approximation, as pointed out by Shen [55], is that it is equivalent to neglecting the component of the $\mathbf{E}$, generated by $\mathbf{P}^{NL}(\omega)$, which is propagating in the direction opposite to the input electric field. With the help of the above assumption we can replace $\nabla\times\nabla\times\mathbf{E}(\omega)$ by $-\partial^2\mathbf{E}(\omega)/\partial z^2$ in (2.13), ignore the second derivatives $\frac{\partial^2\mathbf{E}}{\partial z^2} \ll k\frac{\partial \mathbf{E}}{\partial z}$ and rewrite (2.13) as

$$\frac{\partial}{\partial z}\mathbf{E}_{\omega_\sigma} = \frac{\imath\omega_\sigma^2\mu_0}{2k_\sigma}\mathbf{P}^{NL}_{\omega_\sigma} \exp(-\imath k_\sigma z). \tag{2.14}$$

This equation describes how the propagation of the electric field at frequency ω_σ and wavevector k_σ in the medium can be determined by the nonlinear polarization $\mathbf{P}^{NL}_{\omega_\sigma}(\omega)$. The nonlinear polarization is coupled to all other electric fields existing in the medium with different frequencies through Eqs. (2.4) and (2.9). All orders of nonlinearity are involved in $\mathbf{P}^{NL}_{\omega_\sigma}(\omega)$ but as mentioned before, usually due to resonance enhancement, phase matching, spectral selectivity or some other discriminating feature, only one order (say n) needs to be considered. This means $\mathbf{P}^{NL}_{\omega_\sigma}(\omega)$

can be written as

$$\mathbf{P}^{NL}_{\omega_\sigma} = \varepsilon_0 K(-\omega_\sigma;\omega_1,\ldots,\omega_n)\boldsymbol{\chi}^{(n)}(-\omega_\sigma;\omega_1,\ldots,\omega_n)|\mathbf{E}_{\omega_1}\ldots\mathbf{E}_{\omega_n}\exp(\imath k_p z), \tag{2.15}$$

where $\omega_\sigma = \omega_1 + \ldots . + \omega_n$ and $k_p = k_1 + \ldots + k_n$. By substituting Eq. (2.15) in Eq. 2.14 and expressing the results in scalar form, one finds

$$\frac{\partial}{\partial z}E_{\omega_\sigma} = \frac{\imath\omega_\sigma^2}{2k_\sigma c^2}K(-\omega_\sigma;\omega_1,\ldots,\omega_n)\chi^{(n)}(-\omega_\sigma;\omega_1,\ldots,\omega_n)E_{\omega_1}\ldots E_{\omega_n}\exp(-\imath\Delta kz), \tag{2.16}$$

where $\mathbf{E}_{\omega_j} = E_j\mathbf{e}_j$, $\Delta k = k_p - k_\sigma$ is the phase mismatch term and $\chi^{(n)}$ is the scalar form of the tensor $\boldsymbol{\chi}^{(n)}$ defined as

$$\chi^{(n)}(-\omega_\sigma;\omega_1,\ldots,\omega_n) = \mathbf{e}^*_\sigma.\boldsymbol{\chi}^{(n)}(-\omega_\sigma;\omega_1,\ldots,\omega_n)|\mathbf{e}_1 \ldots \mathbf{e}_n.$$

The vectors $\mathbf{e}_j$ are unit vectors along the polarisation direction, and scalars E_j and $\chi^{(n)}$ are the components of electric field and susceptibility tensor along the polarisation directions.

2.2.2 Degenerate Four-Wave Mixing (DFWM)

DFWM is a nonlinear process in which two colinear counter-propagating pump beams, $(E_1, \mathbf{k}_1, \omega)$ and $(E_2, \mathbf{k}_2, \omega)$, are incident on a nonlinear material. There is also a weaker probe beam, $(E_3, \mathbf{k}_3, \omega)$, which is incident at a small angle to the pump beam, $(E_1, \mathbf{k}_1, \omega)$. The pump and the probe beams produce an induced polarisation or grating. This induced grating scatters the probe beam into a signal beam, $(E_4, \mathbf{k}_4, \omega)$, where $\mathbf{k}_4 = -\mathbf{k}_3$ and the signal beam is the phase conjugate of the probe beam. The setup for a DFWM experiment is shown in Fig. 2.3. DFWM was first proposed theoretically in 1977 by Hellwarth [56]. The first DFWM experiment was reported by Bloom and Bjorklund [57]. They used CS_2 as the nonlinear media and a frequency-doubled Q-switched Nd:YAG laser and its reflection from a mirror as the two counter-propagating pump beams. They successfully demonstrated the

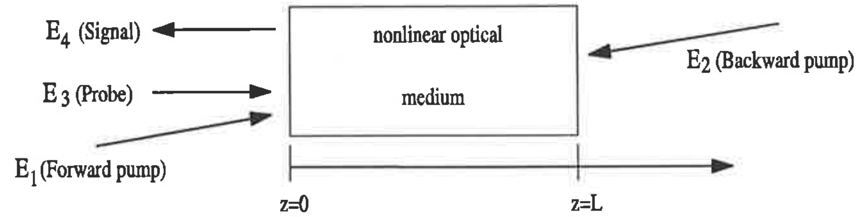

Figure 2.3: Schematic of degenerate four-wave mixing. E_1 and E_2 are two colinear counter-propagating pump beams. E_3 is a weaker probe laser beam incident at a small angle to the pump beams. E_4 is the output and is phase conjugated of E_3.

aberration correction of an Airforce resolution chart using the reflected and phase conjugated signal beam of DFWM. The first Continuous Wave (CW) experiments of DFWM were reported by Liao and Bloom [58]. DFWM has proven to have lots of applications in image processing [59, 60, 61], aberration correction [62], frequency stabilization of lasers [63], narrow band optical filters [59, 64, 65], optical switching [66], and temporal auto-correlating devices [67].

Referring to Fig. 2.3, using the phase matching condition $\Delta\mathbf{k} = \mathbf{0}$, and the fact that $\mathbf{k}_1 = -\mathbf{k}_2$, one can deduce that $\mathbf{k}_4 = -\mathbf{k}_3$ which means that the signal wave retraces the probe beam. For DFWM the dominant term in the polarisation is the third order nonlinear polarisation which is proportion to $\boldsymbol{\chi}^{(3)}(-\omega;\omega,-\omega,\omega)$ with a K factor of $K(-\omega;\omega,-\omega,\omega) = \frac{3}{4}$ [54]. This can be used in Eq. (2.16) to find equations that describe the propagation of the probe and the signal beam as

$$\frac{\partial}{\partial z}E_4 = \imath\frac{3\omega}{8nc}\boldsymbol{\chi}^{(3)}(-\omega;\omega,-\omega,\omega)E_1E_2E_3^* = \imath\kappa^*E_3^*, \qquad (2.17)$$

$$\frac{\partial}{\partial z}E_3^* = \imath\frac{3\omega}{8nc}\boldsymbol{\chi}^{(3)}(-\omega;\omega,-\omega,\omega)E_1^*E_2^*E_4 = \imath\kappa E_4 \qquad (2.18)$$

$$\text{where } \kappa^* = \frac{3\omega}{8nc}\boldsymbol{\chi}^{(3)}(-\omega;\omega,-\omega,\omega)E_1E_2$$

Using the undepleted pump approximation, Eqs. (2.17) and (2.18) can be solved for the geometry shown in the Fig. 2.3 to obtain [50, 5]

$$E_4(z) = \frac{\cos|\kappa|\,z}{\cos|\kappa|\,L}E_4(L) + \imath\frac{\kappa^*\sin|\kappa|\,(z-L)}{|\kappa|\cos|\kappa|\,L}E_3^*(0), \qquad (2.19)$$

$$E_3(z) = -\imath\frac{|\kappa|\sin|\kappa|\,z}{\kappa^*\cos|\kappa|\,L}E_4^*(L) + \frac{\cos|\kappa|\,(z-L)}{|\kappa|\cos|\kappa|\,L}E_3(0). \qquad (2.20)$$

Since only the probe beam is incident on the medium at $z = 0$, and E_4 is due to the scattering of the probe beam from the grating then, $E_4(L) = 0$ and Eq. (2.19) becomes

$$E_4(z) = \imath \frac{\kappa^* \sin |\kappa| (z - L)}{|\kappa| \cos |\kappa| L} E_3^*(0). \tag{2.21}$$

This clearly indicates that the signal beam $E_4(0)$ is the phase conjugate of the incident beam $E_3^*(0)$.

2.3 Summary

In this chapter, we first studied the concept of phase conjugation. Then, a general formulation of the interaction of light and matter was developed. We employed this formulation to study Degenerate Four Wave Mixing DFWM as a third order nonlinear process. This formulation will be used at the beginning of the next chapter to indicate the similarity among all of the stimulated scattering processes. It will be noted that the differential equations describing the stimulated scattering processes are identical. The only term that distinguishes between different processes is a third order nonlinear susceptibility χ^3 that depends explicitly on the nature of material excitation for each stimulated process. In the rest of the next chapter, we discuss the theory and properties of the Stimulated Brillouin Scattering (SBS) as one of the most common ways of achieving phase conjugation.

Chapter 3

Theory of Phase conjugation using SBS

3.1 Introduction

This chapter is devoted to the theory of Stimulated Brillouin Scattering as a phase conjugating nonlinear process. First, it is indicated that the formulations of Raman and Brillouin scattering processes are similar in the context of the parametric interaction. What makes these processes different is the mechanism of the initial excitation of the material. Next, the detailed theory of the SBS is examined. This includes the behaviour of the SBS process in the steady state regime, where there are analytical solutions of the SBS equations, and the transient regime, where only approximated solutions of the SBS equations exist. We explain how the SBS process leads to phase conjugation and define a parameter that indicates the efficiency of the phase conjugation of SBS.

3.2 Stimulated Light Scattering

Stimulated Raman and Brillouin scattering processes, in general, are very similar in nature. First an initial intense laser beam is frequency shifted and scattered from noise. Next, this scattered beam interferes with the incoming beam inducing a nonlinear polarization in the material. This nonlinear polarization is the main source of further stimulated scattering. The initial noise is different for different scattering phenomena. These two stimulated scatterings can be treated in the framework of a parametric interaction, in which the incident light beam at frequency ω_1 interacts with the material excitation wave at frequency Ω to produce a light beam at frequency $\omega_2 = \omega_1 - \Omega$. It can be shown [55] that these stimulated scatterings are third order parametric interactions. This means that the equations for the electric fields amplitudes at frequencies ω_1 and ω_2 are driven by third order nonlinear polarisations $P^{3(NL)}_{\omega_1}$ and $P^{3(NL)}_{\omega_2}$ that are proportional to $|E_2|^2 E_1$ and $|E_1|^2 E_2$, respectively. From this point of view, the differential equations governing the different kinds of stimulated scattering processes (Brillouin or Raman) are similar. Using Eqs. (2.15), (2.16) and Table 2.1, they are given (in the steady state and slowly varying approximation) as

$$\frac{\partial}{\partial z}E_1 = \frac{i3\omega_1^2}{2k_1c^2}\chi^{(3)}(-\omega_1;\omega_1,-\omega_2,\omega_2)\left|E_2\right|^2 E_1 \exp[-i(k_1-k_2+k_2-k_1)z], \tag{3.1}$$

$$\frac{\partial}{\partial z}E_2 = \frac{i3\omega_2^2}{2k_2c^2}\chi^{(3)}(-\omega_2;\omega_1,-\omega_1,\omega_2)\left|E_1\right|^2 E_2 \exp[-i(k_1-k_1+k_2-k_2)z], \tag{3.2}$$

where the two phase mismatch terms in Eqs. (3.1) and (3.2), $(k_1 - k_2 + k_2 - k_1)z$ and $(k_1 - k_1 + k_2 - k_2)z$, are identically zero. Stimulated Raman and Brillouin scatterings can be treated using Eqs. (3.1), (3.2) and different nonlinear susceptibilities $\chi^{(3)}$. $\chi^{(3)}$ summarizes the nature of the material excitation and it therefore depends explicitly on the mechanism of material excitation (i.e. electronic and vibrational in Raman, density wave in Brillouin) for different stimulated scattering processes.

Stimulated Brillouin scattering (SBS) is discussed in detail in the next section. Due to the similarity between stimulated Brillouin and Raman scattering, many of the results in the next section can be extended to stimulated Raman scattering process.

3.3 Stimulated Brillouin Scattering

The optical properties of any medium, usually dielectric constants, fluctuate due to thermal or quantum mechanical effects. The scattering of light from these fluctuations is called *spontaneous* scattering. The intensity of *spontaneously* scattered light is usually very weak in comparison to the incident light. For example, one part in 10^5 of incident power is scattered *spontaneously* in passing through 1 cm of liquid water [5]. In contrast, *stimulated* scattering occurs when an intense beam of light is scattered from fluctuations induced by the light itself. An example of *stimulated* light scattering is *stimulated Brillouin* scattering (SBS) [stimulated Mandelstam-Brillouin scattering according to Russian literature] in which strong monochromatic laser light is scattered from induced density fluctuations in the medium. Using material density variation to describe Brillouin scattering was an approximation first used by Einstein [68] and then by Brillouin [69]. The density ρ of a material is a function of pressure (p) and entropy (s). Any changes in the density can be associated with changes in the pressure and entropy as,

$$\Delta\rho = (\partial\rho/\partial p)_s \Delta p + (\partial\rho/\partial s)_p \Delta s.$$

In this regard Δp describes an acoustic wave and Δs describe an entropy wave[55].

An illustration of the SBS experiment is shown in Fig. 3.1. A laser beam of frequency ω_l is incident on a SBS medium and is scattered from refractive index variations associated with frequency Ω. The acoustic wavefronts move away from the pump beam causing the frequency of the scattered beam (Stokes beam) to be Doppler shifted down to $\omega_s = \omega_l - \Omega$. This scattered beam interferes with the incoming beam to produce a component frequency Ω which acts as a source term for the acoustic wave and magnifies its amplitude. This magnified sound wave together with the incoming laser beam reinforces the Stokes return. Under certain circumstances, the above mechanism repeats over and over leading to the exponential growth of the Stokes beam. The production of the sound wave as a result of the interference between the laser and the Stokes beam can be explained by **electrostriction**. Electrostriction causes the material to become more dense in the

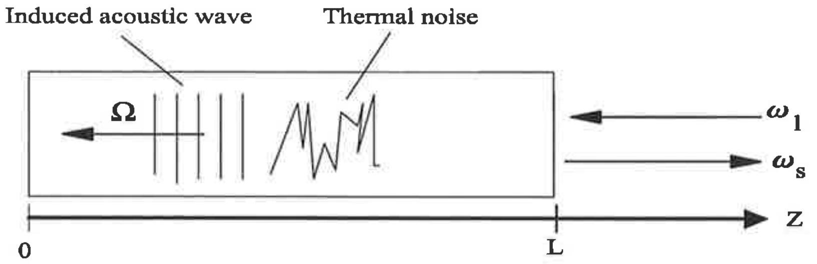

Figure 3.1: SBS experimental setup. Input pump pulse with frequency ω_l is diffracted initially from thermal noise. The diffracted and the incoming beam induce an acoustic wave Ω which propagates in the same direction as the input pulse.

region of high optical intensity. It can be described [5] by considering a capacitor immersed in a dielectric liquid and finding the pressure exerted on the dielectric liquid due to electric field. The energy density associated with an existing total electric field, Ξ, in a medium is $u = \epsilon\Xi^2/8\pi$, where ϵ is the dielectric constant of the medium. For a capacitor immersed in a dielectric liquid, the dielectric liquid is attracted and compressed to the area of high electric fields between the capacitor plates. As a result of this compression the density of the liquid changes by $\Delta\rho$. This change in the density results in a change in the dielectric constant from ϵ to $\epsilon + \Delta\epsilon$, where

$$\Delta\epsilon = \frac{\partial\epsilon}{\partial\rho}\Delta\rho.$$

Consequently, the change in the energy density is

$$\Delta u = \frac{\Xi^2}{8\pi}\Delta\epsilon = \frac{\Xi^2}{8\pi}(\frac{\partial\epsilon}{\partial\rho})\Delta\rho. \tag{3.3}$$

This change in the energy density must be equal to the work done to compress a unit volume of the liquid i.e.,

$$\Delta u = \Delta w = p\frac{\Delta V}{V} = -p\frac{\Delta\rho}{\rho}. \tag{3.4}$$

Combining Eqs. (3.3) and (3.4), yields the pressure

$$p = -\rho\frac{\Xi^2}{8\pi}(\frac{\partial\epsilon}{\partial\rho}) \equiv -\gamma_e\frac{\Xi^2}{8\pi}, \tag{3.5}$$

where $\gamma_e = \rho \dfrac{\partial \epsilon}{\partial \rho}$ is the electrostrictive constant. Any changes in the total electric field Ξ cause variation in the pressure p which in turn produces a sound wave (through the Navier-Stokes equation, Eq. 3.9).

Stimulated Brillouin scattering was first observed by Chiao *et al.* [70]. They studied the scattering of a Q-switched ruby laser from quartz or sapphire. Using a Fabry-Perot interferometer, they detected a frequency shifted component in the scattered laser beam. The process has a high conversion efficiency for transparent materials; up to about 90% of input energy can be reflected back (for optimum configuration). The backscattered laser beam should be isolated from the laser system since otherwise it can damage or add a down shifted frequency component to the laser system.

The SBS process can be described as a coupling between the laser, Stokes and the sound waves which can be represented by plane waves of central frequencies ω_l, ω_s and Ω, respectively.

$$\Xi_l(\mathbf{r},t) = \frac{1}{2}[E_l(\mathbf{r},t)e^{\imath(\omega_l t + k_l z)} + c.c.], \tag{3.6}$$

$$\Xi_s(\mathbf{r},t) = \frac{1}{2}[E_s(\mathbf{r},t)e^{\imath(\omega_s t - k_s z)} + c.c.], \tag{3.7}$$

$$\rho = \rho_0 + \frac{1}{2}[Q(\mathbf{r},t)e^{\imath(\Omega t + q z)} + c.c.]. \tag{3.8}$$

Here the incident laser beam and the acoustic field propagate from right to left and the Stokes field propagates from left to right (Fig. 2.1), $\Omega = \omega_l - \omega_s$, $q = k_l + k_s \approx 2k_l$, and ρ_0 is the mean density of the medium. E_l, E_s and Q are the amplitudes of the laser, Stokes and acoustic waves, respectively and vary slowly as a function of time. Using the usual dispersion relation between the wave vectors q, k_l and k_s and the wave frequencies Ω, ω_l and ω_s, one can find the sound wave frequency Ω as

$$\Omega = \frac{2nv_s}{c}\omega_l,$$

where v_s is the speed of sound in the material and n is the refractive index of the medium. The material density obeys the Navier-Stokes equation [71]

$$-\frac{\partial^2 \rho}{\partial t^2} + v_s^2 \nabla^2 \rho + v_v \frac{\partial}{\partial t} \nabla^2 \rho = -\nabla . f, \tag{3.9}$$

where $f = -\nabla p$ is the driving source term, which represents the change in the density of the material due to the pressure exerted by electric field. Using Eq. (3.5) in Eq. (3.9), we find

$$-\frac{\partial^2 \rho}{\partial t^2} + v_s^2 \nabla^2 \rho + v_v \frac{\partial}{\partial t} \nabla^2 \rho = \frac{\gamma_e}{8\pi} \nabla^2 \Xi^2. \tag{3.10}$$

In this equation v_v is the kinematic viscosity, and Ξ is the total electric field in the material given by:

$$\Xi = \Xi_l(\mathbf{r}, t) + \Xi_s(\mathbf{r}, t). \tag{3.11}$$

Substituting Eqs. (3.11) and (3.6)-(3.8) in Eq. (3.10) yields an equation, which relates the amplitudes of the laser, Stokes and acoustic fields. This equation has a large number of terms which can be simplified using the following relations and approximations [8].

1) The ordinary dispersion relation for the sound wave $q^2 v_s^2 = \Omega^2$.

2) $q \gg \partial(\text{all fields})/\partial z$, or equivalently $\lambda_{sound}($ or $\lambda_l) \ll \partial z/\partial(\text{all fields})$ since $q = 2k_l = 2\pi/\lambda_{(sound)}$, which means that the wavelength of the sound wave is small compared to the length over which the electric and sound fields change considerably. This approximation is similar to the slowly varying approximation that is usually considered for the electric fields.

3) $\Omega \gg \partial/\partial t$. This approximation requires that Ω should be greater than the pump bandwidth, 1/(pump pulse duration), and the SBS decay rate Γ (as defined below). These conditions are usually met for long coherence length lasers and most of the materials (see [5]) but some broad-band lasers do not match these conditions.

4) $2\Gamma/v_s \gg \partial/\partial z$, which means that the phonon propagation distance must be short compared to the distance over which the electric and sound fields vary significantly. This condition is usually met since hypersonic phonons are strongly

damped and thus propagate only over very short distances before being absorbed (the typical absorption coefficient of the sound wave is $\alpha_{(sound)} = \Gamma/v_s \sim 10^5\,\mathrm{m}^{-1}$[5]).

Using these assumptions, the simplified equation for the sound wave that is commonly used (see [8] and references therein) is given by:

$$(\frac{\partial}{\partial t} + \Gamma)Q = -\imath g_1 E_l E_s^*, \tag{3.12}$$

where g_1 is the coupling coefficient constant between the electric fields and the acoustic wave, $\Gamma = 1/2\tau$ is the decay rate of the sound wave in the material and τ is the phonon lifetime of the material.

The coupled equations for the electric fields can be derived from the wave equation

$$\nabla^2\Xi - (\frac{n}{c})^2\frac{\partial^2\Xi}{\partial t^2} = \frac{4\pi}{c^2}\frac{\partial^2 P}{\partial t^2}, \tag{3.13}$$

in which P is the induced and nonlinear polarisation of the material and is given by [5]

$$P = \frac{1}{4\pi\rho_0}\gamma_e\rho\Xi.$$

The left hand side of Eq. 3.13 includes components of electric fields at frequencies ω_s and ω_l. Thus, on the right hand side only those terms of $\rho\Xi$ that contribute to frequencies terms ω_s and ω_l should be considered. In addition to this, one can use the Slowly Varying Approximation (SVA), which requires

$$\begin{aligned} \left|\frac{\partial^2 E_i}{\partial z^2}\right| &\ll \left|k_i\frac{\partial E_i}{\partial z}\right|, \\ \left|\frac{\partial^2 E_i}{\partial t^2}\right| &\ll \left|\omega_i\frac{\partial E_i}{\partial t}\right| \quad \text{for } i = s, l, \end{aligned}$$

to simplify the left and right hand side of Eq. 3.13, using Eqs. (3.6)-(3.8) and (3.11). This yields the following equations

$$\begin{aligned} (\frac{i}{2K_s}\nabla_t^2 + \frac{n}{c}\frac{\partial}{\partial t} + \frac{\partial}{\partial z})E_s &= -ig_2 Q^* E_l, \\ (\frac{-i}{2K_l}\nabla_t^2 + \frac{n}{c}\frac{\partial}{\partial t} - \frac{\partial}{\partial z})E_l &= -ig_2 Q E_s. \end{aligned}$$

Like g_1 in Eq. (3.12), g_2 is the electric and the acoustic fields coupling coefficient and ∇_t^2 is the transverse derivative operator. These two equations together with Eq. 3.12 are the three main coupled differential equations that describe SBS. These three coupled differential equations, or approximate versions of them, are the starting equations for most of the theoretical and numerical studies of SBS [7, 8, 1, 17]

$$(\frac{i}{2K_s}\nabla_t^2 + \frac{n}{c}\frac{\partial}{\partial t} + \frac{\partial}{\partial z})E_s = -\imath g_2 Q^* E_l, \tag{3.14a}$$

$$(\frac{-i}{2K_l}\nabla_t^2 + \frac{n}{c}\frac{\partial}{\partial t} - \frac{\partial}{\partial z})E_l = -\imath g_2 Q E_s, \tag{3.14b}$$

$$(\frac{\partial}{\partial t} + \Gamma)Q = -\imath g_1 E_l E_s^*. \tag{3.14c}$$

3.3.1 Steady state regime of SBS

In the steady state and one-dimensional regime, we can ignore the time and transverse derivatives, $\frac{\partial}{\partial t}$ and∇_t^2, of all the fields and rewrite Eqs. (3.14) as

$$\frac{\partial}{\partial z}E_s = \frac{g_1 g_2}{\Gamma}\left|E_l\right|^2 E_s \tag{3.15}$$

$$\frac{\partial}{\partial z}E_l = \frac{g_1 g_2}{\Gamma}\left|E_s\right|^2 E_l. \tag{3.16}$$

Here, $\left|E_l\right|^2$ is the intensity of the pump wave. We can multiply both sides of these equations by E_s^* and E_l^* respectively to obtain

$$\frac{\partial}{\partial z}I_s = g I_l I_s \tag{3.17}$$

$$\frac{\partial}{\partial z}I_l = g I_l I_s, \tag{3.18}$$

where I_l and I_s are given as

$$I_l = \left|E_l\right|^2 \quad \& \quad I_s = \left|E_s\right|^2.$$

Here, $g = 2g_1 g_2/\Gamma$ is the gain coefficient of the material and is given by [71, 5]

$$g = g_{Max}\frac{1}{1 + (\Delta\omega/\Gamma)^2},$$

Table 3.1: Frequency shift, linewidth and gain coefficient of SBS for some materials. Except Fluorinert and Freon 113, values have been quoted from "*Nonlinear Optics*" by Boyd [5].

Substance	Wave length λ (nm)	Frequency shift $\Omega/2\pi$ (MHz)	Band width $\Gamma/2\pi$ (MHz)	Gain factor g_{Max} cm/MW
CS_2	694	5850	52.3	0.15
Fluorinert FC72 [72]	1060	1100	270	0.0060-0.0065
Freon 113 [73]	1064	1800	190	0.0062
Acetone	694	4600	224	0.02
Toluene	694	5910	579	0.013
CCl_4	694	4390	520	0.006
Methanol	694	4250	250	0.013
Ethanol	694	4550	353	0.012
Benzene	694	6470	289	0.018
H_2O	694	5690	317	0.0048
Cyclohexane	694	5550	774	0.0068
CH_4(140 atm)	694	150	10	0.1
Optical glasses	694	11000-16000	10-106	0.004-0.025
SiO_2	694	17000	78	0.0045

in which $\Delta\omega = \omega - \Omega$ is the deviation from the Brillouin frequency. This shows that the SBS gain has a Lorentzian shape with a maximum at $\omega = \Omega$ and half width Γ. The maximum value of the gain factor g_{Max} is given as,

$$g_{Max} = \frac{\gamma_e^2 \omega_l^2}{2nvc^3\rho_0\Gamma}$$

where γ_e is the electrostrictive coefficient, c and v are the light and sound wave velocities respectively, n is the refractive index of the material and ρ_0 is the mean density of the material. Some typical values of Brillouin frequency shift Ω, gain band width Γ and g_{Max} for different materials are given [71, 5] in Table 3.1.

In the undepleted pump regime, where the interaction between the pump and Stokes beam is not strong and we can ignore $\partial I_l/\partial z$, Eq. (3.17) can be solved for I_s to give

$$I_s = I_{s0}e^{gI_lL_{imm}} = I_{s0}e^{G_0},$$

where I_{s0} is the initial Stokes intensity,

$$G_0 = gI_lL_{imm} \tag{3.19}$$

is the usual steady state gain of the SBS process and L_{imm} is the immersion length of the laser beam into the SBS medium.

Eqs. (3.17) and (3.18) should be solved simultaneously in the pump depleted regime. Using these two equations, we can show that

$$\frac{\partial}{\partial z}I_s = \frac{\partial}{\partial z}I_l \Rightarrow I_l(z) = I_s(z) + a, \tag{3.20}$$

where a is a constant showing the percentage of the input energy not reflected into the Stokes pulse. For a 100% reflection $a = 0$. Eq. (3.20) can be used in Eq. (3.17) to find

$$\frac{\partial}{\partial z}I_s = 2gI_s^2 + 2agI_s. \tag{3.21}$$

This, and a similar equation for I_l, can be solved for I_s and I_l by changing the variables $I_s \to 1/I_s$ and $I_l \to 1/I_l$ and using the geometry shown in the figure 3.1. The final solutions are,

$$I_s(z) = \frac{a[I_l(L) - a]}{I_l(L)e^{ga(L-z)} - [I_l(L) - a]}, \tag{3.22}$$

$$I_l(z) = \frac{aI_l(L)}{I_l(L) - [I_l(L) - a]e^{-ga(L-z)}}, \tag{3.23}$$

where $I_l(L)$ is the input pump intensity. In the limit of 100% reflection ($a \to 0$) these two equations become

$$I_l(z) = I_s(z) = \frac{I_l(L)}{1 + I_l(L)g(L-z)}. \tag{3.24}$$

Although Eqs. (3.17) and (3.18) are derived for one dimensional SBS processes, we can still introduce the focusing geometry into the SBS equations [24, 20].

First, we assume that the pump and the Stokes beams are unaberrated and have

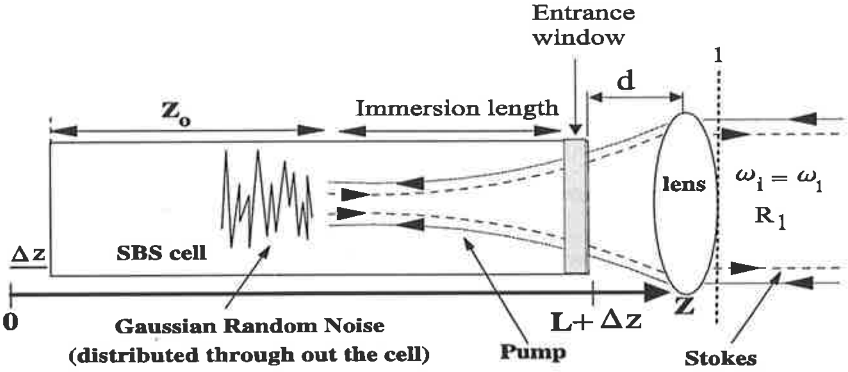

Figure 3.2: Introducing focusing geometry to SBS process.

Gaussian spatial profiles with the same Gaussian beam parameters i.e.,

$$I_l = \frac{P_l}{\pi\omega^2} \quad \text{and} \quad I_s = \frac{P_s}{\pi\omega^2}$$

where

$$\omega^2 = \omega_0^2[1 + (\frac{z - z_0}{z_R})^2].$$

Here, ω_0^2 is the beam waist at the focus, z_0 is the position of the focus inside the cell, as shown in Fig. 3.2, and $z_R = \pi n \omega_0^2/\lambda$ is the Rayleigh range of the laser beam. Using the assumption that the pump and Stokes intensities are changing not only because of the nonlinear interaction with the material but also because of the change in the area of the beams, the source terms in the right hand sides of Eqs. (3.17) and (3.18) can be modified to include the terms that represents the change in laser intensities due to the change in their area. To this end, we add $-[I_s/\pi\omega^2](\partial/\partial z)$ and $-[I_l/\pi\omega^2](\partial/\partial z)$ to the right hand side of Eqs. (3.17) and (3.18), respectively. By adding these two terms and changing the variables $I_s \to P_s$ and $I_l \to P_l$, Eqs. (3.17) and (3.18) can be rewritten as

$$\frac{\partial}{\partial z} P_s = \frac{g}{\pi\omega^2} P_l P_s, \tag{3.25}$$

$$\frac{\partial}{\partial z} P_l = \frac{g}{\pi\omega^2} P_l P_s. \tag{3.26}$$

In the limit of small input power, P_l, where there is not a strong interaction between the pump and the medium, the pump wave passes through the medium without much depletion. Therefore, P_l can be approximated to be constant throughout the medium. We use this approximation to integrate Eq. (3.25) from the focus to the entrance to the cell (see Fig. 3.2) to find

$$\ln\frac{P_s}{P_{s0}} = \frac{gP_l(L)}{\pi\omega_0^2}\int_{focus=z_0}^{entrance=L}\frac{dz}{[1+\frac{(z-z_0)^2}{z_R^2}]} = \frac{gP_l(L)}{\pi\omega_0^2}z_R\tan^{-1}(\frac{L-z_0}{z_R}), \tag{3.27}$$

$$= \frac{gP_l(L)}{\lambda}\tan^{-1}(\frac{L-z_0}{z_R}) = G. \tag{3.28}$$

and therefore

$$P_s(L) = P_{s0}e^G. \tag{3.29}$$

Here,

$$G = G(z_0) = \frac{gP_l(L)}{\pi\omega_0^2}\int_{focus=z_0}^{entrance=L}\frac{dz}{[1+\frac{(z-z_0)^2}{z_R^2}]} \tag{3.30}$$

is the steady state gain (including focusing geometry), λ is the wavelength of the laser beams and $P_{s0} = P_s(z_0)$ and $P_{l0} = P_l(z_0)$ are the pump and the Stokes powers at the focus. We have also assumed that the SBS process initiates at the focus from Stokes photons P_{s0}, created by the spontaneous Brillouin scattering of the pump photons P_{l0} at the focus. Thus, we expect that the Stokes power at the focus P_{s0} to be proportional to the pump power P_{l0} i.e.,

$$P_{s0} = fP_{l0}. \tag{3.31}$$

The reflectivity of the SBS process is defined as the ratio of the Stokes power at the entrance to cell to the input power i.e.

$$R = \frac{P_s(L)}{P_l(L)}. \tag{3.32}$$

Using Eqs. (3.29) and (3.31) and the fact that in the undepleted pump regime the pump power remains constant throughout the cell, we can rewrite Eq. (3.32) as

$$R = \frac{P_{s0}}{P_{l0}} e^G = f e^G. \tag{3.33}$$

Experimental results show that to obtain a reflectivity of order of $R \sim 0.1$, namely threshold reflectivity, G should be order of $G_{th} \sim 25-30$ [74]. This is connected with the fact that the SBS process is initiated from spontaneous scattering of the pump beam from fluctuations in the material density. For $R \sim 0.1$ and $G_{th} \sim 25-30$, f can be evaluated from Eq. (3.33) to be,

$$f = e^{-G_{th}} = e^{(-25)-(-30)} \sim 10^{-12} - 10^{-11}, \tag{3.34}$$

which is similar to the value obtained by Zel'dovich *et al.* [3] from the physical properties of spontaneous scattering. From this value of the steady state threshold gain $G_{th} \sim 25-30$, one can estimate the threshold power, P_{th}, necessary to initiate the SBS process as [using Eq. (3.28)],

$$(P_l)_{th} = \frac{G_{th}\lambda}{g} \frac{1}{\tan^{-1}(\frac{L-z_0}{z_R})}. \tag{3.35}$$

This indicates that the threshold power depends on g, the gain coefficient of the material, L the length of the SBS cell and z_R the Rayleigh range of the focused beam. However, plotting $(P_l)_{th}$ as a function of $L - z_0$ (see Fig. 3.3) shows that for SBS cell length larger than about 2.5×Rayleigh range the threshold power remains constant. This suggests that the effective interaction length for SBS is approximately 2.5×Rayleigh range and the length of the SBS cell does not affect the threshold power as long as it is larger than 2.5×Rayleigh range. This result was found experimentally by Munch *et al.* [12]. In fact, in their experiment they have shown that the effective interaction length for SBS at the threshold is the shorter of the following parameters: the cell length, 3 times the coherence length or 2.5 times the Rayleigh range of the input laser radiation.

Eqs. (3.25) and (3.26) can also be solved for the depleted pump, when the input power is above the threshold power. In this regime it is clear from Eqs. (3.25) and

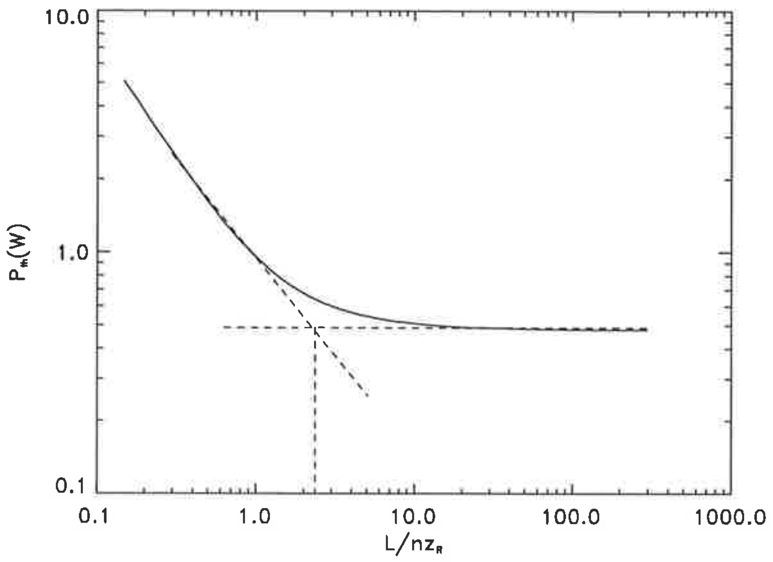

Figure 3.3: Threshold power is examined as a function of cell length/Rayleigh range. For cell lengths over 2.5×Rayleigh range the threshold power remains constant.

(3.26) that

$$\frac{\partial}{\partial z}P_s = \frac{\partial}{\partial z}P_l, \tag{3.36}$$

and therefore

$$P_l(z) = P_s(z) + a. \tag{3.37}$$

Here, a is a constant indicating the degree of pump depletion and is given by

$$a = P_l(L) - P_s(L) = P_l(L)(1 - R).$$

Using Eqs. (3.37) and (3.28) and changing the variables P_s and P_l to $1/P_s$ and $1/P_l$, one can solve Eqs. (3.25) and (3.26) to yield,

$$P_s(L) = \frac{aP_{s0}}{P_{l0}e^{-G(1-R)} - P_{s0}}, \tag{3.38}$$

$$P_l(L) = \frac{aP_{l0}}{P_{l0} - P_{s0}e^{G(1-R)}}. \tag{3.39}$$

The SBS reflectivity $R = P_s(L)/P_l(L)$ can be calculated using Eqs. (3.38), (3.39),

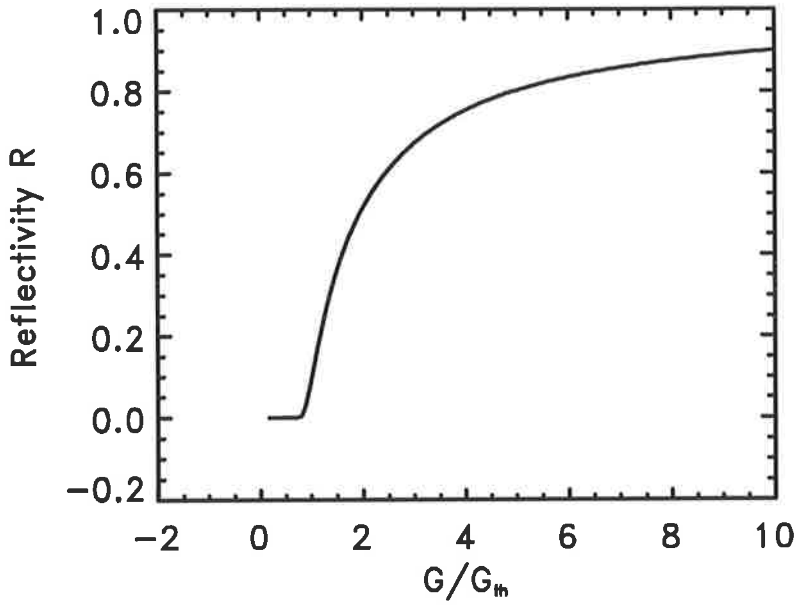

Figure 3.4: Reflectivity as a function of G/G_{th} where $G = \frac{gP_l(L)}{\lambda}\tan^{-1}(\frac{L-z_0}{z_R})$ and $G_{th} = 25$. Threshold reflectivity $R \sim 0.1$ occurs at $G = G_{th}$.

(3.34) and (3.31) as

$$R = \frac{P_s(L)}{P_l(L)} = fe^{G(1-R)}, \tag{3.40}$$

which can be rearranged to give

$$\frac{G}{G_{th}} = \frac{1 + G_{th}^{-1}\ln R}{1 - R}. \tag{3.41}$$

Using this equation to plot R vs G/G_{th} (see Fig. 3.4) shows clearly that the SBS process has a threshold i.e., its reflectivity rises rapidly for values of G larger than G_{th}.

This simple threshold behaviour of SBS has been confirmed by experiment [73, 75, 2] and our numerical model (see next chapter and [20]). Figures 3.5 and 3.6 show the numerical (calculated according to our 1D model) and experimental results [2], respectively, for the pump pulse, Stokes pulse and the reflectivity. Both theory and experiment show that the Stokes pulse grows rapidly just after a certain threshold power is reached.

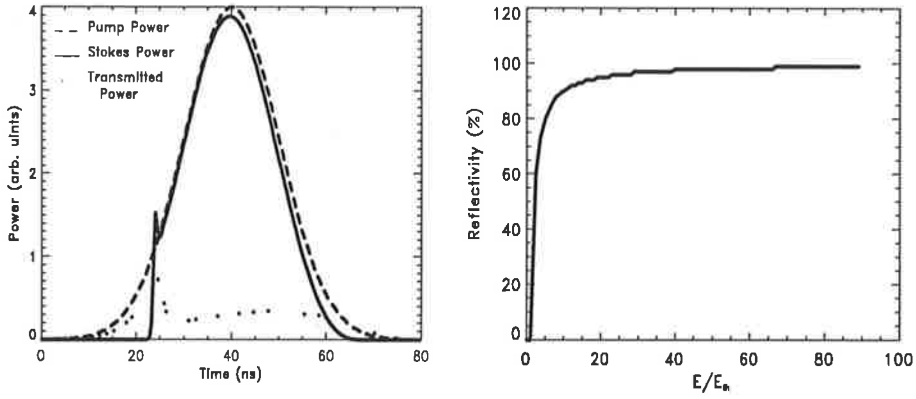

Figure 3.5: Numerical results of the input, Stokes and transmitted pulse. The SBS reflectivity as a function of energy is shown in the right graph. E_{th} is the threshold energy. The numerical results are calculated according to our 1D model developed in Chap. 4.

3.4 Phase conjugation property of SBS

An interesting property of the SBS process is that the reflected beam retraces the incident beam. This property was first observed in 1964 by Brewer [76]. In an SBS experiment with a ruby laser Brewer noticed that "...the back-scattered light retraces the path of the exciting laser beam".

Zel'dovich *et al* [6] were the first group to observe that in a SBS experiment the back-scattered beam is a phase conjugate of the incident beam. The setup of their experiment is shown in the Fig. 3.7. They focused a single mode ruby laser beam into a SBS cell filled with methane gas at 125 atmospheres. They used two cameras to observe the intensity distribution of the incident (measured by camera 1) and reflected (measured by camera 2) beams. To distort the wavefront of the incident beam, they used a glass plate before focusing the beam into the SBS cell. The Stokes return of the SBS mirror then passed through the glass plate into camera 2. It was observed that the Stokes intensity distribution matches that of the incident beam implying that the reflected beam is the phase conjugate of the incident one.

An important practical application of phase conjugation was demonstrated by Nosach *et al.* [49]. In their experiment, a SBS mirror (a cell filled with CS_2) was used to compensate the distortion in a laser beam (6943 Å), caused by a ruby laser amplifier. The reflected beam of this SBS mirror retraces the incident beam and

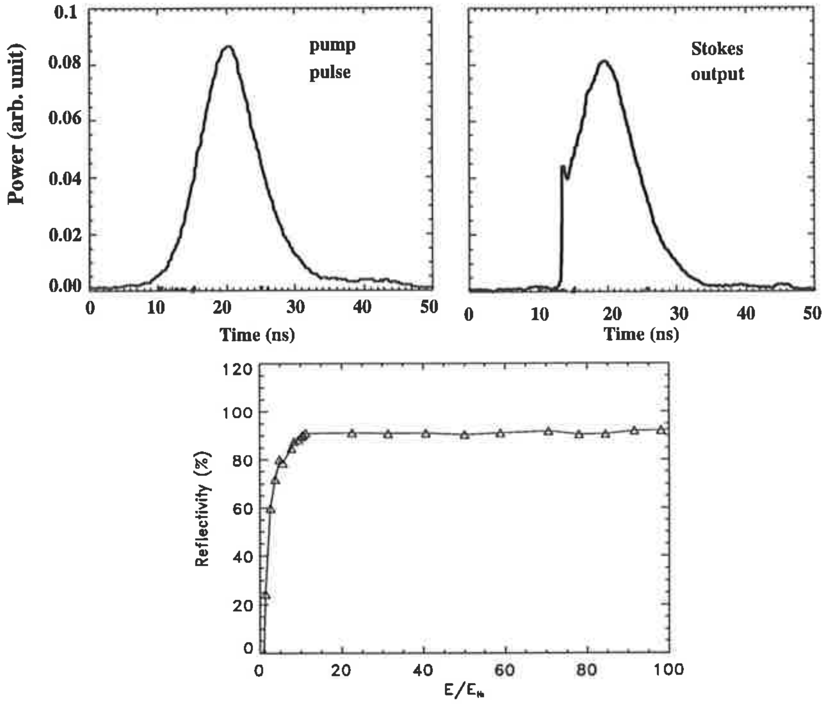

Figure 3.6: Typical experimental results [2] for the pump and Stokes pulses. The reflectivity as a function of energy is shown as well. Experimental results were obtained for Freon-113. E_{th} is the threshold energy.

is the phase conjugate of the incident beam. The distortion in this beam is then compensated in passing back through the ruby amplifier. The experimental set up was the same as in Fig. 3.7 except the phase-distorting plate was replaced by a ruby laser amplifier. This resulted in the extraction of a high power beam with undistorted wavefront.

In degenerate four-wave mixing the phase conjugation property of the reflected beam can be clearly seen from the Equations describing this phenomena. In Eq. (2.21) it is seen that the reflected beam in DFWM is proportion to the complex conjugate of the incident beam and retraces it ($K_4 = -K_3$). In the case of SBS phenomena, however, the fact that the Stokes beam is the phase conjugate of the incident beam is not obvious from the equations. If we ignore $\partial/\partial t$ in Eq. (3.14c) [i.e. the steady state regime] solve for Q and substitute it into Eq. (3.14a), we obtain

$$(\frac{i}{2K_s}\nabla_t^2 + \frac{n}{c}\frac{\partial}{\partial t} + \frac{\partial}{\partial z})E_s = g_1 g_2 \left|E_l\right|^2 E_s.$$

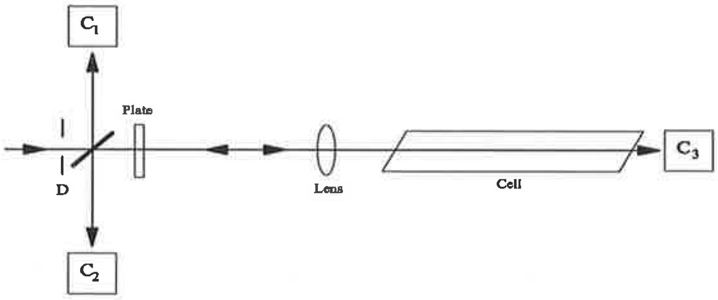

Figure 3.7: The experimental setup to demonstrate the phase conjugation property of SBS. The plate distorts the phase front of the passing beam. The cameras $C_1$and C_2 record the input, and backscattered beam profiles, respectively. The SBS cell is filled with methane. Figure is based on figures in [3]

This shows that the driving force of the Stokes pulse is proportional to $|E_l|^2 E_s$, which contains no phase information of the incident beam. A reason why SBS leads to phase conjugation can be given as follows [37, 5]. For an aberrated input beam the information about the phase distortion of the beam is translated to an intensity pattern once it is focused into the focal volume (far field). The intensity pattern of a highly aberrated beam is highly non-uniform in the focal volume (i.e. a volume speckle pattern). Next, this nonuniform-intensity beam scatters off the density noise of the material. It is initially scattered to the all possible spatial modes but, only the mode that can best match the far field pattern of the incident beam has the maximum gain. This mode is in fact the phase conjugate of the input, and when it grows it will suppress all the other modes.

The degree of phase conjugation can be quantified by defining a parameter, namely *fidelity* [37], as

$$H(z,t) = \frac{\left|\int E_l(r,z,t)E_s(r,z,t)d^2r\right|^2}{\int |E_l(r,z,t)|^2\, d^2r \int |E_s(r,z,t)|^2\, d^2r}, \tag{3.42}$$

in which $0 \leq H \leq 1$. The numerator expression shows the correlation between the laser and the Stokes fields. For perfect replication of the laser pulse $H = 1$ otherwise $H < 1$. This definition for the fidelity, although useful for numerical modeling, is very hard to measure in experiments. In SBS experiments using short pulse lasers, fidelity is usually measured using the power-in-bucket technique [12, 77]. In this method the

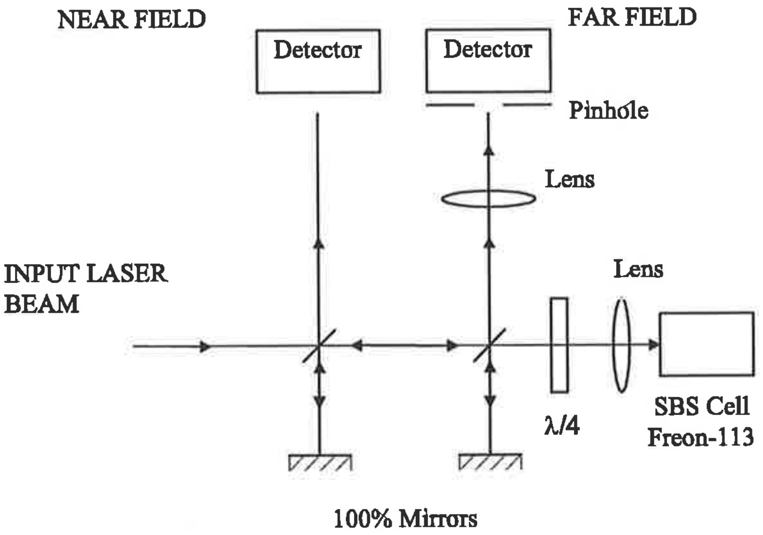

Figure 3.8: Diagram of the Near and Far field diagnostic technique for the measurement of the time resolved and time averaged fidelity [2].

transmission of the SBS Stokes return power is measured through a single diffraction limited pinhole located at the far field of a lens. This power, divided by the near field Stokes power and multiplied by the chosen, theoretical transmission factor of the pinhole, gives a Stokes beam merit (merit is here proportional to the square root of the conventional definition of beam quality). Fidelity can be obtained, once the Stokes beam merit is compared to that of the original laser beam. A typical schematic of the diagnostic technique for measuring fidelity [2] is shown in Fig. 3.8. By measuring the pump and the Stokes powers at the Near and Far fields, one can define the fidelity by

$$\text{Fidelity} = \frac{\text{SBS beam merit}}{\text{Laser beam merit}}, \text{ where} \tag{3.43}$$

$$\text{SBS beam merit} = \frac{\text{Far SBS power through pinhole}}{\text{Near field SBS power } \times \text{T\%}} \text{ and} \tag{3.44}$$

$$\text{Laser beam merit} = \frac{\text{Far field laser power through pinhole}}{\text{Near field laser power} \times \text{ T\%}}. \tag{3.45}$$

Numerical and experimental plots (see Fig. 3.9) of fidelity versus input energy show that it grows very rapidly when the input energy is close to the threshold energy and saturates at values of the order of 90% for very high input energies.

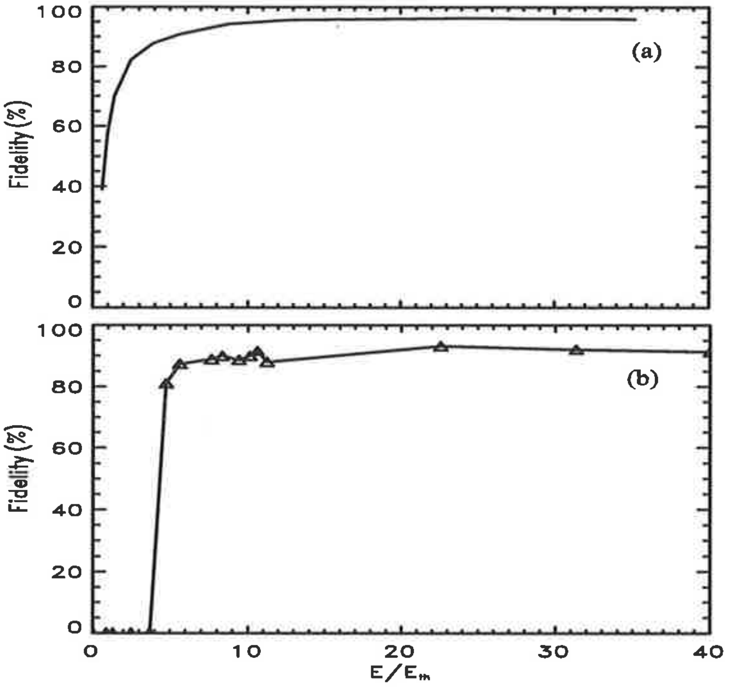

Figure 3.9: (a) Typical numerical (see Chap. 5 for details) and (b) experimental [2] results for the fidelity of SBS. Experimental results are obtained for Freon-113.

3.4.1 Transient regime of SBS

The transient regime of SBS is usually considered when the duration of the pump beam, t_p, is shorter than the phonon lifetime of the SBS material ($t_p < \tau$). Most numerical models of SBS deal with pump pulses whose durations are much longer than the phonon lifetime of the SBS material. This enables them to use the steady state approximation. However, as Wandzura [9] and Afshaarvahid *et al.* [20, 35] pointed out, in reality there is no steady state regime for SBS. The steady state regime of SBS fails to give a true picture of SBS, even with pump pulses longer than the phonon lifetime of the SBS material. Two reasons can be given for this: 1) the threshold behaviour of SBS and 2) the observation of large scale fluctuations in the output Stokes pulse.

1) The SBS process has a threshold, i.e., at a certain input power the reflectivity increases rapidly. Such a rapid increase causes a relaxation oscillation in the Stokes pulse which is due to the transient behaviour of the SBS process at the threshold. This will be studied in Chap.4.

2) Depending on focusing geometry, input intensity and pulse duration, there is always a finite probability to have large scale fluctuations in the Stokes pulse. However, there are conditions for which this probability decreases. From this point of view, the steady state regime of SBS can be considered as the parameter regime of SBS which results in the minimum probability of observing fluctuations. We will discuss this in the rest of this section and in Chap. 4.

The SBS process starts from spontaneous emission of thermal noise. This noisy spontaneous emission is amplified through two main regions, namely region I and II [18], which are discussed as follows. In region I, the initial Stokes signal is amplified exponentially where its intensity becomes the order of $\sim 0.1\%$ of the pump pulse. The gain coefficient of the amplification in this region is roughly gI_{th} where I_{th} is the threshold intensity of the SBS process [37, 13]. At the end of this region the Stokes intensity is a noise-like signal. This is expected, since in this region the pump pulse is almost undepleted and the SBS medium behaves like a linear amplifier for the spontaneous emission initiated from thermal noise. This thermal noise initiation of SBS can be included in the SBS equations by adding a Langevin noise term $f(z,t)$ to the right hand side of Eq. (3.14c) as

$$(\frac{\partial}{\partial t}+\Gamma)Q=-\imath g_1 E_l E_s^* + f(z,t). \tag{3.46}$$

Assuming that the pump depletion is negligible and neglecting the transverse derivatives, Eqs. (3.14a), (3.14b), and (3.46) can be solved to find [78, 79, 13]

$$E_s(L,t)=\imath g_2 E_l \int_{-\infty}^{t} dt' \int_0^L dz' e^{-(\Gamma)(t-t')} f^*(z',t') \times I_0(\sqrt{2G\Gamma z'(t'-t)/L}), \tag{3.47}$$

where I_0 is the zeroth-order modified Bessel function. Using the above equation, one can show [13, 11, 80, 81] that the spectrum linewidth of the Stokes pulse in this region (for $G \gg 1$) is

$$\Delta\omega=\Gamma\sqrt{\frac{\ln 2}{G}}. \tag{3.48}$$

This indicates that the spectrum of the Stokes field narrows as G increases. Depending on the focusing geometry and input energy, the duration of temporal fluctuations in the Stokes pulse at the end of region I can be the order of $4\tau \sim \frac{1}{10}\tau$ [18].

The final and main amplification of the Stokes pulse occurs in the region II [18] or the *depletion region* [13]. The length of this region (which can be shown [20] to be the length over which the Stokes intensity drops to $1/e$ of its maximum) is given as $l_{dep} = l_{imm}/G_0$ [13, 18, 20], where l_{imm} is shown in Fig. 3.2. The propagation time through this region, $T_{l_{dep}}$, the duration of the temporal variations in the Stokes pulse at the beginning of this region, T_s, and the phonon lifetime of the material, τ are crucial parameters in determining the dynamics of the temporal variations in this region. In fact a useful parameter

$$\gamma = \frac{T_{l_{dep}}}{\tau} = \frac{nl_{imm}}{cG_0\tau} = \frac{T_t\Gamma}{G_0} \tag{3.49}$$

can be introduced to classify the dynamics of the temporal evolution of the Stokes pulse in the depletion region (see the following discussion).

Consider the following boundary conditions for the depletion region (see Fig. 3.1)

$$\begin{aligned} P_l(L) &= \text{input pump power} \\ P_s(L - l_{dep}, t) &= F(t) \text{ Stokes power at the beginning of the depletion region} \end{aligned}$$

In the steady state regime, when the duration of the temporal variations in the Stokes pulse at the beginning of the depletion region is much longer than both the phonon lifetime and the propagation time through the depletion region i.e.,

$$T_s \gg \tau \gg T_{l_{dep}},$$

one can find

$$\gamma = \frac{T_{l_{dep}}}{\tau} \ll 1 \Rightarrow \frac{T_t\Gamma}{G_0} \ll 1 \Rightarrow G_0 \gg T_t\Gamma. \tag{3.50}$$

Using Eqs. (3.25), (3.26), (3.36), (3.37), the pump and Stokes power $P_l(z)$ and $P_s(z)$

can be solved as a function of z and input pump power $P_l(L)$ as

$$P_l(z) = \frac{aP_l(L)}{P_l(L) - [P_l(L) - a]e^{-aG(z)/P_l(L)}}, \tag{3.51}$$

$$P_s(z) = \frac{a[P_l(L) - a]}{P_l(L)e^{aG(z)/P_l(L)} - [P_l(L) - a]}. \tag{3.52}$$

In the limit of 100% conversion of the pump energy to the Stokes energy i.e. $a \longrightarrow 0$, one can show that

$$\lim_{a \to 0} P_l(z) = \lim_{a \to 0} P_s(z) = \frac{P_l(L)}{1 + G(z)}. \tag{3.53}$$

This indicates that for $G_0 \gg T_t\Gamma$ and a heavily depleted pump , the Stokes pulse variations at the beginning of region II causes only a slight change in the output of the Stokes pulse and therefore fluctuations will be smoothed in the output of the Stokes pulse.

For a pulsed pump, however, $G_0 = gI_l(t)L_{imm}$ is a function of time. Therefore, the SBS gain G_0 is highest for the middle part of the input pulse and decreases towards the beginning and end of the input pulse. From the above discussion, two conditions $G_0 \gg T_t\Gamma$ and $\tau \ll T_s$ are necessary to avoid fluctuations in the output Stokes pulse. Applying these conditions for a pulsed input pump imply that; a) the probability of observing fluctuations in the middle part of the output Stokes pulse decreases because in this region $G_0 \gg T_t\Gamma$ and b) the fluctuations in the Stokes pulse, if any, have durations of order of $\lesssim \tau$, thus containing very little energy.

By considering the time dependent SBS equations (in one dimension, see Eqs. 3.14a, 3.14b and 3.14c)

$$(\frac{n}{c}\frac{\partial}{\partial t} + \frac{\partial}{\partial z})E_s = -ig_2Q^*E_l, \tag{3.54}$$

$$(\frac{n}{c}\frac{\partial}{\partial t} - \frac{\partial}{\partial z})E_l = -ig_2QE_s, \tag{3.55}$$

$$(\frac{\partial}{\partial t} + \Gamma)Q = -ig_1E_lE_s^*, \tag{3.56}$$

one can generalise the above simple discussion to a more realistic condition in which the phonon lifetime, τ, the propagation time, $T_{l_{dep}}$, and the duration of temporal variations in the Stokes pulse, T_s, are finite. Eqs. (3.54)-(3.56) can be rewritten for intensities $I_l(z)$ and $I_s(z)$, if we ignore the change in the sign of the phase of the fields (this is not generally speaking true and in the next chapter a more realistic case will be considered). As a first order of approximation the solution of the intensity equations can be written as a stationary part plus a small non-stationary part, i.e.,

$$I_l(\widetilde{z},\widetilde{t}) = I_l^0(\widetilde{z}) + I_l^1(\widetilde{z},\widetilde{t}), \tag{3.57}$$

$$I_s(\widetilde{z},\widetilde{t}) = I_s^0(\widetilde{z}) + I_s^1(\widetilde{z},\widetilde{t}). \tag{3.58}$$

Here, $I_l^0(\widetilde{z})$ and $I_s^0(\widetilde{z})$ are the stationary parts, given by Eqs. (3.22) and (3.23), $I_l^1(\widetilde{z},\widetilde{t})$ and $I_s^1(\widetilde{z},\widetilde{t})$ are the small non-stationary parts, and $\widetilde{t} = t/T_{l_{dep}}$ and $\widetilde{z} = zG_0/l_{imm}$ are dimensionless time and position inside the SBS medium. These relations [Eqs. (3.57) and (3.58)] can be substituted in the SBS equations for intensities to find a set of differential equations for $I_l^1(\widetilde{z},\widetilde{t})$ and $I_s^1(\widetilde{z},\widetilde{t})$. These equations can then be solved using Laplace transform [82, 18]. A specific and interesting example is when the Stokes intensity at the beginning of the depletion region is

$$I_s(L,\widetilde{t}) = I_s^0(L) + A\sin(\omega\widetilde{t}), \tag{3.59}$$

i.e., the Stokes intensity is the stationary part plus a small intensity noise term $I_s^1(L,\widetilde{t}) = A\sin(\omega\widetilde{t})$. Here L is the length of the depletion region in dimensionless coordinates. It can be shown that for such a boundary condition, one can solve the differential equations [18] for the Stokes pulse and find the output Stokes intensity at the entrance window as

$$I_s(L,\widetilde{t}) = I_s^0(L) + \kappa A\sin(\omega\widetilde{t} + \phi),$$

where κ is the response function given by

$$\kappa = |G(i\omega)|\,,$$

$$G(s) = (2L+1)^{\alpha+1}\frac{(2\pi)^{1/2}}{s^{1/2}e^{s/2}[K_{\alpha+1}(\frac{s}{2}) + K_\alpha(\frac{s}{2})]}.$$

Here $\alpha = \dfrac{\gamma}{2(\gamma + s)}$ and $K_\alpha(x)$ is the Bessel function. The response function, κ, shows how the intensity modulation $A \sin \omega t$ at the beginning of the depletion region is magnified through this region and appears at the output as $\kappa A \sin \omega t$. The behavior of κ as a function of ω is quite different for different values of γ. This is shown in Fig. 3.10, in which κ is plotted as a function of ω for different values of γ. For

$$\gamma \gg 1 \Rightarrow G_0 \ll \Gamma T_t \ (\gamma = \infty \text{ in Fig.3.10}),$$

there is no maximum in the response function, which indicates that all the frequency components of the Stokes intensity modulation at the beginning of the depletion region will be magnified and thus the spectrum of the Stokes pulse does not change in passing through the depletion region. Therefore, it is most likely that the intensity fluctuations appear in the final Stokes output when $G_0 \ll \Gamma T_t$ [13]. For

$$\gamma \approx 1 \Rightarrow G_0 \approx \Gamma T_t \ (\gamma = 1.5, 1., 0.5 \text{ in Fig.3.10}),$$

the response function has a pronounced peak at frequencies $\omega \approx \gamma$ or

$$\frac{1}{t/T_{l_{depl}}} \approx \frac{T_{l_{dep}}}{\tau} \Rightarrow t \approx \tau.$$

This means that the medium has the property to amplify selectively those fluctuations for which $T_s = \tau$. Since $T_s \sim 4\tau - \frac{1}{10}\tau$, in the regime when $\gamma \approx 1$, only fluctuations with $T_s = \tau$ will be magnified and all the other fluctuations will be smoothed out in the output Stokes intensity. Finally, when

$$\gamma \ll 1 \Rightarrow G_0 \gg \Gamma T_t \ (\gamma = .1, 0.005 \text{ in Fig.3.10}),$$

there is no maximum in the response function and it becomes smaller for smaller γ. Plotting the maximum of the response function κ as a function of γ shows (see Fig. 3.11) how rapidly the maximum of κ decreases for small values of γ. This results in

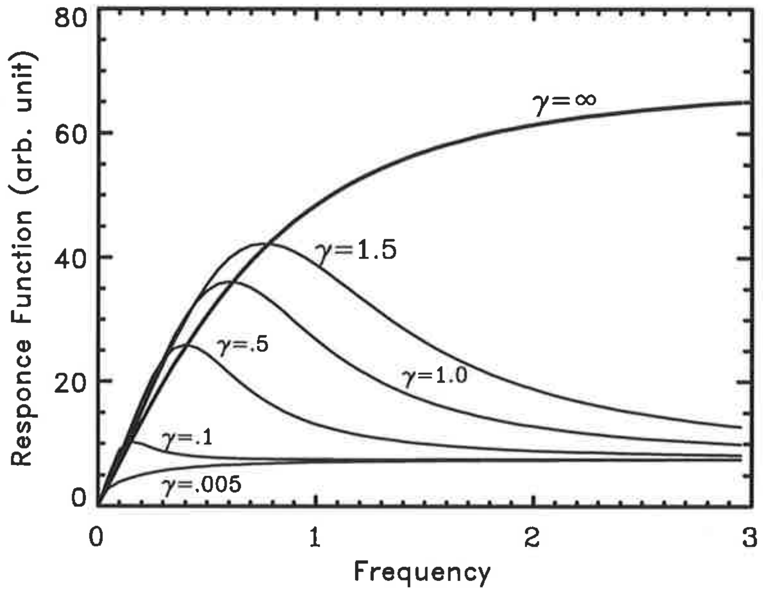

Figure 3.10: Response function as a function of frequency for different values of γ. There is no maximum for large and small values of γ. L is a dimentionless length paprameter and is $L = 40$ for the above plot.

(using Eqs. 3.58 and 3.59) a smaller (noise intensity)/(total intensity) ratio as

$$\frac{\text{(noise intensity)}}{\text{(total intensity)}} = \frac{I_s^1(L)}{I_s^0(L) + I_s^1(L)} = \frac{\kappa A \sin \omega t}{R I_l(L) + \kappa A \sin \omega t},$$

where R is the reflectivity. For $\gamma \ll 1$ or $G_0 \gg \Gamma T_t$ the reflectivity approaches 1 while the noise intensity decreases, resulting in a smaller (noise/total) intensity ratio. This indicates that in the regime of $G_0 \gg \Gamma T_t$ the fluctuations in the Stokes pulse are suppressed.

3.5 Summary

In this chapter we have reviewed the general behaviour of the SBS process and its application as a phase conjugator. The fundamental equations that describe SBS were developed. Simple analytical solutions of the SBS process (in the steady state regime and one dimension) were discussed. It was shown that these solutions can explain the simple experimental observations of the SBS process. In the transient regime, an approximated analytical solution of the SBS process in the depleted

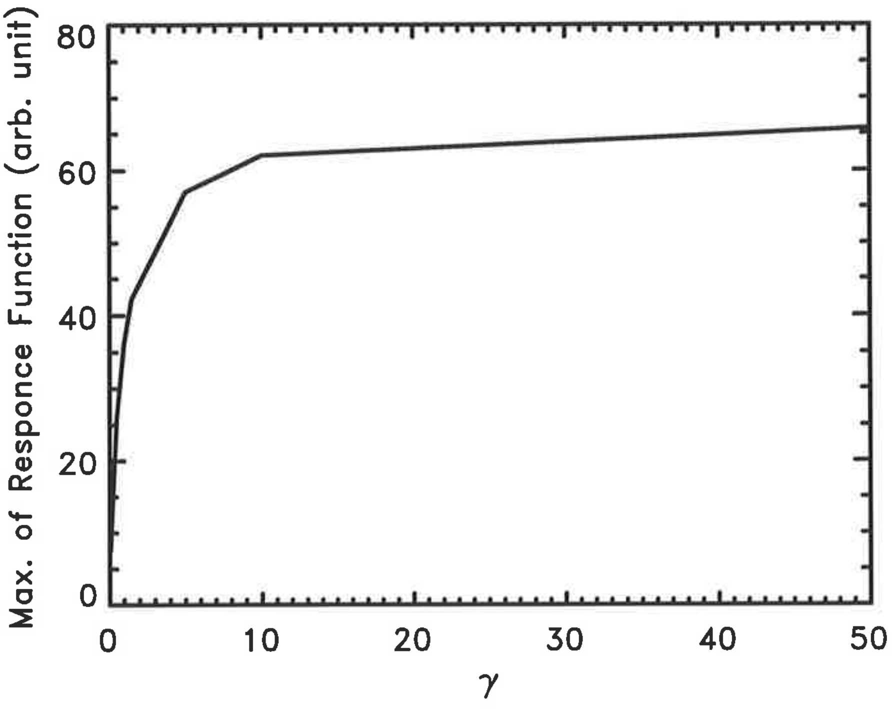

Figure 3.11: Maximum value of the response function κ as function of γ. For small γ i.e., $G_0 \gg \Gamma T_t$, the maximum of the response function is very small resulting a smaller ratio of noise/(total stokes intensity).

region (a region over which the Stokes signal gains the most of its amplification) was explained. This solution gave a qualitative description of the dynamics of the Stokes signal evolution through the depletion region. Introducing a parameter $\gamma = T_t\Gamma/G_0$, it was shown that for $\gamma \gg 1$ the Stokes signal at the end of depletion region may show large amplitude fluctuations. Contrary to this, for $\gamma \ll 1$, there is no amplitude fluctuations in the Stokes signal.

Although, simple analytical or numerical solutions of the SBS process, can explain most of the experimental observations, they cannot, explain some important experimental aspects of the SBS process, especially for the focused cell geometry. One example of this is the use of SBS in practical applications that require considerations of transients or short coherence length regimes. In chapters 4 and 5, we get to the heart of this thesis and develop two transient (one and three dimensional) numerical models of SBS to examine the transient phenomena that affect the SBS performance. In the next chapter, we develop a transient one dimensional numerical model of SBS in the focused cell geometry. The model is then employed to examine in detail two different transient phenomena, threshold oscillations and stochastic intensity fluctuations. It will be shown how these phenomena affect the performance of the SBS in the transient regime.

Chapter 4

1-dimensional model of SBS

4.1 Abstract

In this chapter, we develop a transient one dimensional numerical model of SBS. In our model, we have simulated the noise initiation of SBS for a focused beam in a finite length cell. The details of the numerical method is explained. We then use the model to study two different transient phenomena: 1) threshold oscillations and 2) stochastic fluctuations in the Stokes intensity. For each phenomenon, the effects of parameters such as phonon lifetime, immersion length and input energy are examined and compared with the available experimental results.

4.2 Introduction

The original motivation to develop a 1-dimensional model of SBS came from some unexplained experimental observations. Some fluctuations were observed (see Fig. 4.1) in the reflected Stokes pulse in SBS experiments using Freon, (Experiment setup is shown in Fig. 3.8). Further experiments revealed that these fluctuations had stochastic nature i.e., they sometimes appeared and sometimes did not, in the output Stokes pulse, even though the experimental setup was the same for every shot. It was also observed that the temporal positions of these fluctuations within each pulse as well as their durations and heights were different from shot to shot. In addition to these, the measurement of the phase of the Stokes pulse also showed

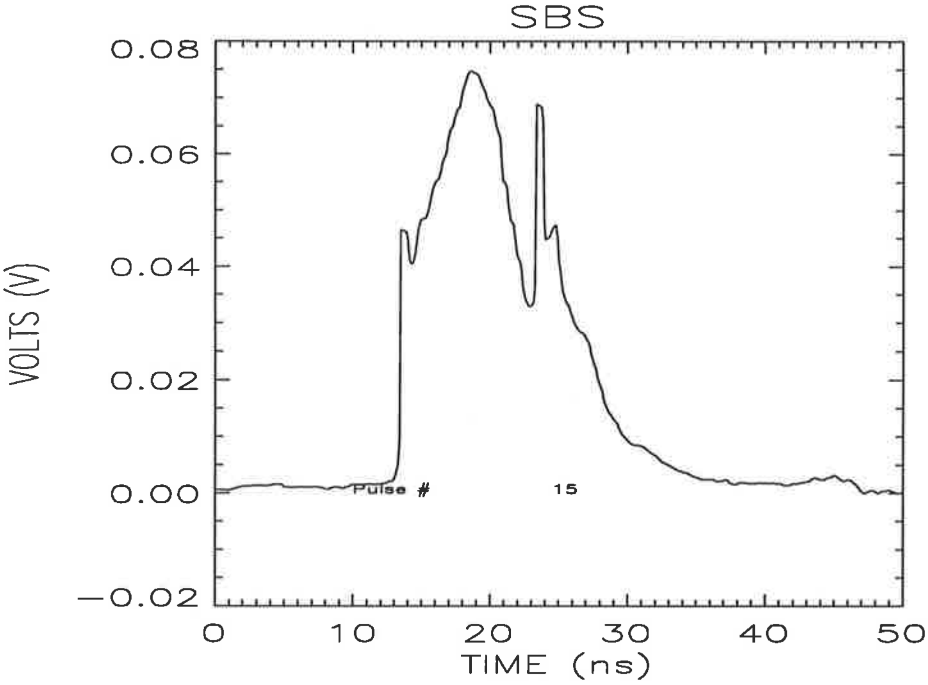

Figure 4.1: Typical occurrence of fluctuation in the output of Stokes pulse in SBS experiment using Freon 113. After V. Devrelis [2]

some random sudden changes, phase jumps as shown in Fig. 4.2. Early experimental observations of the presence of phase jumps and amplitude fluctuations in SBS were reported in 1980 [83, 81, 80]. More recent theoretical and experimental investigations of these fluctuations in optical fibers have been made by Dianov et al.[11], Gaeta and Boyd [13] and Kuzin et al [18]. Intensity and phase fluctuations have been investigated experimentally also for short interaction lengths typical of a focused geometry [12, 14, 16]. These fluctuations are important in practical applications since they reduce the coherence length of the scattered beam [14] as well as the temporal and spatial fidelity of the SBS process [10, 12, 19, 2]. Simultaneous fluctuations in the Stokes amplitude and beam quality have been observed [12] as have actual variations in the phase of the Stokes beam, and measured directly by heterodyne detection [14]. In addition, the effect of experimental parameters such as the interaction length and input energy on these simultaneous fluctuations have been reported [16, 19]. Numerical models have also shown simultaneous occurrence of jumps in the Stokes phase and fluctuations in the Stokes reflectivity and fidelity [9, 10]. These fluctuations are important in practical applications since they reduce

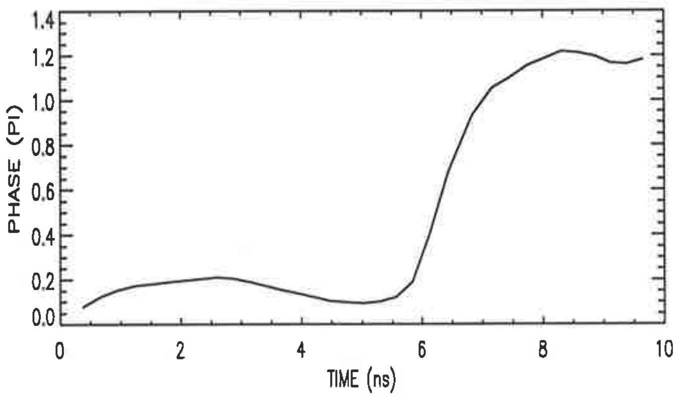

Figure 4.2: Experimental results showing the occurrence of phase jumps in the phase of the output Stokes pulse. After V. Devrelis [2]

the coherence length of the scattered beam [14] and have been observed to reduce the temporal and spatial fidelity of SBS [10, 12, 19].

A Review of the SBS literature indicated that While the intensity fluctuations in the Stokes pulse had been studied mainly in fibers, they had not been fully examined and understood, specially for the finite cell geometries. Most of the publications in this field were conference papers that had reported (theoretically or experimentally) some aspects of these fluctuations. Theoretical and numerical studies of these phenomena had been especially difficult due to the transient nature of these fluctuations and the fact that these fluctuations depend on the focusing geometry. In fact at the time that we started our study there was not a published unified theoretical or numerical study of this phenomena that could explain all aspects of this phenomenon. This lack of understanding together with the fact that these fluctuations are important in practical applications motivated us to study (experimentally and theoretically) three main questions:

1. The source of these fluctuations,
2. How the intensity fluctuations and phase jumps are related,
3. What experimental parameters affect these fluctuations, in SBS experiments

in a focused cell geometry and how we can achieve the best parameter space for excellent Stokes beam quality.

1. **The source of intensity fluctuations**

The SBS process starts from thermal density fluctuations of a medium. This stochastic initiation of the SBS process is believed to be the cause of the large scale fluctuations in the intensity and phase of the Stokes output [37, 9, 11, 79, 13, 16]. Similar phenomena are observed in superfluorescence [84] and stimulated Raman scattering (SRS). Vacuum fluctuations of the radiation field are thought to be the origin of the spontaneous noise that initiates the SRS process. Such a spontaneous noise initiation leads to the existence of solitons in the depleted pump pulse due to a π phase shift in the Stokes seeds [85, 86, 87, 88, 89, 90, 91, 92]. Including a Gaussian random noise term in the transient SBS equations enables us to simulate the noise initiation of the SBS process and to study the temporal behaviour of the Stokes intensity fluctuations.

2. **How the intensity fluctuations and phase jumps are related**

Experimental observations suggest that the intensity fluctuations and phase jumps can be simultaneous [12, 14]. It is also believed that, like SRS, the phase jumps are responsible for the intensity fluctuations [11, 13]. In some studies (e.g. [93, 1]) researchers have omitted the phase of the fields from the SBS equations by considering a phase locked relation between the phase of the pump, Stokes and the acoustic field i.e., $\phi_l - \phi_s - \phi_q = \frac{\pi}{2}$ (this will be discussed later in this chapter). Such a simplification leads to SBS coupled differential equations of real fields. However, such a simplification can not simulate the relation between the phase jumps and the Stokes intensity fluctuations. In our model, complex differential equations are considered in order to study the underlying mechanism of the phase-intensity relation in the SBS process.

3. **What experimental parameters affect these fluctuations**

The effect of experimental parameters on the intensity fluctuations for the focused cell geometry has not been fully investigated. There are some unpublished studies on the effects of interaction length and the input energy on these fluctuations [16]. Although, our model is a one dimensional model, we have used an approach, similar to that of Menzel and Eichler [24] (discussed in detail in Sec. 4.3.2), to introduce the focusing geometry to the SBS equations. This enables us to investigate the effect of different focusing geometries on the intensity fluctuations.

4.3 Theory

The equations describing our 1-dimensional model are the transient Eqs. (3.54)-(3.56) i.e.,

$$(\frac{n}{c}\frac{\partial}{\partial t}+\frac{\partial}{\partial z})E_s=-ig_2Q^*E_l, \tag{4.1}$$

$$(\frac{n}{c}\frac{\partial}{\partial t}-\frac{\partial}{\partial z})E_l=-ig_2QE_s, \tag{4.2}$$

$$(\frac{\partial}{\partial t}+\Gamma)Q=-ig_1E_lE_s^*+f(z,t), \tag{4.3}$$

except that we have added f to the right hand side of Eq. (4.3) to represent a Langevin noise source that describes the thermal initiation of the acoustic wave.

4.3.1 Langevin noise

Before we carry on with the solution of Eqs. (4.1)-(4.3), it is necessary to discuss the statistical property of the Langevin noise term f. We can divide the whole nonlinear material volume into small sub-volumes of $\Delta V = \Delta x\Delta y\Delta z$ centered around any arbitrary point x_i, y_i, z_i and with a mean density of Q_i. In the absence of driving electric fields, one can rewrite Eq. (4.3) for sub-volume i as

$$(\frac{d}{dt}+\Gamma)Q_i=f_i(t), \tag{4.4}$$

where $f_i(t)$ denotes the Langevin noise term $f(x,y,z,t)$ averaged over subregion i. We assume that f_i is a Gaussian random variable with zero mean i.e., $\langle f_i\rangle = 0$, and is δ correlated in the sense that

$$\left\langle f_i(t) f_j^*(t') \right\rangle = \widetilde{G}\delta_{ij}\delta(t-t'). \tag{4.5}$$

This relation indicates that for an ensemble of similar cells the value of f in a cell i at time t is uncorrelated with the value of f in a cell j at time t'. To find the coefficient $\widetilde{G}$ we integrate Eq. (4.4) to find the Q_i:

$$Q_i(t) = \int_{-\infty}^{t} e^{\Gamma(t-\tau)} f_i(\tau) d\tau. \tag{4.6}$$

This and Eq. (4.5) can be used to evaluate $\left\langle Q_i(t) Q_j^*(t) \right\rangle$:

$$\begin{aligned} \left\langle Q_i(t) Q_j^*(t) \right\rangle &= \left\langle \int_{-\infty}^{t} d\tau_1 d\tau_2 e^{\Gamma(t-\tau_1)} f_i(\tau_1) e^{\Gamma(t-\tau_2)} f_j^*(\tau_2) \right\rangle \\ &= \int_{-\infty}^{t} d\tau_1 d\tau_2 e^{\Gamma(t-\tau_1)} e^{\Gamma(t-\tau_2)} \left\langle f_i(\tau_1) f_j^*(\tau_2) \right\rangle \\ &= \frac{\widetilde{G}}{\Gamma}\delta_{ij}. \end{aligned} \tag{4.7}$$

The quantity $\langle Q_i(t) Q_i^*(t) \rangle$ can be related to the total energy in the sub-volume i. The energy density of a sound wave is given by (see Eq. 64.1 [94])

$$\langle u \rangle = \frac{1}{2}\rho_0 \left\langle V^2 \right\rangle + \frac{1}{2} v^2 \left\langle Q^2 \right\rangle / \rho_0$$

Thus the total sound wave energy in a the sub-volume i is

$$(E_{Total})_i = (\frac{1}{2}\rho_0 \left\langle V^2 \right\rangle + \frac{1}{2} v^2 \left\langle Q_i^2 \right\rangle / \rho_0)\Delta V.$$

According to the equipartition theorem, the contribution of each term in the total energy is $1/2(KT)$ therefore,

$$\begin{aligned} \frac{1}{2} v^2 \left\langle Q_i^2 \right\rangle / \rho_0)\Delta V &= \frac{1}{2} v^2 \langle Q_i(t) Q_i^*(t) \rangle / \rho_0)\Delta V = \frac{1}{2} KT, \\ &\Downarrow \\ \langle Q_i(t) Q_i^*(t) \rangle &= \frac{2KT\rho_0}{v^2 \Delta V}. \end{aligned}$$

Comparing this with Eq. (4.7), we find

$$\widetilde{G} = \frac{2KT\rho_0\Gamma}{v^2\Delta V}. \tag{4.8}$$

In the continuum limit, the Langevin term is $f(\mathbf{r},t)$ with zero mean and an autocorrelation function:

$$\begin{aligned} \langle f(\mathbf{r},t)f^*(\mathbf{r}',t')\rangle &= G\delta(\mathbf{r}-\mathbf{r}')\delta(t-t'), \\ &\quad \text{where} \\ G &= \widetilde{G}\Delta V = \frac{2KT\rho_0\Gamma}{v^2}. \end{aligned} \tag{4.9}$$

Here ρ_0 is the mean density of the material, T is the temperature, v is the speed sound in the material, and K is the Boltzman constant. The Langevin term f has a Gaussian distribution with zero mean. Thus the distribution function has the form

$$p(f) = \frac{1}{(\pi)^{1/2}\sigma} e^{\frac{-f^2}{2\sigma}},$$

where σ is the variance. Consider

$$\begin{aligned} f(\mathbf{r}_1,t) &= f_1, \\ f(\mathbf{r}_2,t') &= f_2, \end{aligned}$$

then the correlation function $\langle f(\mathbf{r}_1,t)f^*(\mathbf{r}_2,t')\rangle$ can be calculated to be

$$\langle f(\mathbf{r}_1,t)f^*(\mathbf{r}_2,t')\rangle \propto \frac{1}{\sigma^2}\int_{-\infty}^{+\infty} f_1 f_2 e^{\frac{-f_1^2}{2\sigma^2}} e^{\frac{-f_2^2}{2\sigma^2}} df_1 df_2.$$

Evaluating the above integral, we find

$$\begin{aligned} \langle f(\mathbf{r}_1,t)f^*(\mathbf{r}_2,t')\rangle &= 0 \ \text{ if } f_1 \neq f_2, \\ \langle f(\mathbf{r}_1,t)f^*(\mathbf{r}_2,t')\rangle &\propto \sigma \ \text{ if } f_1 = f_2. \end{aligned}$$

Comparing this result with Eq. (4.9), we can see that

$$G \propto \sigma, \tag{4.10}$$

i.e., the variance of the Gaussian distribution is proportional to the constant $G = 2KT\rho_0\Gamma/v^2$. In App. (A), the generation of random variables with a Gaussian distribution is discussed.

4.3.2 Numerical Solution of the SBS Equations

In Eqs. (4.1)-(4.3), $E_l(z,t)$, $E_s(z,t)$ and $Q(z,t)$ are complex amplitudes. To find the equations for the real amplitudes and the phase of the fields we write the complex amplitudes Q and E_p (where $p = s, l$) as

$$\begin{aligned} E_p &= A_p e^{-i\phi_p}, \\ Q &= A_q e^{-i\phi_q}, \end{aligned}$$

where the A's and the ϕ's are real functions. Substituting the new definition into the above equations results in a set of six coupled differential equations:

$$(\frac{\partial}{\partial z} - \frac{n}{c}\frac{\partial}{\partial t})A_p = -g_2 \sin(\phi_p - \phi_s - \phi_q)A_q A_s \tag{4.11a}$$

$$(\frac{\partial}{\partial z} + \frac{n}{c}\frac{\partial}{\partial t})A_s = g_2 \sin(\phi_s + \phi_q - \phi_p)A_q A_p \tag{4.11b}$$

$$(\frac{\partial}{\partial t} + \Gamma)A_q = g_1 \sin(\phi_s + \phi_q - \phi_p)A_s A_p + f_1 \tag{4.11c}$$

$$(\frac{\partial}{\partial z} - \frac{n}{c}\frac{\partial}{\partial t})\phi_p = -g_2 \cos(\phi_p - \phi_s - \phi_q)\frac{A_q A_s}{A_p} \tag{4.11d}$$

$$(\frac{\partial}{\partial z} + \frac{n}{c}\frac{\partial}{\partial t})\phi_s = g_2 \cos(\phi_s + \phi_q - \phi_p)\frac{A_q A_p}{A_s} \tag{4.11e}$$

$$(\frac{\partial}{\partial t})\phi_q = g_1 \cos(\phi_s + \phi_q - \phi_p)\frac{A_s A_p}{A_q} + f_2 \tag{4.11f}$$

Here, f_1 and f_2 are two Langevin noise terms representing the noise initiation of the SBS process for amplitude and phase.

As mentioned above, some authors (e.g. [93, 1]) have used the phase locked condition for which

$$\sin(\phi_p - \phi_s - \phi_q) = 1 \Rightarrow \phi_p - \phi_s - \phi_q = \frac{\pi}{2},$$

and the SBS process has the highest gain. When SBS starts from noise, a random noise distribution of $\phi_p - \phi_s - \phi_q$ is initially present. But as the phase-locked waves, (those with $\phi_p - \phi_s - \phi_q = \frac{\pi}{2}$), have the highest gain in the medium, they become the dominant Stokes waves in the medium. By applying the phase locked condition to the equations (4.11), they are simplified to a set of three real coupled equations for the amplitudes. However, in order to explain the experimental observation of the simultaneous occurrence of intensity fluctuations and phase jumps[14], we have retained the complex equations since this is the only way that the phase of the Stokes field can be coupled to its intensity.

The equations (4.11) are nonlinear due to the terms $\sin(\phi_s+\phi_q-\phi_p)$ and $\cos(\phi_p-\phi_s-\phi_q)$. These equations are useful for showing the qualitative behaviour of the fields and their phases. However, solutions of the equations require that we rewrite them for the real and imaginary parts of the fields. Using

$$\begin{aligned} E_p &= W_p + iV_p \quad p = l, s, \\ Q &= W_q + iV_q \end{aligned}$$

in Eqs. (4.1)-(4.3), the equations for the real and imaginary parts of the fields are:

$$
\begin{aligned}
(\frac{\partial}{\partial z} - \frac{n}{c}\frac{\partial}{\partial t})W_l &= -g_2(W_qV_s + V_qW_s)\\
(\frac{\partial}{\partial z} + \frac{n}{c}\frac{\partial}{\partial t})W_s &= g_2(W_qV_l - V_qW_l)\\
(\frac{\partial}{\partial t} + \Gamma)W_q &= -g_1(W_lV_s - V_lW_s) + f_1\\
\\
(\frac{\partial}{\partial z} - \frac{n}{c}\frac{\partial}{\partial t})V_p &= g_2(W_qW_s - V_qV_s)\\
(\frac{\partial}{\partial z} + \frac{n}{c}\frac{\partial}{\partial t})V_s &= -g_2(W_qW_l + V_qV_l)\\
(\frac{\partial}{\partial t} + \Gamma)V_q &= -g_1(W_lW_s + V_lV_s) + f_2
\end{aligned}
\tag{4.12}
$$

The focusing geometry required for simulation of experiments is introduced using an approach similar to Menzel and Eichler [24]. Although, SBS is primarily used to compensate for optical aberrations, we have chosen not to include spatial aberrations in this treatment, but concentrate entirely on temporal fluctuations or the "temporal fidelity" of the Stokes beam. This is important, because lack of temporal fidelity leads to the degradation of the Stokes return and hence a reduction in the average reflectivity and efficiency of a phase conjugated laser system [10, 12, 19]. In this initial model, we are thus using spatially unaberrated Gaussian beams for both the pump and Stokes fields, and we have made the further approximation that both these fields have the same Gaussian beam parameters (see figure 4.3):

$$
\omega^2(z) = \omega_\circ^2 \left[1 + \left(\frac{(z - z_\circ)\lambda}{\pi\omega_\circ^2 n}\right)^2\right], \tag{4.13}
$$

where $\omega_\circ$ is the radius at the waist of the beam, λ is the wavelength and n is the appropriate index of refraction as a function of z. This is a reasonable approximation in an efficient phase conjugating system where the fields are well above threshold and is justified by experimental results showing that the beam quality and divergence of the Stokes beam are indistinguishable from those of the pump beam when well above threshold.

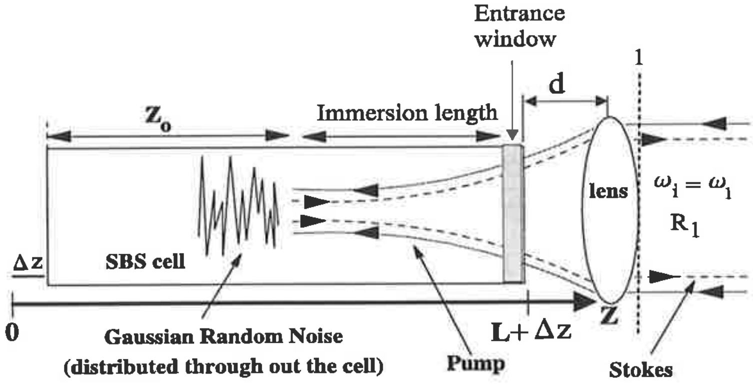
Entrance window
d
1
Z_0
Immersion length
lens
$\omega_1 = \omega_1$
R_1
Δz
SBS cell
0
Gaussian Random Noise
(distributed through out the cell)
L+Δz
Z
Pump
Stokes

Figure 4.3: Geometry used for modeling of the SBS process.

As a result, the pump and Stokes intensities, $I_l = W_l^2 + V_l^2$ or $I_s = W_s^2 + V_s^2$, change not only because of the nonlinear interaction with the material but also because of the change in the area of the beams. Keeping in mind that, for a Gaussian beam, the electric field amplitude has a $\omega(z)$ in the denominator, we add $-\frac{W_p}{\omega(z)}\frac{\partial}{\partial z}\omega(z)$ or $-\frac{V_p}{\omega(z)}\frac{\partial}{\partial z}\omega(z)$ to the right hand side of the equations for W_p or V_p ($p = l$ or s) to represent the change in the intensity due to the focussing geometry [24]. Defining

$$\begin{aligned} E_p &= \frac{E'_p}{\omega(z)} = \frac{W'_p}{\omega(z)} + i\frac{V'_p}{\omega(z)} \\ E'_p &= W'_p + iV'_p \end{aligned}$$

and hence,

$$\begin{aligned} W_p &= \frac{W'_p}{\omega(z)} \\ V_p &= \frac{V'_p}{\omega(z)}, \end{aligned}$$

it can be easily seen that $\left|E'_p\right|^2 = |E_p|^2 \times \omega^2(z)$ is proportional to the local power of the pump or the Stokes fields. Substituting the prime fields into Eq. (4.12) we find:

$$\begin{aligned}
(\frac{\partial}{\partial z} - \frac{n}{c}\frac{\partial}{\partial t})W_l' &= -g_2(W_q V_s' + V_q W_s') && \text{(4.14a)}\\
(\frac{\partial}{\partial z} + \frac{n}{c}\frac{\partial}{\partial t})W_s' &= g_2(W_q V_l' - V_q W_l') && \text{(4.14b)}\\
(\frac{\partial}{\partial t} + \Gamma)W_q &= -\frac{g_1}{\omega^2(z)}(W_l' V_s' - V_l' W_s') + f_1 && \text{(4.14c)}
\end{aligned}$$

$$\begin{aligned}
(\frac{\partial}{\partial z} - \frac{n}{c}\frac{\partial}{\partial t})V_l' &= g_2(W_q W_s' - V_q V_s') && \text{(4.14d)}\\
(\frac{\partial}{\partial z} + \frac{n}{c}\frac{\partial}{\partial t})V_s' &= -g_2(W_q W_l' + V_q V_l') && \text{(4.14e)}\\
(\frac{\partial}{\partial t} + \Gamma)V_q &= -\frac{g_1}{\omega^2(z)}(W_l' W_s' + V_l' V_s') + f_2 && \text{(4.14f)}
\end{aligned}$$

We see that the new equations have a form similar to equations (4.12). The only difference is that the prime fields are the power components instead of the intensity components in equations (4.12). The same procedure can be done for equations (4.11) to obtain the following equations for the Stokes, pump and acoustic grating power:

$$\begin{aligned}
(\frac{\partial}{\partial z} - \frac{n}{c}\frac{\partial}{\partial t})A_l' &= -g_2 \sin(\phi_l - \phi_s - \phi_q) A_q A_s' && \text{(4.15a)}\\
(\frac{\partial}{\partial z} + \frac{n}{c}\frac{\partial}{\partial t})A_s' &= g_2 \sin(\phi_s + \phi_q - \phi_l) A_q A_l' && \text{(4.15b)}\\
(\frac{\partial}{\partial t} + \Gamma)A_q &= g_1 \sin(\phi_s + \phi_q - \phi_l)\frac{A_s' A_l'}{\omega^2(z)} + f_1 && \text{(4.15c)}
\end{aligned}$$

The equation for the acoustic field shows how the amplitude of the field depends on the intensity of the Stokes and pump waves, implying a high acoustic field at high intensities of the pump and the Stokes fields.

Numerical Method

The phonon fields in Eqs. (4.14c) and (4.14f) can be integrated to yield

$$W_q = \frac{g_1}{\omega^2(z)} \int_0^t d\tau e^{-\Gamma(t-\tau)}[-(W_l'V_s' - V_l'W_s') + f_1], \qquad (4.16)$$

$$V_q = \frac{g_1}{\omega^2(z)} \int_0^t d\tau e^{-\Gamma(t-\tau)}[-(W_l'W_s' + V_l'V_s') + f_2]. \qquad (4.17)$$

If we substitute W_q and V_q into the remaining equations (4.14), we can reduce the equations to four coupled differential equations for the field amplitudes. The numerical analysis starts with these four equations. To solve these equations numerically, we change the continuous field amplitudes $W_l(z,t), V_l(z,t), W_s(z,t)$ and $V_s(z,t)$ to discrete field amplitudes $W_l{}_j^m, V_l{}_j^m, W_s{}_j^m$ and $V_s{}_j^m$, where $m = 0, 1, 2, ...M$ are time indices ($t = m\Delta t$) and $j = 1, 2, ...n+1$ are space indices ($z = j\Delta z$ and $L = n\Delta z$). Referring to Fig. 4.3, it is clear that $W_s{}_1^m$ and $V_s{}_1^m$ (i.e., Stokes field at $z = \Delta z$) are the boundary conditions for the Stokes field. For SBS generators these values are always zero i.e.,

$$W_s{}_1^m = 0 \quad \text{at all times}$$

$$V_s{}_1^m = 0 \quad \text{at all times.}$$

Similarly, $W_l{}_{n+1}^m, V_l{}_{n+1}^m$ [i.e., laser field at $z = (n+1)\Delta z$] are the boundary conditions for the laser field and are determined by the input laser field to the cell. We can use Simpson's rule

$$\int_{x_1}^{x_2} f(x)dx = \frac{1}{2}\Delta x[f(x_1) + f(x_2)],$$

and the discrete field amplitudes $W_l{}_j^m, V_l{}_j^m, W_s{}_j^m$ and $V_s{}_j^m$ to find the acoustic fields $W_q{}_j^m$and $V_q{}_j^m$ (acoustic field at time $t = m\Delta t$ and position $z = j\Delta z$) in Eqs. (4.16) and (4.17)

$$W_q{}_j^m = g_1\frac{\Delta t}{2}[-\frac{1}{[\omega^2]_j}(W_l'{}_j^m V_s'{}_j^m - V_l'{}_j^m W_s'{}_j^m) + f_1{}_j^m + P_1{}_j^{m-1}], \qquad (4.18)$$

$$V_q{}_j^m = g_1\frac{\Delta t}{2}[-\frac{1}{[\omega^2]_j}(W_l'{}_j^m W_s'{}_j^m + V_l'{}_j^m V_s'{}_j^m) + f_2{}_j^m + P_2{}_j^{m-1}]. \qquad (4.19)$$

Here, $P_1{}_j^{m-1}$ and $P_2{}_j^{m-1}$ (evaluated at the time slot $m-1$) are related to P_{1j}^{m-2} and $P_2{}_j^{m-2}$ by

$$\begin{aligned}
P_1{}_j^{m-1} &= e^{-\Gamma\Delta t}\{P_1{}_j^{m-2} + 2[-\frac{1}{[\omega^2]_j}(W_l'{}_j^{m-1}V_s'{}_j^{m-1} - V_l'{}_j^{m-1}W_s'{}_j^{m-1}) + f_1{}_j^{m-1}]\}, \\
P_2{}_j^{m-1} &= e^{-\Gamma\Delta t}\{P_2{}_j^{m-2} + 2[-\frac{1}{[\omega^2]_j}(W_l'{}_j^{m-1}W_s'{}_j^{m-1} + V_l'{}_j^{m-1}V_s'{}_j^{m-1}) + f_2{}_j^{m-1}]\}, \\
&\text{where finally} \\
P_1{}_j^0 &= e^{-\Gamma\Delta t}[-\frac{1}{[\omega^2]_j}(W_l'{}_j^0V_s'{}_j^0 - V_l'{}_j^0W_s'{}_j^0) + f_1{}_j^0], \\
P_2{}_j^0 &= e^{-\Gamma\Delta t}[-\frac{1}{[\omega^2]_j}(W_l'{}_j^0W_s'{}_j^0 + V_l'{}_j^0V_s'{}_j^0) + f_2{}_j^0].
\end{aligned}$$

We use a differenceing method to convert the differentiation of the fields to the difference between discrete fields e.g.,

$$\begin{aligned}
\frac{n}{c}\frac{\partial}{\partial t}W_l' &= \frac{n}{c\Delta t}(W_l'{}_j^{m+1} - W_l'{}_j^m), \\
\frac{\partial}{\partial z}W_l' &= \frac{1}{\Delta z}(W_l'{}_{j+1}^{m+1} - W_l'{}_j^{m+1}).
\end{aligned}$$

Using this and the discrete acoustic field amplitudes [Eqs. (4.18) and (4.19)], we can rewrite Eqs. (4.14a), (4.14b), (4.14d) and (4.14e) for the discrete field amplitudes as

$$\begin{aligned}
&{W'_l}_{j+1}^{m+1} - {W'_l}_{j}^{m+1} - \frac{n\Delta z}{c\Delta t}({W'_l}_{j}^{m+1} - {W'_l}_{j}^{m}) = \\
&\quad - g{V_s}_{j}^{m+1}\frac{\Delta z\Delta t}{2}[-\frac{1}{[\omega^2]_j}({W'_l}_{j}^{m+!}{V'_s}_{j}^{m+1} - {V'_l}_{j}^{m+1}{W'_s}_{j}^{m+1}) + {f_1}_{j}^{m+1} + {P_1}_{j}^{m}] \\
&\quad - g{W_s}_{j}^{m+1}\frac{\Delta z\Delta t}{2}[-\frac{1}{[\omega^2]_j}({W'_l}_{j}^{m+1}{W'_s}_{j}^{m+1} + {V'_l}_{j}^{m+1}{V'_s}_{j}^{m+1}) + {f_2}_{j}^{m+1} + {P_2}_{j}^{m}]
\end{aligned} \tag{4.20}$$

$$\begin{aligned}
&{W'_s}_{j+1}^{m+1} - {W'_s}_{j}^{m+1} + \frac{n\Delta z}{c\Delta t}({W'_s}_{j}^{m+1} - {W'_s}_{j}^{m}) = \\
&\quad g{V_l}_{j}^{m+1}\frac{\Delta z\Delta t}{2}[-\frac{1}{[\omega^2]_j}({W'_l}_{j}^{m+!}{V'_s}_{j}^{m+1} - {V'_l}_{j}^{m+1}{W'_s}_{j}^{m+1}) + {f_1}_{j}^{m+1} + {P_1}_{j}^{m}] \\
&\quad - g{W_l}_{j}^{m+1}\frac{\Delta z\Delta t}{2}[-\frac{1}{[\omega^2]_j}({W'_l}_{j}^{m+1}{W'_s}_{j}^{m+1} + {V'_l}_{j}^{m+1}{V'_s}_{j}^{m+1}) + {f_2}_{j}^{m+1} + {P_2}_{j}^{m}]
\end{aligned} \tag{4.21}$$

$$\begin{aligned}
&{V'_l}_{j+1}^{m+1} - {V'_l}_{j}^{m+1} - \frac{n\Delta z}{c\Delta t}({V'_l}_{j}^{m+1} - {V'_l}_{j}^{m}) = \\
&\quad g{W_s}_{j}^{m+1}\frac{\Delta z\Delta t}{2}[-\frac{1}{[\omega^2]_j}({W'_l}_{j}^{m+!}{V'_s}_{j}^{m+1} - {V'_l}_{j}^{m+1}{W'_s}_{j}^{m+1}) + {f_1}_{j}^{m+1} + {P_1}_{j}^{m}] \\
&\quad - g{V_s}_{j}^{m+1}\frac{\Delta z\Delta t}{2}[-\frac{1}{[\omega^2]_j}({W'_l}_{j}^{m+1}{W'_s}_{j}^{m+1} + {V'_l}_{j}^{m+1}{V'_s}_{j}^{m+1}) + {f_2}_{j}^{m+1} + {P_2}_{j}^{m}]
\end{aligned} \tag{4.22}$$

$$\begin{aligned}
&{V'_s}_{j+1}^{m+1} - {V'_s}_{j}^{m+1} - \frac{n\Delta z}{c\Delta t}({V'_s}_{j}^{m+1} - {V'_s}_{j}^{m}) = \\
&\quad - g{W_l}_{j}^{m+1}\frac{\Delta z\Delta t}{2}[-\frac{1}{[\omega^2]_j}({W'_l}_{j}^{m+!}{V'_s}_{j}^{m+1} - {V'_l}_{j}^{m+1}{W'_s}_{j}^{m+1}) + {f_1}_{j}^{m+1} + {P_1}_{j}^{m}] \\
&\quad - g{V_l}_{j}^{m+1}\frac{\Delta z\Delta t}{2}[-\frac{1}{[\omega^2]_j}({W'_l}_{j}^{m+1}{W'_s}_{j}^{m+1} + {V'_l}_{j}^{m+1}{V'_s}_{j}^{m+1}) + {f_2}_{j}^{m+1} + {P_2}_{j}^{m}]
\end{aligned} \tag{4.23}$$

On the right hand side of Eqs. (4.20)-(4.23) there are nonlinear coefficients of either $|{W_s}_{j}^{m+1}|^2$, $|{V_s}_{j}^{m+1}|^2$, $|{W_l}_{j}^{m+1}|^2$ or $|{V_l}_{j}^{m+1}|^2$. As a linear approximation (in our model) we have replaced these coefficients with the same coefficients evaluated at the time slot m instead of $m+1$ [1]. To justify the validity of the linearization assumption, we used the field amplitudes at time slot $m+1$ to reevaluate iteratively the nonlinear coefficient involved on the right hand side of Eqs. (4.20)-(4.23). An improvement of only 4% was achieved after 5 iterations. Eqs. (4.20)-(4.23) can be written in a matrix form by introducing field vectors at the time $(m+1)\Delta t$:

$$\overrightarrow{W_p}^{m+1} = \begin{pmatrix} W_{p\ 1} \\ W_{p\ 2} \\ \cdot \\ \cdot \\ \cdot \\ W_{p\ n} \end{pmatrix}^{m+1} ; \overrightarrow{V_p}^{m+1} = \begin{pmatrix} V_{p\ 1} \\ V_{p\ 2} \\ \cdot \\ \cdot \\ \cdot \\ V_{p\ n} \end{pmatrix}^{m+1}$$

$$\overrightarrow{W_s}^{m+1} = \begin{pmatrix} W_{s\ 2} \\ W_{s\ 3} \\ \cdot \\ \cdot \\ \cdot \\ W_{s\ n+1} \end{pmatrix}^{m+1} ; \overrightarrow{V_s}^{m+1} = \begin{pmatrix} V_{s\ 2} \\ V_{s\ 3} \\ \cdot \\ \cdot \\ \cdot \\ V_{s\ n+1} \end{pmatrix}^{m+1} ,$$

where n is the total number of discrete points in space and $W_{p\ n+1}$, $V_{p\ n+1}$, $W_{s\ 1}$ and $V_{s\ 1}$ are the boundary values. The equivalent matrix forms of Eqs. (4.20)-(4.23) are

$$A^m\overrightarrow{W_p}^{m+1} + C^m\overrightarrow{W_s}^{m+1} + D^m\overrightarrow{V_s}^{m+1} = \overrightarrow{V}, \tag{4.24}$$

$$E^m\overrightarrow{W_s}^{m+1} + F^m\overrightarrow{W_p}^{m+1} + G^m\overrightarrow{V_p}^{m+1} = \overrightarrow{U}, \tag{4.25}$$

$$A^m\overrightarrow{V_p}^{m+1} - D^m\overrightarrow{W_s}^{m+1} + C^m\overrightarrow{V_s}^{m+1} = \overrightarrow{W}, \tag{4.26}$$

$$E^m\overrightarrow{V_s}^{m+1} - G^m\overrightarrow{W_p}^{m+1} + F^m\overrightarrow{V_p}^{m+1} = \overrightarrow{Z}. \tag{4.27}$$

Here, A^m is upper tridiagonal, C^m, D^m,E^m are lower tridiagonal and F^m, and G^m

are diagonal $n \times n$ coefficient matrices evaluated at time $m\Delta t$ and are given as

$$A^m = \begin{pmatrix} \beta_1 & 1 & 0 & \cdots & 0 \\ 0 & \beta_2 & 1 & \ddots & 0 \\ \vdots & \ddots & \ddots & \ddots & \vdots \\ \vdots & \vdots & \ddots & \ddots & 1 \\ 0 & 0 & \cdots & \cdots & \beta_n \end{pmatrix} \quad C^m = \begin{pmatrix} 0 & 0 & \cdots & \cdots & 0 \\ \gamma_2 & 0 & \ddots & \ddots & 0 \\ 0 & \ddots & \ddots & \ddots & \vdots \\ \vdots & \vdots & \ddots & \ddots & 0 \\ 0 & 0 & \cdots & \gamma_n & 0 \end{pmatrix},$$

$$D^m = \begin{pmatrix} 0 & 0 & \cdots & \cdots & 0 \\ \eta_2 & 0 & \ddots & \ddots & 0 \\ 0 & \ddots & \ddots & \ddots & \vdots \\ \vdots & \vdots & \ddots & \ddots & 0 \\ 0 & 0 & \cdots & \eta_n & 0 \end{pmatrix} \quad E^m = \begin{pmatrix} 1 & 0 & \cdots & \cdots & 0 \\ \alpha_2 & 1 & \ddots & \ddots & 0 \\ \vdots & \ddots & \ddots & \ddots & \vdots \\ \vdots & \vdots & \ddots & \ddots & 0 \\ 0 & 0 & \cdots & \alpha_n & 1 \end{pmatrix},$$

$$F^m = \begin{pmatrix} \gamma_1 & 0 & \cdots & \cdots & 0 \\ 0 & \gamma_2 & \ddots & \ddots & 0 \\ \vdots & \ddots & \ddots & \ddots & \vdots \\ \vdots & \vdots & \ddots & \ddots & 0 \\ 0 & 0 & \cdots & 0 & \gamma_n \end{pmatrix} \quad G^m = \begin{pmatrix} -\eta_1 & 0 & \cdots & \cdots & 0 \\ 0 & -\eta_2 & \ddots & \ddots & 0 \\ \vdots & \ddots & \ddots & \ddots & \vdots \\ \vdots & \vdots & \ddots & \ddots & 0 \\ 0 & 0 & \cdots & 0 & -\eta_n \end{pmatrix}.$$

Here,

$$\begin{aligned} \beta_n &= -1 - \frac{\Delta z}{c\Delta t} - \frac{g\Delta z\Delta t}{2\omega_n^2}\left(|V_{s\,n}^{\;m}|^2 + |W_{s\,n}^{\;m}|^2\right), \\ \gamma_n &= \frac{g\Delta z\Delta t}{2}\left(f_{2\,n}^{\;m} + P_{2\,n}^{\;m}\right), \\ \eta_n &= \frac{g\Delta z\Delta t}{2}\left(f_{1\,n}^{\;m} + P_{1\,n}^{\;m}\right), \\ \alpha_n &= -1 + \frac{\Delta z}{c\Delta t} - \frac{g\Delta z\Delta t}{2\omega_n^2}\left(|V_{l\,n}^{\;m}|^2 + |W_{l\,n}^{\;m}|^2\right). \end{aligned}$$

The right hand side of Eqs. (4.24)-(4.27) i.e., $\overrightarrow{V}$, $\overrightarrow{U}$, $\overrightarrow{W}$ and $\overrightarrow{Z}$ are $n \times 1$ vectors containing boundary conditions for the pump and Stokes at time $t = (m)\Delta t$. They can be calculated as

$$
\begin{aligned}
\overrightarrow{V}^m &= \begin{pmatrix} -\eta_1 {V_s}_1^m - \gamma_1 {W_s}_1^m - \frac{\Delta z}{c\Delta t}{W_p}_1^m \\ -\frac{\Delta z}{c\Delta t}{W_p}_2^m \\ -\frac{\Delta z}{c\Delta t}{W_p}_3^m \\ \vdots \\ -{W_p}_{n+1}^{m+1} - \frac{\Delta z}{c\Delta t}{W_p}_n^m \end{pmatrix}, \\
\overrightarrow{U}^m &= \begin{pmatrix} -\alpha_1 {W_s}_1^m + \frac{\Delta z}{c\Delta t}{W_s}_1^m \\ \frac{\Delta z}{c\Delta t}{W_s}_2^m \\ \frac{\Delta z}{c\Delta t}{W_s}_3^m \\ \vdots \\ \frac{\Delta z}{c\Delta t}{W_s}_n^m \end{pmatrix}, \\
\overrightarrow{W}^m &= \begin{pmatrix} -\gamma_1 {V_s}_1^m + \eta_1 {W_s}_1^m - \frac{\Delta z}{c\Delta t}{V_p}_1^m \\ -\frac{\Delta z}{c\Delta t}{V_p}_2^m \\ -\frac{\Delta z}{c\Delta t}{V_p}_3^m \\ \vdots \\ -{V_p}_{n+1}^{m+1} - \frac{\Delta z}{c\Delta t}{V_p}_n^m \end{pmatrix}, \\
\overrightarrow{Z}^m &= \begin{pmatrix} -\alpha_1 {V_s}_1^m + \frac{\Delta z}{c\Delta t}{V_s}_1^m \\ \frac{\Delta z}{c\Delta t}{V_s}_2^m \\ \frac{\Delta z}{c\Delta t}{V_s}_3^m \\ \vdots \\ \frac{\Delta z}{c\Delta t}{V_s}_n^m \end{pmatrix}.
\end{aligned}
$$

Using Eqs. (4.25) and (4.27), one can easily show that

$$
\begin{aligned}
\overrightarrow{V_p}^{m+1} &= (G^2+F^2)^{-1}[-GE\overrightarrow{W_s}^{m+1} - FE\overrightarrow{V_s}^{m+1} + G\overrightarrow{U^m} + F\overrightarrow{Z^m}], \quad (4.28) \\
\overrightarrow{W_p}^{m+1} &= (G^2+F^2)^{-1}[+GE\overrightarrow{V_s}^{m+1} - FE\overrightarrow{W_s}^{m+1} - G\overrightarrow{Z^m} + F\overrightarrow{U^m}]. \quad (4.29)
\end{aligned}
$$

These two equations in turn can be substituted in Eqs. (4.24) and (4.26) to find

$\overrightarrow{W_s}^{m+1}$ and $\overrightarrow{V_s}^{m+1}$ as

$$\begin{aligned} (HL^{-1}H+L)\overrightarrow{V_s}^{m+1} &= \overrightarrow{\zeta^m} - HL^{-1}\overrightarrow{\xi^m}, \qquad (4.30) \\ \overrightarrow{W_s}^{m+1} &= L^{-1}\overrightarrow{\xi^m} + L^{-1}H\overrightarrow{V_s}^{m+1}, \qquad (4.31) \end{aligned}$$

where known matrices H, L and vectors $\overrightarrow{\zeta^m}$ and $\overrightarrow{\xi^m}$ are given as

$$\begin{aligned} H &= -A(G^2+F^2)^{-1}GE - D, \\ L &= -A(G^2+F^2)^{-1}FE + C, \\ \overrightarrow{\zeta^m} &= \overrightarrow{W^m} - A(G^2+F^2)^{-1}(G\overrightarrow{U^m} + F\overrightarrow{Z^m}), \\ \overrightarrow{\xi^m} &= \overrightarrow{V^m} - A(G^2+F^2)^{-1}(F\overrightarrow{U^m} - G\overrightarrow{Z^m}). \end{aligned}$$

Using the above matrices and vectors, we can calculate $\overrightarrow{V_s}^{m+1}$ in Eq. (4.30) and substitute it into Eq. (4.31) to obtain $\overrightarrow{W_s}^{m+1}$. Once the Stokes fields have been calculated they can be substituted into Eqs. (4.28) and (4.29) to find the laser fields. The advantage of the above method is that the set of equations can be solved numerically without the need for iteration. The matrix coefficients and vectors $\overrightarrow{V}$, $\overrightarrow{U}$, $\overrightarrow{W}$ and $\overrightarrow{Z}$ are evaluated recursively using the initial values of the Stokes and pump fields at $t = 0$. Here the field amplitudes at any time slot $m+1$ have been determined from those at the preceding time slot m.

4.4 Results of the 1-dimensional model

Depending on the geometry of the SBS process and the energy of the input pulse, the model results in Stokes oscillations or fluctuations similar to those observed experimentally [83, 81, 80, 12, 19, 2] as will be discussed below. We shall see that the intensity modulation can be categorised into two groups: A) deterministic amplitude oscillations at the time when the energy of the pump reaches the threshold energy and B) stochastic fluctuations due to noise in the amplitude and phase of the Stokes beam.

4.4.1 Model parameters and geometry

Solutions of equations (4.24)-(4.27) are found for a Gaussian pump pulse with an electric field of the form $E_0 \exp(-2[\frac{t-t_\circ}{t_p}]^2)$, where t_p is the pulse width. Referring to figure 4.2, we apply the following geometrical and material parameters to examine the typical results of the SBS process: cell length = 60 cm, focal length = 50 cm, immersion length = 15 cm, initial waist of the beam = 0.4 cm, input energy = 320 mJ, gain of the medium (Freon 113) = 0.0063 cm/MW, phonon lifetime = 0.85 ns and arbitrary index of refraction, $n = 1.0$. The above parameters were chosen arbitrarily for the numerical study only. There is a free parameter in our computer code that determines the strength of the initial random noise. Experimental results are necessary to set the value of this parameter. The results in this chapter show the general behaviour of SBS for an arbitrary value of the free parameter resulting in arbitrary units for the Stokes and pump powers. However, in Chap. 5 we use experimental parameters to set the free parameter of our computer code and make accurate comparisons between the numerical and experimental results.

4.4.2 A: Deterministic Threshold Oscillation

The finite phonon lifetime provides an energy interchange mechanism between the Stokes and laser fields via the acoustic field. In the case of Gaussian pump beams, it takes some time for the energy contained in the pump to reach the threshold energy required for Stokes initiation. At the threshold, the Stokes power increases very rapidly and overshoots the pump power resulting in the depletion of the pump field and reduction of the gain. Because of this gain reduction, the Stokes power also decreases causing an increase in the pump energy which in turn causes an increase in the Stokes field again. This energy interchange between the Stokes and pump fields continues and resembles a relaxation oscillation (see figure 4.4). The rate of this energy interchange is controlled by the reaction time of the acoustic field, i.e. phonon lifetime. Such an energy interchange mechanism has also been discussed in Ref. [7] and [1]. Chu et al. [1] report relaxation oscillations which are visible in the transmitted pulse. However, our simulation results show that for a long cell and a geometry in which the laser beam has been focused deeply into the cell, we

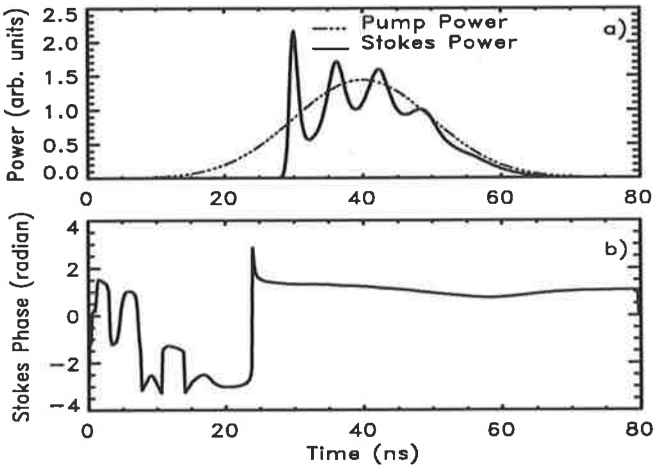

Figure 4.4: (a) Typical threshold oscillation in the Stokes beam obtained for the following parameters: cell length100 cm, focal length 100 cm, immersion length 70 cm, phonon lifetime 0.85 ns, medium gain 0.006 cm/MW, FWHM pulse length 20 ns, and input energy 114 mJ. (b) shows no corresponding variation in the phase of the Stokes.

predict relaxation oscillation in the Stokes return as shown in Fig. 4.4. Experimental evidence of such a oscillation is reported by Damzen and Hutchinson [7], although they used tapered waveguides in their experiments. In the focused cell geometry, the relaxation oscillation has not been observed (to the best of our knowledge) to the extent that is observed in Chu et al. [1] and our results (Fig. 4.4). However, there are some experimental results that show the first peak of the relaxation oscillation in the Stokes pulse. Fig. 4.5 shows the experimental results of SBS in Freon reported by O'Connor [4]. The first peak of the relaxation oscillation is apparent in the output Stokes pulses. He observed that the position and the magnitude of the first peak was very reproducible from shot-to-shot. He also observed no degradation in the time-resolved phase fidelity during the relaxation oscillation. The amplitude of the first peak is a function of focusing depth. When the focusing depth is less than few centimeters no apparent peak is observed. However, as the focusing depth increases, the amplitude of the first peak also increases, see Fig. 4.5. This is in a qualitative agreement with the numerical results of our model. Numerical results, Figs. 4.4 and 4.13, show that the threshold oscillations are present for long focusing depth and disappeared for short focusing depth (detailed comparisons are not possible due to lack of sufficient experimental details in [4], see Sec. 5.5).

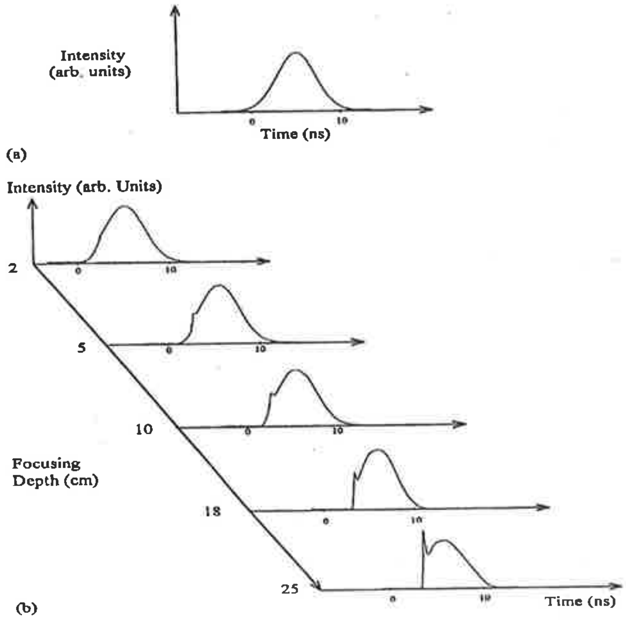

Figure 4.5: Experimental results showing: (a) Near field temporal profile of laser input pulse, (b) Near field temporal profiles of Stokes returns for different focusing depths. After M. O'Connor [4]

In order to categorise the behaviour of threshold oscillation we use the following parameters (in the simulation): Cell length 100 cm, focal length 100 cm, immersion length 70 cm, phonon lifetime 0.85 ns, gain of the medium 0.006 cm/MW and input energy 114 mJ. Any changes to these parameters are specified in the figure captions. Figure 4.4 shows a typical threshold oscillation in the Stokes beam. Different parameters such as phonon lifetime, laser intensity at the focal point and immersion length affect the behaviour of the threshold oscillation. There are no predicted phase jumps corresponding to these oscillations.

Effect of Phonon Lifetime on the Threshold Oscillation

If the finite phonon lifetime is responsible for the relaxation oscillation at the threshold energy, we would expect that the behaviour of the threshold oscillations depends on this parameter. Figure 4.6 shows the threshold oscillation for two different phonon lifetimes. Defining T_o to be the time interval over which the threshold oscillations are observable (see figure 4.6), our simulation predicts that T_o is reduced for long

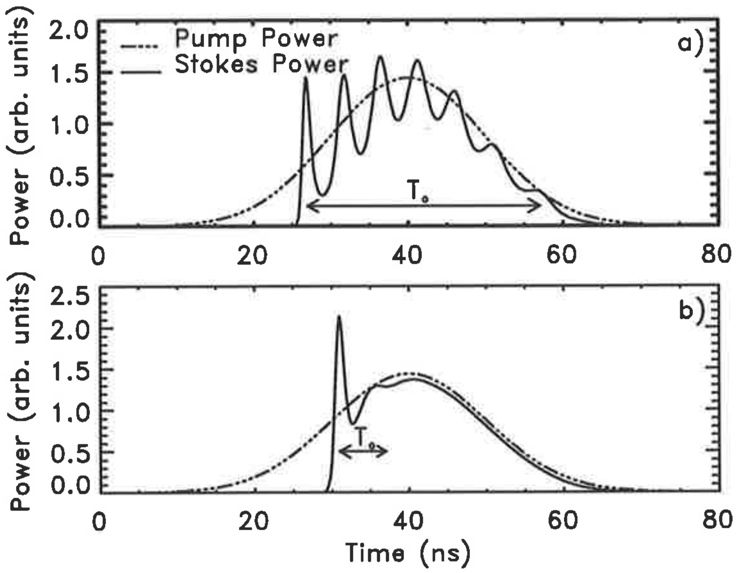

Figure 4.6: Threshold oscillations are reduced for longer phonon lifetime. (a) Phonon lifetime is 0.5 ns and (b) phonon lifetime is 1.25 ns. Other parameters are as those of Fig. 4.4.

phonon lifetimes (see figure 4.7). It is seen that for longer phonon lifetimes, oscillations in the Stokes return come to equilibrium faster than those for short phonon lifetimes. Our model permits a detailed investigation of the above mentioned relaxation oscillation and the role of the phonon lifetime.

The acoustic field is described by equation (4.11c). For early times in the process, the first source term in the right hand side of the equation may be ignored and for the second term we can write $f_1 = \sum_k a \cos\omega_k t$. Equation (4.11c) can then be solved to yield

$$A_q = A_{0q}e^{-\Gamma t} + \sum_k a'_k \cos\omega_k t + \sum_k b'_k \sin\omega_k t,$$

in which $a'_k = a_k\Gamma(\Gamma^2 + \omega_k^2)^{-1}$ and $b'_k = a_k\omega_k(\Gamma^2 + \omega_k^2)^{-1}$. In the limit of a long phonon lifetime i.e. $\Gamma \to 0(\tau \to \infty)$ we find $a'_k = 0$ and $b'_k = \frac{a_k}{\omega_k}$, which results in a solution of $\Psi_q = \sum_k \frac{a_k}{\omega_k} \sin\omega_k t$ for the acoustic field. Comparing this result with the source term f_1, it is seen that, in the limit of a large phonon lifetime, the medium will not respond to the rapid fluctuations in the source term, but rather responds to the integral of rapid changes. In the other limit of $\Gamma \to \infty(\tau \to 0)$, $b'_k \to 0$ and $a'_k = \frac{a_k}{\Gamma}$ Eq. (4.11c) gives a solution of $\Psi_q = \sum_k \frac{a_k}{\Gamma} \cos\omega_k t$. In this case the medium

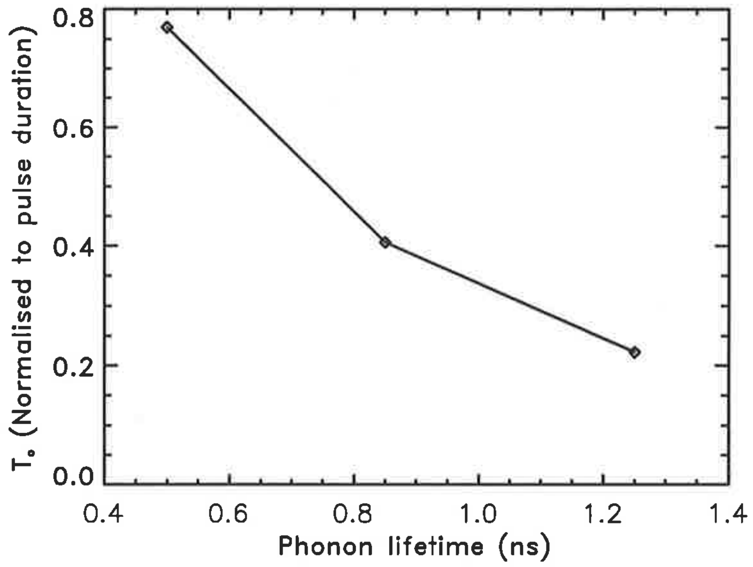

Figure 4.7: A shorter relaxation oscillation is achieved for long phonon lifetime. The graph shows how $T_\circ$ (a time interval over which the oscillations are visible, see Fig. 4.6) is reduced for long phonon lifetime.

can cope with the rapid changes in the source term, thus resulting in a modulated Stokes pulse. As an example, we have tried a periodic driving force f_1, with period $2\pi/b$, given by

$$f_1(x) = A\,|x| = \left\{ \begin{array}{cc} Ax & 0 < x < \pi/b \\ -Ax & -\pi/b < x < 0 \end{array} \right\} \text{ over one period,}$$

where A is a constant. This function represents a zig-zag function with a width of $2\pi/b$ (see the solid curves in Fig. 4.8) and can be expanded using the Fourier series:

$$f_1(x) = a_0 + \sum_{n=1}^{\infty} a_n \cos nbx,$$

where

$$\begin{aligned} a_0 &= A\frac{\pi}{2b} \\ a_n &= \frac{4b}{\pi n^2} \quad \text{for } n = 1, 3, 5, \cdots . \end{aligned}$$

Using the above discussion, one can find the acoustic response function as

$$A_q = A_{0q}e^{-\Gamma t} + \sum_k a_k' \cos\omega_k t + \sum_k b_k' \sin\omega_k t,$$

where

$$\begin{aligned} b_0' &= 0,\ a_0' = \frac{a_0}{\Gamma} = \frac{A\pi}{2b\Gamma} \\ b_n' &= \frac{bn}{\Gamma^2 + b^2n^2}\frac{4b}{\pi n^2} \qquad n = 1,3,5,\cdots \\ a_n' &= \frac{\Gamma}{\Gamma^2 + b^2n^2}\frac{4b}{\pi n^2} \qquad n = 1,3,5,\cdots . \end{aligned}$$

Ignoring the first term in the acoustic response function and plotting it as a function of time, reveals that in the limit of

$$\tau \gg 2\pi/b \Rightarrow \Gamma \ll b/2\pi,$$

where the phonon lifetime is much longer than the width of the zig-zag modulation in the driving force, the acoustic field response is the integral of the driving force, Fig 4.8a and 4.8b. On the other hand, in the limit of

$$\tau \leq 2\pi/b \Rightarrow \Gamma \geq b/2\pi,$$

the acoustic field can respond to the rapid changes in the driving force, Fig 4.8c and 4.8d. Fig. 4.8 also shows that for very short phonon lifetime, the delay between the driving force and the response function is reduced while the modulation depth of the response function approaches that of the driving force. The above discussion is applicable not only for the beginning of the process but also for any rapid changes in the source fields of the acoustic field. The phonon lifetime thus represents a measure of the inertia of the acoustic field. The larger the phonon lifetime, the higher is the inertia of the acoustic field and the slower is the response of the medium to the rapid changes in the Stokes and the laser field. This is similar to the response of a low bandwidth electronic analog amplifier to a short pulse. The amplifier can not respond quickly to the pulse, resulting in a broadened output pulse.

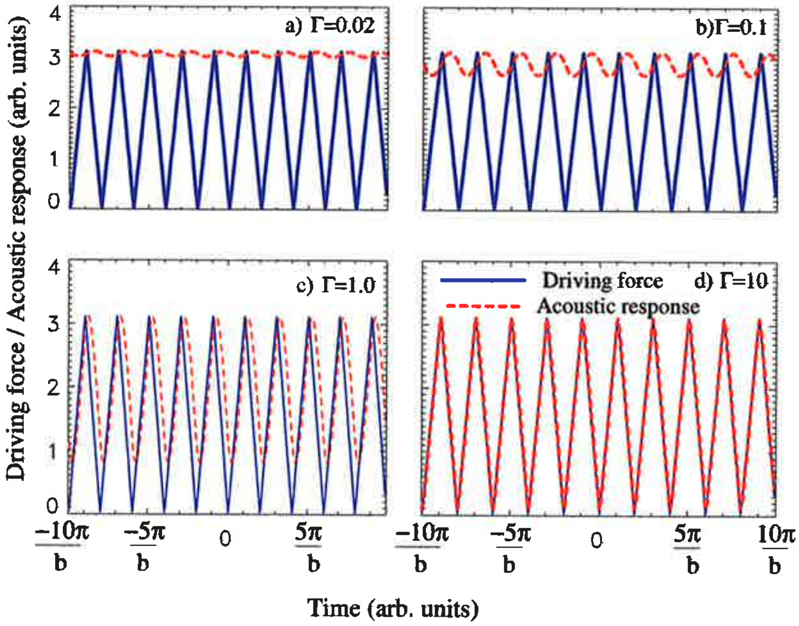

Figure 4.8: Response of the acoustic field to a zig-zag driving force. The driving force is shown as solid lines in graphs (a)-(d). The responses of the acoustic field are shown for different values of Γ as dashed-lines. The width of the driving force is $2\pi/b$, where $b = 1$. See the text for explanation.

Effect of the laser intensity at the focal plane

According to the equation (4.15c), the amplitude of the acoustic field depends on the intensity of the input pulse. A shorter focal length results in a higher intensity at the focal plane hence a higher power acoustic wave. As a result, the gain for the Stokes field amplitude, which depends on the pump and acoustic field amplitudes through Eq. (4.15b), does not reduce very quickly after the initial overshooting of the Stokes pulse, i.e., the Stokes pulse can use the energy stored in the acoustic field. Thus, the Stokes amplitude does not reduce as quickly after the first peak, which in turn causes a shorter duration of the relaxation oscillation. This is illustrated in figure 4.9.

Effect of the immersion length

As it was discussed in section 3.4.1, the dynamics of the Stokes return pulse is greatly affected by the depletion region of SBS. This is a region close to the entrance window of the SBS medium in which most of the depletion of the pump pulse occurs. The

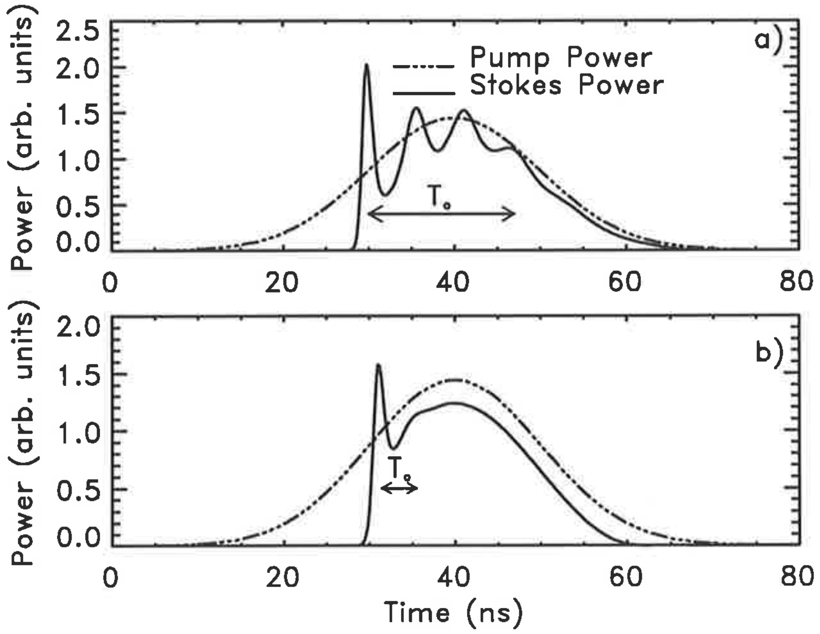

Figure 4.9: Smaller focal spot (higher intensity) results in a suppression of threshold oscillations. Oscillations are reduced in graph (b) (focal length 60 cm) in comparison with graph(a) (focal length 90 cm). Other parameters as in Fig. 4.4.

length of this region is given by $l_{dep} = \dfrac{l_{imm}}{G}$, where l_{imm} is the immersion length (see Fig. 4.3) and G_0 is the steady state gain of SBS. The smoothing of the Stokes modulation occurs if the propagation time through this region is much less than the temporal variation of the modulation in the Stokes pulse at the beginning of this region, i.e., $T_{l_{dep}} \ll T_s$. According to this discussion reducing the depletion length by decreasing the immersion length, smooths out the modulation in the Stokes pulse. We have tried the effect of immersion length on the threshold oscillation by changing the distance between the cell and the lens. As expected, a shorter relaxation oscillation is obtained when shorter immersion length is used. Figure 4.10 shows the behaviour of the threshold oscillation for two different immersion lengths. For a smaller immersion length, Fig. 4.10 (b), the depletion region of the pump beam is confined to a small region at the entrance of the cell resulting in a shorter relaxation oscillation.

From another point of view, the first peak of the threshold relaxation oscillation is due to the strong saturation of the pump wave by the leading edge of the counter-propagating Stokes wave. The characteristic of the first peak then depends on the

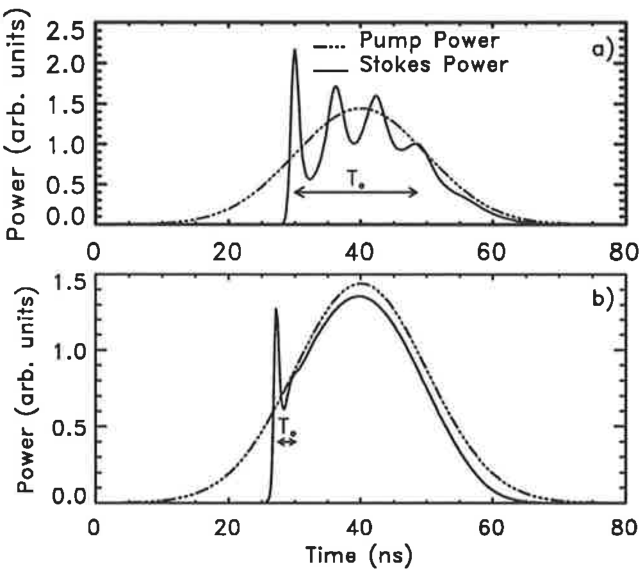

Figure 4.10: Modulations present in (a) (focal length=100 cm, immersion length=40 cm) are almost suppressed in (b) (focal length=100 cm, immersion length=10 cm). Shorter immersion length provides a better suppression. Other parameters as in Fig. 4.4.

threshold and the time it takes the Stokes return to propagate to the front entrance of the SBS cell. By increasing the immersion length the interaction time between the pump and counter propagating Stokes return increases resulting in a longer relaxation oscillation, Fig. 4.10a.

Pulse Compression

As mentioned previously, the threshold relaxation oscillation is due to the energy interchange between the pump and the Stokes fields, which causes the saturation of the pump wave by the leading edge of the Stokes return. Thus, we can expect to achieve a single and narrow Stokes pulse (pulse compression) if we do not provide the appropriate amount of energy for the Stokes pulse to rebuild after the first impulse of relaxation oscillation. Considering the effect of the focal and immersion length, one can find a focusing geometry resulting in a threshold oscillation with few peaks. For such a focusing geometry, reducing the input power should remove the secondary impulses in the Stokes return after the first peak. Figure 4.11 shows how the relaxation oscillation converts to a compressed pulsed as the input energy is reduced from graph a) to d).

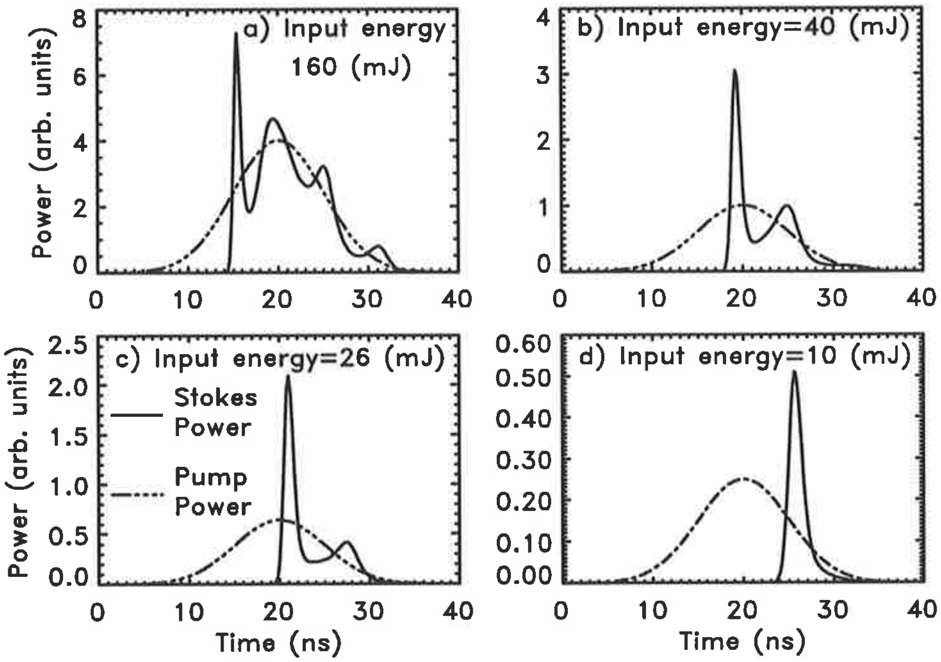

Figure 4.11: Pump and Stokes as function of time at the entrance to the cell. By reducing the pump energy, we remove extra oscillations from the threshold oscillations, resulting in a pulse compressed beam. Cell length=80 cm, focal length=80 cm and immersion length =70 cm with all other parameters as in Fig. 4.4. In 9(d) the delay in peak Stokes and peak pump is due to the round trip time of the cell and building to threshold.

The process of pulse compression can be seen better if we look at the 3D graph of the Stokes power, figure 4.12. At early times of the process, the center of maximum reflectivity (maximum of the Stokes pulse) is close to the focal region. This center moves towards the entrance of the cell at a later time. As a result, latter parts of the incoming pulse are traveling a shorter distance before generating the Stokes return, resulting in pulse compression [95, 7].

Summary of the results

We have shown how the focusing geometry affects the threshold relaxation oscillation. By choosing appropriate focusing parameters, we are able either to avoid them or to make them apparent in the Stokes return pulse. Long cell and deep focusing results in apparent threshold oscillation while short cell and shallow focusing result

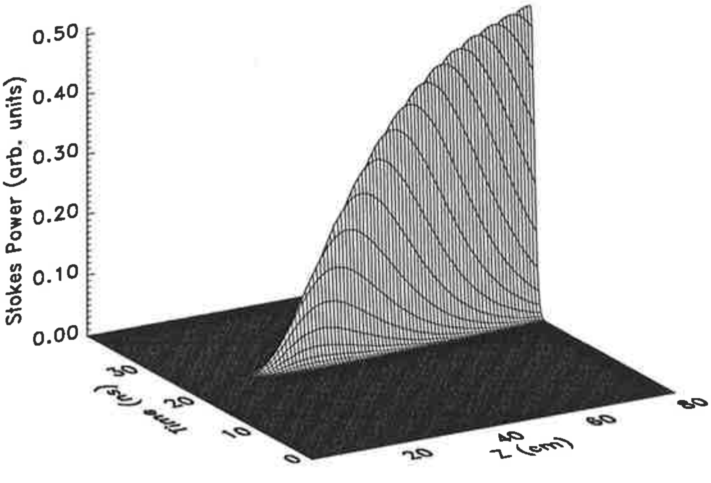

Figure 4.12: 3D graph of pulse compression [(d) in Fig. 4.11]. Stokes power in time and space shows how the center of maximum reflectivity moves towards the entrance of the SBS cell ($z = 80$ cm) resulting in pulse compression. Parameters as in Fig. 4.11.

in smooth Stokes output. Numerical results show that for short focal and immersion lengths the threshold oscillations disappear in the Stokes pulse, as shown in Fig. 4.13.

4.4.3 B: Stochastic fluctuations of phase and amplitude

Noise initiation of the SBS process results in large scale fluctuations in the Stokes output. These fluctuations are of stochastic nature in the sense that there is a random probability for the occurrence of the fluctuations as well as for their temporal position in the output Stokes pulse. The inclusion of the Langevin forces into the SBS equations, Eq. (4.3), does produce intensity fluctuations and phase jumps in the output Stokes pulse. The computer code can be run for different initial noise distributions resulting in different output results. For some initial noise distributions, intensity fluctuations are apparent in the output Stokes intensity. Fig. 4.14 shows an example of this and also shows that corresponding and simultaneous to these fluctuations in the Stokes power, there are some rapid changes in the Stokes phase. The simultaneous occurrence of phase jumps in the Stokes phase and fluctuations in the stokes power can be understood by looking at the main equations governing SBS i.e. equations (4.11). On the right hand side of these equations we have two

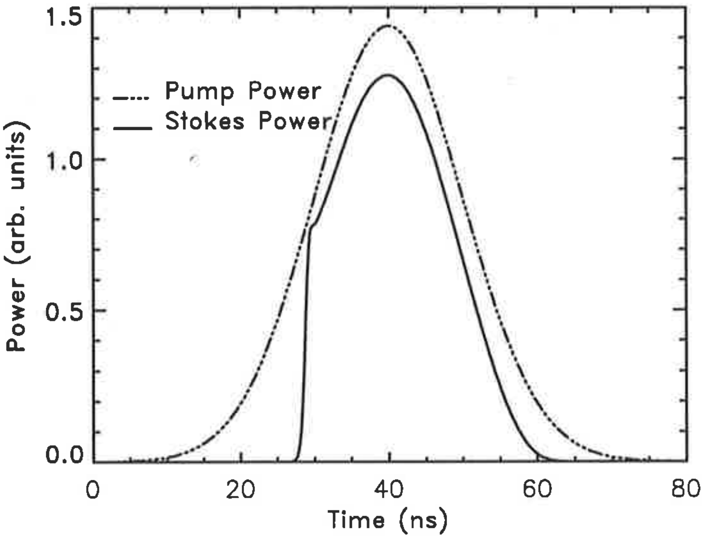

Figure 4.13: Threshold oscillations disappear for short focal length and immersion length. Immersion length =20 cm and focal length =60 cm, other parameters as standard set shown in Fig. 4.4.

effective gain terms, $g\sin(\phi_q+\phi_s-\phi_p)$ or $g\cos(\phi_q+\phi_s-\phi_p)$ which are affected by rapid changes in the phase of the fields. Figure 4.14 (b) shows how the normalized effective gain $g\sin(\phi_q+\phi_s-\phi_p)$ suffers a reduction at the time when a phase jump occurs in the Stokes field. Depending on the size of the phase jump and the phase behaviour of the pump and acoustic field, the effective gain can be reduced to a smaller positive value or even to a negative value, which interchanges the role of Stokes and pump field i.e. the pump field gains while the Stokes field depletes. This is similar to what happens in the generation of solitons in stimulated Raman scattering [87]. The final temporal position of the phase jumps as well as the shape of fluctuations in the output of the Stokes phase and power depend on how they propagate and amplify from the initiation point (focal point) towards the entrance of the cell. Stokes pulses, initiated from noise, are amplified through two main regions as they propagate towards the output of the cell. In the first region, basic amplification and spectral changes of the Stokes beam take place [80, 96, 97, 13, 98, 18] and in the other one (namely depletion region specified by depletion length $l_{dep}=\frac{l_{imm}}{G_0}$) the final amplification of the Stokes power to a level approximately equal to the pump power occurs. The final Stokes output can be greatly affected by the dynamic processes in the depletion region. As we discussed, this region plays a crucial role in

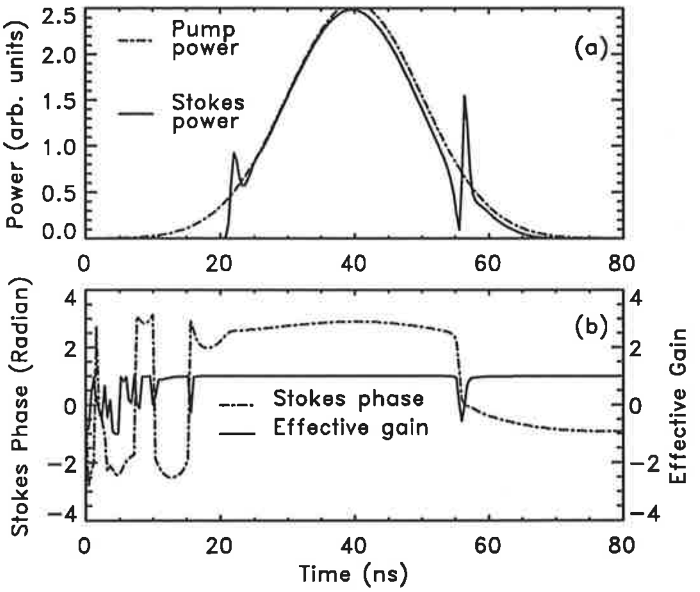

Figure 4.14: Corresponding and simultaneous to each fluctuation in the Stokes output (a) there is a jump in the Stokes phase [dashed curve in (b)]. Parameters are set as: cell length 60 cm, focal length 60 cm, immersion length 30 cm, Phonon lifetime 0.85 ns, gain of the medium 0.0063 cm/MW, refractive index 1.36 and input energy 119 mJ.

suppression of fluctuations (existing in the Stokes signal) in the case when $T_{l_{dep}} < T_s$. For the case of $T_{l_{dep}} > T_s$, fluctuations in the Stokes pulse at the beginning of this region experience amplification and appear in the final output [18]. Depending on the phonon lifetime and the length of this region, different spectral components of the fluctuations in the Stokes pulse experience different gain and as a result, the spectrum of the fluctuation varies as it propagates through the depletion region [98, 18]. Considering this and the fact that the depletion lengths corresponding to different temporal parts of the Stokes pulse are different [since $G_0(t) = gI_l(t)l_{imm}$], we expect that the shape of the fluctuation varies while propagating towards the output of the cell. For example, figure 4.15 (a)-(d) shows how the temporal position of the phase jump and the beginning of the fluctuation in the figure 4.14, vary from 39 ns at position $z = 0.46L$ inside the cell (a) to 55 ns at the entrance, $z = L$, of the cell(d) (where L is the length of the medium, see figure 4.3).

The focusing geometry of the SBS cell, input energy and phonon lifetime of the material affect the phase jump fluctuations. Due to the stochastic nature of the

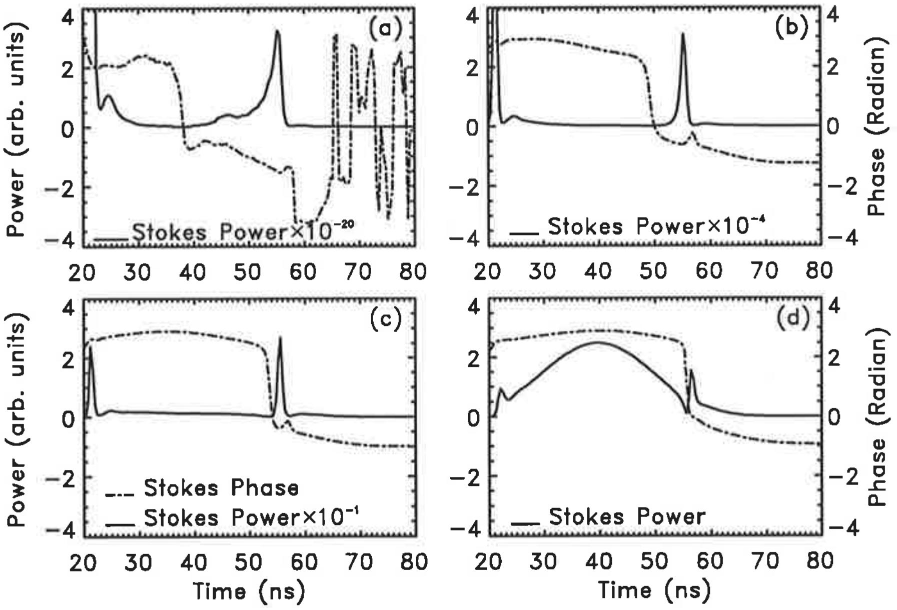

Figure 4.15: The temporal position of phase jump and the beginning of the amplitude fluctuation (in Fig. 4.14) as they initiate at about $z = 0.46L$ (a) inside the cell (where L is the cell length) and propagate through points $z = 0.56L$ (b) and $z = 0.71L$ (c) to the entrance of the cell (d).

fluctuations, the width, magnitude and the number of fluctuations vary from pulse to pulse. As a result, we have chosen the fraction of the Stokes energy contained in the fluctuations i.e. $< \frac{E_{fluc}}{E_{output}} >$ (where $<>$ means statistical average over all number of pulses) as the best parameter to show the importance of the fluctuations to a practical deployment of SBS in a laser system. Unless otherwise stated, the following parameters are used in the numerical simulations: cell length = 60 cm, focal length = 60 cm, immersion length = 30 cm, input beam radius at window = 0.3 cm, input energy = 119 mJ, gain of the medium = 0.0063 cm/MW, phonon lifetime = 0.85 ns, and refractive index = 1.36.

Phonon lifetime effect on the phase jump fluctuations

As was previously discussed, the phonon lifetime is a measure of the acoustic field inertia. For a medium with a long phonon lifetime, the acoustic field can not respond quickly to the rapid fluctuations in the noise initiated Stokes field, and it thus broadens and smooths out the fluctuations in the Stokes field. This is illustrated in Fig. 4.8 in which the response of the acoustic field to a zig-zag driving force for

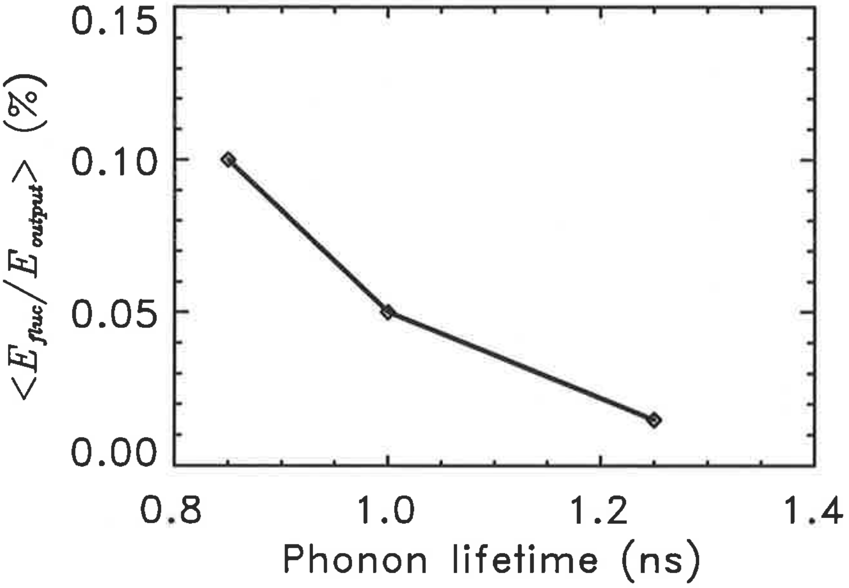

Figure 4.16: The average of the fluctuation energies (normalised to output energy) reduces for longer phonon lifetimes. Other parameters are as in Fig. 4.14.

different values of phonon lifetimes is examined. For a long phonon lifetime, the response function is just the integral of the noisy driving force. To examine the effect of phonon lifetime on the phase jump fluctuations, the simulation was run with different initial noise distributions for three different phonon lifetimes. The fluctuation energy (normalised to the output energy and averaged over a certain number of shots) is calculated for these different phonon lifetimes. Figure 4.16 shows how the energy of the fluctuations decreases for higher phonon lifetimes, indicating a better suppression of the fluctuations.This is consistent with the condition $G_0 \gg \Gamma T_t$, Eq. (3.50), required for smoothing the fluctuations. The longer the phonon lifetime, the smaller is Γ and the better is the fulfillment of $G_0 \gg \Gamma T_t$.

Effect of immersion length:

As mentioned previously, the two key parameters in suppressing the fluctuations are the propagation time through the depletion region $T_{l_{dep}}$ and the temporal variation of the Stokes signal, T_s, which reaches the depletion region. In the case when $T_{l_{dep}} < T_s$ the fluctuations in the Stokes signal are suppressed as they pass through the depletion region while in the other case, $T_{l_{dep}} > T_s$, they are magnified and appear in the final Stokes output. The depletion length l_{dep} depends (roughly) on the steady state gain G_0 and the immersion length l_{imm} ($l_{dep} \simeq \frac{l_{imm}}{G_0}$). By controlling G_0 and l_{imm} we are thus able to change the length of depletion region. From the condition $T_{l_{dep}} > T_s$, it is clear that reducing $T_{l_{dep}}$, implies a reduction on the number of fluctuations as well as their durations in the final Stokes output.

A shorter depletion length can be obtained for a short immersion length (achieved by long cell-lens separation) and as a result, we would expect a better suppression of the fluctuations. Figure 4.17 shows how the averaged fluctuation energy $< \frac{E_{fluc}}{E_{out}} >$ % (normalised to the output energy) changes as a function of the immersion length. We thus conclude that a small immersion length, achieved by large cell to lens separation, provides better suppression of fluctuations. Experimental results predict similar effects: the intensity fluctuations are suppressed for short immersion lengths. In Fig. 4.18 [2] the amplitude of the fluctuations as a percentage of the Stokes peak, and averaged over 1600 pulses, has been plotted for different values of the immersion length. It indicates that in SBS experiments, focusing geometries with shorter interaction lengths can be used to suppress the Stokes intensity fluctuations. Such a behaviour has also been reported previously [11, 13, 92].

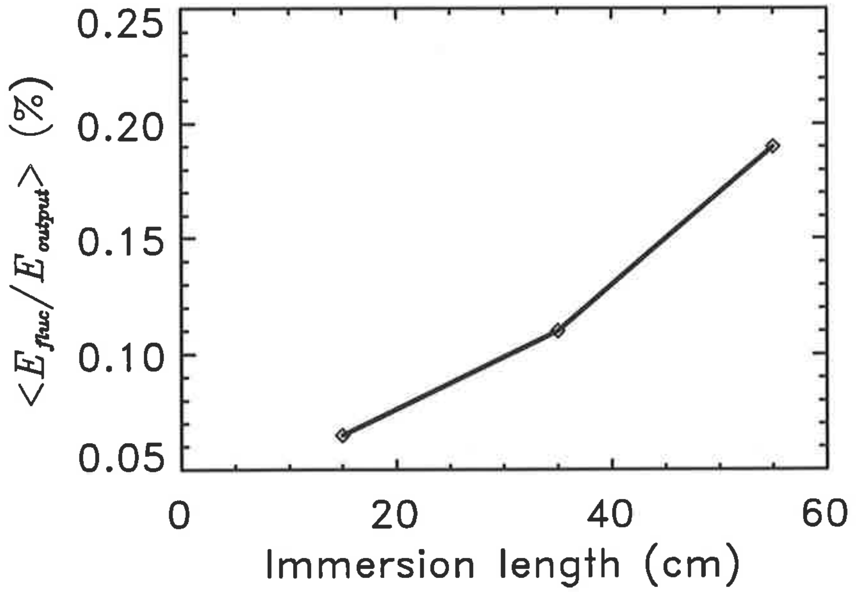

Figure 4.17: The effect of the energy fluctuations, measured by $\langle E_{fluc}/E_{output}\rangle$ % is reduced for shorter immersion lengths (constant focal length and large cell to lens separation).

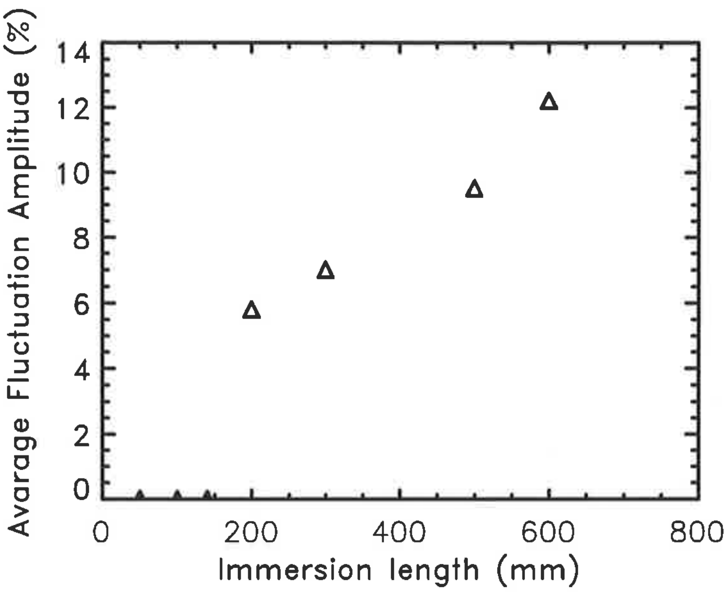

Figure 4.18: Experimental results of the effect of the immersion length on intensity fluctuations. Average of the fluctuation amplitudes as a percentage of the Stokes peak versus the immersion length. After V. Devrelis [2].

Effect of input energy:

Another parameter that can affect the depletion length is the input energy. A higher input energy results in a higher gain, G_0, which in turn reduces the depletion length, l_{dep}, of the SBS. As discussed above, we thus expect that fluctuations in the output Stokes beam have smaller duration i.e. they carry less energy. In order to examine the effect of input energy, we have studied the output Stokes beam of 500 simulated pulses with different initial noise distributions and at different energies. Considering the histogram of $\frac{E_{out}}{(E_{out})}$ for these 500 pulses, where $\overline{E}_{out}$ is the mean energy of all output pulses, and fitting a Gaussian function to it, we find that the width of the Gaussian fit is reduced at higher energy i.e. the variation in output energy per pulse around the mean value is reduced for high energy (see figures 4.19). Another parameter that can show how fluctuations are suppressed for high energies is the average of the fluctuation energy (normalised to output energy). Simulation results in figure 4.20 show a reduction in the averaged fluctuation energy for higher input energies. This result is consistent with the experimental results shown in Fig. 4.21 [2] in which higher input energies result in better suppression of

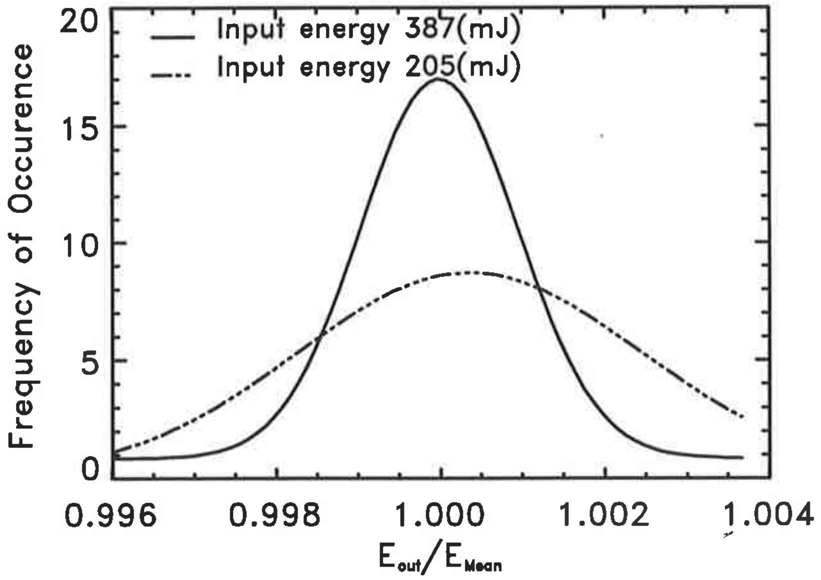

Figure 4.19: Histogram of output energies (normalised to the mean) for two different input energies 387 mJ and 205 mJ. Operating at high input energy reduces the effect of fluctuations.

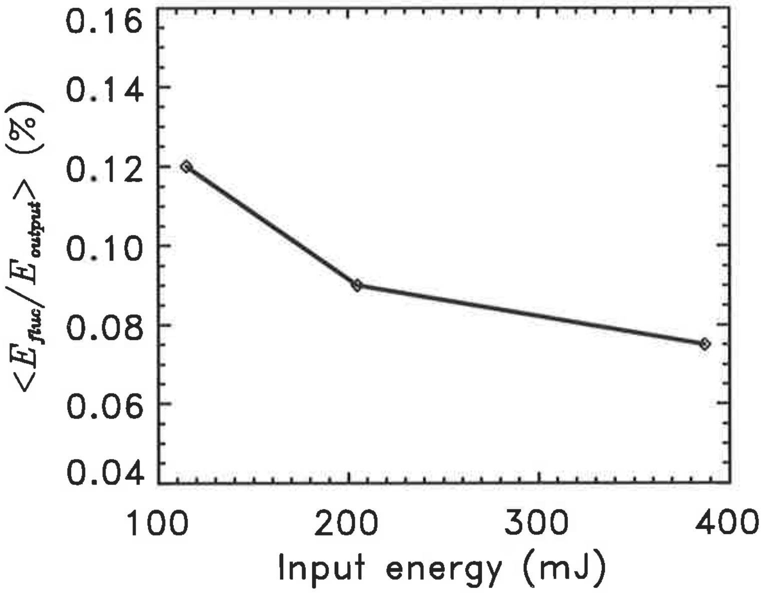

Figure 4.20: A reduction in averaged fluctuation energy ($\langle E_{fluc}/E_{output}\rangle$ %) occurs at high energies.

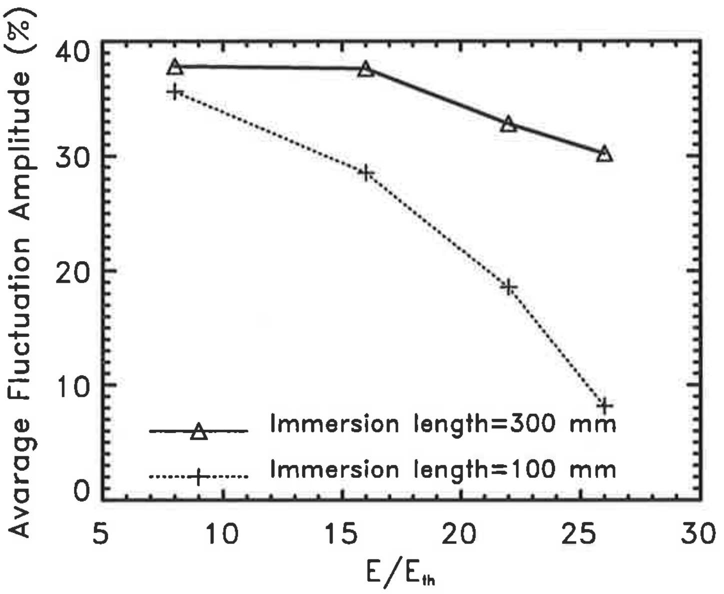

Figure 4.21: Experimental results of the effects of the input energy and interaction length on intensity fluctuations. Average of fluctuation amplitudes as a percentage of the Stokes peak versus the input energy for two focusing geometries. For focal length =100 mm, the interaction length is 100 mm and for focal length = 300 mm, the interaction length is 300 mm. After V. Devrelis [2].

fluctuations.The Experimental results of Dianov et al. [11] (in fibers) shows that the depth of the intensity modulation reduces when the excess energy over the threshold energy increases. Gaeta et al. [13] as well reported less Stokes intensity modulation for larger values of G_0.

Effect of pulse duration:

In the above section, we kept the duration of the input pulse constant and we studied the effect of parameters such as input energy and beam area on the fluctuations. In order to observe the role of pulse duration, we have chosen to keep the input energy of the pulse constant and reduced the pulse duration, i.e. we increase the peak injected power. Simulation results show a dramatic reduction in the number of fluctuations for short pulse durations which in turn results in a smaller averaged fluctuation energy (figure 4.22).

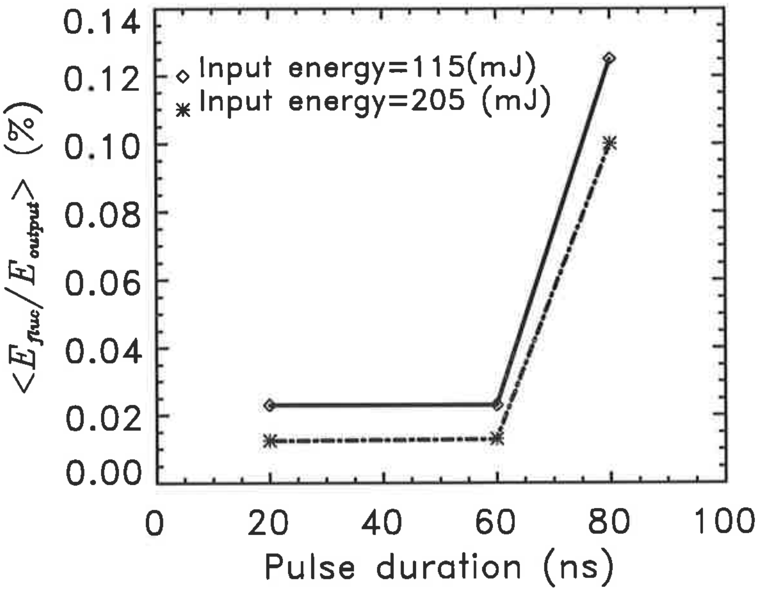

Figure 4.22: For a constant energy, reducing the duration of the input pulse dramatically suppress the fluctuation in the output Stokes. The effect of pulse duration on the suppression of fluctuations is shown for two energies: 115 mJ and 205 mJ.

4.4.4 Conclusion

To describe different kinds of temporal amplitude and phase modulations in Stimulated Brillouin Scattering, we extended the plane-wave equations, for complex fields describing SBS in a finite cell, to include focusing geometry and initiation from a Gaussian random noise distributed over space and time. Two kinds of modulations were found:

(1) Deterministic relaxation oscillation at the threshold energy,

(2) Random fluctuations in the output Stokes power.

The finite phonon lifetime of a material is responsible for an energy interchange between the pump and Stokes field resulting in relaxation oscillations at the threshold. There is no modulation of the Stokes phase corresponding to these oscillations. It is predicted that materials with shorter phonon lifetimes can exhibit relaxation oscillations of longer duration than those with long phonon lifetimes. It was found that an initially stronger acoustic wave (resulting from a high focal intensity determined by the focal length of the lens) shortens the relaxation oscillations at the threshold energy since the Stokes pulse can use the energy stored in the acoustic field after initially overshooting. Also, a small immersion length achieved by a large cell to lens separation reduces the threshold relaxation oscillations. Altogether, short focal length, short immersion length and large phonon lifetime provide the best parameter space for removing the threshold relaxation oscillations. Experimental and numerical results are in a qualitative agreement, see Figs. 4.5, 4.9, 4.10 and 4.13. They indicate that the threshold oscillations are present for long focusing depth and disappeared for short focusing depth. Although weak threshold oscillations are usually observed in experiments, they have, to the best of our knowledge, not previously been the subject of investigation, and have not been described to the extend predicted in our model.

Stimulated Brillouin Scattering initiated from microscopic noise shows large scale stochastic amplitude modulation in the output Stokes beam. Simultaneous jumps in the Stokes phase are found. We have determined a parameter regime where this modulation is minimised or eliminated, thus predicting conditions for optimised, reliable SBS:

1) Longer phonon lifetime provides a better suppression of instabilities in the Stokes pulse.

2) Depending on the input energy and focused spot size, the pump and Stokes field can be confined to a small region near the entrance of the cell (high energies, short immersion length) or distributed towards the focal point for low energies and long immersion length. For high input energies or short immersion length the time for propagation through this region $T_{l_{dep}}$is small enough to suppress many of the fluctuations reaching this region with duration $T_s > T_{l_{dep}}$. Short immersion length, achieved by large cell to lens separation, is more desirable since $T_{l_{dep}}$ can be reduced more effectively and a higher reflectivity can be achieved, but will in practice be limited by optical break down of the SBS material or cell window. These results are in qualitative agreement with experimental results, see Figs. 4.21 and 4.18.

3)Another parameter that can be used effectively to suppress the fluctuations is the pulse duration. Our results showed that for a shorter pulse duration (i.e. higher peak power) the number of fluctuations was reduced dramatically.

In this chapter, we examined thoroughly for the first time, the Stokes intensity

UNIVERSITY OF ADELAIDE LIBRARY

modulations phenomenon in the cell geometry. As it will be shown in the next chapter, these intensity fluctuations degrade the temporal and spatial fidelity of the SBS experiment. Thus the significance of our findings, specially in practical applications, is that they can be used to determine the best parameter space for excellent Stokes beam quality.

The model developed here is one of the most complete and efficient one dimensional numerical models of SBS. It includes all important features of SBS such as transience, focusing geometry and initiation from noise. The model can be used in the designing of a variety of practical laser systems wherever a SBS mirror is needed either as a phase conjugating mirror or pulse compressor.

Chapter 5

3-Dimensional model of SBS

5.1 Abstract

Our previous 1-dimensional numerical model is extended to a 3-dimensional one with transverse circular symmetry in this chapter. The model describes a cylindrically symmetric, 3-dimensional, transient SBS process initiated from noise. We use a decomposition method and a new efficient numerical algorithm to solve the SBS equations. The details of this numerical algorithm are presented. The model is then used to examine the effects of transient phenomena on the efficiency of phase conjugation of aberrated and unaberrated circularly symmetric beams by SBS. The model is also employed to study the spatial mode structure of the Stokes and pump pulses inside the SBS cell. The effect of parameters, such as phonon lifetime, input pulse shape and input energy, on the transient fidelity of SBS is investigated. A new transient phenomenon which causes SBS fidelity degradation at high focal intensity (short Rayleigh range) is examined.

5.2 Introduction

The one dimensional model developed in the previous chapter enabled us to study the transient phenomena that affect the temporal fidelity and reflectivity of the SBS process. However, it does not enable us to study the phase conjugation fidelity with an aberrated input beam due to its one-dimensional nature. To overcome this problem, the model should be extended to three dimensions. The mathematical approach to develop three dimensional model of SBS is straight forward [28]. Although such a model enables us to study the phase conjugation of astigmatic and aberrated input laser beams, it requires an extensive computational effort to solve the SBS equations. For this reason and in order to reduce the computational effort, here, I developed a three dimensional numerical model with transverse circular symmetry i.e., the laser fields have circular symmetry in the plane perpendicular to the propagation direction. Thus, only one transverse dimension is considered in the SBS equations. This limits the current model to cylindrically symmetric aberrations, but the approach used can in principle easily be expanded to non-symmetric three dimensions. The model developed here has the following characteristics: (i) it is a three-dimensional numerical model of SBS in the cell geometry with transversal circular symmetry i.e., the laser fields have radial symmetry, (ii) the process is initiated from a Gaussian random noise [11, 13, 20] for both amplitude and phase to simulate the actual thermal fluctuations in the density of the medium and (iii) transient equations and a depleted pump have been used to study the threshold, saturation and transient regime of SBS, and to provide an understanding of the transient fidelity of SBS. This new model enables us to study the transient behaviour of the phase fidelity of SBS. We have used a decomposition method to expand the fields in terms of transverse spatial modes. By introducing block-vectors and matrices, App. B, and using a noniterative method employed by Chu *et al.* [1], we have developed a numerical algorithm that enables us to treat compactly any arbitrary finite number of spatial modes of the Stokes and pump fields. This efficient numerical algorithm could also be useful for the simulation of broad-band SBS, where many temporal modes exist in the input pulse. To the best of our knowledge, a complete numerical model of broadband transient SBS, which takes focusing into account, has not previously been developed.

5.3 Theory

The equations describing the pump, Stokes and acoustic fields propagating along the z direction in the SBS process are [Eqs. (3.14a)-(3.14c)]

$$(\frac{i}{2K_s}\nabla_t^2 + \frac{n}{c}\frac{\partial}{\partial t} + \frac{\partial}{\partial z})E_s = -ig_2 Q^* E_l, \tag{5.1}$$

$$(\frac{-i}{2K_l}\nabla_t^2 + \frac{n}{c}\frac{\partial}{\partial t} - \frac{\partial}{\partial z})E_l = -ig_2 Q E_s, \tag{5.2}$$

$$(\frac{\partial}{\partial t} + \Gamma)Q = -\imath g_1 E_l E_s^*. \tag{5.3}$$

Here ∇_t^2 refers to the derivatives in the transverse directions x and y, g_1 and g_2 are coupling constants, n is the refractive index of the medium and $k_s \approx k_l$ are the Stokes and pump wave numbers, respectively. In the transverse directions, we use a decomposition method [99, 21, 22, 100, 27, 28] to expand the electric fields in terms of orthonormal bases modes A_m and B_m,

$$E_l(\mathbf{r}_\perp, z, t) = \sum_m a_m(z,t) A_m(\mathbf{r}_\perp, z), \tag{5.4}$$

$$E_s(\mathbf{r}_\perp, z, t) = \sum_m b_m(z,t) B_m(\mathbf{r}_\perp, z), \tag{5.5}$$

where $\mathbf{r}_\perp$ is the position vector in the plane perpendicular to the propagation direction z, and the particular set of A_m and B_m used in our model will be given below. By substituting Eqs. (5.4) and (5.5) into Eqs. (5.1) and (5.2) and assuming that A_m and B_m satisfy the homogeneous Maxwell equations, i.e.,

$$\begin{aligned}(\frac{i}{2K_s}\nabla_t^2 + \frac{\partial}{\partial z})A_m(\mathbf{r}_\perp, z) &= 0,\\ (\frac{i}{2K_s}\nabla_t^2 + \frac{\partial}{\partial z})B_m(\mathbf{r}_\perp, z) &= 0,\end{aligned}$$

these equations can be rewritten as

$$\sum_m B_m(\frac{n}{c}\frac{\partial}{\partial t} + \frac{\partial}{\partial z})b_m = -ig_2 Q^* E_l, \tag{5.6}$$

$$\sum_m A_m(\frac{n}{c}\frac{\partial}{\partial t} - \frac{\partial}{\partial z})a_m = -ig_2 Q E_s. \tag{5.7}$$

The expansions of the electric fields in Eqs. (5.4) and (5.5) can also be used in the right hand side of the acoustic field equation, Eq. (5.3), to write

$$(\frac{\partial}{\partial t}+\Gamma)Q=-ig_1\sum_{i,j}A_i(\mathbf{r}_\perp,z)B_j^*(\mathbf{r}_\perp,z)[a_i(z,t)b_j^*(z,t)+f_{ij}(z,t)]. \tag{5.8}$$

Like the one-dimensional model, to represent the noise initiation of the SBS process, we have added a term for the Langevin noise term $f_{ij}(z,t)$ to the right hand side of Eq. (5.8), with spatial and temporal Gaussian distributions [13, 20]. f_{ij} are δ correlated functions in the sense that

$$\langle f_{ij}(z,t)f_{kl}^*(z',t')\rangle=Q_\circ\delta_{ik}\delta_{jl}\delta(z-z')\delta(t-t'),$$

where $Q_\circ$ is given in chapter 4 by

$$Q_\circ=\frac{2KT\rho_\circ\Gamma}{v^2}.$$

Here K is the Boltzman constant, T is the temperature, $\rho_\circ$ is mean density, v is the velocity of sound in the material. The acoustic field in Eq. (5.8) can be integrated to yield

$$Q=-ig_1\sum_{i,j}A_i(\mathbf{r}_\perp,z)B_j^*(\mathbf{r}_\perp,z)C_{ij}(z,t), \tag{5.9}$$

where

$$C_{ij}(z,t)=\int_0^t[a_i(z,\tau)b_j^*(z,\tau)+f_{ij}(z,\tau)]e^{-\Gamma(t-\tau)}d\tau. \tag{5.10}$$

This expression for Q in turn can be substituted in Eqs. (5.6) and (5.7) to obtain

$$\sum_m B_m(\frac{n}{c}\frac{\partial}{\partial t}+\frac{\partial}{\partial z})b_m=g_1g_2\sum_{i,j,k}A_i^*A_kB_jC_{ij}^*a_k, \tag{5.11}$$

$$\sum_m A_m(\frac{n}{c}\frac{\partial}{\partial t}-\frac{\partial}{\partial z})a_m=-g_1g_2\sum_{i,j,k}A_iB_j^*B_kC_{ij}b_k. \tag{5.12}$$

Since A_m and B_m are orthonormal bases, we can multiply both sides of Eqs. (5.11) and (5.12) by B_n^* and A_n^*, respectively and integrate over space to find the following differential equations for b_n and a_n:

$$\begin{aligned}(\frac{n}{c}\frac{\partial}{\partial t}+\frac{\partial}{\partial z})b_n &= g_1g_2\sum_{i,j,k}C_{ij}^*a_k\int_{-\infty}^{+\infty}A_i^*A_kB_jB_n^*d^2r, && (5.13)\\ (\frac{n}{c}\frac{\partial}{\partial t}-\frac{\partial}{\partial z})a_n &= -g_1g_2\sum_{i,j,k}C_{ij}b_k\int_{-\infty}^{+\infty}A_iB_kB_j^*A_n^*d^2r. && (5.14)\end{aligned}$$

In Eqs. (5.13) and (5.14), obtained for any general form of A_i and B_j, the only term that depends on the form of A_i and B_j is the tensor

$$g_{knij}=\int_{-\infty}^{+\infty}A_i^*A_kB_jB_n^*d^2r \tag{5.15}$$

Our model can thus equivalently be developed for any kind of orthonormal bases A_i and B_j that satisfy the paraxial wave equation. Since we are interested in the phase conjugation properties of SBS, we chose the complex conjugate of A_n as the basis for the Stokes wave, i.e., $B_n(\mathbf{r}_\perp,z)=A_n^*(\mathbf{r}_\perp,z)$. This enables us to examine how much of the energy in a particular input mode is reflected into the conjugated mode. For the basis A_n, we have examined two important cases: (1) the Hermite-Gaussian functions used by Moore and Boyd [28] and (2) the Laguerre-Gaussian functions used by Miller *et al.* [22]. For the case (1) a Hermite-Gaussian function is used for each transverse directions x, y i.e.,

$$A_{nm}(\mathbf{r}_\perp,z)=A_n(x,z)A_m(y,z),$$

where $A_n(x,z)$, for example, is given by

$$A_n(x,z)=(\frac{2}{\pi})^{\frac{1}{4}}(2^nn!\omega(z))^{\frac{-1}{2}}e^{i(n+\frac{1}{2})\psi(z)}H_n(\frac{\sqrt{2}x}{\omega(z)})\exp[-i\frac{kx^2}{2R(z)}-\frac{x^2}{\omega(z)^2}]. \tag{5.16}$$

For the case (2) a cylindrically symmetric Laguerre-Gaussian function is used as the basis for the transverse direction i.e., [101]

$$\begin{aligned} A_n(r,z) &= (\frac{2}{\pi})^{\frac{1}{2}}\frac{1}{\omega(z)}e^{i(n+\frac{1}{2})\psi(z)}L_n(\frac{2r^2}{\omega(z)^2})\exp\big[-i\frac{kr^2}{2R(z)}-\frac{r^2}{\omega(z)^2}\big], \\ \text{where } r &= |\mathbf{r}_\perp| = (x^2+y^2)^{1/2}. \end{aligned} \tag{5.17}$$

Here, H_n and L_n are the n-th order Hermite and Laguerre functions, respectively and the spot size, $\omega^2(z)$, radius of curvature, $R(z)$ and Gouy phase angle, $\psi(z)$, are given by

$$\omega^2(z) = \omega_0^2[1+(\frac{z-z_0}{z_R})^2], \tag{5.18}$$

$$R(z) = z - z_0 + \frac{z_R^2}{z-z_0}, \text{ and} \tag{5.19}$$

$$\psi(z) = \tan^{-1}(\frac{z-z_0}{z_R}). \tag{5.20}$$

As usual, z_0 is the position of the beam waist, the Rayleigh range z_R is related to the beam waist radius ω_0 (for the fundamental mode) and wave length λ as $z_R = \pi\omega_0^2 n/\lambda$, n is the refractive index of the SBS material, and ω_0 is related to the input fundamental beam radius ω_1 and its curvature R_1 (see Fig. D.1). In App. D we have shown how ω_0 (the beam radius) and its location inside the SBS cell l is related to ω_1 and R_1.

For odd values of n, Hermite-Gaussian functions A_n have odd parity i.e., $A_n(-x) = -A_n(x)$ so they play a less important role than the even modes. These functions are suitable for the modeling of the aberrated beams that are not cylindrically symmetric (e.g. when there is astigmatism). The disadvantage of choosing these functions as the basis is that we need one basis set for the x-direction and another one for the y-direction which, when combined to represent the three-dimensional model, produce complicated equations that are difficult to solve numerically. This necessitates a further approximation of circularly symmetric electric fields i.e., $a_{nm} = a_{mn}$ and $b_{nm} = b_{mn}$ to reduce the numerical effort (see [27, 28]). In the case of Laguerre-Gaussian functions there is no parity consideration and the functions are cylindrically symmetric with the fields completely determined by their values at any transverse position $r = |\mathbf{r}_\perp|$ and along the direction of propagation z. The mathematical development of equations for both Laguerre-Gaussian and the Hermite-Gaussian bases is similar. We have used our numerical approach for both the Laguerre-Gaussian basis and the Hermite-Gaussian basis with radial symmetry. Here we present just one approach using Laguerre-Gaussian functions. Utilizing the expressions for the basis A_n, Eq. (5.17), the two integrals in Eqs. (5.13) and (5.14) can be evaluated as

$$\begin{aligned} g_{knij} &= \int_{-\infty}^{+\infty} A_i^* A_k B_j B_n^* d^2 r = \frac{e^{i(k+n-i-j)\psi(z)}}{\omega(z)^2} \varepsilon_{knij}, \\ g_{knij}^* &= \int_{-\infty}^{+\infty} A_i B_k B_j^* A_n^* d^2 r = \frac{e^{-i(k+n-i-j)\psi(z)}}{\omega(z)^2} \varepsilon_{knij}, \end{aligned} \tag{5.21}$$

where ε_{knij} is a symmetrical real tensor given by the overlap integral:

$$\varepsilon_{knij} = (\frac{2}{\pi}) \int_0^{+\infty} dx e^{-2x} L_k(x) L_n(x) L_i(x) L_j(x). \tag{5.22}$$

The gain tensor g_{knij} depends on the phase mismatch factor $e^{i(k+n-i-j)\psi(z)}$ and the mode coupling constant ε_{knij}. It will be shown that the overall gain of any mode is entirely determined by these two factors. Some values of ε_{knij} are shown in the table 5.1, while the recurrence relations for ε_{knij} are given in App. C. The definition of the gain tensor g_{knij}, Eq. (5.21), can be used in Eqs. (5.13) and (5.14) to write

$$(\frac{n}{c}\frac{\partial}{\partial t} + \frac{\partial}{\partial z}) b_n = G \sum_{i,j,k} C_{ij}^* a_k g_{knij}(z), \tag{5.23}$$

$$(\frac{n}{c}\frac{\partial}{\partial t} - \frac{\partial}{\partial z}) a_n = -G \sum_{i,j,k} C_{ij} b_k g_{knij}^*(z), \tag{5.24}$$

where $G = g_1 g_2$. We have developed a numerical algorithm to solve these equations. We change the continuous field amplitudes $b_n(z,t)$ and $a_n(z,t)$ to discrete amplitudes $(b_n)_\beta^{\alpha+1}$ and $(a_n)_\beta^{\alpha+1}$. Here, $n, i, j, k = 0, 1, 2, ..., p$ are the spatial mode indices in the transverse direction, $\alpha = 0, 1, 2, ..., M$ are time indices ($t = \alpha\Delta t$) and $\beta = 0, 1, 2, ..., N+1$ are space indices in the propagation direction ($z = \beta\Delta z$ and $L = N\Delta z$). Referring to Fig. 5.1, it is clear that $(b_n)_1^{\alpha+1}$ and $(a_n)_{N+1}^{\alpha+1}$ (i.e., complex amplitudes of the Stokes field at $z = \Delta z$ and the pump field at $z = \Delta z + L$) are the boundary values for the Stokes and pump fields. Both SBS generators and amplifiers can be considered in our model. In amplifiers the SBS process starts from an injected Stokes signal. For SBS generators, however, there is no external seeding and the process starts from noise. Thus, the boundary value of the Stokes field is always zero i.e.,

$$(b_n)_1^{\alpha+1} = 0 \quad \text{for all } \alpha \text{ and all modes } n.$$

$(a_n)_{N+1}^{\alpha+1\prime}s$ are the pump input fields at the time slot $(\alpha+1)\Delta t$. Any temporal function can be considered as an input. In addition, by considering a linear combination of the functions $(a_n)_{N+1}^{\alpha+1}$ one can introduce any spatial aberration to the input pulse. Similarly,

$$\begin{aligned}(b_n)_\beta^0 &= 0 \text{ for all } \beta \\ (a_n)_\beta^0 &= 0 \text{ for all } \beta \text{ except } \beta = N+1\end{aligned}$$

are the initial values of the Stokes and pump fields. Using Simpson's rule

$$\int_{x_1}^{x_2} f(x)dx = \frac{1}{2}\Delta x[f(x_1) + f(x_2)],$$

and the discrete field's amplitudes $(b_n)_1^{\alpha+1}$ and $(a_n)_{N+1}^{\alpha+1}$, we can evaluate C_{ij} in Eq. (5.10) as

$$(C_{ij})_\beta^{\alpha+1} = \frac{\Delta t}{2}[(a_i)_\beta^{\alpha+1}(b_j^*)_\beta^{\alpha+1} + (f_{ij})_\beta^{\alpha+1} + (P_{ij})_\beta^\alpha], \tag{5.25}$$

where

$$\begin{aligned}(P_{ij})_\beta^\alpha &= e^{-\Gamma\Delta t}\{(P_{ij})_\beta^{\alpha-1} + 2[(a_i)_\beta^\alpha(b_j^*)_\beta^\alpha + (f_{ij})_\beta^\alpha]\}, \\ & \quad \text{and} \\ (P_{ij})_\beta^0 &= e^{-\Gamma\Delta t}[(a_i)_\beta^0(b_j^*)_\beta^0 + (f_{ij})_\beta^0].\end{aligned}$$

This expression for C_{ij} can then be substituted in Eq. (5.23) and (5.24) to find the following algebraic equations for the discrete field amplitudes

$$\begin{aligned}(b_n)^{\alpha+1}_{\beta+1} - (b_n)^{\alpha+1}_{\beta} + \frac{\Delta z}{c\Delta t}[(b_n)^{\alpha+1}_{\beta} - (b_n)^{\alpha}_{\beta}] = \\ G\frac{\Delta z\Delta t}{2}\sum_{i,j,k}(a_k)^{\alpha+1}_{\beta}[(a^*_i)^{\alpha+1}_{\beta}(b_j)^{\alpha+1}_{\beta} + (f_{ij})^{\alpha+1}_{\beta} + (p^*_{ij})^{\alpha}_{\beta}]g_{knij},\end{aligned} \tag{5.26}$$

and

$$\begin{aligned}(a_n)^{\alpha+1}_{\beta+1} - (a_n)^{\alpha+1}_{\beta} - \frac{\Delta z}{c\Delta t}[(a_n)^{\alpha+1}_{\beta} - (a_n)^{\alpha}_{\beta}] = \\ G\frac{\Delta z\Delta t}{2}\sum_{i,j,k}(b_k)^{\alpha+1}_{\beta}[(a_i)^{\alpha+1}_{\beta}(b^*_j)^{\alpha+1}_{\beta} + (f_{ij})^{\alpha+1}_{\beta} + (p_{ij})^{\alpha}_{\beta}]g^*_{knij}.\end{aligned} \tag{5.27}$$

Next, we introduce the Stokes and pump vectors in the transverse modes subspace as

$$\vec{b}^{\alpha+1}_{\beta} = \begin{pmatrix} b_1 \\ b_2 \\ \vdots \\ b_p \end{pmatrix}; \vec{a}^{\alpha+1}_{\beta} = \begin{pmatrix} a_1 \\ a_2 \\ \vdots \\ a_p \end{pmatrix}, \tag{5.28}$$

to convert Eqs. (5.26) and (5.27) to a matrix form:

$$I\vec{b}^{\alpha+1}_{\beta+1} + [(-1 + \frac{\Delta z}{c\Delta t})I - F^{\alpha}_{\beta}]\vec{b}^{\alpha+1}_{\beta} - G^{\alpha}_{\beta}\vec{a}^{\alpha+1}_{\beta} = \frac{\Delta z}{c\Delta t}\vec{b}^{\alpha}_{\beta}, \tag{5.29}$$

$$I\vec{a}^{\alpha+1}_{\beta+1} + [(-1 - \frac{\Delta z}{c\Delta t})I - E^{\alpha}_{\beta}]\vec{a}^{\alpha+1}_{\beta} - D^{\alpha}_{\beta}\vec{b}^{\alpha+1}_{\beta} = \frac{-\Delta z}{c\Delta t}\vec{a}^{\alpha}_{\beta}. \tag{5.30}$$

Here, I is the unit matrix and the elements of the four matrices F^{α}_{β}, G^{α}_{β}, E^{α}_{β} and

D^{α}_{β} (elements in the transverse modes subspace) are

$$\begin{aligned}
(F^{\alpha}_{\beta})_{ij} &= \frac{G\Delta z\Delta t}{2}\sum_{lk}(a_k)^{\alpha}_{\beta}(a^*_l)^{\alpha}_{\beta}g_{kilj}, && (5.31)\\
(G^{\alpha}_{\beta})_{ij} &= \frac{G\Delta z\Delta t}{2}\sum_{lk}[(f_{lk})^{\alpha}_{\beta}+(P^*_{lk})^{\alpha}_{\beta}]g_{jilk}, && (5.32)\\
(E^{\alpha}_{\beta})_{ij} &= \frac{G\Delta z\Delta t}{2}\sum_{lk}(b_k)^{\alpha}_{\beta}(b^*_l)^{\alpha}_{\beta}g^*_{kijl}, && (5.33)\\
(D^{\alpha}_{\beta})_{ij} &= \frac{G\Delta z\Delta t}{2}\sum_{lk}[(f_{lk})^{\alpha}_{\beta}+(P_{lk})^{\alpha}_{\beta}]g^*_{jilk}. && (5.34)
\end{aligned}$$

By representing the Stokes and pump field as a "block-vector" (see below and App. B) fields $(\overset{\rightrightarrows}{b})^{\alpha+1}$ and $(\overset{\rightrightarrows}{a})^{\alpha+1}$ at the time $(\alpha+1)\Delta t$ as

$$(\overset{\rightrightarrows}{b})^{\alpha+1} = \begin{pmatrix} \overrightarrow{b_2} \\ \overrightarrow{b_3} \\ \cdot \\ \cdot \\ \cdot \\ \overrightarrow{b_{N+1}} \end{pmatrix}^{\alpha+1} ; (\overset{\rightrightarrows}{a})^{\alpha+1} = \begin{pmatrix} \overrightarrow{a_1} \\ \overrightarrow{a_2} \\ \cdot \\ \cdot \\ \cdot \\ \overrightarrow{a_N} \end{pmatrix}^{\alpha+1}, \qquad (5.35)$$

we can compact the two Eqs. (5.29) and (5.30) into matrix equations:

$$\begin{aligned}
\mathbf{C}^{\alpha}(\overset{\rightrightarrows}{b})^{\alpha+1} - \mathbf{D}^{\alpha}(\overset{\rightrightarrows}{a})^{\alpha+1} &= (\overset{\rightrightarrows}{V})^{\alpha}, && (5.36)\\
\mathbf{H}^{\alpha}(\overset{\rightrightarrows}{a})^{\alpha+1} - \mathbf{K}^{\alpha}(\overset{\rightrightarrows}{b})^{\alpha+1} &= (\overset{\rightrightarrows}{U})^{\alpha}. && (5.37)
\end{aligned}$$

Block-vectors $(\overset{\rightrightarrows}{b})^{\alpha+1}$ and $(\overset{\rightrightarrows}{a})^{\alpha+1}$ are $N \times 1$ vectors, whose elements are vectors $\overrightarrow{b}_{\beta}$ and $\overrightarrow{a}_{\beta}$, representing the electric fields at the point $z = \beta\Delta z$. Each of the $\overrightarrow{b}_{\beta}$ and $\overrightarrow{a}_{\beta}$ are themselves $p \times 1$ vectors whose elements represent the different spatial modes of the electric fields. $\mathbf{C}^{\alpha}$, $\mathbf{D}^{\alpha}$, $\mathbf{H}^{\alpha}$ and $\mathbf{K}^{\alpha}$ are $N \times N$ upper or lower tridiagonal "block-matrices" evaluated at time $\alpha\Delta t$ with elements that are $p \times p$

matrices in transverse modes subspace. They are given as

$$C^\alpha = \begin{pmatrix} I & 0 & 0 & \cdots & 0 \\ M_2^\alpha & I & 0 & \ddots & 0 \\ \vdots & M_3^\alpha & \ddots & \ddots & \vdots \\ \vdots & \vdots & \ddots & \ddots & 0 \\ 0 & 0 & \cdots & M_N^\alpha & I \end{pmatrix}, D^\alpha = \begin{pmatrix} G_1^\alpha & 0 & 0 & \cdots & 0 \\ 0 & G_2^\alpha & 0 & \ddots & 0 \\ \vdots & 0 & \ddots & \ddots & \vdots \\ \vdots & \vdots & \ddots & \ddots & 0 \\ 0 & 0 & \cdots & 0 & G_N^\alpha \end{pmatrix}, \tag{5.38}$$

$$H^\alpha = \begin{pmatrix} N_1^\alpha & I & 0 & \cdots & 0 \\ 0 & N_2^\alpha & I & \ddots & 0 \\ \vdots & 0 & \ddots & \ddots & \vdots \\ \vdots & \vdots & \ddots & \ddots & I \\ 0 & 0 & \cdots & 0 & N_N^\alpha \end{pmatrix}, K^\alpha = \begin{pmatrix} 0 & 0 & 0 & \cdots & 0 \\ D_2^\alpha & 0 & 0 & \ddots & 0 \\ \vdots & D_3^\alpha & \ddots & \ddots & \vdots \\ \vdots & \vdots & \ddots & \ddots & 0 \\ 0 & 0 & \cdots & D_N^\alpha & 0 \end{pmatrix} \tag{5.39}$$

where

$$\begin{aligned} M_\beta^\alpha &= (-1 + \frac{\Delta z}{c\Delta t})I - F_\beta^\alpha, \\ N_\beta^\alpha &= (-1 - \frac{\Delta z}{c\Delta t})I - E_\beta^\alpha, \end{aligned}$$

and G_β^α and D_β^α are given in Eqs. (5.32) and (5.34).

The known block-vectors $(\overrightarrow{\overrightarrow{V}})^\alpha$ and $(\overrightarrow{\overrightarrow{U}})^\alpha$ can be evaluated, using the boundary conditions and the values of the fields at the time slot $\alpha\Delta t$, as

$$(\overrightarrow{\overrightarrow{V}})^\alpha = \begin{pmatrix} -M_1^\alpha \overrightarrow{b}_1^{\alpha+1} + \frac{\Delta z}{c\Delta t} \overrightarrow{b}_1^\alpha \\ \frac{\Delta z}{c\Delta t} \overrightarrow{b}_2^\alpha \\ \vdots \\ \frac{\Delta z}{c\Delta t} \overrightarrow{b}_N^\alpha \end{pmatrix}, \tag{5.40}$$

$$(\overrightarrow{\overrightarrow{U}})^\alpha = \begin{pmatrix} D_1^\alpha \overrightarrow{b}_1^{\alpha+1} - \frac{\Delta z}{c\Delta t} \overrightarrow{a}_1^\alpha \\ -\frac{\Delta z}{c\Delta t} \overrightarrow{a}_2^\alpha \\ \vdots \\ -\overrightarrow{a}_{N+1}^{\alpha+1} - \frac{\Delta z}{c\Delta t} \overrightarrow{a}_N^\alpha \end{pmatrix}. \tag{5.41}$$

From Eq. (5.36), block-vector $(\overset{\rightrightarrows}{a})^{\alpha+1}$ can be determined:

$$(\overset{\rightrightarrows}{a})^{\alpha+1} = (\mathbf{D}^{\alpha})^{-1}\mathbf{C}^{\alpha}(\overset{\rightrightarrows}{b})^{\alpha+1} - (\mathbf{D}^{\alpha})^{-1}(\overset{\rightrightarrows}{V})^{\alpha}, \tag{5.42}$$

this can be in turn substituted in Eq. (5.37) to find

$$(\overset{\rightrightarrows}{b})^{\alpha+1} = [\mathbf{H}\mathbf{D}^{-1}\mathbf{C} - \mathbf{K}]^{-1}\mathbf{H}\mathbf{D}^{-1}(\overset{\rightrightarrows}{V})^{\alpha} + [\mathbf{H}\mathbf{D}^{-1}\mathbf{C} - \mathbf{K}]^{-1}(\overset{\rightrightarrows}{U})^{\alpha}. \tag{5.43}$$

Using the method describing in the App. B, we can solve Eqs. (5.42) and (5.43) for the field amplitudes $(\overset{\rightrightarrows}{b})$ and $(\overset{\rightrightarrows}{a})$ at any time slot $\alpha + 1$ using the values at time slot α. We used an Alpha Digital Workstation 500 Au, with a 500 MHz processor and 256 Mb RAM to solve the SBS equations numerically.

5.4 Results and Discussion

The geometry of the process is shown in Fig. 5.1. An input laser beam is focused from right into a SBS cell whose refractive index is n_2. The refraction of light at the boundaries air to the entrance window (thickness t and refractive index n_1) and optical propagation through the entrance window to the SBS material has been considered. In App. D, we have calculated the position and waist of the laser beam inside the SBS cell. As for the one-dimensional model discussed in Chap. 4, we use a temporally Gaussian pump pulse of the form $E_0 \exp\{-2[(t-t_0)/t_p]^2\}$, where t_p is the pulse width. Unless otherwise stated, the other parameters are as follows: cell length 60 cm, focal length 50 cm, immersion length 40 cm, input energy 140 mJ, phonon lifetime 0.85 ns, gain of the medium 0.006 cm/MW, FWHM pulse length 20 ns, and an arbitrary chosen index of refraction, n_2=1.0. The above parameters were chosen arbitrarily for the numerical study only. There is a free parameter in our computer code that determines the strength of the initial random noise. Experimental results are necessary to set the value of this parameter. The results in this chapter show the general behaviour of SBS for an arbitrary value of the free parameter resulting in arbitrary units for the Stokes and pump powers. However, in Sec. 5.5 we use

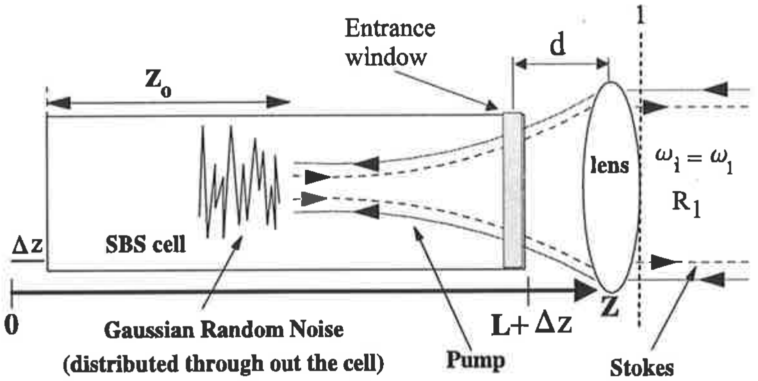
Entrance window
d
1
Z_0
lens
$\omega_1 = \omega_1$
R_1
Δz
SBS cell
0
Gaussian Random Noise
(distributed through out the cell)
Pump
L+Δz
Z
Stokes

Figure 5.1: The geometry used for the SBS process. Input beam parameters are shown at input plane 1.

experimental parameters to set the free parameter of our computer code and make accurate comparisons between the numerical and experimental results.

5.4.1 Single-mode input beams

Before discussing the results of the 3D model in the transient regime, we develop a simple argument to show how phase conjugation using SBS works in the steady state regime. In the steady state regime of SBS [i.e., ignoring all $(\partial/\partial t)$], Eqs. (5.8) and (5.9) can be simplified to find C_{ij} (ignoring f_{ij}):

$$C_{ij} = \frac{1}{\Gamma} a_i b_j^*.$$

This value of C_{ij} then can be substituted in the Eq. (5.23) to yield

$$\left(\frac{\partial}{\partial z}\right) b_n = \frac{G}{\Gamma} \sum_{i,j,k} a_i^* b_j a_k g_{knij}(z). \tag{5.44}$$

We assume a single mode input pump pulse (m) to be the only dominant pump mode inside the cell. Thus, with the help of Eq. (5.21), the sum in Eq. (5.44) can be written as

$$\left(\frac{\partial}{\partial z}\right) b_n = \frac{G\left|a_m\right|^2}{\Gamma \omega^2(z)} \sum_j \varepsilon_{mmnj} e^{i(n-j)\psi(z)} b_j. \tag{5.45}$$

Rewriting this equation for the phase conjugated mode b_m and the two adjacent modes $b_{m\pm1}$ yields

$$\left(\frac{\partial}{\partial z}\right) b_m = \frac{G\left|a_m\right|^2}{\Gamma\omega^2(z)}(\varepsilon_{mmmm}b_m + \varepsilon_{mmmm+1}e^{-i\psi(z)}b_{m+1} + \varepsilon_{mmmm-1}e^{i\psi(z)}b_{m-1} + ...), \tag{5.46a}$$

$$\left(\frac{\partial}{\partial z}\right) b_{m+1} = \frac{G\left|a_m\right|^2}{\Gamma\omega^2(z)}(\varepsilon_{mmm+1m+1}b_{m+1} + \varepsilon_{mmmm+1}e^{i\psi(z)}b_m + ...), \tag{5.46b}$$

$$\left(\frac{\partial}{\partial z}\right) b_{m-1} = \frac{G\left|a_m\right|^2}{\Gamma\omega^2(z)}(\varepsilon_{mmm-1m-1}b_{m-1} + \varepsilon_{mmmm-1}e^{-i\psi(z)}b_m + ...). \tag{5.46c}$$

The first terms on the right hand side of these equations are phase-matched terms and the second and third terms are non-phase-matched terms. In our model we have solved Eqs. (5.23) and (5.24) for the conjugated and non-conjugated modes simultaneously, including the phase-matched and non-phase-matched terms.

Above the threshold, it is assumed that $b_n \ll b_m$ for $n \neq m$. This assumption is valid if the phase conjugated mode has suppressed the other modes in competition for gain through the threshold. In reality, there are conditions for which the phase conjugated mode is not the dominant mode after the threshold has been reached. To study these conditions we require the time dependent equations and this will be discussed later in this chapter. Ignoring $b_{m\pm1}$ and all the other higher order modes on the right hand side of Eq. (5.46a), results in

$$\left(\frac{\partial}{\partial z}\right) b_m = \frac{G\left|a_m\right|^2}{\Gamma\omega^2(z)}\varepsilon_{mmmm}b_m. \tag{5.47}$$

This indicates that in this model the gain of the phase conjugated mode in the steady state regime is determined mainly by the phase matched coupling constant ε_{mmmm}. The numerical value of ε_{mmmm} is smaller for higher order modes (see table 5.1) resulting in lower reflectivity for these modes as will be shown in Fig. 5.17 (a). This is expected since the far field diffraction pattern of higher order modes will have finer spatial details, that are less likely to correlate with other modes, hence reducing the overlap integral in Eq. (5.22). Ignoring $b_{m\pm1}$ and all the other

Table 5.1: Numerical values of ε_{knij}.

k	i	j	n	ε_{knij}
0	0	0	0	0.3183
0	0	0	1	0.1592
0	0	1	1	0.1592
0	1	1	1	0.0796
1	1	1	1	0.1592
1	1	1	2	0.0796
1	1	2	2	0.0995
1	2	2	2	0.0547
2	2	2	2	0.1094
2	2	2	3	0.0547
2	2	3	3	0.0746
3	3	3	3	0.0846

non-conjugated modes on the right hand side of Eq. 5.46b yields

$$\frac{\partial}{\partial z}b_{m+1} = \frac{G\left|a_m\right|^2}{\Gamma\omega^2(z)}\varepsilon_{mmmm+1}e^{i\psi(z)}b_m,$$

which shows that the gain of non-conjugated modes is determined by non-phase matched terms. This equation can be combined with Eq. (5.47) to find

$$\frac{\partial}{\partial z}b_{m+1} = \frac{\varepsilon_{mmmm+1}}{\varepsilon_{mmmm}}e^{i\psi(z)}\frac{\partial}{\partial z}b_m. \tag{5.48}$$

Numerical calculations of ε_{mmmm} show that $\varepsilon_{mmmm+1} = \varepsilon_{mmmm-1} = \varepsilon_{mmmm}/2$ (see table 5.1) i.e., the gain of the phase conjugated mode is twice that of the nearest modes. This discrimination against non-conjugated modes, acts to suppress them in the competition for gain with the conjugated mode, resulting in a dominant phase conjugated pulse at the output in the steady state regime.

Fundamental mode

Next, we examine the SBS process of a single mode input by focusing into an SBS cell a perfect Gaussian beam, which is described totally by the fundamental mode of the Laguerre-Gaussian functions with the beam radius of $\omega_i = 0.5$ cm. The input pulse is Gaussian both in space and in time. The quality of phase conjugation by SBS is studied, using the following definition for the fidelity[37]

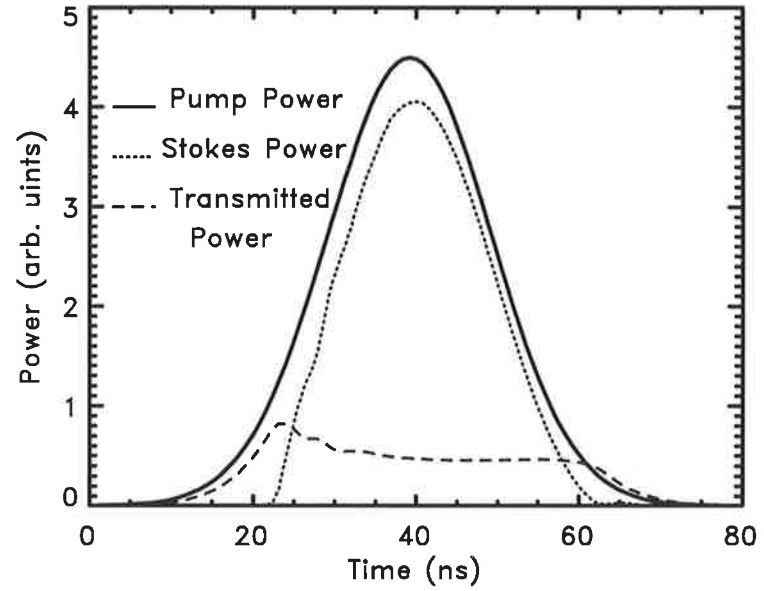

Figure 5.2: Typical results for the Stokes, pump and transmitted pulses obtained when a perfect Gaussian beam (fundamental mode of the Laguerre-Gaussian functions) is focused into a SBS cell with the standard set of parameters: cell length 60 cm, focal length 50 cm, immersion length 40 cm, input energy 140 mJ, phonon lifetime 0.85 ns and refractive index, n=1.0.

$$H(z,t) = \frac{\left|\int E_l(\mathbf{r}_\perp, z, t) E_s(\mathbf{r}_\perp, z, t) d^2r\right|^2}{\int \left|E_l(\mathbf{r}_\perp, z, t)\right|^2 d^2r \int \left|E_s(\mathbf{r}_\perp, z, t)\right|^2 d^2r}, \tag{5.49}$$

which can be simplified, using Eqs. (5.4) and (5.5), to

$$H(z,t) = \frac{\left|\sum_i b_i(z,t) a_i(z,t)\right|^2}{(\sum_i |a_i(z,t)|^2)(\sum_i |b_i(z,t)|^2)}. \tag{5.50}$$

Figure 5.2 shows the typical results for the Stokes, pump and transmitted pulses with an overall reflectivity of 78% and fidelity of 94%. The time-resolved reflectivity and fidelity at the entrance of the cell ($z = L + \Delta z$, Fig. 5.1) is shown in Fig. 5.3. In our previous model discussed in Chap. 4, we showed that there exist some fluctuations in the Stokes intensity and phase due to noise initiation of the SBS process. These temporal fluctuations in the Stokes pulse have been observed experimentally to cause degradation in the fidelity of the SBS process [10, 12, 19, 2], but our current 3-D model was required to study the behaviour of the spatial fidelity. The numerical

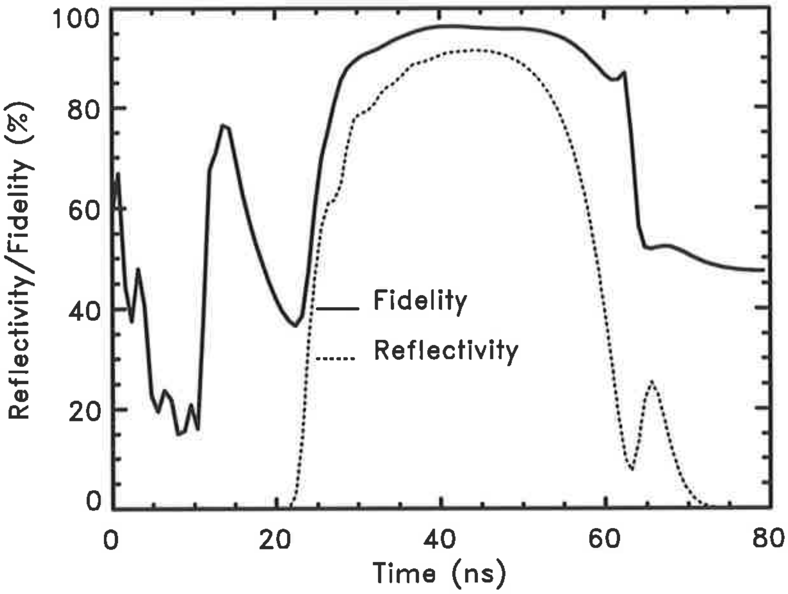

Figure 5.3: Time-resolved reflectivity and fidelity. Other parameters as in Fig. 5.2.

results indicate that intensity fluctuations do cause degradation in the time-resolved and overall fidelity as shown in Fig. 5.4.

The mode structure of the pump and Stokes fields can be examined by the 3-D model. Focusing the fundamental Laguerre-Gaussian mode, different modes of the Stokes field existing in the noise source term are initiated. The gains for each of these modes are different and given by Eq. (5.21). The distribution of the output energy in the different Stokes modes is shown in Fig. 5.5, which indicates that the main part of the reflected energy (93.3%) is in the conjugated mode (i.e., the fundamental mode). The energy in the other Stokes modes is decreasing as the mode number increases (mode I 4.2%, mode II 0.7%, mode III 0.6%, mode IV 0.3%, and so on). The initiation of the different modes of the Stokes field at the focal point and their propagation towards the entrance of the cell at the specific instant $t = 40$ ns are shown in Fig. 5.6. The model predicts that when the zero order mode of the Laguerre-Gaussian function is incident on the cell it initiates the other modes, not only in the Stokes field but also in the pump field. Although the input energy of all non-zero modes is zero, energy is coupled into the non-zero modes of the Stokes and pump fields, propagating in the backward and forward directions, respectively. Fig. 5.7 shows how the zero mode of the pump field decays from the entrance of

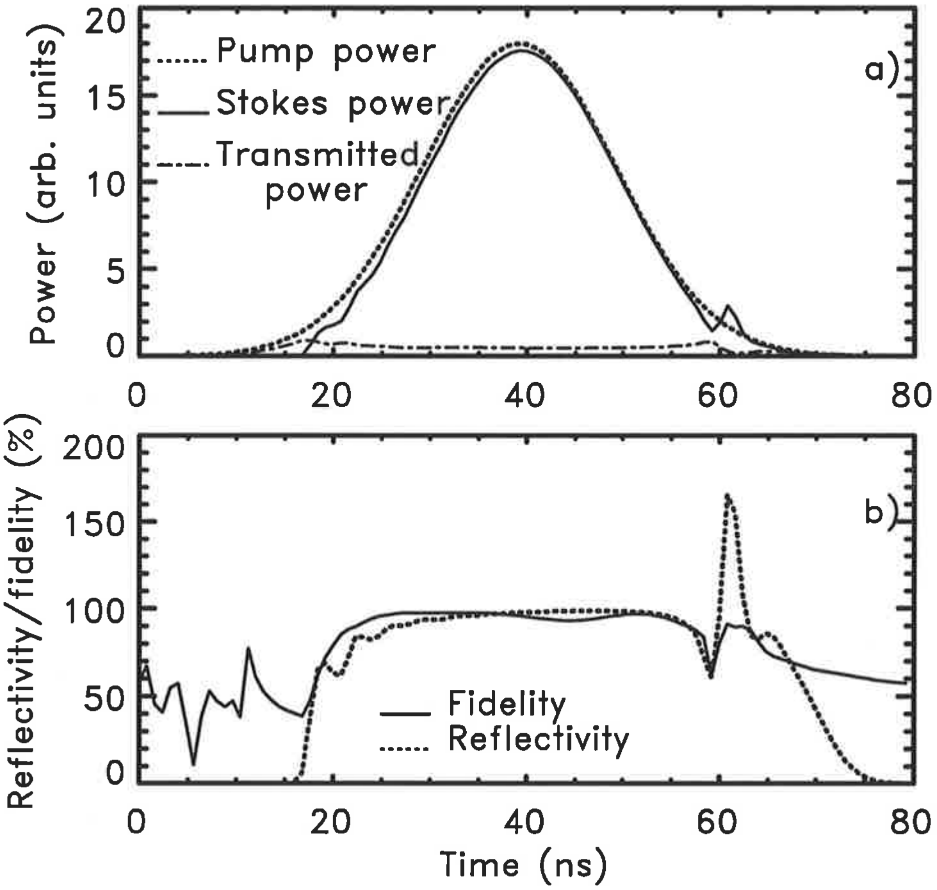

Figure 5.4: Time-resolved fidelity [solid line in graph (b)] shows a rapid reduction, simultaneous to the fluctuation in the Stokes pulse.

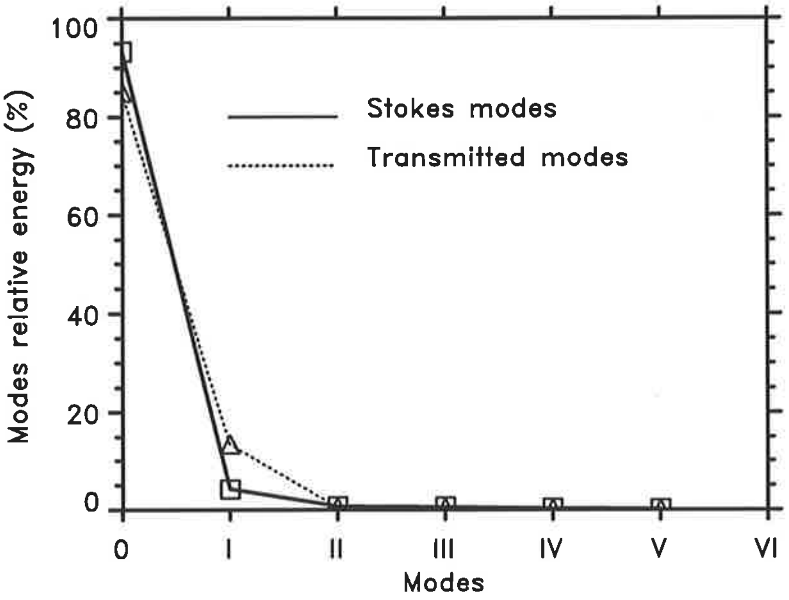

Figure 5.5: The relative distribution of the Stokes energy, into different modes, $E_i/E_{Tot}(\%)$. Other parameters are as in Fig. 5.2

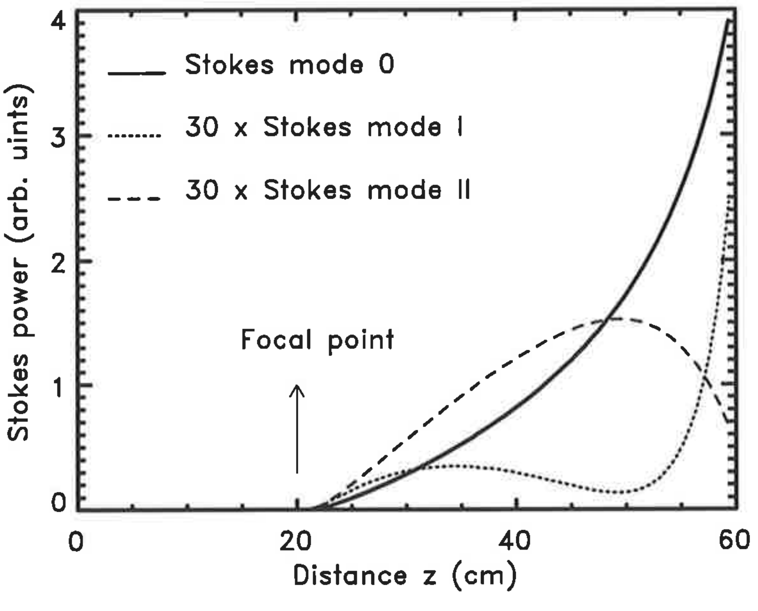

Figure 5.6: Different modes of the Stokes pulse are initiated at the focal plane ($z = 20$ cm) and propagated towards the entrance of the cell. The distribution of the fields inside the cell is shown at time $t = 40$ ns. The entrance of the cell is at z=60 cm. See Fig 5.1 for the focusing geometry and propagation directions. Other parameters as in Fig. 5.2

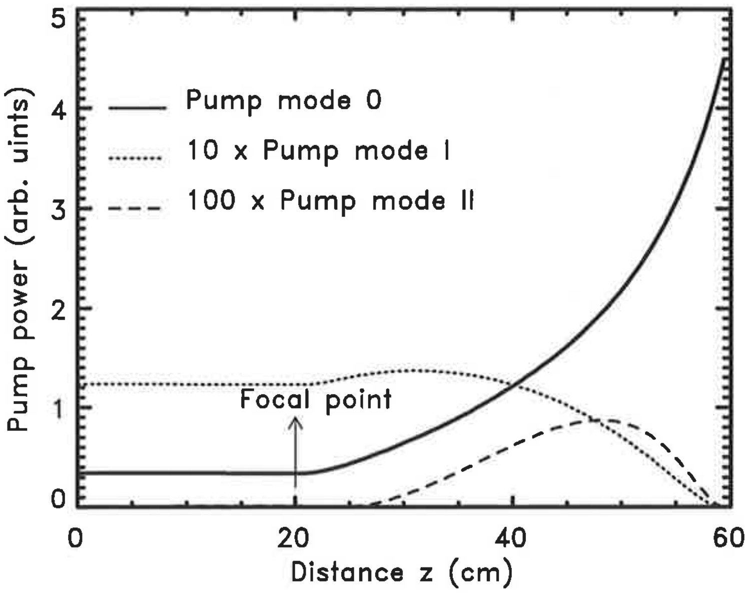

Figure 5.7: The fundamental mode of the pump beam is depleted as it propagates towards the end of the cell (z=0 cm). The other modes of the pump are initiating at the entrance (z=60 cm) and propagating to the end of the cell. Fields are shown inside the cell at the time $t = 40\ ns$. See Fig 5.1 for the focusing geometry and propagation directions. Other parameters as in Fig. 5.2.

the cell to the end of the cell while the first and second modes are arising at the front of the cell and are growing towards the end of the cell. As a result, part of the transmitted energy is carried by the non-zero modes (see Figs. 5.5 and 5.8). Another parameter that is related to the mode structure of the fields inside the cell is the beam spot size $W^2(z)$ which is important for the evolution of beam quality or fidelity. We follow the convention used by Siegman [102] and define the beam spot size at any plane along the direction of propagation z of the beam as

$$W^2(z) \equiv 4\sigma_r^2(z), \tag{5.51}$$

where $\sigma_r(z)$ is the effective radius of the beam or so called [102] the standard deviation of the time-averaged beam intensity in the r direction, at plane z, and is given by:

$$\sigma_r^2(z) = \frac{\int\int r^2 I(r,z) d^2r}{\int\int I(r,z) d^2r}. \tag{5.52}$$

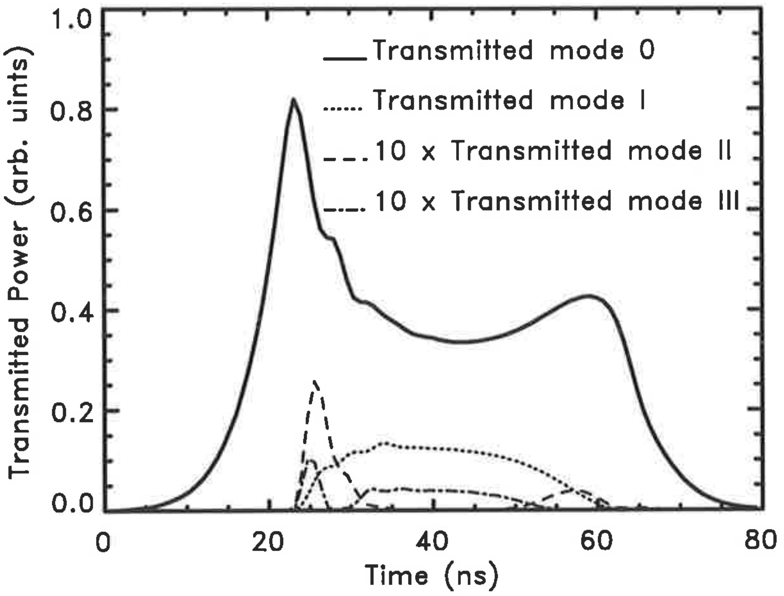

Figure 5.8: The transmitted power for different modes is shown as a function of time. Not only the fundamental mode but also all the other modes contribute in the transmitted power.

By using the explicit form of the basis functions $A_n(x)$, i.e., Eq. (5.17), and the recurrent relation for the Laguerre functions i.e.,

$$(n+1)L_{n+1}(x) = (2n+1-x)L_n(x) - nL_{n-1}(x),$$

one can evaluate the integral $\int\int r^2 I(r,z)d^2r$ for the pump and the Stokes beam respectively as

$$\begin{aligned}\int\int r^2 I_l(r,z)d^2r &= \sum_{n,m} a_n a_m^* \int r^2 A_n(r,z)A_m^*(r,z)d^2r \\ &= \sum_{n,m} a_n a_m^* e^{i(n-m)\psi(z)} \int_0^\infty xL_n(x)L_m(x)e^{-x}dx \\ &= \sum_n \frac{\omega^2(2n+1)}{2}|a_n|^2 - \sum_n \frac{\omega^2(n+1)}{2}[a_n a_{n+1}^* e^{-i\psi(z)} + C.C.], \\ \int\int r^2 I_s(r,z)d^2r &= \sum_n \frac{\omega^2(2n+1)}{2}|b_n|^2 - \sum_n \frac{\omega^2(n+1)}{2}[b_n^* b_{n+1} e^{-i\psi(z)} + C.C.],\end{aligned}$$

where a_n and b_n are the pump and the Stokes field coefficients as in Eqs. (5.4) and (5.5) and $C.C.$ is the complex conjugate. The mode structure of the fields appears in

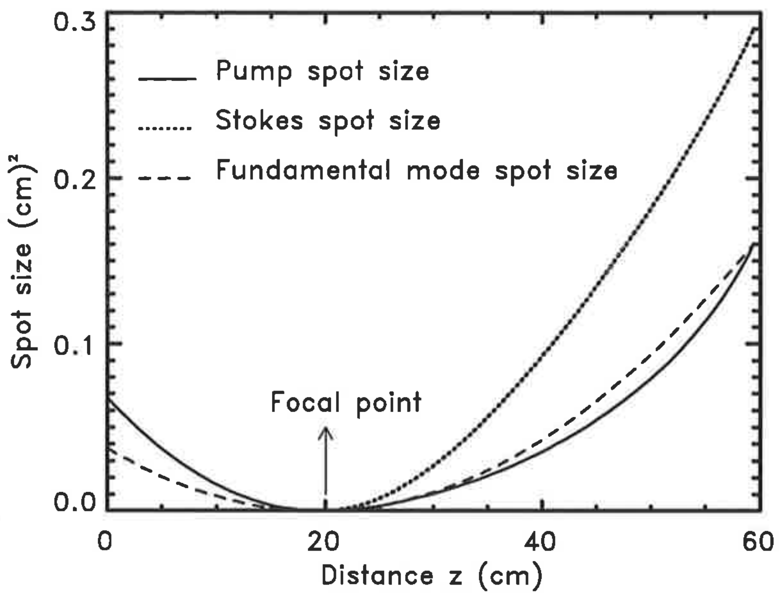

Figure 5.9: The spot sizes of the Stokes and pump beams are compared with the spot size of the fundamental mode as functions of z. The entrance of the cell is at z=60 cm. See Fig 5.1 for the focusing geometry and propagation directions.

the expression for $\sigma_r^2(z)$ which affects the spot size of the fields. Fig. (5.9), shows the spot size of the Stokes, pump [calculated according to Eq. (5.51)] and fundamental mode [calculated according to Eq. (5.18)], as a function of z . At the entrance to the cell, at $z = 60$ cm, the pump and the fundamental mode have the same spot size indicating that the input pulse is purely in the fundamental mode but inside the cell they are different, which is due to the mode structure of the pump field.

Effect of Energy Using the fundamental mode of the Laguerre-Gaussian function as an input and the set of geometrical and material parameters given above, we find that the fidelity of SBS increases as a function of energy and saturates at some level (see Fig. 5.10). This result, although seemingly simple, has been a matter of great debate over the past 15 years. There was much discussion about the behaviour of the phase conjugation fidelity at high energy between two groups of researchers, one believing that the fidelity at high energy decreases (theoretical work by [103, 30] and experimental work by[104, 105]) while the other one claiming that the fidelity increases (theoretical investigation by [106, 37] and experimental investigation by [12, 107, 108]). This was resolved by observing that the lack of high fidelity at high energy was related to the shape of the input pulse and transient effects. It had been reported earlier that poor phase conjugation fidelity could be obtained for input pulses whose duration was significantly shorter than the phonon lifetime of the SBS material[109, 103]. But later, Dane *et al.* [15] showed that even for long pulses, the time scale of the leading edge of the input pulse compared to the phonon lifetime, plays a key role in determining the fidelity of SBS at high energy. For input pulses with a fast rise time, materials with phonon lifetimes long compared to the time scale of the leading edge of the pulse show large fluctuations and poor fidelity at high energy, while materials with phonon lifetimes comparable to or shorter than the time scale of the leading edge show small fluctuations and high fidelity. To examine the predicted effect of pulse shape on the fidelity of SBS at high energy, we calculated the case of two input pulses focused into the SBS cell, one with a rapid rise time of 0.8 ns and one with a slow smooth rise time as shown in Fig. 5.11. For both input pulses, the simulation model was run for a range of energy extending from below, to well above the threshold energy and for two different phonon lifetimes, $\tau = 2.0$ ns and $\tau = 16.0$ ns. For each input pulse and parameter set, the code was run for 100 different noise source terms and the mean value and standard deviation of fidelity was calculated. For the fast rise time input, the mean value of the fidelity is reduced at high energy for both phonon lifetimes, Fig. 5.11(a) and 5.11(c), although in the case of $\tau = 16.0$ ns the reduction is more obvious. Also for a smooth input pulse, Fig. 5.11(b) and (d) indicate that fidelity, like reflectivity, increases and saturates.

We found that the mode structure of the Stokes and pump fields behave quite differently as a function of energy inside the cell. Near the threshold the reflected Stokes energy is widely distributed among the different modes as shown in Fig. 5.12. As the input energy increases, the energy content of the non-zero modes decreases and most of the energy is concentrated in the conjugated mode. At low input energy, when the pump mode just passes through the cell without an appreciable depletion, just mode 0 exists in the pump field and contains all of the energy. At the higher energy, however, the mode structure of the pump field becomes richer, with higher modes also contributing to the transfer of energy. Figure 5.13 shows how the energy content of the transmitted pump modes vary as the input energy increases.

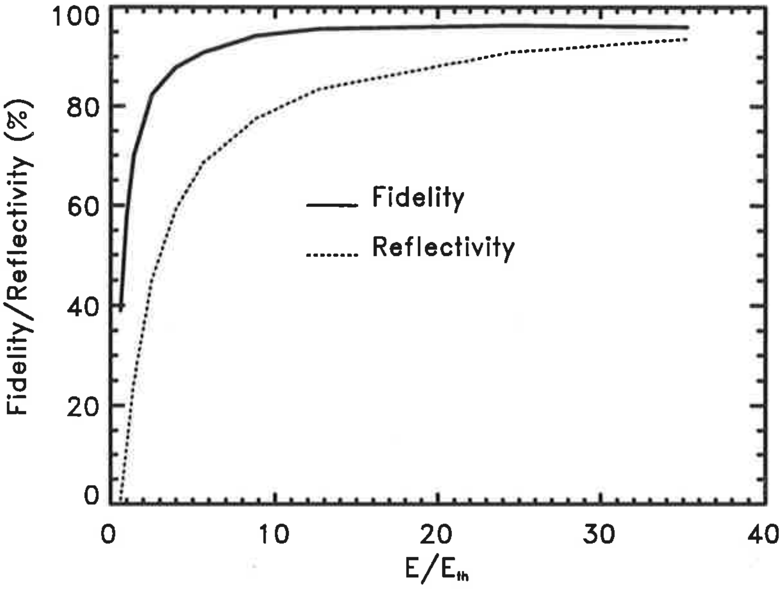

Figure 5.10: Reflectivity and Fidelity saturate at high energy. Energy is varied from below to 30 times above threshold energy ($E_{th} \approx 16\ mJ$) while the other parameters are as in Fig. 5.2.

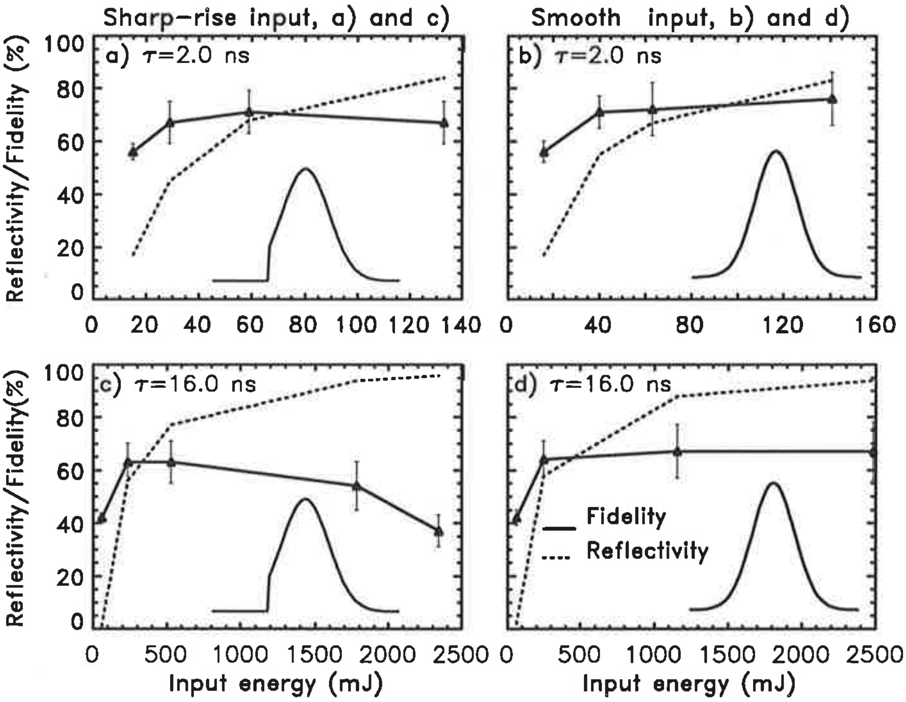

Figure 5.11: Reflectivity and fidelity are shown for sharp rise [(a) phonon lifetime $\tau = 2.0\ ns$ and (c) phonon lifetime $= 16.0\ ns$] and smooth input [(b) phonon lifetime $\tau = 2.0\ ns$ and (d) phonon lifetime $\tau = 16.0\ ns$]. Input pulses are shown in the bottom of each graph.

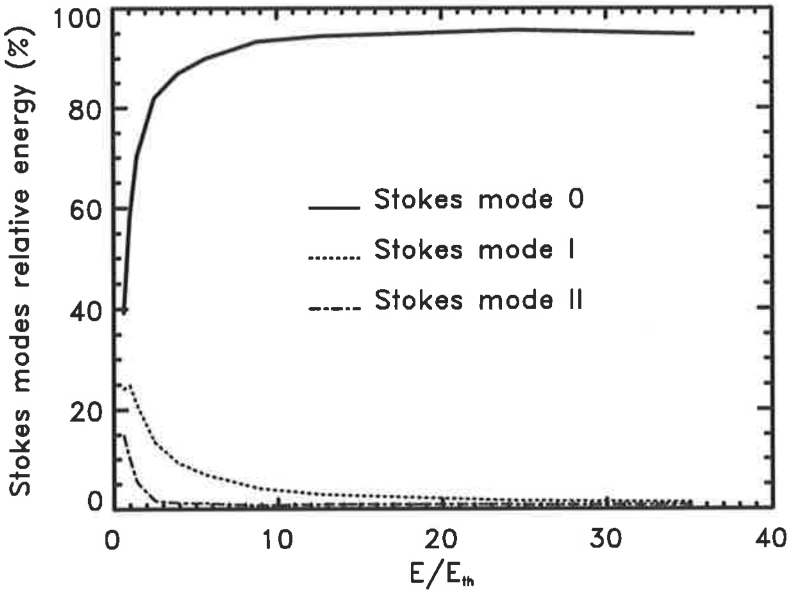

Figure 5.12: The relative distribution of the Stokes energy among the different modes E_i/E_{Tot} (%) varies as the input energy increases. Near threshold (reflectivity about 11% and fidelity about 58%) the Stokes energy is distributed as 58% in mode 0, 25% in mode I, 10% in mode II etc. At high input energy $E_i/E_{Tot} = 30$, the reflected Stokes energy is concentrated mainly in the fundamental mode resulting in a higher fidelity. The energy range and other parameters are as in Fig. 5.10.

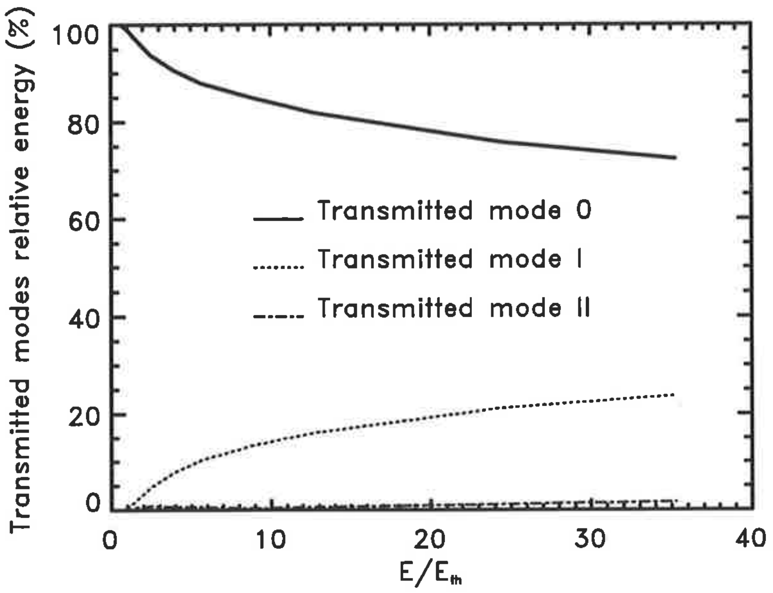

Figure 5.13: The relative distribution of the transmitted energy among the different modes E_i/E_{Tot} (%) as a function of input energy.

As a result of the variation in the mode structure of the Stokes and pump fields (for different energies), the spot size of the Stokes and pump beams changes as a function of energy. At low energies, when the pump field inside the cell can be described entirely by the fundamental mode, its spot size [according to Eq. (5.52)] is very close to that of the fundamental mode whereas the Stokes pulse has a rich mode structure with a spot size far from that of the fundamental mode as shown in Fig. 5.14(a). At high energies, when the fidelity is high, additional modes of the pump field contribute to the transfer of energy, resulting in a deviation of the pump spot size from that of the fundamental mode, whereas the Stokes beam energy is mainly concentrated in the fundamental mode resulting in a smaller spot size, Fig. 5.14(b). The behaviour of the output Stokes beam spot size as a function of energy is shown in Fig. 5.15. Close examination of the Stokes and pump spot sizes near the focal plane ($z \simeq 20\ cm$), Fig. 5.16, reveals that the Stokes beam has a smaller spot size than that of pump beam, which causes the Stokes beam to be diffracted more than the pump beam in propagating toward the entrance to the cell. This is expected, since the pump intensity drops off (in the transverse direction) towards its wings and there are points where the pump intensity is not enough to initiate the SBS process. As the input energy increases, the initial Stokes spot size increases and approaches to that of the pump beam. This in turn results in a smaller Stokes spot size at the entrance to the cell, as shown in Fig. 5.15.

Non-fundamental modes

The 3D model can be used to investigate phase conjugation of spatially aberrated, cylindrically symmetric input beams, by describing them as a sum of higher order spatial modes. Initially, we chose Laguerre-Gaussian modes, and calculated the SBS reflectivity and fidelity for each mode separately as shown in Fig. 5.17. Consistent with expectations, the model predicts lower reflectivity for higher order modes, because higher order modes have a smaller gain due to a smaller coupling constant ε_{mmmm} (Sec. 5.4.1). We also found that the fidelity decreases for higher modes even in regimes of saturated reflectivity, Fig. 5.17(b). Further, we calculated the fidelity for different intensities in the focal plane. This was done by varying the

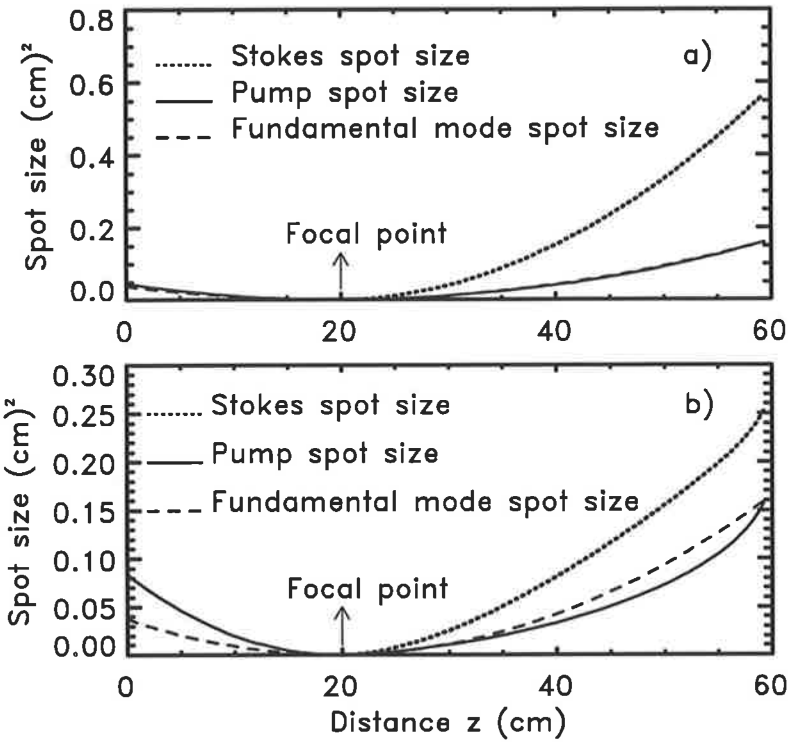

Figure 5.14: The behaviour of the Stokes and pump spot size at low (a), 23mJ, and high energy (b), 392mJ, are shown. The entrance of the cell is at z=60 cm. See Fig 5.1 for the focusing geometry and propagation directions.

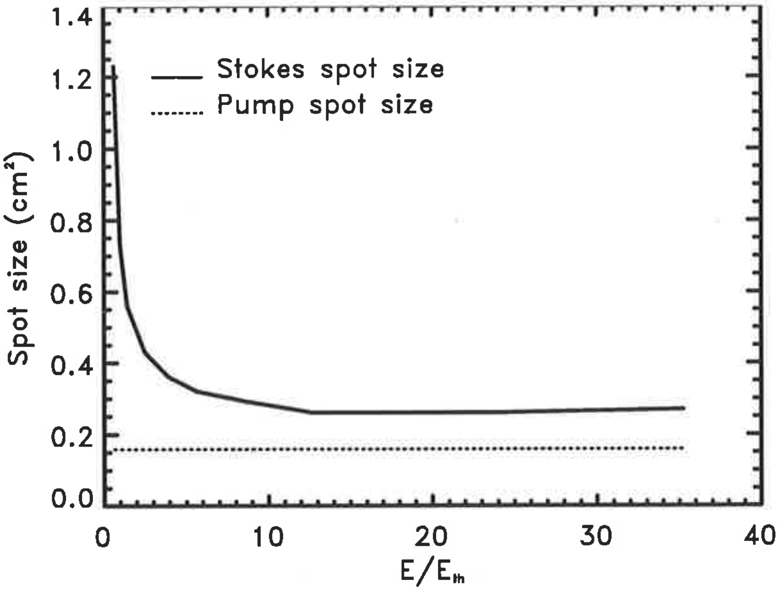

Figure 5.15: The near field Stokes spot size approaches that of the pump at high energy.

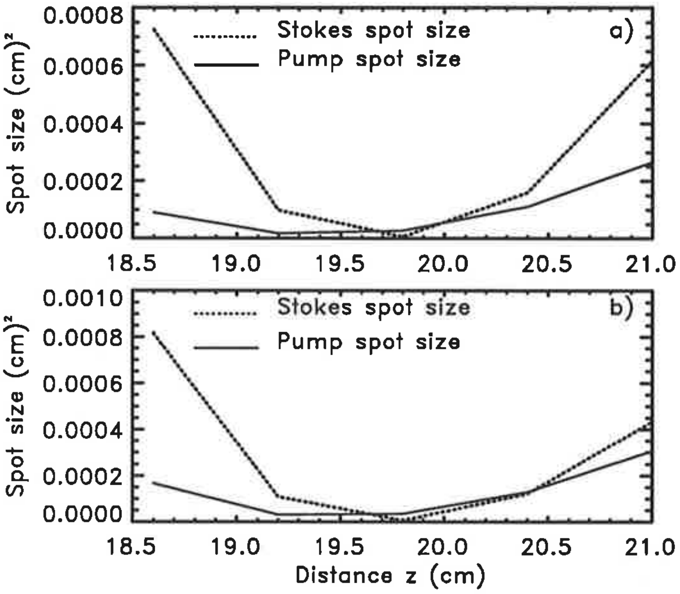

Figure 5.16: The spot size of the pump and Stokes beams at the focal plane $z \simeq 20$ *cm* and at low (a) 23mJ, and high energy (b), 392mJ.

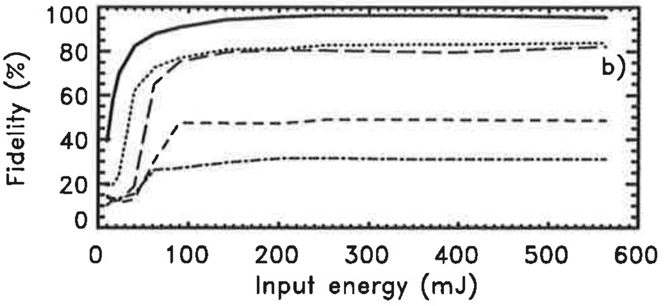

Figure 5.17: Using different individual modes of Laugerre-Gaussian functions as an input pump pulse (with parameters given as in Fig. 5.2), the behaviour of the reflectivity (a) and fidelity (b) is shown as a function of energy. The threshold is increasing while the fidelity saturation level is decreasing for higher order modes.

fundamental beam parameter $\omega_i = \omega_1$ (see Fig. 5.1), which changes the input spot size of higher order modes through Eqs. (5.17) and (5.18). Input beams with a larger spot size at the lens have a smaller spot size at the focal plane resulting in a higher intensity at the focal plane. In Fig. 5.17(b) the fundamental beam parameter $\omega_i = 0.5cm$. A higher fidelity is obtained when the parameter ω_i is reduced to $\omega_i = 0.3cm$, i.e., the focal plane intensity is reduced. The fidelity and reflectivity results for different values of ω_i and different input modes are shown in Fig. 5.18. It shows a decrease in the fidelity of all higher order modes when ω_i is increased beyond 0.3 cm (Rayleigh range smaller than 0.94 cm) due to high focal volume intensity. We investigated this behaviour further by selecting the conditions for the best and worst fidelity for mode II in Fig. 5.18, labelled "A" and "B" respectively, and calculating the temporal variation in reflectivity and fidelity for both cases, as illustrated in Fig. 5.19. The poor fidelity obtained for a high intensity in the focal plane may be explained using arguments similar to those for our one-D model in Chap. 4, where a threshold relaxation oscillation was found. In Chap. 4 we found that for high pump intensities in the focal volume, the threshold intensity for SBS was significantly exceeded before the Stokes radiation could saturate the SBS gain. Thus for a large input beam spot size, when the interaction length is short and the pump intensity is high in the focal volume, the rate of change of the Stokes intensity is large and threshold for SBS will be greatly exceeded. This implies that the competition between the phase conjugating mode and all the other possible, non-phase conjugating modes is reduced, and reflectivity from other modes above threshold is more likely to occur, thereby reducing the fidelity. The results in Fig. 5.19 show a behaviour consistent with this explanation: using a large input beam spot size results in a poor fidelity at the threshold and throughout the pulse as shown in Fig. 5.19(B).

The simulations also showed that whenever the fidelity for a particular mode was low, and the total reflectivity high, the excess energy was coupled primarily into the next lower mode. This can possibly be explained by comparing the phase matched coupling constants $(\varepsilon_{mmmm}, \varepsilon_{mmm+1m+1}, \varepsilon_{mmm-1m-1})$ of Eqs. (5.46) for a specific single mode, e.g. $m = 2$ (see table 5.1). The coupling constants are given by the

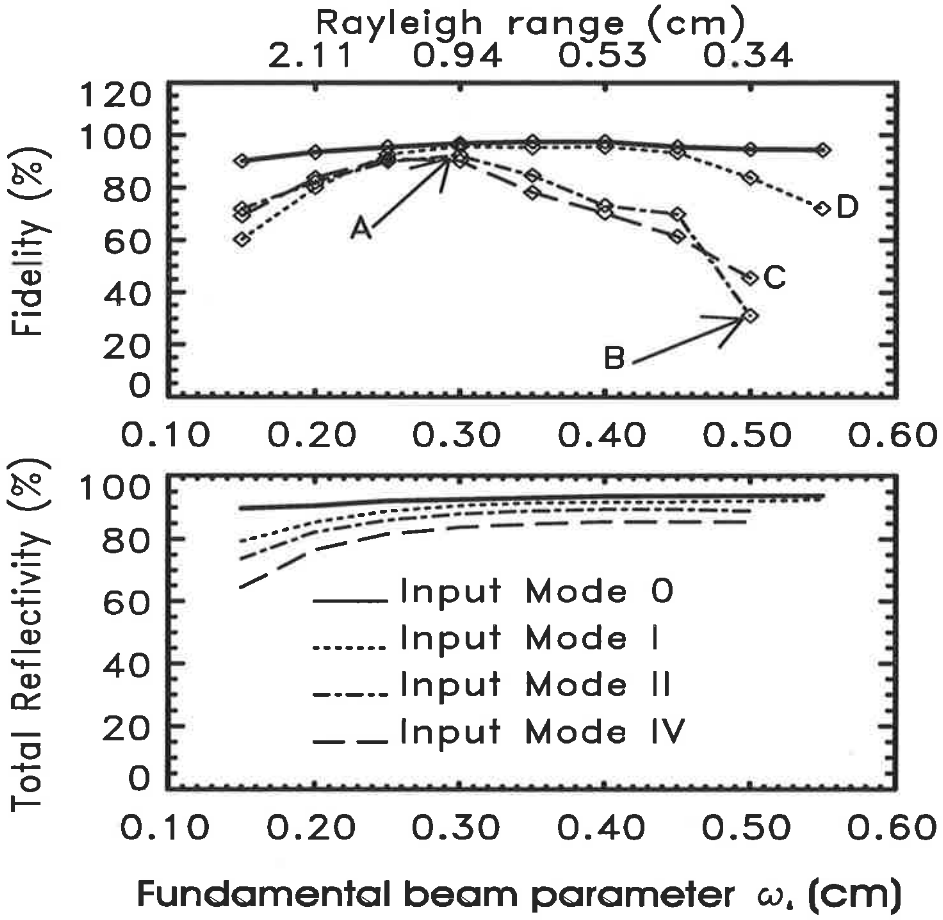

Figure 5.18: Fidelity and reflectivity as a function of the fundamental beam parameter ω_i. Here the input intensity has been kept constant by increasing the power. Although the reflectivity saturates at large values of ω_i, the fidelity of the non-fundamental modes decreases. Points "A" and "B" correspond to the highest (92%) and lowest (31%) fidelity of mode II and are discussed in the text. The Rayleigh range values corresponding to different ω_i are shown. All the other parameters are as in Fig. 5.2.

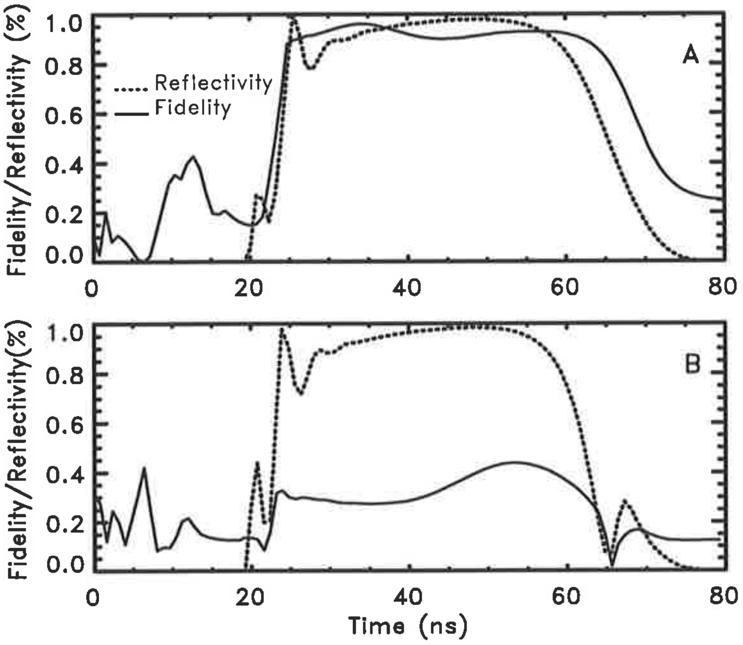

Figure 5.19: Time-resolved reflectivity and fidelity for the two points "A" and "B", marked in Fig. 5.18. For the point "B" the fidelity curve fails to follow the reflectivity right at the threshold.

overlap integral, Eq. 5.22, which is a measure of the transverse spatial correlation of the Stokes mode with the pump mode. How quickly a mode grows at the threshold thus depends on the focal intensity and what fraction of this intensity is coupled into the particular mode. At high focal intensities, modes with higher phase matched coupling constants grow faster at threshold and have better chance to compete with the phase conjugated mode. This explanation is consistent with the results shown in Fig. 5.20, in which the temporal variation of the fidelity for a single mode (mode II) is shown for various mode II to mode I coupling constants. Close examination of the threshold fidelity shows that it reduces as the coupling constant between mode II and mode I, ε_{2211}, increases.

A possible explanation of this behaviour can be given based on equations similar to Eqs. (5.46). For a short time interval around the threshold, and in a small volume close to the focus the spatial derivative term $(\partial/\partial z)$ in Eq. (5.23) can be ignored. Furthermore, we ignore the $(\partial/\partial t)$ term for the acoustic field in Eq. (5.3). This can be shown to be equivalent to approximating $(\partial^2 b_n/\partial t^2) \ll \Gamma(\partial/\partial t)b_n$ i.e., the slowly varying approximation. Applying these approximations and using Eq. (5.21), one

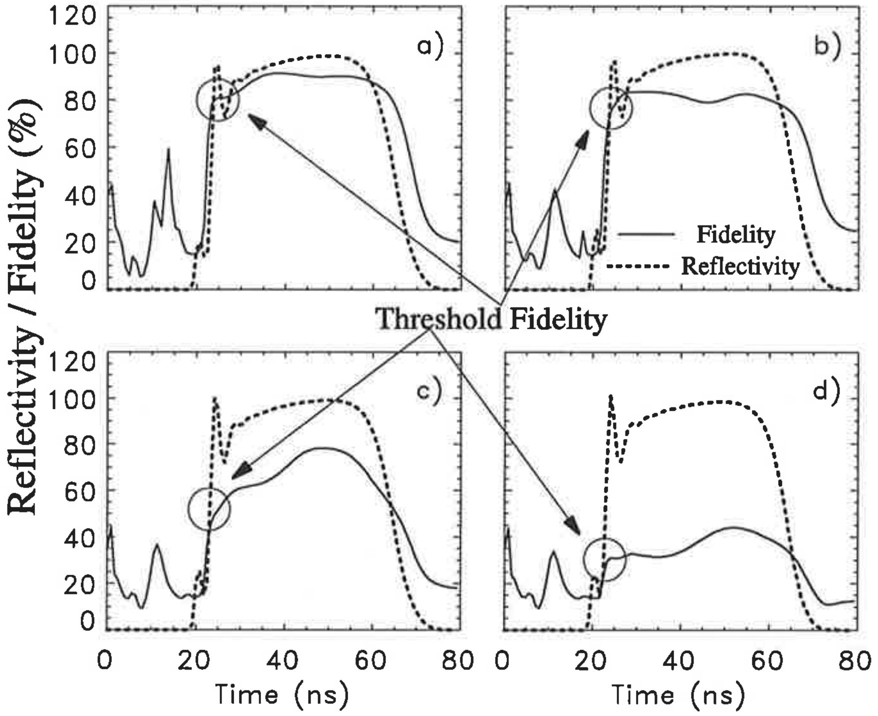

Figure 5.20: Reflectivity and fidelity as a function of time. The value of the mode II to mode I phase matched coupling constant, ε_{2211}, has been changed manually from (a) $\varepsilon_{2211} = 0.0$ to (b) $\varepsilon_{2211} = 0.08$, (c) $\varepsilon_{2211} = 0.0995$, and (d) $\varepsilon_{2211} = 0.11$. The threshold fidelity (indicated by circles) decreases from (a) to (d). The total reflectivity (time averaged) for all of the (a)-(d) curves is 90%, while the the total fidelities (time averaged) are 90%, 82%, 69% and 35% for (a), (b), (c) and (d) curves, respectively. The value of $\varepsilon_{2211} = 0.0995$ for curve (c), is the actual value of ε_{2211} calculated according to Eq. 5.22.

can write

$$\frac{n}{c}\frac{\partial}{\partial t}b_n = \frac{G\left|a_m\right|^2}{\Gamma\omega^2(z)}\sum_j \varepsilon_{mmnj}e^{i(n-j)\psi(z)}b_j,$$

in which we have assumed that the SBS cell has been pumped by mode m and that this is the only dominant pump mode inside the cell. Expanding this equation for the phase conjugated mode b_m and the nearest modes $b_{m\pm1}$, results in equations similar to Eqs. (5.46)

$$\begin{aligned}
\frac{n}{c}\frac{\partial}{\partial t}b_m &= \frac{G\left|a_m\right|^2}{\Gamma\omega^2(z)}(\varepsilon_{mmmm}b_m + \varepsilon_{mmmm+1}e^{-i\psi(z)}b_{m+1} + \varepsilon_{mmmm-1}e^{i\psi(z)}b_{m-1} + ...), \\
&\qquad\qquad\qquad\qquad\qquad\qquad\qquad\qquad\qquad\qquad\qquad\qquad\qquad (5.53a) \\
\frac{n}{c}\frac{\partial}{\partial t}b_{m+1} &= \frac{G\left|a_m\right|^2}{\Gamma\omega^2(z)}(\varepsilon_{mmm+1m+1}b_{m+1} + \varepsilon_{mmmm+1}e^{i\psi(z)}b_m + ...), \qquad (5.53b) \\
\frac{n}{c}\frac{\partial}{\partial t}b_{m-1} &= \frac{G\left|a_m\right|^2}{\Gamma\omega^2(z)}(\varepsilon_{mmm-1m-1}b_{m-1} + \varepsilon_{mmmm-1}e^{-i\psi(z)}b_m + ...). \qquad (5.53c)
\end{aligned}$$

These equations describe how the Stokes modes grow and compete through the threshold. The phase matched terms on the right hand side of these equations result in a solution of the form

$$\begin{aligned}
b_i &\propto \exp\left[\left(\frac{G\left|a_m\right|^2 c}{\Gamma\omega^2(z)n}\varepsilon_i\right)t\right], \\
(\text{where } \varepsilon_i &= \varepsilon_{mmmm}, \varepsilon_{mmm+1m+1}, \varepsilon_{mmm-1m-1} \text{for } i = m, m+1, m-1 \text{ respectively}).
\end{aligned}$$

This shows that the rate of temporal change of the Stokes modes, at the threshold, depends on: (1) the pump intensity and (2) the phase matched coupling constants, which is consistent with the above discussion and results in Figs. 5.19 and 5.20.

Our model has demonstrated the effect of the phase matched coupling constants on transient fidelity. By their very nature, steady state models [27, 28] have omitted this transient phenomenon. These models are based on equations similar to Eqs. (5.46), which describe the growth of the backward Stokes modes above the threshold and in the steady state regime (see Sec. 5.4.1 and [27, 28]). Therefore, they do not give a complete description of the growth and competition of the Stokes modes through the threshold.

The transient phenomenon predicted in our model is similar to the transient effect of a sharp leading edge of the pump, which was studied by Dane *et al.*[15] and discussed here in Sec. 5.4.1. The significance of our finding is that the fidelity is degraded at high energy not only when there is a sharp rise in the leading edge of the pump pulse but also when there is a sharp rise in the Stokes pulse.

5.4.2 Aberrated input beams

We next examined the behaviour of multi-mode beams as an approximation to aberrated beams. As an example we have considered an input beam with energy distributed among the different modes as follows: 4.5% in mode 0, 44.5% in mode II and 51% in mode IV. As in the single-mode case, we found a geometry that resulted in maximum fidelity. Fig. 5.21 shows the input and output intensity distributions for two geometries: one resulting in low fidelity, and one resulting in the highest fidelity. In this figure, we have kept the input intensity constant, but have changed the size of the beam at the input to the cell. As before this was done by changing the fundamental beam parameter, $\omega_i = \omega_1$, from $\omega_1 = 0.5$ cm in Fig. 5.21(a) to 0.35 cm in Fig. 5.21(b). In figure 5.21, the input power has thus been reduced to keep the intensity constant. Examination of the reflectivity and fidelity for a range of ω_1 (or Rayleigh range) in Fig. 5.22, shows a behaviour similar to the single mode results from above: the fidelity of the aberrated beam is degraded for beams with large input spot sizes (short Rayleigh range).

In the above example we chose an input beam with energy arbitrarily distributed among several modes. The model allows us to use any arbitrary, cylindrically symmetric aberrated input beam with any mode distribution. Assume an arbitrary input spatial profile of

$$E_l(r, z = L) = f(r, L).$$

Using the orthonormal property of the Gauss-Laguerre functions, one can expand $E_l(r, L)$ in the transverse direction as

$$E_l(r, L) = \sum_{\alpha} a_\alpha A_\alpha(r, L), \text{ where} \tag{5.54}$$

$$a_\alpha = \int_0^\infty A_\alpha^*(r, L) f(r, L) d^2r. \tag{5.55}$$

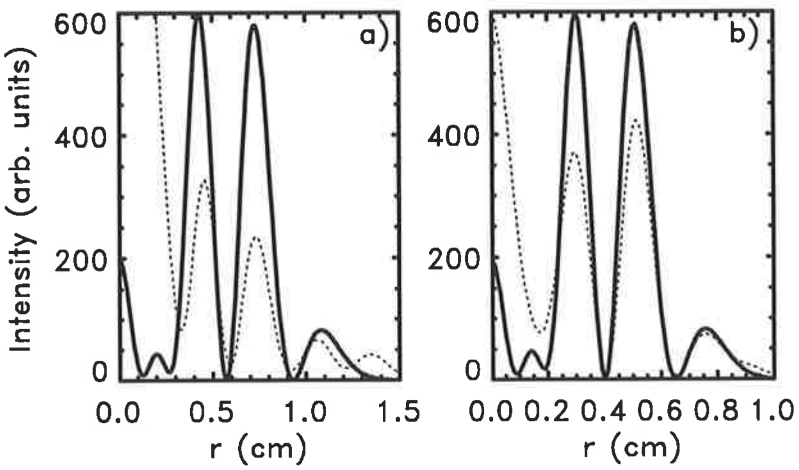

Figure 5.21: Input (solid lines) and output (dashed lines) intensity distributions for an aberrated input beam at two different geometries. In (a) the fundamental beam parameter ω_1 is 0.5 cm (Rayleigh-range 0.34 cm) and the input energy is 823 mJ, while in (b) ω_1 is 0.35 cm (Rayleigh-range 0.70 cm) and the input energy is 403 mJ. A fidelity of 88% is achieved for (b) while only 47% fidelity is obtained for (a).

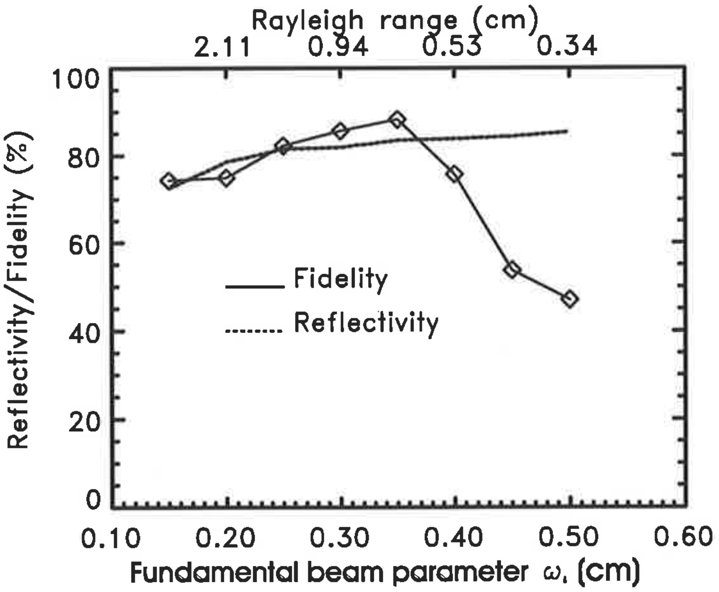

Figure 5.22: As for single-mode input beams (see Fig. 5.18), there is a focusing geometry that results in a maximum fidelity for aberrated input beams. The Rayleigh range values corresponding to different ω_1 are shown.

Here $|a_\alpha|^2$ gives the contribution of the α-th mode in the total input energy. Finding a_α's from Eq. (5.55), we can use them as inputs to our computer code to study the SBS fidelity and reflectivity for any aberrated input beam. This is thus an enabling theory and code to be used in future studies and detailed comparison with experiments.

5.5 Comparison between numerical and experimental results

Just recently, after visits by Prof. Ralf Menzel and Dr. A. Heuer of The University of Potsdam, Germany, we have initiated a collaboration between the two optics groups to compare in detail experimental results from Potsdam with the predictions of our present numerical model. Experiments have been done on the overall reflectivity and the temporal profiles of the Stokes pulses in the SBS process for two materials with extreme (short and long) phonon lifetimes; 1) Freon 113 with phonon lifetime τ =0.84 ns and 2) SF_6 gas at 20 bar pressure with phonon lifetime τ = 17.4 ns. Using the experimental parameters (including geometrical, material and input pulse parameters) in our model, we have produced primary numerical results that are in a excellent agreement with the experiments. In the following, we present both the experimental and numerical results which are the initial results for a detailed collaboration paper currently in initial presentation.

5.5.1 SBS experiment using Freon 113

The experimental and numerical parameters are as follows; cell length 200 mm, focal length 120 mm, distance between the lens and the entrance window 45 mm, entrance window thickness 2 mm (BK7), phonon lifetime 0.84 ns, gain of the medium 0.0062 cm/MW, index of refraction, n=1.36, Laser wavelength 1064 nm, input beam radius 1.45 mm and input beam radius of curvature 2403 mm. The experimental and numerical results for the overall reflectivity and the temporal profiles of the Stokes pulses at different energies are shown in Figs. 5.23 and 5.24. We have used the experimental results of the overall reflectivity as a function of energy, Fig. 5.23,

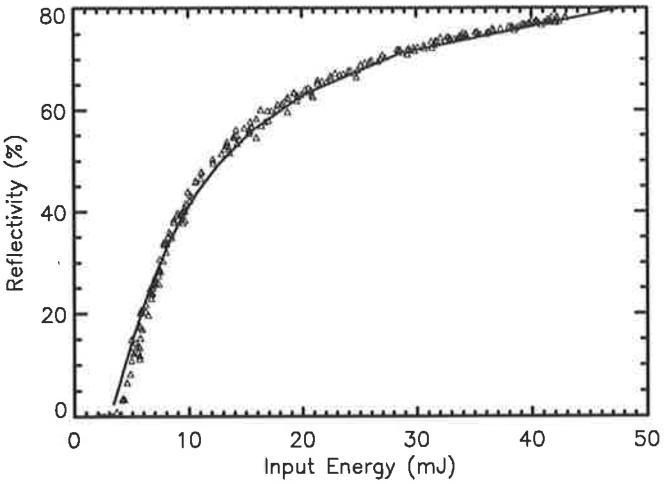

Figure 5.23: Experimental and Numerical results of the SBS reflectivity vs. energy for Freon 113. The triangles are the experimental results obtained by A. Heuer and R. Menzel. The solid line is the numerical model results.

to set the free parameter of our computer code. Once the free parameter is set, we have kept it constant for all the other results. The numerical curves in Figs. 5.23 and 5.24 have been obtained for free parameter of 2.79×10^{-8}.

5.5.2 SBS experiment using SF_6

The following experimental and numerical parameters were used for the SBS experiment in a cell filled with pure SF6 at a pressure of 20.5 bar; cell length 139 mm, focal length 120 mm, distance between the lens and the entrance window 45 mm, entrance window thickness 2 mm (BK7), phonon lifetime 17.3 ns, gain of the medium 0.014 cm/MW, index of refraction, n=1.023, Laser wavelength 1064 nm, input beam radius 2.0 mm and input beam radius of curvature 2403 mm. The experimental and numerical results for the overall reflectivity and the temporal profiles of the Stokes pulses at different energies are shown in Figs. 5.25 and 5.26. Like the Freon case, we have used the experimental results of the overall reflectivity as a function of energy, Fig. 5.25, to set the free parameter of our computer code for SF_6. Once the free parameter is set, we have kept it constant for all the other results. The numerical curves in Figs. 5.25 and 5.26 have been obtained for free parameter of 1.194×10^{-8}.

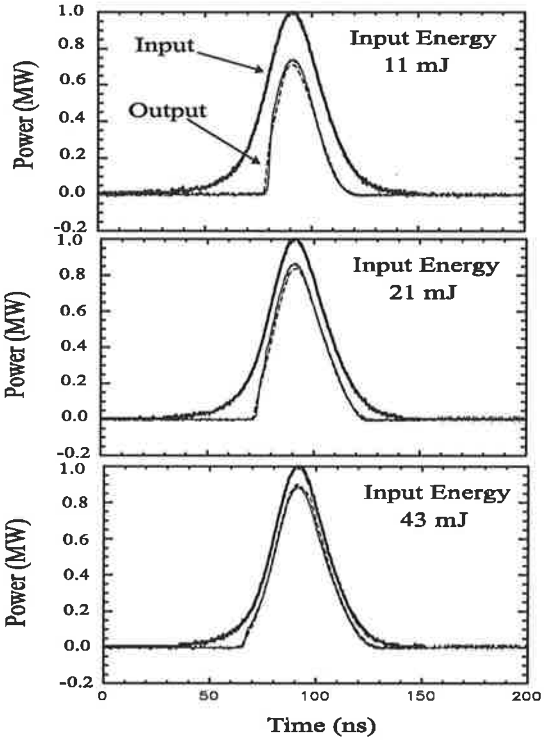

Figure 5.24: The temporal profiles of the input and output (Stokes) pulses in the SBS experiment in Freon 113. The solid lines are the experimental results obtained by A. Heuer and R. Menzel. The dashed lines are the results of the numerical model. In all cases the input pulses for the experiment and numerical model are the same. All the powers are in MW but have been normalised to peak pump power of 1MW to make the comparison easier.

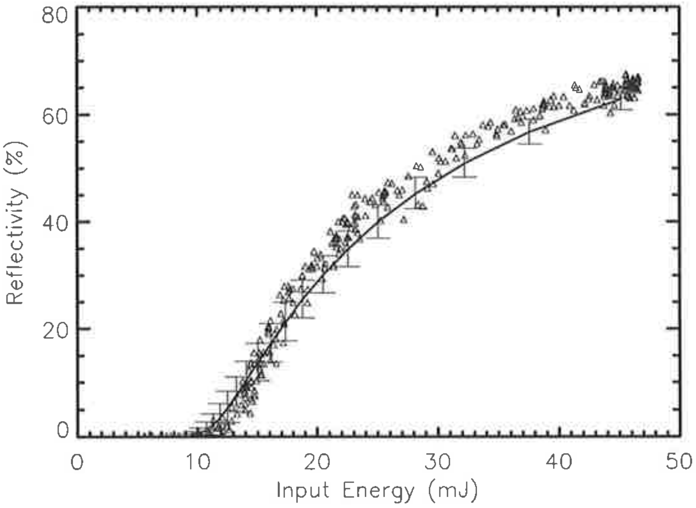

Figure 5.25: SBS reflectivity vs. energy for pure SF_6 at 20 bar pressure. The triangles are the experimental results obtained by A. Heuer and R. Menzel. The solid line is the numerical results. The error bars are showing the range of numerical values for the reflectivity for different initial noise term.

5.6 Conclusions

We have developed an efficient numerical model to investigate the phase conjugating properties of stimulated Brillouin scattering. By retaining transverse and time derivatives in the coupled differential equations and using a spatial mode decomposition model, we have developed a new and efficient algorithm, which has made it uniquely possible to study the fidelity and mode structure of the Stokes and pump beams in the transient regime, for single or multi-mode, cylindrically symmetric input pulses.

Among the experimental and theoretical studies of intensity fluctuations in the Stokes pulse of SBS [10, 12, 11, 79, 13, 16, 19, 2], only a few have indicated that these fluctuations degrade the SBS fidelity [10, 12, 19, 2]. Using our model we have confirmed numerically that these fluctuations do degrade the SBS fidelity. In our model we have included a Langevin force noise term with a spatial and temporal Gaussian distribution in the SBS equations, which not only simulates the shot to shot variation of fidelity and reflectivity but also demonstrates the reduction in the time-resolved and overall fidelity of SBS due to intensity fluctuations in the Stokes pulse. This result together with the results of the previous chapter, Chap

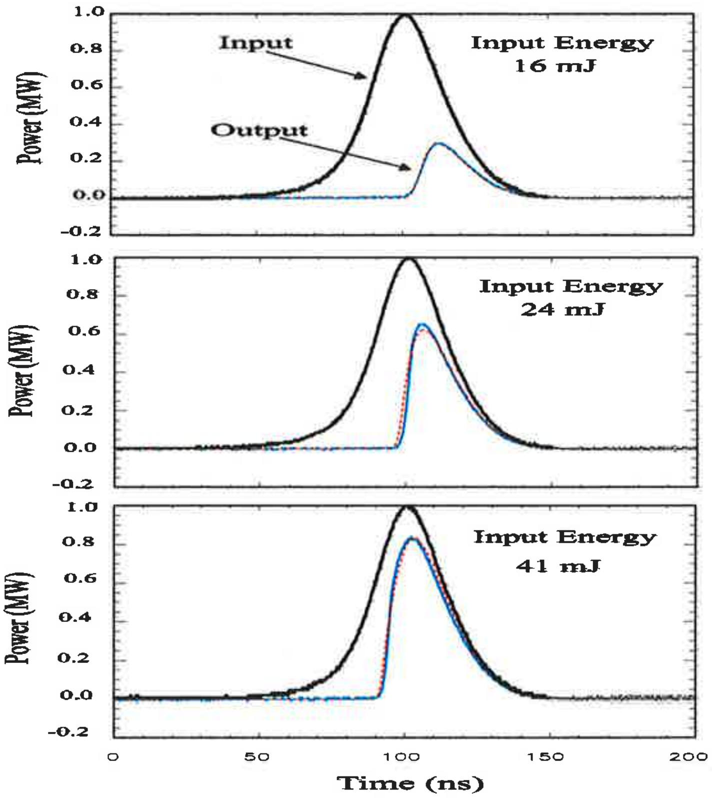

Figure 5.26: Temporal profiles of the input and output pulses in a SBS experiment using pure SF_6 at 20 bar pressure. The blue lines are the experimental results obtained by A. Heuer and R. Menzel. The red lines are the numerical model results. All the powers are in MW but have been normalised to peak pump power of 1MW to make the comparison easier.

4 are important in practice since they can be used to select the best experimental parameter space for excellent fidelity in applications of SBS.

It was determined that, due to transient effects, the temporal shape of the input pulse can greatly affect the fidelity of SBS at high energy. Input pulses with a sharp rise, leading edge show poor ability for producing a phase conjugated return at high energy, although this ability improves for short phonon lifetimes. This is in agreement with the experimental work by Dane *et.al.* [15].

There have been many experimental and theoretical studies of SBS of broadband laser pulses including [8, 110, 74, 12, 111, 112, 113, 114, 115, 116, 2, 117]. It is generally accepted that the fidelity of phase conjugation is degraded for short coherence length lasers. This degradation is usually attributed to the onset of competing nonlinear optical phenomena such as break down, stimulated Raman scattering and self focusing, at high pump intensities [74, 12, 111, 112, 113, 114, 116, 2]. Although our model is a single frequency simulation of SBS, the results suggest that this problem is an integral problem of SBS itself. Our model predicts a new transient phenomenon: fidelity degradation due to a very rapid build up of the Stokes pulse at the threshold for smooth input pulses, which enables energy to be absorbed by the non-phase conjugated modes and thus reduce the overall fidelity. The rate of build up of the Stokes radiation at the threshold depends on the focal intensity and the phase matched coupling constants. Thus, apart from the well known fact that a sufficiently high intensity is needed to achieve a good fidelity, an excess focal intensity result in poor fidelity. The usual discrimination between conjugated and non-conjugated modes (the steady state gain of conjugated mode is almost twice that of non-conjugated modes) does not work when all the Stokes modes turn on suddenly. To ensure phase conjugation, the Stokes modes should reach the threshold adiabatically. This result can be used to explain why phase conjugation of broad band lasers is not successful even if the interaction length is shorter than the coherence length.

Chapter 6

Conclusion and Future works

Theoretical studies of SBS have usually considered only the steady state regime of SBS. Although it makes the coupled equations describing the process easy to understand, this approach does not give a complete picture of the SBS process. In fact, there are phenomena and practical regimes that cannot be treated in the steady state. Throughout this thesis we have focused on the transient regime and examined, in detail, those phenomena and regimes in which the steady state approximation fails to work.

We developed a transient one-dimensional model of SBS initiated from noise and including cell geometries (see Chap. 4 for detailed explanations). Two transient phenomena were studied using the 1-D model:

1) Intensity and phase modulation in the Stokes intensity pulse,

2) Threshold oscillations at the beginning of the Stokes pulse.

Rapid thermal fluctuations in the density of the medium are initial sources of SBS. Under certain circumstances these initial fluctuations can be amplified through the SBS process and appear in the Stokes intensity and phase. Numerical results suggest that these fluctuations are likely to be seen in the SBS process, using materials with short rather than long phonon lifetimes. Experimental setups with long interaction lengths and low energies are more likely to encounter intensity fluctuations. However, even when there are no intensity fluctuations in the Stokes pulse, there are still shot-to-shot fluctuations in the Stokes energy. More stable output energy can be obtained at high input energies. These fluctuations degrade the fidelity (degree of phase conjugation) of the SBS process. It was demonstrated by our three-dimensional model (developed in Chap. 5) that fluctuations in the Stokes intensity cause a reduction in the time-resolved and overall fidelity of the SBS process. These findings are of practical importance for designing high power laser systems with excellent beam quality using phase conjugating SBS mirrors.

SBS is a threshold process, meaning a certain amount of input power is required before the process is initiated. The time dependent growth of the stokes pulse at the threshold is exponential. It was shown that this exponential growth of the Stokes pulse sometimes leads to overshooting of the input power and resembles a relaxation oscillation in the Stokes power. This relaxation oscillation is a function of the phonon lifetime, the intensity of the pump at the focus and the immersion length. It was also shown that the pulse compression phenomena can be explained in the context of a threshold oscillation in which the first peak of the oscillation has been magnified and the other peaks have been omitted. From this point of view, even for pulses much longer than the phonon lifetime, (the usual condition for the steady state regime) the transient regime must be considered at the threshold.

The three-dimensional model has been developed in Chap. 5. By introducing block-vectors and block-matrices, we have developed a new and efficient algorithm that uses the advantageous of having lots of zero elements in the coefficient matrices in the SBS differential equations. This algorithm enabled us, for the first time, to solve numerically the transient SBS equations in three dimensions for cylindrically symmetric laser fields.

A transient effect that can be investigated by our model is the effect of the input pulse leading edge on the SBS fidelity. It was shown that the SBS fidelity can be degraded, especially at high energies, if the time scale of the leading edge is shorter than the phonon lifetime of the material. Using the model, a new and interesting transient phenomenon has been predicted: the SBS fidelity degrades when the focal intensity is too high. High focal volume intensity causes all the spatial modes (conjugated and non-conjugated) to grow so rapidly at the threshold that the usual gain differences between modes (gain of the conjugated mode is almost twice as much as non-conjugated modes) can not discriminate the conjugate mode over the non-conjugated ones.

6.1 Future work

The algorithm developed here for the three-dimensional model with cylindrical symmetry (see Chap. 5 and App. B) treats the transverse direction as discrete modes of some orthonormal functions. What is new about our algorithm is that it avoids the computationally intensive calculations using the large coefficient matrices and instead allows calculations using small matrices in the sub-space of transverse modes. We believe that this key element of our algorithm can be used in the next generations of SBS models, where the laser beam is not cylindrically symmetric or is not single frequency. For such a case of for example non-symmetric or astigmatic laser beams, two sets of orthonormal bases (modes) are necessary to represent the subspace of the transverse directions. We have proposed to carry on the development of our model to short coherence length (multi-frequency) and non-symmetric laser beams. We believe that our present model will contribute to the future development of phase conjugation of short coherence length and astigmatic laser beams.

Appendix A

Generating a Gaussian Distribution

Consider a probability density function $p(x)$, for which $p(x)dx$ gives the probability of finding the variable x in the range $[x, x + dx]$. If we introduce a new variable $y = f(x)$, then there will be a new probability density function $q(y)$ in the y space, which describes the probability density function of y. However, the probability of having a state in a certain range in the x space should be equal to the probability of having that state in the corresponding range in the y space. i.e.,

$$p(x)dx = q(y)dy. \tag{A.1}$$

Giving the two probability density function $p(x)$ and $q(y)$, one can use Eq. A.1 to find the relation between the two variables x and y [i.e., $y = f(x)$].

As an example, consider a uniform distribution in the y space (over the range [0,1]) such that

$$q(y) = 1,$$

and an exponential distribution in the x space:

$$p(x) = \lambda e^{-\lambda x}.$$

Then , using Eq. (A.1), we find

$$\begin{aligned} \lambda e^{-\lambda x} dx &= dy, \\ \lambda \int_0^x e^{-\lambda x} dx &= y, \\ &\Downarrow \\ x &= \frac{-1}{\lambda} \ln(1-y). \end{aligned} \tag{A.2}$$

Hence, given the variable y is uniformly distributed over [0,1] then the variable x, defined in Eq. $A.2$, is exponentially distributed over $[0, \infty)$.

Consider two variables x_1, x_2 that have a Gaussian distributions with mean values of $\overline{x}_1, \overline{x}_2$ and a variance σ of:

$$\frac{1}{\pi\sigma^2} e^{-\frac{(x_1-\overline{x}_1)+(x_2-\overline{x}_2)}{\sigma^2}}.$$

Then using the following transformations and variables

$$\begin{aligned} x_1' &= x_1 - \overline{x}_1 \text{ and } x_2' = x_2 - \overline{x}_2 \\ r &= x_1'^2 + x_2'^2 \text{ and } \tan\theta = \frac{x_2'}{x_1'}, \end{aligned}$$

one can show that

$$\begin{aligned} \frac{1}{\pi\sigma^2} e^{-\frac{(x_1-\overline{x}_1)+(x_2-\overline{x}_2)}{\sigma^2}} dx_1 dx_2 &= \frac{1}{\pi\sigma^2} e^{-\frac{x_1'^2+x_2'^2}{\sigma^2}} dx_1' dx_2' = \\ \frac{1}{\pi\sigma^2} e^{\frac{-r^2}{\sigma^2}} r dr d\theta &= \frac{1}{\pi\sigma^2} e^{\frac{-u}{\sigma^2}} du d\theta, \end{aligned}$$

where $u = r^2$. Hence, if the variable u is generated exponentially (probability density function $\frac{1}{\sigma^2} e^{-u/\sigma^2}$) over $[0, \infty)$ and variable θ is generated uniformly over $[0, \pi]$, then the two variables

$$\begin{aligned} x_1 &= \overline{x}_1 + \sqrt{u}\cos\theta, \\ x_2 &= \overline{x}_2 + \sqrt{u}\sin\theta, \end{aligned}$$

will be distributed normally over $(-\infty, +\infty)$ with variance σ and mean values $\overline{x}_1, \overline{x}_2$. We have used these two variables to generate Langevin noise terms in our 1D and 3D model. To generate the variable u over $[0, \infty)$ with the probability density function $\frac{1}{\sigma^2} e^{-u/\sigma^2}$ one can use Eq. (A.2) to find

$$u = -\sigma^2 \ln(1 - y),$$

where y is distributed uniformly over $[0, 1]$.

Appendix B

Block-matrices

This appendix deals with square matrices of $n \times n$, whose elements themselves are $p \times p$ matrices (referred to here as block-matrices). As an example, $\mathbf{S}_{4\times4}$ is given by

$$\mathbf{S} = \begin{pmatrix} A_{p\times p} & B_{p\times p} & C_{p\times p} & D_{p\times p} \\ E_{p\times p} & F_{p\times p} & G_{p\times p} & H_{p\times p} \\ I_{p\times p} & J_{p\times p} & K_{p\times p} & L_{p\times p} \\ M_{p\times p} & N_{p\times p} & O_{p\times p} & P_{p\times p} \end{pmatrix}_{4\times4},$$

where A, B, ..., P are all $p \times p$ matrices. Consider the multiplication of two such 4×4 matrices $\mathbf{S}$ and $\mathbf{T}$:

$$\begin{pmatrix} A_{p\times p} & B_{p\times p} & C_{p\times p} & D_{p\times p} \\ E_{p\times p} & F_{p\times p} & G_{p\times p} & H_{p\times p} \\ I_{p\times p} & J_{p\times p} & K_{p\times p} & L_{p\times p} \\ M_{p\times p} & N_{p\times p} & O_{p\times p} & P_{p\times p} \end{pmatrix}_{4\times4} \times \begin{pmatrix} A'_{p\times p} & B'_{p\times p} & C'_{p\times p} & D'_{p\times p} \\ E'_{p\times p} & F'_{p\times p} & G'_{p\times p} & H'_{p\times p} \\ I'_{p\times p} & J'_{p\times p} & K'_{p\times p} & L'_{p\times p} \\ M'_{p\times p} & N'_{p\times p} & O'_{p\times p} & P'_{p\times p} \end{pmatrix}_{4\times4} =$$

$$\begin{pmatrix} A''_{p\times p} & B''_{p\times p} & C''_{p\times p} & D''_{p\times p} \\ E''_{p\times p} & F''_{p\times p} & G''_{p\times p} & H''_{p\times p} \\ I''_{p\times p} & J''_{p\times p} & K''_{p\times p} & L''_{p\times p} \\ M''_{p\times p} & N''_{p\times p} & O''_{p\times p} & P''_{p\times p} \end{pmatrix}_{4\times4}.$$

It can be shown that the multiplication rule for ordinary matrices can be applied to find the elements of the resultant matrix $\mathbf{S} \times \mathbf{T}$ i.e.,

$$(\mathbf{S} \times \mathbf{T})_{ij} = \sum_k \mathbf{S}_{ik} \times \mathbf{T}_{kj},$$

where $\times$ is the matrix multiplication operator and $\mathbf{S}_{ik}$ and $\mathbf{T}_{kj}$ are $p \times p$ matrices. As an example, for the above 4×4 block matrices we find

$$\begin{aligned} A'' &= A \times A' + B \times E' + C \times I' + D \times M', \\ B'' &= A \times B' + B \times F' + C \times J' + D \times N', \\ &\vdots \\ P'' &= M \times D' + N \times H' + O \times L' + P \times P'. \end{aligned}$$

As an application of this multiplication rule, the inverse of a diagonal block-matrix can be written as

$$\begin{pmatrix} (A_1)_{p\times p} & 0 & \dots & 0 \\ 0 & (A_2)_{p\times p} & & 0 \\ \vdots & \vdots & \ddots & \vdots \\ 0 & 0 & \dots & (A_n)_{p\times p} \end{pmatrix}_{n\times n}^{-1} = \begin{pmatrix} (A_1)^{-1}_{p\times p} & 0 & \dots & 0 \\ 0 & (A_2)^{-1}_{p\times p} & & 0 \\ \vdots & \vdots & \ddots & \vdots \\ 0 & 0 & \dots & (A_n)^{-1}_{p\times p} \end{pmatrix}_{n\times n}$$

In the theory section of Chap. 5, Sec. 5.3, where we developed a three-dimensional model of SBS, we obtained a final algebraic equation for $(\overrightarrow{\overrightarrow{b}})^{\alpha+1}$, Eq. (5.43), in the form:

$$A\overrightarrow{\overrightarrow{b}} = \overrightarrow{\overrightarrow{X}}. \tag{B.1}$$

In this equation, A is a block-matrix $n \times n$ with blocks $p \times p$ and $\overrightarrow{\overrightarrow{b}}$ and $\overrightarrow{\overrightarrow{X}}$ are block vectors $n \times 1$ with blocks $p \times 1$. In our model, the matrix A turns out to be a tridiagonal block matrix of the form:

$$\begin{pmatrix} (b_1)_{p\times p} & (c_1)_{p\times p} & 0 & \cdots & & 0 \\ (a_2)_{p\times p} & (b_2)_{p\times p} & (c_2)_{p\times p} & 0 & & \vdots \\ 0 & (a_3)_{p\times p} & (b_3)_{p\times p}. & \ddots & \ddots & \\ \vdots & 0 & \ddots & \ddots & \ddots & 0 \\ . & & \ddots & \ddots & \ddots & (c_{n-1})_{p\times p} \\ 0 & & \cdots & 0 & (a_n)_{p\times p} & (b_n)_{p\times p} \end{pmatrix}_{n\times n}.$$

It is interesting that Eq. (B.1) is similar to the equations obtained for the one-dimensional model in Chap. 4. The only difference is that for the one-dimensional model, the matrix A is an ordinary tridiagonal matrix and $\overrightarrow{X}$ and $\overrightarrow{b}$ are ordinary vectors. In other words, in the three-dimensional model ordinary elements of matrices and vectors are replaced with $p \times p$ matrices and $p \times 1$ vectors in the subspace $p \times p$ of the spatial modes. To solve Eq. (B.1), (similar to ordinary matrices) we apply a LU decomposition method to decompose A to a lower and a upper tridiagonal block-matrices of L and U of the form

$$L = \begin{pmatrix} (I)_{p\times p} & 0 & 0 & \cdots & & 0 \\ (l_2)_{p\times p} & (I)_{p\times p} & 0 & 0 & & \vdots \\ 0 & (l_3)_{p\times p} & (I)_{p\times p}. & \ddots & \ddots & \\ \vdots & 0 & \ddots & \ddots & \ddots & 0 \\ & & \ddots & \ddots & \ddots & 0 \\ 0 & \cdots & & 0 & (l_n)_{p\times p} & (I)_{p\times p} \end{pmatrix}_{n\times n},$$

and

$$U = \begin{pmatrix} (u_1)_{p\times p} & (c_1)_{p\times p} & 0 & \cdots & & 0 \\ 0 & (u_2)_{p\times p} & (c_2)_{p\times p} & 0 & & \vdots \\ 0 & 0 & (u_3)_{p\times p}. & \ddots & \ddots & \\ \vdots & 0 & \ddots & \ddots & \ddots & 0 \\ & & \ddots & \ddots & \ddots & (c_{n-1})_{p\times p} \\ 0 & \cdots & & 0 & 0 & (u_n)_{p\times p} \end{pmatrix}_{n\times n},$$

such that $A = L \times U$. Here, $(I)_{p \times p}$ is the unit matrix of the spatial modes subspace. Using the above multiplication rules for the block matrices, it can be shown that

$$\begin{aligned} u_1 &= b_1, \\ l_n &= a_n \times (u_n)^{-1}, \\ u_n &= b_n - a_n \times (u_n)^{-1} \times c_{n-1}. \end{aligned}$$

Now, the decomposed form of A can be utilized to solve the equation

$$\begin{aligned} L \times (U \overset{\rightrightarrows}{b}) &= \overset{\rightrightarrows}{X}, \\ L \times \overset{\rightrightarrows}{Y} &= \overset{\rightrightarrows}{X}, \end{aligned}$$

first for $\overset{\rightrightarrows}{Y}$ and then substituted back into the equation

$$U \overset{\rightrightarrows}{b} = \overset{\rightrightarrows}{Y},$$

to find the solution for $\overset{\rightrightarrows}{b}$.

Appendix C

Recurrence Relation

According to the definition of ε_{ijkn} (5.22), one can write ε_{ijkn+1} as

$$\varepsilon_{ijkn+1} = (\frac{2}{\pi}) \int_0^{+\infty} dx e^{-2x} L_i(x) L_j(x) L_k(x) L_{n+1}(x). \tag{C.1}$$

Replacing L_{n+1} in C.1 according to the recurrence relation for Laguerre functions (p. 1037 in ref. [118]) i.e.,

$$(n+1)L_{n+1}(x) = (2n+1-x)L_n(x) + nL_{n-1}(x),$$

and integrating by parts taking into account

$$x\frac{d}{dx}L_n(x) = nL_n(x) - nL_{n-1}(x),$$

yields

$$\begin{aligned} \varepsilon_{ijkn+1} &= \frac{[3n+1-i-j-k]}{2(n+1)}\varepsilon_{ijkn} - \frac{n}{2(n+1)}\varepsilon_{ijkn-1} \\ &+ \frac{1}{2(n+1)}[i\varepsilon_{i-1jkn} + j\varepsilon_{ij-1kn} + k\varepsilon_{ijk-1n}]. \end{aligned}$$

A specific case of this recurrence relation is when $i = j = k = n$ which results in

$$\varepsilon_{nnnn+1} = \frac{1}{2(n+1)}\varepsilon_{nnnn} + \frac{n}{n+1}\varepsilon_{nnnn-1}. \tag{C.2}$$

A useful recurrence relation can be obtained for ε_{000m} using the integral (p. 844 in ref. [118])

$$\int_0^{+\infty} e^{-bx} L_m(x) dx = (b-1)^m b^{-m-1}.$$

Then

$$\varepsilon_{000m} = \frac{2}{\pi} \int_0^{+\infty} e^{-2x} L_m(x) dx = \frac{2}{\pi} 2^{-m-1} = \frac{1}{2^m} \varepsilon_{0000}. \tag{C.3}$$

Appendix D

SBS focusing system

The focusing geometry used in the SBS model is shown in Fig. D.1.

A laser beam with radius ω_1 and curvature R_1 is focused into a SBS cell using a lens of focal length f. The thickness of the entrance window is t and the refractive indices of the window and the SBS material are n_1 and n_2, respectively. Given the input beam radius and curvature ω_1 and R_1, one can find the radius and curvature of the beam anywhere inside the cell by finding the position of the waist inside the cell, l, and its radius ω_0. Once we know these two parameters, the beam radius and curvature at any other point inside the cell are

$$\begin{aligned} \omega^2(z) &= \omega_\circ^2[1+(\frac{z}{z_R})^2], \\ R(z) &= z+\frac{z_R^2}{z}, \end{aligned} \tag{D.1}$$

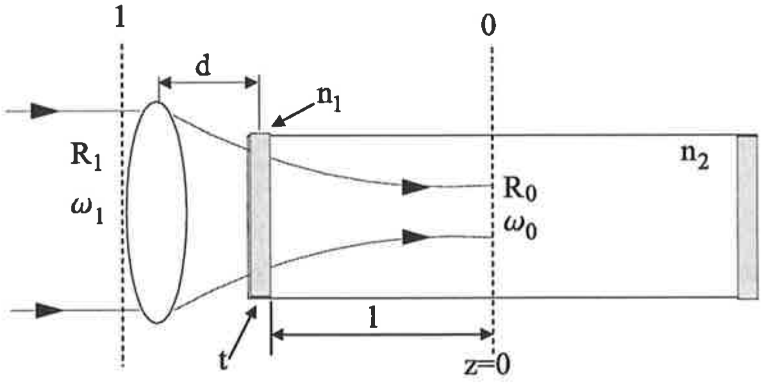

Figure D.1: Focusing geometry used for SBS process.

where z is the distance from the focus, ω_0 is the beam radius at the focus and the Rayleigh range, z_R, is related to the beam waist radius $\omega_\circ$ (for the fundamental mode) and wave length λ as $z_R = \pi\omega_\circ^2 n/\lambda$.

The ABCD matrix that transfers beam parameters from plane 1 to plane 0 (see Fig. D.1) is

$$\begin{aligned} ABCD &= \begin{pmatrix} 1 & l \\ 0 & 1 \end{pmatrix} \begin{pmatrix} 1 & 0 \\ 0 & \frac{n_1}{n_2} \end{pmatrix} \begin{pmatrix} 1 & t \\ 0 & 1 \end{pmatrix} \times \\ & \quad \begin{pmatrix} 1 & 0 \\ 0 & \frac{1}{n_1} \end{pmatrix} \begin{pmatrix} 1 & d \\ 0 & 1 \end{pmatrix} \begin{pmatrix} 1 & 0 \\ \frac{-1}{f} & 1 \end{pmatrix} \\ & \Downarrow \\ ABCD &= \begin{pmatrix} 1 - \frac{1}{f}[d + \frac{t}{n_1} + \frac{l}{n_2}] & d + \frac{t}{n_1} + \frac{l}{n_2} \\ -\frac{1}{n_2 f} & \frac{1}{n_2} \end{pmatrix}. \end{aligned} \tag{D.2}$$

Beam parameters at plane 1 and plane 0 can be related using the above $ABCD$ matrix as [119]

$$q_0 = \frac{Aq_1 + B}{Cq_1 + D}, \tag{D.3}$$

where q at any point is

$$\frac{1}{q} = \frac{1}{R} + i\frac{\lambda}{n\pi\omega^2}. \tag{D.4}$$

Inverting both sides of Eq. (D.4) and introducing new variables α and β, one can write q as

$$\begin{aligned} q &= \alpha + i\beta, \\ \alpha &= \frac{(\frac{n\pi\omega^2}{\lambda})^2 R}{(\frac{n\pi\omega^2}{\lambda})^2 + R^2} \\ \beta &= \frac{-(\frac{n\pi\omega^2}{\lambda})R^2}{(\frac{n\pi\omega^2}{\lambda})^2 + R^2} \end{aligned} \tag{D.5}$$

At plane 0, the curvature of the laser beam is ∞ and thus

$$q_0 = -\frac{i\pi n\omega_0^2}{\lambda} = -iz_R = \frac{A(\alpha_1 + i\beta) + B}{C(\alpha_1 + i\beta) + D}, \tag{D.6}$$

where we have used Eq. (D.3)-(D.5). Equating the real part of the right hand side of Eq. (D.6) to zero and imaginary part to $-z_R$, we find

$$\begin{aligned} (A\alpha_1 + B)(C\alpha_1 + D) + AC\beta_1^2 &= 0 \\ \frac{(C\alpha_1 + D)A\beta_1 - (A\alpha_1 + B)C\beta_1}{(C\alpha_1 + D) + C^2\beta_1^2} &= -z_R \end{aligned} \tag{D.7}$$

Eq. (D.7) can be solved for l to find

$$l = \frac{n_2 f[\beta_1^2 - \alpha(f - \alpha_1)]}{\beta_1^2 + (f - \alpha_1)^2}. \tag{D.8}$$

Substituting this value of l into Eq. (D.7) yields

$$\omega_0^2 = \frac{\lambda}{n\pi} \frac{(A\alpha_1 + B)C\beta_1 - (C\alpha_1 + D)A\beta_1}{(C\alpha_1 + D)^2 + C^2\beta_1^2}. \tag{D.9}$$

Appendix E

Publications

E.1 Papers

1. S. Afshaarvahid V. Devrelis and J. Munch, "*The Nature of Intensity and Phase Modulations in Stimulated Brillouin Scattering*", Phys. Rev. A 57, 3961 (1998).
2. S. Afshaarvahid and J. Munch, "*A Transient, 3-dimensional model of Stimulated Brillouin Scattering*", accepted for publication in the "Journal of Nonlinear Optical Physics and Materials". To be appeared in JNOPM, Vol. 9, either No. 3 or 4.

E.2 Conferences

1. S. Afshaarvahid and J. Munch, "*Transient Phase Conjugation Using Stimulated Brillouin Scattering (A Numerical Study)*", Technical Digest CLEO 99, pp 94-95 (Optical; Society of America, Washington DC,1999)
2. S. Afshaarvahid V. Devrelis and J. Munch, "*Numerical Study of Stochastic intensity fluctuations in Stimulated Brillouin Scattering*", Book of Abstracts XI AOS Conference, FP35, Adelaide, Australia December 1997.
3. S. Afshaarvahid V. Devrelis and J. Munch, "*Numerical Study of Stimulated Brillouin Scattering Initiated from Noise*", Technical Digest CLEO/Pacific

Rim’97, pp 223, Chiba, Japan, July 1997.

E.3 Paper I

S. Afshaarvahid V. Devrelis and J. Munch, "*The Nature of Intensity and Phase Modulations in Stimulated Brillouin Scattering*", Phys. Rev. A 57, 3961 (1998).

PHYSICAL REVIEW A VOLUME 57, NUMBER 5 MAY 1998

Nature of intensity and phase modulations in stimulated Brillouin scattering

Shahraam Afshaarvahid,* Vladimyros Devrelis,† and Jesper Munch
Department of Physics and Mathematical Physics, The University of Adelaide, Adelaide, South Australia 5005, Australia

(Received 14 August 1997)

The nature of stimulated Brillouin scattering (SBS) temporal modulations for a focused beam in a finite-length cell with homogeneous medium is examined numerically. The finite phonon lifetime produces deterministic oscillations at the threshold while the inclusion of the random noise as an initiation source of SBS leads to stochastic fluctuations in Stokes intensity and phase. A unified study of both modulations under different parameters is presented. The results indicate a large useful parameter space for excellent Stokes beam quality. [S1050-2947(98)05405-5]

PACS number(s): 42.65.Es, 42.65.Hw

I. INTRODUCTION

The dynamics of stimulated Brillouin scattering (SBS) has been widely investigated because of its importance in optical phase conjugation [1,2], pulse compression [3,4], and beam combination [5–7]. SBS is a nonlinear process where energy is exchanged from the laser beam to the Stokes beam through an interaction with a sound wave. When used in an optical element, SBS is usually deployed either as an amplifier with an externally applied Stokes field, or as a SBS generator. The theory of SBS amplifiers is simpler than that of SBS generators since the Stokes field is externally applied, whereas the analysis of SBS generators requires the inclusion of the thermal density fluctuations of the medium as the source for the initiation of the process. This stochastic initiation of SBS leads to fluctuations in the Stokes field's amplitude and phase [1,8–12]. These fluctuations are important in practical applications since they reduce the coherence length of the scattered beam [13] and have been observed to reduce the temporal and spatial fidelity of the SBS process [14–17]. Early experimental observations of the presence of phase jumps and amplitude fluctuations in SBS were reported in 1980 [18–20]. More recent theoretical and experimental investigations of these fluctuations in optical fibers have been made by Dianov *et al.* [9], Gaeta and Boyd [11], and Kuzin *et al.* [21]. Their investigations showed that large scale fluctuations in the Stokes intensity occur when the transit time through the interaction region is much greater than the phonon lifetime. Intensity and phase fluctuations have been investigated experimentally also for short interaction lengths typical of a focused geometry [15,13,12,16]. Simultaneous fluctuations in the Stokes amplitude and beam quality have been observed [15] as has actual variation in the phase of the Stokes beam, measured directly by heterodyne detection [13]. In addition, the effect on these simultaneous fluctuations of experimental parameters such as the interaction length and input energy have been reported [12,16]. Numerical models have also shown simultaneous occurrence of jumps in the Stokes phase and fluctuations in the Stokes reflectivity and fidelity [8,14]. Similar fluctuations were also predicted [22,23] and observed [24,25] in stimulated Raman scattering and recognized as solitons.

Most published theoretical studies of SBS have dealt with SBS amplifiers or generators in the undepleted or steady state regime where the Stokes wave was either applied externally or initiated inside the medium from a constant or localized source. In this paper we present a single unified theoretical approach to SBS in a focused cell geometry, for the transient and depleted regimes while seeded from distributed random noise typical of most practical applications. We have developed a numerical model to examine in detail how the scattered Stokes beam is initiated from noise and propagated through the medium, and what parameters affect its amplitude and phase modulation. We use a Gaussian random noise distribution [9,11] (both in space and time) as a source for the SBS process in order to simulate the actual thermal fluctuations in the density of the medium.

Our model predicts two kinds of amplitude modulation: (a) deterministic relaxation oscillations at the threshold due to finite phonon lifetime and (b) stochastic fluctuations caused by the random noise source. An extensive examination of the behavior of the deterministic oscillations includes the following parameters: phonon lifetime, focal length, immersion length, and input energy, and it reveals under what parameter regimes these oscillations result in a pulse-compressed Stokes beam. This is followed by the study of stochastic fluctuations and their dependence on parameters such as phonon lifetime, immersion length, input energy, and pulse duration. Although many authors identify these fluctuations as being due to phase jumps, our model shows that phase and intensity fluctuations are coupled via the nonlinear interaction, and thus occur simultaneously, denying the existence of a causal relationship to the phenomenon. This was determined by tracing the fluctuations back to the time of initiation. The parameter regime required for achieving excellent beam quality (amplitude and phase fidelity) is evaluated.

II. THEORY

The equations describing the SBS process are derived from Maxwell's equations for the electric fields and Navier-Stokes equation for the acoustic field inside the material. Writing the electric and acoustic fields as [26]

---

*Electronic address: shahraam@physics.adelaide.edu.au

†Present address: DSTO, Salisbury SA 5108, Australia.

1050-2947/98/57(5)/3961(11)/$15.00 © 1998 The American Physical Society

$$E_p=\frac{1}{2}[\Psi_p(z,t)e^{i(\omega_p t+k_p z)}+\Psi_p^*(z,t)e^{-i(\omega_p t+k_p z)}],$$

$$E_s=\frac{1}{2}[\Psi_s(z,t)e^{i(\omega_s t-k_s z)}+\Psi_s^*(z,t)e^{-i(\omega_s t-k_s z)}], \quad (1)$$

$$E_q=\frac{1}{2}[\Psi_q(z,t)e^{i(\omega_q t+k_q z)}+\Psi_q^*(z,t)e^{-i(\omega_q t+k_q z)}]$$

(where E_p, E_s, and E_q are the pump, Stokes, and acoustic fields, respectively), neglecting the transverse field variations, and using the slowly varying envelope approximation, the following coupled wave equations can be derived [27].

$$\left(\frac{\partial}{\partial z}-\frac{n}{c}\frac{\partial}{\partial t}\right)\Psi_p=ig_1\Psi_q\Psi_s,$$

$$\left(\frac{\partial}{\partial z}+\frac{n}{c}\frac{\partial}{\partial t}\right)\Psi_s=-ig_1\Psi_q^*\Psi_p, \quad (2)$$

$$\left(\frac{\partial}{\partial t}+\Gamma\right)\Psi_q=-ig_2\Psi_p\Psi_s^*.$$

Here g_1 and g_2 are coupling coefficients, Γ is the damping rate (i.e., $\Gamma=1/2\tau$ where τ is the phonon lifetime of the medium), and n is the refractive index of the medium.

In order to find the equations for the amplitudes and the phases of the fields we write the complex amplitudes Ψ_μ (where $\mu=p,s,q$) as

$$\Psi_\mu=A_\mu e^{-i\phi_\mu},$$

where A_μ and ϕ_μ are real functions. Substituting the new definition into the above equations results in a set of six coupled differential equations:

$$\left(\frac{\partial}{\partial z}-\frac{n}{c}\frac{\partial}{\partial t}\right)A_p=-g_1\sin(\phi_p-\phi_s-\phi_q)A_qA_s, \quad (3a)$$

$$\left(\frac{\partial}{\partial z}+\frac{n}{c}\frac{\partial}{\partial t}\right)A_s=g_1\sin(\phi_s+\phi_q-\phi_p)A_qA_p, \quad (3b)$$

$$\left(\frac{\partial}{\partial t}+\Gamma\right)A_q=g_2\sin(\phi_s+\phi_q-\phi_p)A_sA_p+f_1, \quad (3c)$$

$$\left(\frac{\partial}{\partial z}-\frac{n}{c}\frac{\partial}{\partial t}\right)\phi_p=-g_1\cos(\phi_p-\phi_s-\phi_q)\frac{A_qA_s}{A_p}, \quad (3d)$$

$$\left(\frac{\partial}{\partial z}+\frac{n}{c}\frac{\partial}{\partial t}\right)\phi_s=g_1\cos(\phi_s+\phi_q-\phi_p)\frac{A_qA_p}{A_s}, \quad (3e)$$

$$\left(\frac{\partial}{\partial t}\right)\phi_q=g_2\cos(\phi_s+\phi_q-\phi_p)\frac{A_sA_p}{A_q}+f_2. \quad (3f)$$

To represent the noise initiation of the SBS process, we have added two Langevin forces f_1 and f_2, with spatial and temporal Gaussian distributions [11]. Both f_1 and f_2 are δ correlated functions in the sense that

$$\langle f_i(z,t)f_i^*(z',t')\rangle=Q\delta(z-z')\delta(t-t'),$$

where Q is given by [10]

$$Q=\frac{2kT\rho_0\Gamma}{v^2A}.$$

Here k is the Boltzmann constant, T is the temperature, ρ_0 i mean density, v is the velocity of sound in the material, an A is the cross sectional area of the interaction region.

For the phase-locked condition [i.e., $\sin(\phi_s+\phi_q-\phi_p)=1$ and the steady state regime of SBS [i.e., ignoring al $(\partial/\partial t)A_\mu$], Eq. (3b) can be written as

$$\frac{\partial}{\partial z}A_s=\frac{g_1g_2}{\Gamma}A_p^2A_s, \quad (4$$

which has a solution of $A_s=A_{s0}\exp[(g_1g_2/\Gamma)A_p^2l_{\mathrm{imm}}]$ valid near threshold and without pump depletion. This leads directly to the usual expression for the steady state gain, given by $G=gI_pl_{\mathrm{imm}}$, where I_p is the input pump intensity, l_{imm} is the active medium immersion length, and $g=g_1g_2\Gamma^{-1}$.

Some authors (e.g., [28,29]) have used the phase-locked condition for which SBS has the highest gain, i.e., $\phi_p-\phi_s-\phi_q=\pi/2$. When SBS starts from noise, a random noise distribution of $\phi_p-\phi_s-\phi_q$ is initially present. But as the phase-locked waves (those with $\phi_p-\phi_s-\phi_q=\pi/2$) have the highest gain in the medium, they suppress other Stokes waves with unlocked phases. By applying this condition to Eqs. (3), they are simplified to a set of three real coupled equations for the amplitudes. However, in order to explain the experimental observation of the simultaneous occurrence of intensity fluctuations and phase jumps [13], we have retained the complex equations since this is the only way that the phase of the Stokes field can be coupled to its intensity.

Equations (3) are nonlinear due to the terms $\sin(\phi_s+\phi_q-\phi_p)$ or $\cos(\phi_p-\phi_s-\phi_q)$. Although the behavior of the fields and their phases is seen better by these equations, and we use them whenever we want to provide a qualitative explanation, solutions of the equations require that we rewrite them for the real and imaginary parts of the fields. Using

$$\Psi_\mu=W_\mu+iV_\mu,$$

the equations for the real and imaginary parts of the fields are

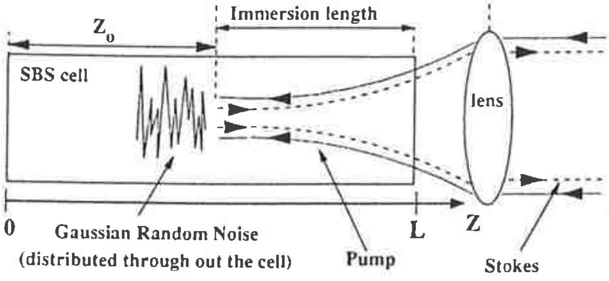

FIG. 1. The geometry used for the SBS process.

$$\left(\frac{\partial}{\partial z}-\frac{n}{c}\frac{\partial}{\partial t}\right)W_p=-g_1(W_qV_s+V_qW_s),$$

$$\left(\frac{\partial}{\partial z}+\frac{n}{c}\frac{\partial}{\partial t}\right)W_s=g_1(W_qV_p-V_qW_p),$$

$$\left(\frac{\partial}{\partial t}+\Gamma\right)W_q=-g_2(W_pV_s-V_pW_s)+f_1,$$

$$\left(\frac{\partial}{\partial z}-\frac{n}{c}\frac{\partial}{\partial t}\right)V_p=g_1(W_qW_s-V_qV_s), \qquad (5)$$

$$\left(\frac{\partial}{\partial z}+\frac{n}{c}\frac{\partial}{\partial t}\right)V_s=g_1(W_qW_p+V_qV_p),$$

$$\left(\frac{\partial}{\partial t}+\Gamma\right)V_q=-g_2(W_pW_s+V_pV_s)+f_2.$$

The focusing geometry required for simulation of experiments is introduced using an approach similar to that of Menzel and Eichler [30]. Although SBS is primarily used to compensate for optical aberrations, we have chosen not to nclude spatial aberrations in this treatment, but concentrate entirely on temporal fluctuations or "temporal fidelity" of he Stokes beam. This is important, because lack of temporal idelity leads to degradation of the Stokes return and hence a eduction in average reflectivity and efficiency of a phase conjugated laser system [14–16]. We are thus using spatially unaberrated Gaussian beams for both pump and Stokes ields, and we have made the further approximation that both hese fields have the same Gaussian beam parameters (see ig. 1):

$$\omega^2(z)=\omega_0^2\left[1+\left(\frac{(z-z_0)\lambda}{\pi\omega_0^2 n}\right)^2\right],$$

where ω_0 is the radius at the waist of the beam, λ is the wavelength, and n is the appropriate index of refraction as a unction of z. This is a reasonable approximation in an efficient phase conjugating system where the fields are well bove threshold and is justified by experimental results howing that the beam quality and divergence of the Stokes eam are indistinguishable from those of the pump beam when well above threshold. For an unaberrated beam this is nly an approximation but is justified in our case where we concentrate on the temporal fidelity only.

As a result, the pump and Stokes intensities, $I_p=W_p^2$ V_p^2 or $I_s=W_s^2+V_s^2$, are changing not only because of the onlinear interaction with the material but also because of e change in area of the beams. Keeping in mind that for Gaussian beam the electric field amplitude has $\omega(z)$ in e denominator, we add $-[W_\nu/\omega(z)](\partial/\partial z)\,\omega(z)$ or $[V_\nu/\omega(z)](\partial/\partial z)\omega(z)$ to the right hand side of equations r W_ν or V_ν ($\nu=p$ or s) to represent the change in the tensity due to focusing geometry [30]. Defining

$$\Psi_\nu=\frac{\Psi'_\nu}{\omega(z)}=\frac{W'_\nu}{\omega(z)}+i\frac{V'_\nu}{\omega(z)},$$

$$\Psi'_\nu=W'_\nu+iV'_\nu,$$

and hence,

$$W_\nu=\frac{W'_\nu}{\omega(z)},$$

$$V_\nu=\frac{V'_\nu}{\omega(z)},$$

it can be easily seen that $|\Psi'_\nu|^2=|\Psi_\nu|^2\omega^2(z)$ is the local power of the pump or the Stokes fields. Adding $-[W_\nu/\omega(z)](\partial/\partial z)\,\omega(z)$ or $-[V_\nu/\omega(z)](\partial/\partial z)\omega(z)$ to the right hand side of equations for W_ν or V_ν [i.e., Eqs. (5)] and rewriting these equations for prime fields, we find

$$\left(\frac{\partial}{\partial z}-\frac{n}{c}\frac{\partial}{\partial t}\right)W'_p=-g_1(W_qV'_s+V_qW'_s), \qquad (6a)$$

$$\left(\frac{\partial}{\partial z}+\frac{n}{c}\frac{\partial}{\partial t}\right)W'_s=g_1(W_qV'_p-V_qW'_p), \qquad (6b)$$

$$\left(\frac{\partial}{\partial t}+\Gamma\right)W_q=-\frac{g_2}{\omega^2(z)}(W'_pV'_s-V'_pW'_s)+f_1, \qquad (6c)$$

$$\left(\frac{\partial}{\partial z}-\frac{n}{c}\frac{\partial}{\partial t}\right)V'_p=g_1(W_qW'_s-V_qV'_s), \qquad (6d)$$

$$\left(\frac{\partial}{\partial z}+\frac{n}{c}\frac{\partial}{\partial t}\right)V'_s=-g_1(W_qW'_p+V_qV'_p), \qquad (6e)$$

$$\left(\frac{\partial}{\partial t}+\Gamma\right)V_q=-\frac{g_2}{\omega^2(z)}(W'_pW'_s+V'_pV'_s)+f_2. \qquad (6f)$$

We see that the new equations have a form similar to Eqs. (5). The only difference is that the prime fields are the power components instead of intensity components in Eqs. (5). The same procedure can be done for Eqs. (3) to get the following equations for the Stokes, pump, and acoustic grating power:

$$\left(\frac{\partial}{\partial z}-\frac{n}{c}\frac{\partial}{\partial t}\right)A'_p=-g_1\sin(\phi_p-\phi_s-\phi_q)A_qA'_s, \qquad (7a)$$

$$\left(\frac{\partial}{\partial z}+\frac{n}{c}\frac{\partial}{\partial t}\right)A'_s=g_1\sin(\phi_s+\phi_q-\phi_p)A_qA'_p, \qquad (7b)$$

$$\left(\frac{\partial}{\partial t}+\Gamma\right)A_q=g_2\sin(\phi_s+\phi_q-\phi_p)\frac{A'_sA'_p}{\omega^2(z)}+f_1. \qquad (7c)$$

The equation for the acoustic field shows how the amplitude of the field depends on the intensity of the Stokes and pump waves, implying a high acoustic field at high intensities of the pump and the Stokes fields.

Integrating the phonon fields [Eqs. (6c) and (6f)] and substituting in the rest of Eqs. (6), reduces the set of equations

(6a)–(6f) to four coupled differential equations for the field amplitude. The numerical analysis starts with these four equations. An efficient noniterative algorithm is used in which Simpson's rule is applied to approximate the phonon's integral and an implicit finite differencing in time and backward differencing scheme in space are used to write the equations for discrete field amplitudes W_{pj}^{m}, V_{pj}^{m}, W_{sj}^{m}, and V_{sj}^{m}, where $m=0,1,2,\ldots,M$ are time indices ($t=m\Delta t$) and $j=0,1,2,\ldots,n+1$ are space indices ($z=j\Delta z$) [29]. Field vectors at the time $(m+1)\Delta t$ are defined as

$$\vec{W}_p^{\,m+1}=\begin{pmatrix} W_{p1}\\ W_{p2}\\ \cdot\\ \cdot\\ \cdot\\ W_{pn}\end{pmatrix}^{m+1}, \quad \vec{V}_p^{\,m+1}=\begin{pmatrix} V_{p1}\\ V_{p2}\\ \cdot\\ \cdot\\ \cdot\\ V_{pn}\end{pmatrix}^{m+1},$$

$$\vec{W}_s^{\,m+1}=\begin{pmatrix} W_{s2}\\ W_{s3}\\ \cdot\\ \cdot\\ \cdot\\ W_{sn+1}\end{pmatrix}^{m+1}, \quad \vec{V}_s^{\,m+1}=\begin{pmatrix} V_{s2}\\ V_{s3}\\ \cdot\\ \cdot\\ \cdot\\ V_{sn+1}\end{pmatrix}^{m+1},$$

where $n+1$ is the total number of discrete points in space and W_{pn+1}, V_{pn+1}, W_{s1}, and V_{s1} are the initial values at boundaries.

Using the linearization scheme defined by Chu *et al.* [29], we obtain the final form of the set of algebraic equations for the vector fields as

$$\begin{aligned} &A^{m}\vec{W}_p^{m+1}+C^{m}\vec{W}_s^{m+1}+D^{m}\vec{V}_s^{m+1}=\vec{V},\\ &E^{m}\vec{W}_s^{m+1}+F^{m}\vec{W}_p^{m+1}+G^{m}\vec{V}_p^{m+1}=\vec{U},\\ &A^{m}\vec{V}_p^{m+1}-D^{m}\vec{W}_s^{m+1}+C^{m}\vec{V}_s^{m+1}=\vec{W},\\ &E^{m}\vec{V}_s^{m+1}-G^{m}\vec{W}_p^{m+1}+F^{m}\vec{V}_p^{m+1}=\vec{Z}. \end{aligned} \tag{8}$$

Here, A^m, C^m, E^m, F^m, D^m, and G^m are $n\times n$ upper or lower tridiagonal matrices evaluated at time $m\Delta t$ and $\vec{V}$, $\vec{U}$, $\vec{W}$, and $\vec{Z}$ are $n\times 1$ vectors containing boundary conditions on the pump and Stokes at time $t=(m+1)\Delta t$. This set of equations can be solved numerically without the need for iteration. The matrix coefficients and vectors $\vec{V}$, $\vec{U}$, $\vec{W}$, and $\vec{Z}$ are evaluated recursively using the initial values of the Stokes and pump fields at $t=0$. Here the field amplitudes at any time slot $m+1$ have been determined from those at the preceding time slot m. To justify the validity of the linearization assumption, we used the field amplitudes at time slot $m+1$ to reevaluate iteratively the nonlinear coefficient involved in the differential equations. An improvement of only 4% was achieved after five iterations.

Solutions of Eqs. (8) are found for a Gaussian pump pulse of the form $E_0\exp\{-2[(t-t_0)/t_p]^2\}$, where t_p is the pulse width. Referring to Fig. 1, we apply the following geometrical and material parameters to examine the typical results of the SBS process: cell length 60 cm, focal length 50 cm, immersion length 15 cm, initial waist of the beam 0.4 cm, gain of the medium 0.0063 cm/MW, input energy 320 mJ, full width at half maximum (FWHM) pulse length 20 ns, phonon lifetime 0.85 ns, and index of refraction, $n=1.0$, with results shown in Fig. 2.

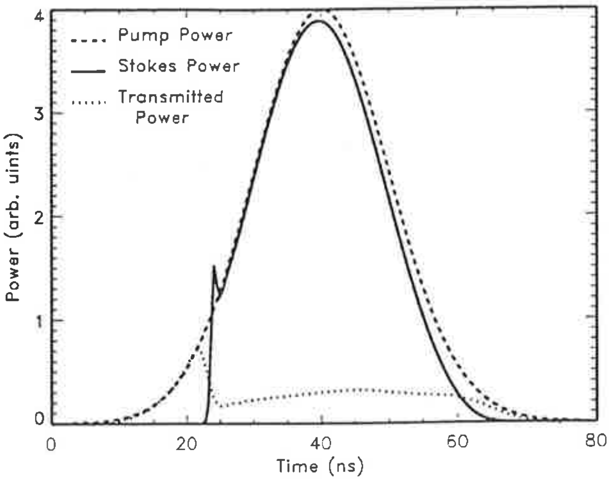

FIG. 2. Typical results for the Stokes, pump, and transmitted pulse.

III. RESULTS AND DISCUSSION

Depending on the geometry of the SBS process and the energy of the input pulse, our model results in Stokes oscillations or fluctuations similar to those observed experimentally [18–20,15–17]. The intensity modulation can be categorized into two groups: (a) deterministic amplitude oscillations at the time when the energy of the pump reaches the threshold energy and (b) stochastic fluctuations due to noise in amplitude and phase of the Stokes beam.

A. Deterministic threshold oscillation

The finite phonon lifetime provides an energy interchange mechanism between the Stokes and laser field via the acoustic field. In the case of Gaussian pump beams, it takes some time for the energy contained in the pump to reach the threshold energy for Stokes initiation. At the threshold, the Stokes power increases very rapidly and overshoots the pump power, resulting in the depletion of the pump field and reduction of gain. Because of this gain reduction the Stokes power drops, causing an increase in the pump energy which in turn causes an increase in the Stokes field again. This energy interchange between the Stokes and pump fields continues and resembles a relaxation oscillation (see Fig. 3). The rate of this energy interchange is controlled by the reaction time of the acoustic field, i.e., phonon lifetime. Such an energy interchange mechanism has also been discussed in Refs. [4] and [29]. Chu *et al.* [29] report relaxation oscillations which are visible in the transmitted pulse. However, our simulation results show that for a long cell and a geometry in which the laser beam has been focused deeply into the cell, relaxation oscillation should be visible in the Stokes return as shown in Fig. 3.

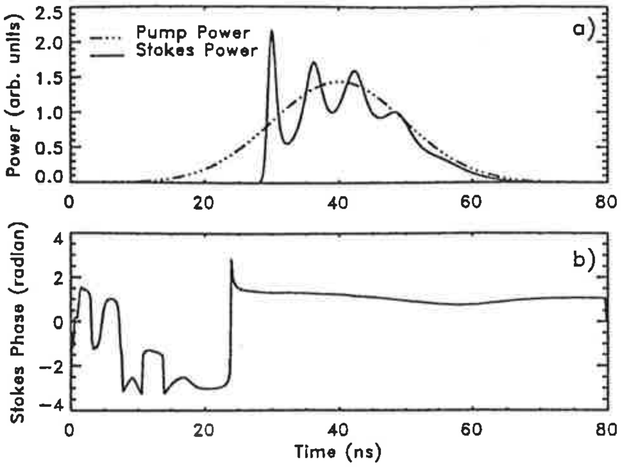

FIG. 3. (a) Typical threshold oscillation in the Stokes beam obtained for the following parameters: cell length 100 cm, focal length 100 cm, immersion length 70 cm, phonon lifetime 0.85 ns, medium gain 0.006 cm/MW, FWHM pulse length 20 ns, and input energy 114 mJ. (b) shows no corresponding variation in the phase of the Stokes.

In order to categorize the behavior of threshold oscillation we use the following parameters to run the simulation: Cell length 100 cm, focal length 100 cm, immersion length 70 cm, phonon lifetime 0.85 ns, gain of the medium 0.006 cm/MW, FWHM pulse length 20 ns, and input energy 114 mJ. Any changes to these parameters are specified in the captions of the figures. Figure 3 shows a typical threshold oscillation in the Stokes beam. Different parameters such as phonon lifetime, laser intensity at the focal point, and immersion length affect the behavior of the threshold oscillation. There are no phase jumps predicted corresponding to these oscillations.

1. Effect of phonon lifetime on the threshold oscillation

If the finite phonon lifetime is responsible for the relaxation oscillation at the threshold energy, we would expect that the behavior of the threshold oscillations depends on this parameter. Figure 4 shows the threshold oscillation for two different phonon lifetimes. Defining T_0 to be the time interval over which the threshold oscillations are observable (see Fig. 4), our simulation predicts that T_0 is reduced for long phonon lifetime (see Fig. 5). It is seen that for longer phonon lifetimes, oscillations in the Stokes return come to an equilibrium faster than those for short phonon lifetimes. Our model permits a detailed investigation of the above mentioned relaxation oscillation and the role of the phonon lifetime.

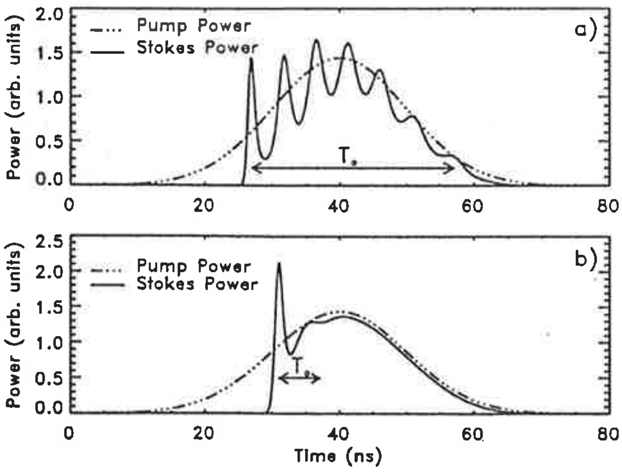

FIG. 4. Threshold oscillations are reduced for longer phonon lifetime. (a) Phonon lifetime is 0.5 ns and (b) phonon lifetime is 1.25 ns. Other parameters are as those of Fig. 3.

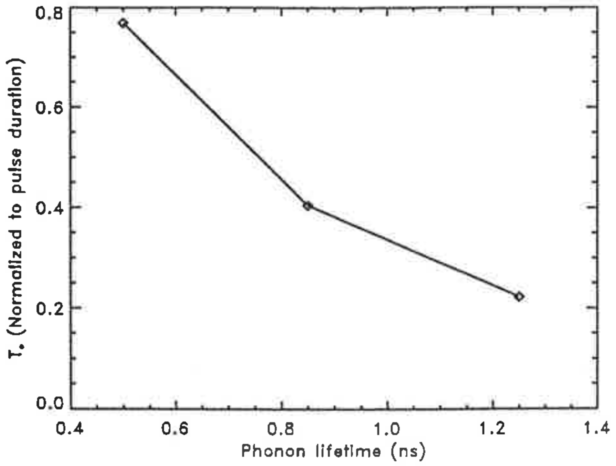

FIG. 5. A shorter relaxation oscillation is achieved for long phonon lifetime. The graph shows how T_0 (a time interval over which the oscillations are visible, see Fig. 4) is reduced for long phonon lifetime.

The acoustic field is described by Eq. (3c). For early times in the process, the first source term in the right hand side of the equation may be ignored and for the second term we can write $f_1=\Sigma_k a_k \sin \omega_k t$. Equation (3c) can then be solved as

$$\Psi_q=\Psi_{0q}e^{-\Gamma t}+\sum_k a_k' \sin \omega_k t+\sum_k b_k' \cos \omega_k t,$$

in which $a_k'=a_k\Gamma(\Gamma^2+\omega_k^2)^{-1}$ and $b_k'=-a_k\omega_k(\Gamma^2+\omega_k^2)^{-1}$. In the limit of a long phonon lifetime, i.e., $\Gamma\rightarrow 0(\tau\rightarrow\infty)$, we find $a_k'=0$ and $b_k'=-a_k/\omega_k$, which results in a solution of $\Psi_q=\Sigma_k-(a_k/\omega_k)\cos \omega_k t$ for the acoustic field. Comparing this result with the source term f_1, it is seen that in the limit of a large phonon lifetime the medium will not respond to the rapid fluctuations in the source term, but rather responds to the integral of rapid changes. In the other limit of $\Gamma\rightarrow\infty(\tau\rightarrow 0)$, $b_k'\rightarrow 0$ and $a_k'=a_k/\Gamma$ which gives a solution of $\Psi_q=\Sigma_k(a_k/\Gamma)\sin \omega_k t$. In this case the medium can cope with the rapid changes in the source term, thus resulting in a modulated Stokes pulse. The above discussion is applicable not only for the beginning of the process but also for any rapid changes in the source fields of the acoustic field. The phonon lifetime thus represents a measure of the inertia of the acoustic field. The larger the phonon lifetime, the higher is the inertia of the acoustic field and the slower is the response of the medium to the rapid changes in the Stokes and the laser field.

2. Effect of laser intensity at the focal plane

According to Eq. (7c), the amplitude of the acoustic field depends on the intensity of the input pulse. A shorter focal

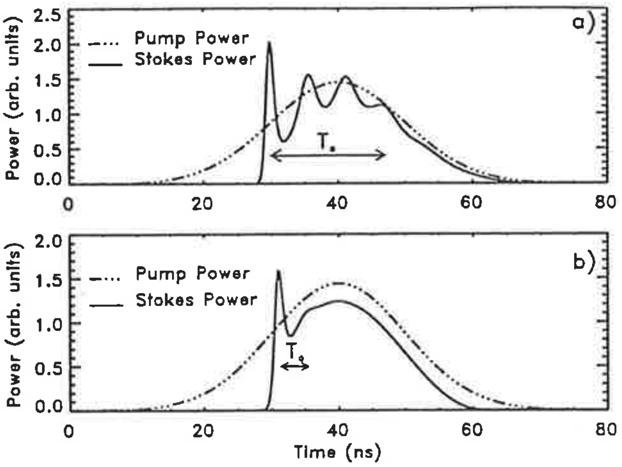

FIG. 6. Smaller focal spot (higher intensity) results in a suppression of threshold oscillations. Oscillations are reduced in (b) (focal length 60 cm) in comparison with (a) (focal length 90 cm). Other parameters as in Fig. 3.

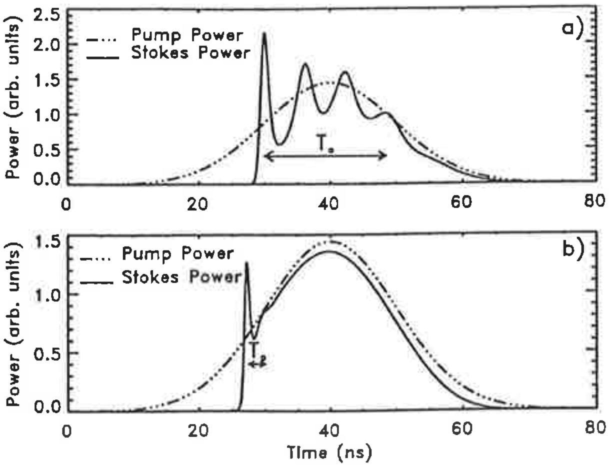

FIG. 7. Modulations present in (a) (focal length 100 cm, immersion length 40 cm) are almost suppressed in (b) (focal length 100 cm, immersion length 10 cm). Shorter immersion length provides a better suppression. Other parameters as in Fig. 3.

length results in a higher intensity at the focal plane hence a higher power acoustic wave. As a result of this strong acoustic field, the Stokes amplitude does not reduce as quickly after overshooting, which in turn causes a shorter duration of the relaxation oscillation. This is illustrated in Fig. 6.

3. *Effect of immersion length*

Kuzin *et al.* [21] have discussed the influence of the depletion length (the length over which the laser pump beam experiences most of its depletion) on the suppression of fluctuations in the Stokes field. They emphasized that if the propagation time through the depletion length $T_{l_{\mathrm{dep}}}$ is smaller than the temporal variation of the Stokes field at the beginning of the depletion region T_s, a smoothing of the Stokes field towards the output of the cell would take place. In this case we are in the steady state regime of SBS, and can rewrite Eqs. (3) in the phase-locked condition, as

$$\begin{aligned} \frac{\partial}{\partial z} I_p &= 2 g I_p I_s, \\ \frac{\partial}{\partial z} I_s &= 2 g I_p I_s. \end{aligned} \tag{9}$$

Moving the origin of z to the entrance of the cell and writing $I_p(z)=I_s(z)+I_l$ [31] (where I_l is a constant indicating the degree of pump depletion), we can solve the differential equations (9) to find

$$I_s(z)=\frac{I_l I_s(0)}{I_p(0)\exp(-2gI_l z)-I_s(0)}.$$

Defining the depletion length as the length over which the Stokes intensity drops to $1/e$ of its maximum [i.e., $I_s(l_{\mathrm{dep}})=(1/e)I_s(0)$], we find

$$l_{\mathrm{dep}}=\frac{1}{2gI_l}\ln\left(1+\frac{I_l(e-1)}{I_p(0)}\right),$$

which can be approximated as

$$l_{\mathrm{dep}}\approx\frac{l_{\mathrm{imm}}}{G} \tag{10}$$

for highly depleted pump (i.e., $I_l\rightarrow 0$), and using the definition of G.

A parallel physical explanation of conditions under which temporal fluctuations are suppressed is given by Gaeta and Boyd [11]. They discuss how a spike with temporal variation $T_s=\Gamma^{-1}$ is suppressed when $G>\Gamma T_t$ (where $T_t=nl_{\mathrm{imm}}c^{-1}$ is the transit time and $G=gI_p l_{\mathrm{imm}}$ is the steady state gain). This condition ($G>\Gamma T_t$) is similar to the Kuzin *et al.* [21] condition (i.e., $T_{l_{\mathrm{dep}}}<T_s$), if we use the depletion length given by Eq. (10).

Keeping constant all other parameters and varying only the immersion length, by changing the cell to lens separation, we can examine the effect of immersion length on the threshold oscillations. Figure 7 shows the behavior of the threshold oscillation for two different immersion lengths. For a smaller immersion length, Fig. 7(b), the depletion region of the pump beam is confined to a small region at the entrance of the cell resulting in a shorter relaxation oscillation.

It thus appears possible to use the advantages of a short focal length and a short immersion length to smooth out the oscillations. These conditions are confirmed to provide the best temporal fidelity of pump pulse in SBS process, Fig. 8, and appear to agree with preliminary experimental results [32]. A more complete experimental investigation is planned for a later publication.

4. *Pulse compression*

As mentioned previously the threshold relaxation oscillation is due to the energy interchange between the pump and the Stokes fields. We can expect to achieve pulse compression if we do not provide the appropriate amount of energy for the Stokes pulse to rebuild after the first impulse of relaxation oscillation. Figure 9 shows how the relaxation oscillation converts to a compressed pulse as input energy is reduced from (a) to (d). The process of pulse compression can be better seen if we look at the three-dimensional (3D) graph

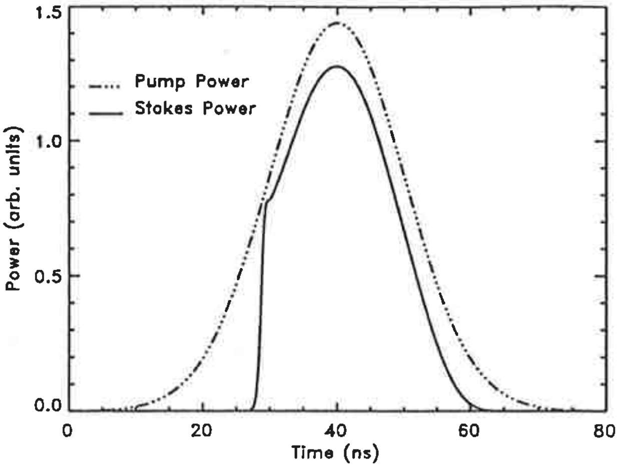

FIG. 8. Threshold oscillations disappear for short focal length and immersion length. Immersion length 20 cm and focal length 60 cm, other parameters as standard set shown in Fig. 3.

of the Stokes power, Fig. 10. At early times of the process, the center of maximum reflectivity (maximum of the Stokes pulse) is close to the focal region. This center moves towards the entrance of the cell at a later time. As a result, latter parts of the incoming pulse are traveling a shorter distance before generating the Stokes return, resulting in pulse compression [3,4].

B. Stochastic fluctuations of phase and amplitude

Noise initiation of the SBS process results in large scale fluctuations in the Stokes output. These fluctuations are of stochastic nature in the sense that there is a random probability for the occurrence of the fluctuations as well as for their temporal position in the output Stokes pulse. Corresponding and simultaneous to these fluctuations in the Stokes power, there are some rapid changes in the Stokes phase (see Fig. 11). The simultaneous occurrence of jumps in the Stokes phase and fluctuations in the Stokes power can be understood from the main equations governing SBS [Eqs. (3)]. On the right hand side of these equations there are two effective gain terms, $g\ \sin(\phi_q+\phi_s-\phi_p)$ or $g\ \cos(\phi_q+\phi_s-\phi_p)$ which are affected by rapid changes in phase of the fields. Figure 11(b) shows how the normalized effective gain $g\ \sin(\phi_q+\phi_s-\phi_p)$ suffers a reduction at the time when a phase jump occurs in the Stokes field. Depending on the size of the phase jump and the phase behavior of the pump and acoustic field, the effective gain can be reduced or even become negative, which interchanges the role of Stokes and pump field, i.e., the pump field gains while the Stokes field depletes. This is similar to what happens in the generation of solitons in stimulated Raman scattering [33]. The final temporal position of phase jumps as well as the shape of the fluctuations in the output of the Stokes phase and power depend on how they propagate and amplify from the initiation point (focal

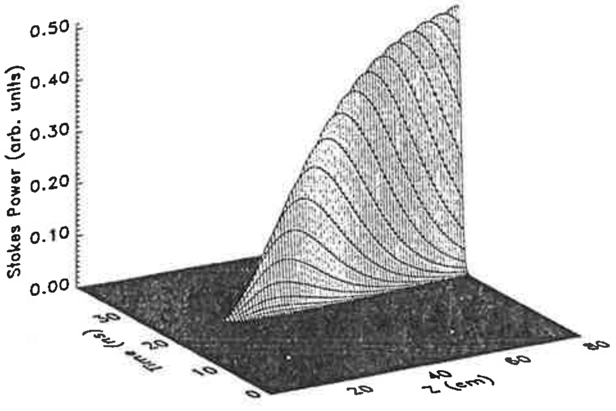

FIG. 10. 3D graph of pulse compression [(d) in Fig. 9]. Stokes power in time and space shows how the center of maximum reflectivity moves towards the entrance of the SBS cell ($z=80$ cm) resulting in pulse compression. Parameters as in Fig. 9.

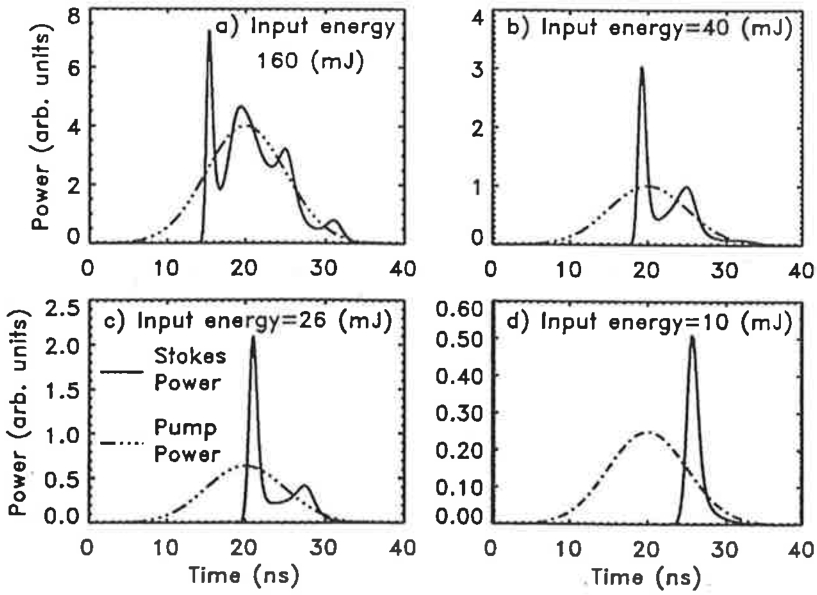

FIG. 9. Pump and Stokes power as function of time at the entrance to the cell. By reducing the pump energy, we remove extra oscillations from the threshold oscillations, resulting in a pulse-compressed beam. Cell length 80 cm, focal length 80 cm, and immersion length 70 cm with all other parameters as in Fig. 3. In (d) the delay in peak Stokes and peak pump is due to the round-trip time of the cell and building to threshold.

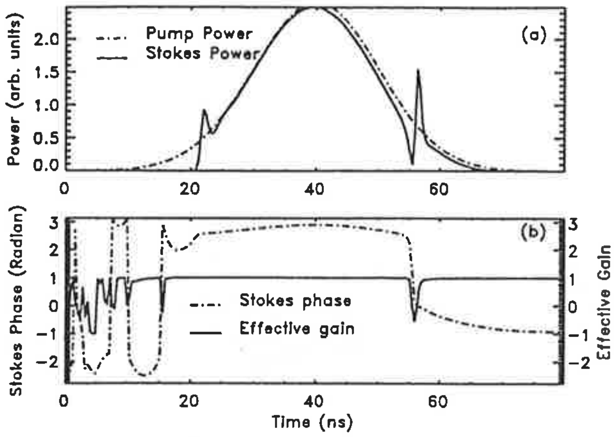

FIG. 11. Corresponding and simultaneous to each fluctuation in the Stokes output, (a), there is a jump in the Stokes phase [dashed curve in (b)]. Parameters are set as cell length 60 cm, focal length 60 cm, immersion length 30 cm, phonon lifetime 0.85 ns, gain of the medium 0.0063 cm/MW, refractive index 1.36, FWHM pulse length 20 ns, and input energy 119 mJ.

point) towards the entrance of the cell. Stokes pulses, initiated from noise, are amplified in two main regions as they propagate towards the output of the cell. In the first region, initial amplification and spectrum narrowing of the Stokes beam growing from noise take place [20,34,35,11,36,21]. The second region of length $l_{\rm dep}$ [Eq. (10)] is where the final amplification of the Stokes beam to a level approximately equal to the pump power occurs. The final Stokes output can be greatly affected by the dynamic processes in the depletion region. As previously discussed, this region plays a crucial role in the suppression of fluctuations in the Stokes signal when $T_{l_{\rm dep}} < T_s$. For $T_{l_{\rm dep}} > T_s$, however, fluctuations in the Stokes pulse experience amplification and spectrum changes, and appear in the final output [21]. It has been shown that different spectra of the fluctuations in the Stokes pulse experience different gain depending on the phonon lifetime and the length of this region [36,21]. As a result, the output spectrum of the fluctuations is different from the input when propagating through the depletion region [36,21]. Considering this and the fact that the depletion lengths $l_{\rm dep}$ corresponding to different temporal parts of the Stokes beam are different [see Eq. (10), where the gain $G(t)=gI_p(t)l_{\rm imm}$ is a function of time], lead to changes in the shape of fluctuations as well as the temporal position of corresponding phase jumps in propagating through the depletion region. The results from our model also display such behavior, as shown in Fig. 12. It shows the temporal position of the phase jump and the beginning of the fluctuation in Fig. 11 as a function of time at different positions in the cell.

The focusing geometry of the SBS cell, input energy, and phonon lifetime of the material affect the phase jump fluctuations. Due to the stochastic nature of the fluctuations, the width, magnitude, and the number of fluctuations vary from pulse to pulse. As a result, we have chosen the fraction of the Stokes energy contained in the fluctuations, i.e., $\langle E_{\rm fluc}/E_{\rm output}\rangle$ (where $\langle\ \rangle$ means statistical average over all number of pulses) as the best parameter to show the importance of the fluctuations to a practical deployment of SBS in a laser system. Unless otherwise stated, the following parameters are applied for the numerical simulations: cell length 60 cm, focal length 60 cm, immersion length 30 cm, phonon lifetime 0.85 ns, input beam radius at window 0.3 cm, gain of the medium 0.0063 cm/MW, input energy 119 mJ, FWHM pulse length 20 ns, and refractive index 1.36.

1. Phonon lifetime effect on the phase jump fluctuations

As was previously discussed, the phonon lifetime is a measure of the acoustic field inertia. For a medium with a long phonon lifetime, the acoustic field cannot respond quickly to the rapid fluctuations in the noise initiated Stokes field, and it thus broadens and smoothens out the fluctuations in the Stokes field. To examine the effect of phonon lifetime

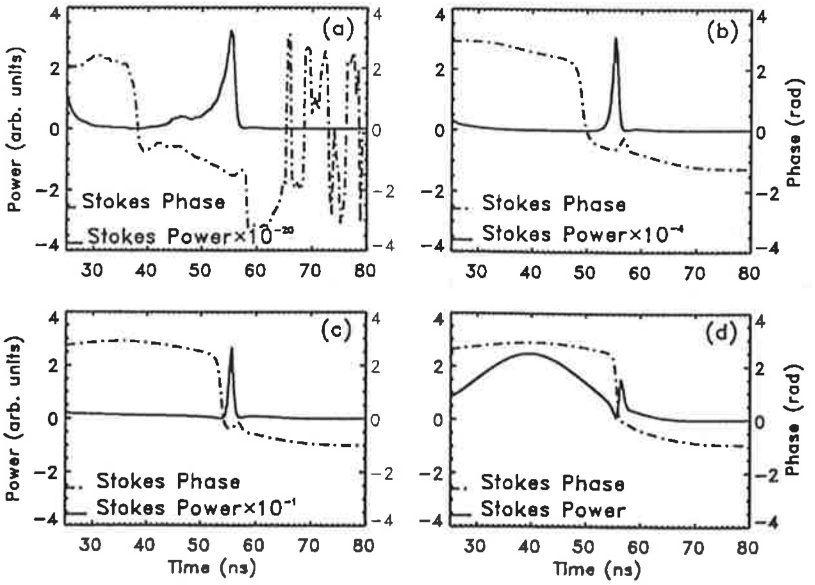

FIG. 12. The temporal position of phase jump and the beginning of the amplitude fluctuation (in Fig. 11) as they initiate at about $z=0.46L$ (a) inside the cell (where L is the cell length) and propagate through points $z=0.56L$ (b) and $z=0.71L$ (c) to the entrance of the cell (d).

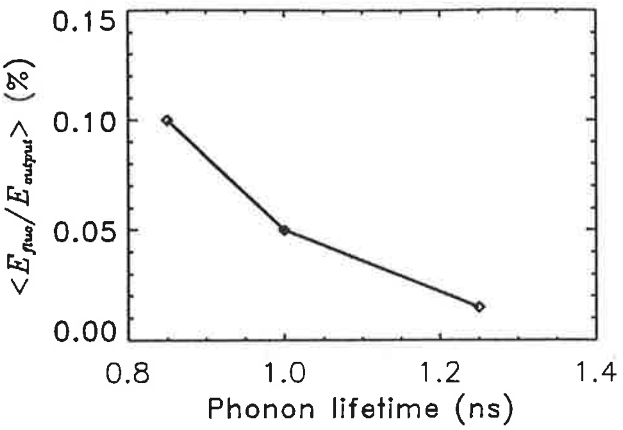

FIG. 13. Averaged fluctuation's energy (normalized to output energy) reduces for longer phonon lifetimes. Other parameters are as in Fig. 11.

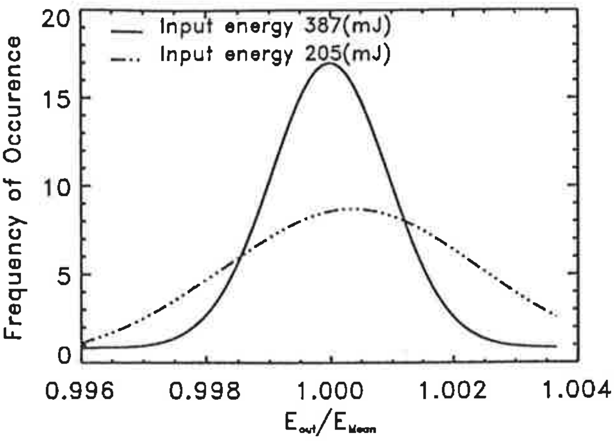

FIG. 15. Histogram of output energies (normalized to the mean) for two different energies 387 mJ and 205 mJ. Operating at high input energy reduces the effect of fluctuations.

on the phase jump fluctuations, the simulation model was run with different initial noise distributions for three different phonon lifetimes. The fluctuation energy (normalized to the output energy and averaged over a certain number of shots) is calculated for these different phonon lifetimes. Figure 13 shows how the energy of the fluctuations decreases for higher phonon lifetime, indicating a better suppression of fluctuations for long phonon lifetimes.

2. *Effect of immersion length*

As mentioned previously, the two key parameters in suppressing the fluctuations are the propagation time through the depletion region $T_{l_{\mathrm{dep}}}$ and the temporal variation of Stokes signal T_s which reaches the depletion region. In the case when $T_{l_{\mathrm{dep}}} < T_s$ the fluctuations in the Stokes signal are suppressed as they pass through the depletion region while in the other case, $T_{l_{\mathrm{dep}}} > T_s$, they are magnified and appear in the final Stokes output. The depletion length l_{dep} depends (roughly) on the steady state gain G and the immersion length l_{imm} [see Eq. (10)]. By controlling G and l_{imm} we are thus able to change the length of depletion region. From the condition $T_{l_{\mathrm{dep}}} > T_s$, it is clear that reducing $T_{l_{\mathrm{dep}}}$ implies a reduction in the number of fluctuations as well as their durations in the final Stokes output.

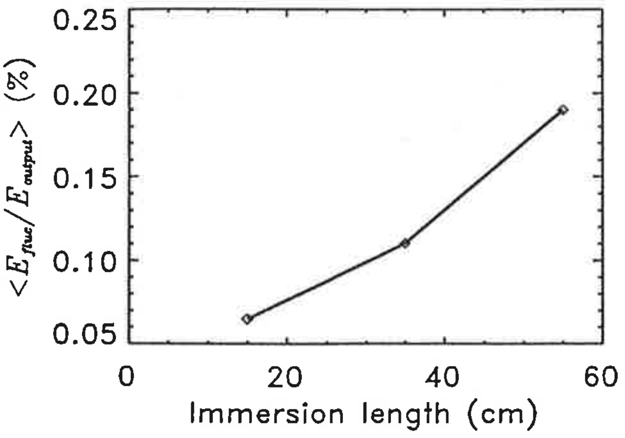

FIG. 14. The effect of the energy fluctuations, measured by $\langle E_{\mathrm{fluc}}/E_{\mathrm{output}}\rangle\%$, is reduced for shorter immersion lengths (constant focal length and large cell to lens separation).

A shorter depletion length can be obtained for a short immersion length (achieved by long cell-lens separation) and as a result, we would expect a better suppression of fluctuations. Figure 14 shows how averaged fluctuation energy $\langle E_{\mathrm{fluc}}/\bar{E}_{\mathrm{out}}\rangle\%$ (normalized to output energy) changes as a function of the immersion length. We thus conclude that a small immersion length achieved by large cell to lens separation provides better suppression of fluctuations.

3. *Effect of input energy*

Another parameter that can affect the depletion length is input energy. Higher input energy results in a higher gain G, which in turn reduces the depletion length l_{dep} of the SBS. As discussed above, we thus expect that fluctuations in the output Stokes beam have smaller duration, i.e., they carry less energy. In order to examine the effect of input energy, we have studied the output Stokes beam of 500 simulated pulses with different initial noise distribution and at different energies. Considering the histogram of $E_{\mathrm{out}}/(\bar{E}_{\mathrm{out}})$ for these 500 pulses, where $\bar{E}_{\mathrm{out}}$ is the mean energy of all output

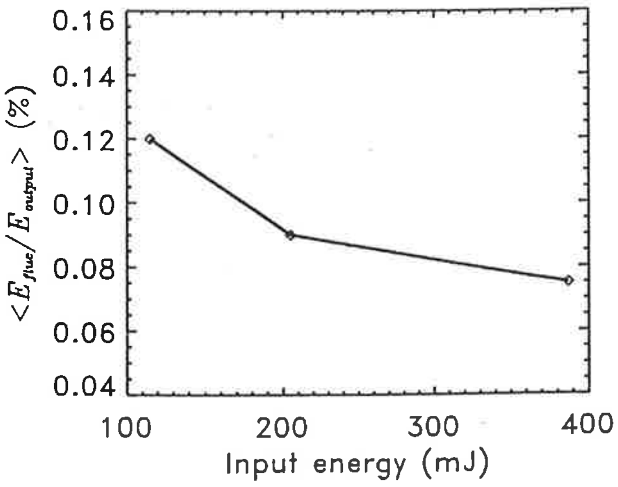

FIG. 16. A reduction in averaged fluctuation energy $(\langle E_{\mathrm{fluc}}/E_{\mathrm{output}}\rangle\%)$ occurs at high energies.

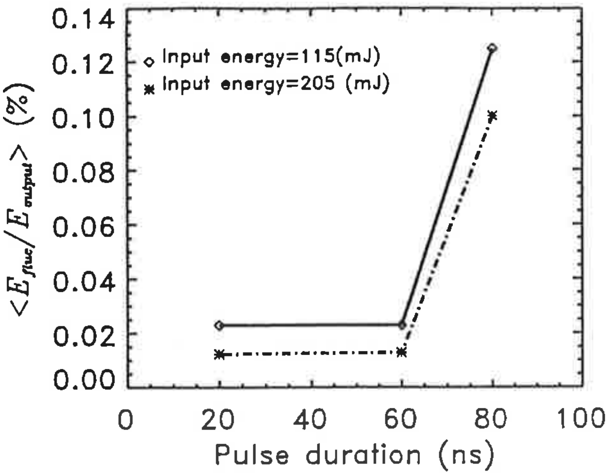

FIG. 17. For a constant energy, reducing the duration of the input pulse dramatically suppresses the fluctuation in the output Stokes. The effect of pulse duration on the suppression of fluctuations is shown for two energies: 115 mJ and 205 mJ.

pulses, and fitting a Gaussian function to it, we find that the width of the Gaussian fit is reduced at higher energy, i.e., the variation in output energy per pulse around the mean value is reduced for high energy (see Fig. 15). Another parameter that can show how fluctuations are suppressed for high energies is the average of the fluctuation energy (normalized to output energy). Simulation results in Fig. 16 show a reduction in the averaged fluctuation energy for higher input energies.

4. *Effect of pulse duration*

In the above section, we kept the duration of the input pulse constant and we studied the effect of parameters such as input energy and beam area on the fluctuations. In order to observe the role of pulse duration, we have chosen to keep the input energy of the pulse constant and reduced the pulse duration, i.e., we increased the peak injected power. Simulation results show a dramatic reduction in the number of fluctuations for short pulse durations which in turn results in a smaller averaged fluctuation energy (Fig. 17).

IV. CONCLUSION

To describe different kinds of temporal amplitude and phase modulations in SBS, we extended the plane-wave equations for complex fields describing SBS in a finite cell to include focusing geometry and initiation from a Gaussian random noise distributed over space and time. Two kinds of modulations were found: (1) Deterministic relaxation oscillation at the threshold energy and (2) random fluctuations in the output Stokes power.

The finite phonon lifetime of a material is responsible for an energy interchange between the pump and Stokes field resulting in relaxation oscillations at the threshold. There is no modulation of the Stokes phase corresponding to these oscillations. It is predicted that materials with shorter phonon lifetimes can exhibit relaxation oscillations of longer duration than those with long phonon lifetimes. It was found that an initially stronger acoustic wave (resulting from a high focal intensity determined by the focal length of the lens) shortens the relaxation oscillations at the threshold energy since the Stokes pulse can use the energy stored in the acoustic field after initially overshooting. Also, a small immersion length achieved by a large cell to lens separation reduces the threshold relaxation oscillations. All together, short focal length, short immersion length, and large phonon lifetime provide the best parameter space for removing the threshold relaxation oscillations.

SBS initiated from microscopic noise shows large scale stochastic amplitude modulation in the output Stokes beam. Simultaneous and corresponding jumps in the Stokes phase are observed. We have determined a parameter regime where this modulation is minimized or eliminated, thus predicting conditions for optimized, reliable SBS.

(1) Longer phonon lifetime provides a better suppression of instabilities in the Stokes pulse.

(2) Depending on the input energy and focused spot size, the pump and Stokes field can be confined to a small region near the entrance of the cell (high energies, short immersion length) or distributed towards the focal point for low energies and long immersion length. For high input energies or short immersion length the time for propagation through this region $T_{l_{\rm dep}}$ is small enough to suppress many of the fluctuations reaching this region with duration $T_s > T_{\rm dep}$. Short immersion length achieved by large cell to lens separation is more desirable since $T_{l_{\rm dep}}$ can be reduced more effectively and a higher reflectivity can be achieved, but will in practice be limited by optical breakdown of the SBS material or cell window.

(3) Another parameter that can be used effectively to suppress the fluctuations is pulse duration. Our results showed that for a shorter pulse duration (i.e., higher peak power) the number of fluctuations was reduced dramatically.

[1] B. Y. Zel'dovich, N. F. Pilipetsky, and V. Shkunov, *Principles of Phase Conjugation* (Springer-Verlag, Berlin, 1985).

[2] D. A. Rockwell, IEEE J. Quantum Electron. **24**, 1124 (1988).

[3] D. T. Hon, Opt. Lett. **5**, 516 (1980).

[4] M. J. Damzen and H. Hutchinson, IEEE J. Quantum Electron. **19**, 7 (1983).

[5] N. G. Basov, V. F. Efimkov, I. G. Zubarev, A. V. Kotov, S. I. Mikhailov, and M. G. Smirnov, Pis'ma Zh. Éksp. Teor. Fiz. **28**, 215 (1978) [JETP Lett. **28**, 197 (1978)].

[6] M. Valley, G. Lombardi, and R. Aprahamian, J. Opt. Soc. Am. B **3**, 1492 (1986).

[7] K. D. Ridley and A. M. Scott, J. Opt. Soc. Am. B **13**, 900 (1996).

[8] S. M. Wandzura, in *Proceedings of the Conference on Laser and Electro-Optics, Anaheim, CA, 1988* (Optical Society of America, Washington, DC, 1988), p. 8.

[9] E. M. Dianov, A. Y. Karasik, A. V. Lutchnikov, and A. N. Pilipetskii, Opt. Quantum Electron. **21**, 381 (1989).

[10] R. W. Boyd, K. Rzazewski, and P. Narum, Phys. Rev. A **42**, 5514 (1990).

[11] A. L. Gaeta and R. W. Boyd, Phys. Rev. A **44**, 3205 (1991).

[12] T. R. Moore, A. L. Gaeta, and R. W. Boyd, in *Proceedings of International Quantum Electronics Conference, USA, 1993* (Optical Society of America, Washington, DC, 1993), pp. 394–395.

[13] M. S. Mangir, J. J. Ottusch, D. C. Jones, and A. Rockwell, Phys. Rev. Lett. **68**, 1702 (1992).

[14] W. P. Brown and S. M. Wandzura, in *Proceedings of the Conference on Laser and Electro-Optics, Anaheim, CA, 1988* (Ref. [8]), p. 10.

[15] J. Munch, R. F. Wuerker, and M. J. LeFebvre, Appl. Opt. **28**, 3099 (1989).

[16] V. Devrelis, M. O'Connor, J. Munch, S. Afshaarvahid, C. J. Wei, and A. M. Grisogono, in *Proceedings of International Quantum Electronics Conference, Sydney, Australia, 1996* (Optical Society of America, Washington, DC, 1996), p. 164.

[17] V. Devrelis, Ph.D. thesis, University of Adelaide, 1997 (unpublished).

[18] N. G. Basov, I. G. Zubarev, A. B. Miranov, S. I. Mikhailov, and A. Y. Okulov, Pis'ma Zh. Éksp. Teor. Fiz. **31**, 685 (1980) [JETP Lett. **31**, 645 (1980)].

[19] M. V. Vasil'ev, A. L. Gyulameryan, A. V. Mamaev, V. V. Ragul'skii, P. M. Semenov, and V. G. Siderovich, Pis'ma Zh. Éksp. Teor. Fiz. **31**, 673 (1980) [JETP Lett. **31**, 634 (1980)].

[20] V. I. Bespalov, A. A. Betin, G. A. Pasmanik, and A. A. Shilov, Pis'ma Zh. Éksp. Teor. Fiz. **31**, 668 (1980) [JETP Lett. **31**, 630 (1980)].

[21] E. Kuzin, M. Petrov, and A. Fotiadi, *Principles of Phase Conjugation* (Springer-Verlag, Berlin, 1994).

[22] J. C. Englund and C. M. Bowden, Phys. Rev. Lett. **57**, 2661 (1986).

[23] C. M. Bowden and J. C. Englund, Opt. Commun. **67**, 71 (1988).

[24] Y. Akiyama, K. Midorikawa, M. Obara, and H. Tashiro, J. Opt. Soc. Am. B **8**, 2459 (1991).

[25] D. C. MacPherson, R. C. Swanson, and J. L. Carlsten, Phys. Rev. Lett. **61**, 66 (1988).

[26] W. Kaiser and M. Maier, in *Stimulated Rayleigh, Brillouin and Raman Spectroscopy, Laser Handbook*, edited by F. T. Arecchi and E. O. Schuls-Dubis (North-Holland, Amsterdam, 1972), Vol. 2, pp. 1077–1149.

[27] G. C. Valley, IEEE J. Quantum Electron. **22**, 704 (1986).

[28] A. Kummrow and H. Meng, Opt. Commun. **83**, 342 (1991).

[29] R. Chu, M. Kanefsky, and J. Falk, J. Appl. Phys. **71**, 4653 (1992).

[30] R. Menzel and H. J. Eichler, Phys. Rev. A **46**, 7139 (1992).

[31] C. L. Tang, J. Appl. Phys. **37**, 2945 (1966).

[32] M. O'Conor, Ph.D. thesis, University of Adelaide, 1997 (unpublished).

[33] D. C. MacPherson and J. L. Carlsten, J. Opt. Soc. Am. B **4**, 1853 (1987).

[34] Z. M. Benenson *et al.*, Pis'ma Zh. Éksp. Teor. Fiz. **42**, 164 (1985) [JETP Lett. **42**, 202 (1985)].

[35] E. M. Dianov, A. Y. Karasik, A. V. Lutchnikov, and A. K. Senatorov, Kvant. Elektron. (Moscow) **16**, 778 (1989) [Sov. J. Quantum Electron. **19**, 508 (1989)].

[36] A. A. Fotiadi and E. A. Kuzin, in *Proceedings of International Quantum Electronics Conference, USA, 1994* (Optical Society of America, Washington, DC, 1994), p. 84.

E.4 Paper II

S. Afshaarvahid and J. Munch, "*A Transient, 3-dimensional model of Stimulated Brillouin Scattering*", accepted for publication in the "Journal of Nonlinear Optical Physics and Materials". To be appeared in JNOPM, Vol. 9, either No. 3 or No. 4.

Afshaarvahid, S. & Munch, J. (2001) A transient 3 dimensional model of stimulated brillouin scattering.
Journal of Nonlinear Optical Physics and Materials, v. 10(1), pp. 1-27

NOTE:
This publication is included after page 168 in the print copy of the thesis held in the University of Adelaide Library.

It is also available online to authorised users at:

http://doi.org/10.1142/S0218863501000401

Bibliography

[1] R. Chu, M. Kanefsky, and J. Falk, J. Appl. Phys. **71**, 4653 (1992).

[2] V. Devrelis, Ph.D. thesis, The University of Adelaide, 1997.

[3] B. Y. Zel'dovich, N. F. Pilipetsky, and V. V. Shkunov, *Principles of Phase Conjugation* (Springer-Verlag, Berlin Heidelberg, 1985).

[4] M. O'Connor, Ph.D. thesis, The University of Adelaide, 1997.

[5] R. W. Boyd, *Nonlinear Optics* (Academic Press Inc., California 92101-4495, USA, 1992).

[6] B. Y. Zel'dovich, V. I. Popovichev, V. I. Ragul'skii, and F. S. Faizullov, Sov. Phys. JETP Lett. **15**, 109 (1972).

[7] M. J. Damzen and H. Hutchinson, IEEE Journal of Quantum Electronics **19**, 7 (1983).

[8] G. C. Valley, IEEE Journal of Quantum Electronics **22**, 704 (1986).

[9] S. M. Wandzura, *Proceedings of the Conference on Laser and Electro-Optics, Anaheim, CA, 1988* (Optical Society of America, Washington, DC, 1988), p. 8.

[10] W. P. Brown and S. M. Wandzura, *Proceedings of the Conference on Laser and Electro-Optics, Anaheim, CA, 1988* (Optical Society of America, Washington, DC, 1988), p. 10.

[11] E. M. Dianov, A. Y. Karasik, A. V. Lutchnikov, and A. N. Pilipetskii, Optical and Quantum Electronics **21**, 381 (1989).

[12] J. Munch, R. F. Wuerker, and M. J. LeFebvre, Applied Optics **28**, 3099 (1989).

[13] A. L. Gaeta and R. W. Boyd, Physical Review A **44**, 3205 (1991).

[14] M. S. Mangir, J. J. Ottusch, D. C. Jones, and A. Rockwell, Physical Review Letters **68**, 1702 (1992).

[15] C. B. Dane, W. A. Neuman, and L. A. Hackel, Optics Letters **17**, 1271 (1992).

[16] T. R. Moore, A. L. Gaeta, and R. W. Boyd, *Proceedings of International Quantum Electronics Conference, USA, 1993* (Optical Society of America, Washington, DC, 1993), pp. 394–395.

[17] R. Chu, M. Kanefsky, and J. Falk, J. Opt. Soc. Am. B **11**, 331 (1994).

[18] E. Kuzin, M. Petrov, and A. Fotiadi, *Principles of Phase Conjugation* (Springer-Verlag, Berlin, 1994).

[19] V. Devrelis, M. O'Connor, J. Munch, S. Afshaarvahid, C. J. Wei, and A. M. Grisogono, *Proceedings of International Quantum Electronics Conference, Sydney, Australia , 1996* (Optical Society of America, Washington, DC, 1996), p. 164.

[20] S. Afshaarvahid, V. Devrelis, and J. Munch, Physical Review A **57**, 3961 (1998).

[21] P. Suni and J. Falk, J. Opt. Soc. Am. B **3**, 1681 (1986).

[22] E. J. Miller, M. D. Skeldon, and R. W. Boyd, Applied Optics **28**, 92 (1989).

[23] C. L. Tang, J. Appl. Phys. **37**, 2945 (1966).

[24] R. Menzel and H. J. Eichler, Physical Review A **46**, 7139 (1992).

[25] R. H. Lehmberg, J. Opt. Scc. Am. **73**, 558 (1983).

[26] P. H. Hu, J. A. Goldstone, and S. Ma, J. Opt. Soc. Am. B **6**, 1813 (1989).

[27] A. Kummrow, Optics Communications **96**, 185 (1993).

[28] T. R. Moore and R. W. Boyd, Journal of Nonlinear Optical Physics and Materials **5**, 387 (1996).

[29] T. R. Moore, G. L. Fischer, and R. W. Boyd, Journal of Modern Optics **45**, 735 (1998).

[30] I. Y. Anikeev, I. G. Zubarev, and S. I. Mikhailov, Sov. J. Quantum Electron **16**, 88 (1986).

[31] M. O'Connor, V. Devrelis, and J. Munch, in *Proceedings of the International Conference on Lasers'95*, edited by V. J. Corcoran and T. A. Goldman (STS Press, Mclean, VA, 1996), p. 500.

[32] I. Y. Anikeev and J. Munch, Optical and Quantum Electronics **31**, 545 (1999).

[33] S. Afshaarvahid, J. Munch, and V. Devrelis, *Technical Digest, CLEO/Pacific Rim'97* (IEEE, Piscataway, Nj 08855-1331, 1997), p. 223.

[34] S. Afshaarvahid, V. Devrelis, and J. Munch, in *XI AOS Conference, Book of Abstracts*, edited by M. W. Hamilton (AOS, Adelaide, Australia, 1997), p. fp35.

[35] S. Afshaarvahid and J. Munch, *In Conference on Lasers and Electro-Optics* (Optical Society of America, Washington DC, 1999), pp. 94–95.

[36] *Optical Phase Conjugation*, edited by R. A. Fisher (Academic Press, 111 Fifth Avenue, New York, New York 10003, 1983).

[37] B. Y. Zel'dovich, N. F. Pilipetsky, and V. Shkunov, *Principles of Phase Conjugation* (Springer-Verlag, Berlin Heidelberg, 1985).

[38] P. W. Milonni and J. H. Eberly, *Lasers* (John Wiley Sons, USA, 1988).

[39] M. Gower and D. Proch, *Optical Phase Conjugation* (Spring-verlag, Berlin Heidelberg, 1994).

[40] D. Gabor, Nature **161**, 777 (1948).

[41] D. Gabor, Proc. R. Soc. London **A 197**, 454 (1949).

[42] E. N. Leith and J. Upatnieks, J. Opt. Soc. Am. **52**, 1123 (1962).

[43] E. N. Leith and J. Upatnieks, J. Opt. Soc. Am. **54**, 1295 (1964).

[44] H. Kogelnik, Bell Syst. Tech. J. **44**, 2451 (1965).

[45] J. Upatnieks, A. V. Lugt, and E. N. Leith, Applied Optics **5**, 589 (1966).

[46] H. Kogelnik and K. S. Pennington, Journal of Optical Society of America **58**, 273 (1968).

[47] H. J. Gerritsen, Appl. Phys. Lett. **10**, 237 (1967).

[48] V. I. Stepanov, E. I. Ivarkin, and A. S. Rubanov, Sov. Phys.-Dokl.-Tech. Phys. **16**, 46 (1971).

[49] O. Y. Nosach, V. I. Popovichev, V. V. Ragul"shy, and F. S. Faizullov, Sov. Phys. JETP Lett. **16**, 435 (1972).

[50] A. Yariv, IEEE J. Quantum Electron **QE-14**, 650 (1978).

[51] *CRC Handbook of Laser Science and Technology*, edited by M. J. Weber (CRC Press, Boca Raton, Florida 33431, 1995).

[52] B. Y. Zel'dovich and V. V. Shkunov, Sov. J. Quantum Electron. **7**, 610 (1977).

[53] A. D. Kudryavtseva, A. I. Sokolovskaia, J. Gazengel, N. P. Xuan, and G. Rivoire, Opt. Commun. **26**, 446 (1978).

[54] P. N. Butcher and D. Cotter, *The Elements of Nonlinear Optics* (Cambridge University Press, Cambridge CB2 1RP UK, 1990).

[55] Y. R. Shen, *The Principles of Nonlinear Optics* (John Wiley Sons, USA, 1984).

[56] R. W. Hellwarth, J. Opt. Soc. Am. **67**, 1 (1977).

[57] D. M. Bloom and G. C. Bjorklund, Appl. Phys. Lett **31**, 592 (1977).

[58] P. F. Liao and D. M. Bloom, Opt. Lett. **3**, 4 (1978).

[59] D. M. Pepper, J. AuYeung, D. Fekete, and A. Yariv, Opt. Lett. **3**, 7 (1978).

[60] G. Martin and R. W. Hellwarth, Appl. Phys. Lett. **6**, 371 (1979).

[61] F. T. S. Yu, S. Wu, S. Rajan, and A. Mayers, Opt. Comm. **92**, 205 (1992).

[62] L. P. Schelonka and M. A. Karmer, Opt. Lett. **14**, 949 (1989).

[63] P. Kurz and T. Mukai, Opt. Lett. **21**, 1369 (1996).

[64] J. Nilsen and A. Yariv, Appl. Opt. **18**, 143 (1979).

[65] V. N. Blashchuk, F. F. Pilipetskii, and V. V. Shkunov, Sov. Phys. Dokl. **25**, 185 (1980).

[66] H. G. Winful and J. H. Marburger, Appl. Phys. Lett. **8**, 613 (1980).

[67] J. Buchert, R. Dorsinville, P. Delfyett, S. Krimchansky, and R. R. Alfano, Opt. Comm. **52**, 433 (1985).

[68] A. Einstein, Ann. Phys. **33**, 1275 (1910).

[69] L. Brillouin, Ann. Phys. **17**, 88 (1922).

[70] R. Y. Chiao, C. H. Townes, and B. P. Stoicheff, Phys. Rev. Lett. **12**, 592 (1964).

[71] W. Kaiser and M. Maier, in *"Stimulated Rayleigh, Brillouin and Raman Spectroscopy"*, *Laser Handbook*, edited by F. T. Arecchi and E. O. Schuls-Dubis (North-Holland, Amsterdam, 1972), Vol. 2, pp. 1077–1149.

[72] H. Yoshida, V. Kmetik, H. Fujita, M. Nakatsuka, T. Yamanaka, and K. Yoshida, Applied Optics **36**, 3739 (1997).

[73] N. F. Andreev, E. Khazanov, and G. A. Pasmanik, IEEE Journal of Quantum Electronics **28**, 330 (1992).

[74] R. A. Mullen, R. C. Lind, and G. C. Valley, Opt. Commun. **63**, 123 (1987).

[75] S. Jackel, P. Shalev, and R. Lallouz, Optics Communications **101**, 411 (1993).

[76] R. Brewer, Appl. Phys. Lett. **5**, 127 (1964).

[77] R. S. Pierre, H. Injeyan, and J. Berg, in *Proceedings of the Conference on Laser and Electro-Optics* (Optical Society of America, Washington, DC, 1992), p. 180.

[78] T. V. Forrester and R. J. Glauber, Phys. Rev. A **3**, 1984 (1971).

[79] R. W. Boyd, K. Rzazewski, and P. Narum, Phys. Rev. A **42**, 5514 (1990).

[80] V. I. Bespalov, A. A. Betin, G. A. Pasmanik, and A. A. Shilov, JETP Lett. **31**, 630 (1980).

[81] M. V. Vasil'ev, A. L. Gyulameryan, A. V. Mamaev, V. V. Ragul'skii, P. M. Semenov, and V. G. Siderovich, JETP Lett. **31**, 634 (1980).

[82] A. A. Fotiadi, E. A. Kuzin, M. P. Petrov, and A. A. Ganichev, Sov. Tech. Phys. Lett. **15**, 434 (1989).

[83] N. G. Basov, I. G. Zubarev, A. B. Miranov, S. I. Mikhailov, and A. Y. Okulov, JETP Lett. **31**, 645 (1980).

[84] F. A. Hopf, Phys. Rev. A **20**, 2064 (1979).

[85] K. Druhl, Physical Review Letters **51**, 1171 (1983).

[86] J. C. Englund and C. M. Bowden, Phys. Rev. Lett. **57**, 2661 (1986).

[87] D. C. MacPherson and J. L. Carlsten, J. Opt. Soc. Am. B **4**, 1853 (1987).

[88] D. C. MacPherson, R. C. Swanson, and J. L. Carlsten, Phys. Rev. Lett. **61**, 66 (1988).

[89] D. C. MacPherson, R. C. Swanson, and J. L. Carlsten, Phys. Rev. A **39**, 3487 (1989).

[90] M. G. Raymer, Z. W. Li, and I. A. Walmsley, Physical Review Letters **63**, 1586 (1989).

[91] K. Midorikawa, H. Tashiro, Y. Akiyama, and M. Obara, Physical Review A **41**, 562 (1990).

[92] Y. Akiyama, K. Midorikawa, M. Obara, and H. Tashiro, J. Opt. Soc. Am. B **8**, 2459 (1991).

[93] A. Kummrow and H. Meng, Optics Communications **83**, 342 (1991).

[94] L. D. Landau and E. M. Lifshitz, *Fluid Mechanics* (Pergamon Press, Oxford, England, 1959).

[95] D. T. Hon, Opt. Lett. **5**, 516 (1980).

[96] Z. M. Benenson, F. V. Bunkin, D. V. Vlasov, E. M. Dianov, A. Y. Karasik, A. V. Luchnikov, E. P. Shchebnev, , and T. V. Yakovleva, JETP Lett. **42**, 202 (1985).

[97] E. M. Dianov, A. Y. Karasik, A. V. Lutchnikov, and A. K. Senatorov, Sov. J. Quantum Electron **19**, 508 (1989).

[98] A. A. Fotiadi and E. A. Kuzin, *Proceedings of International Quantum Electronics Conference, USA, 1994* (Optical Society of America, Washington, DC, 1994), p. 84.

[99] I. Y. Anikeev, I. G. Zubarev, and S. I. Mikhailov, Sov. Phys. JETP **57**, 978 (1983).

[100] G. C. Valley, J. Opt. Soc. Am. B **9**, 1440 (1992).

[101] A. E. Siegman, *Lasers* (University Science Books, Mill Valley, California, 1986).

[102] A. E. Siegman, *Proceedings of the International Conference on Lasers'95* (STS Press, McLean, VA, 1995), pp. 1–12.

[103] A. A. Betin, A. F. Vasil'ev, O. V. Kulagin, V. G. Manishin, and V. E. Yashin, Sov. Phys. JETP **62**, 468 (1985).

[104] A. F. Vasil'ev and V. E. Yashin, Sov. J. Quantum Electron. **17**, 644 (1987).

[105] J. J. Ottusch and D. A. Rockwell, Optics Letters **16**, 369 (1991).

[106] R. H. Lehmberg, Optics Communications **43**, 369 (1982).

[107] V. E. Yashin and V. I. Kryzhanovskii, Opt. Spectrosc. **55**, 101 (1983).

[108] L. P. Schelonka and C. M. Clayton, Optics Letters **13**, 42 (1988).

[109] V. E. Yashin, V. I. Kryzhanovskii, and V. A. Serebryakov, Sov. J. Quantum Electron **12**, 1086 (1982).

[110] P. Narum, M. D. Skeldon, and R. W. Boyd, IEEE Journal of Quantum Electronics **22**, 2161 (1986).

[111] M. A. O'Key and M. R. Osborne, Optics Communications **89**, 269 (1992).

[112] A. A. Filippo and M. R. Perrone, IEEE Journal of Quantum Electronics **28**, 1859 (1992).

[113] A. A. Filippo and M. R. Perrone, Appl. Phys. B **55**, 71 (1992).

[114] M. R. Perrone and Y. B. Yao, IEEE Journal of Quantum Electronics **30**, 1327 (1994).

[115] D. L. Bullock, N. M. Nguyen-Vo, and S. J. Pfeifer, IEEE Journal of Quantum Electronics **30**, 805 (1994).

[116] G. Cook and K. D. Ridley, Optics Communications **130**, 192 (1996).

[117] M. S. Jo and C. H. Nam, Applied Optics **36**, 1149 (1997).

[118] I. S. Gradshteyn and I. W. Ryzhik, *Table of Integrals Series and Products* (Academic Press INC, New York, New York 10003, 1965).

[119] F. L. Pedrotti and S. J. L. S. Pedrotti, *Introduction to Optics* (Prentice-Hall, Upper Saddle River, New Jersey 07458, 1993).